Universidad de Granada

Departamento de Física Aplicada

Analysis of the Sierra Nevada ELF station recordings: a contribution to the study of the Schumann Resonances

PhD Thesis

Programa de Doctorado en Física y Ciencias del Espacio

Author:

Jesús Rodríguez Camacho

Supervised by:

María del Carmen Carrión Pérez

Alfonso Salinas Extremera

December 2022

Editor: Universidad de Granada. Tesis Doctorales
Autor: Jesús Rodríguez Camacho
ISBN: 978-84-1117-748-1
URI: https://hdl.handle.net/10481/80703

A mis padres
y a mis abuelos

Agradecimientos

Después de mucho esfuerzo ha llegado el momento de cerrar una de las etapas más importantes de mi vida, unos años llenos de aventuras que ha merecido la pena vivir. Me siento muy afortunado de poder afirmar que todas las personas, compañeros y amigos con quienes he compartido esta etapa han hecho de ella una maravillosa experiencia que ha ayudado a hacer de mí un mejor investigador y una mejor persona. Por ello, debo dedicarles un agradecimiento en las siguientes líneas.

En primer lugar, tengo que agradecer a mis padres el apoyo incondicional que me han dado durante toda mi vida. Jamás han dudado en acompañarme y en ofrecerme todo lo que he podido necesitar, sin importar el esfuerzo necesario para ello. Sin duda, esta tesis no existiría sin ellos.

Otras dos personas sin las que no habría sido capaz de terminar mi tesis son mis dos directores: Mª Carmen y Alfonso. Desde el primer hasta el último día habéis depositado una enorme confianza en mí y habéis tenido una paciencia infinita con mi trabajo. Cuando he necesitado ayuda siempre habéis sabido cómo orientarme, me he sentido muy tranquilo sabiendo que estabais detrás de mí. A Mª Carmen le agradezco el haberme orientado tantas veces en busca de lo mejor para mi carrera científica a largo plazo, incluso desde antes de la tesis, con experiencia e ideas claras, y cuidando cada detalle. A Alfonso le agradezco el haber estado siempre en la primera línea de nuestro campo, sus inagotables propuestas de investigación y su imprescindible empeño en mejorar cada aspecto de los trabajos. Además, ambos sois referentes para mí, no solo en el plano científico, sino también en el plano personal, y os debo una parte de quien soy hoy. Mi tesis y mi desarrollo como investigador han sido en todo momento una prioridad para vosotros. Quiero que sepáis que valoro muchísimo vuestro esfuerzo conmigo. Sois los mejores directores que he podido tener.

Además, quiero agradecer a Jorge Portí su implicación y ayuda en esta tesis. Ha sido muy útil contar con tu experiencia y, en muchas ocasiones, has facilitado que los trabajos salgan adelante. Y a David, Jesús Fornieles y Kiko les agradezco su ayuda en momentos más puntuales de la tesis. He aprendido mucho de ellos, por ejemplo, sobre técnicas de procesado de señal o sobre los detalles técnicos de la estación. Me ha motivado mucho trabajar a vuestro lado.

No puedo evitar acordarme en esta página, además, de todo el Departamento de Física Aplicada, mi Departamento, por integrarme desde el primer día y permitirme

impartir mis asignaturas favoritas: la Física General I y la Física General II. Me he sentido muy valorado y he trabajado muy cómodamente junto a todos vosotros. Siempre recordaré que me levantaba más feliz los días que me tocaba dar clase.

Mención aparte merece todo lo vivido durante mis estancias de investigación. Resulta difícil imaginar cómo en lugares tan distintos como Atenas, México y Toulouse uno puede sentirse incluso más querido que en casa.

Sobre Atenas... Podría mencionar tantas cosas y momentos increíbles que no cabrían ni en la tesis entera. Al ver por la ventana del avión ese paisaje en el que se mezclaban el mar, las islas, los barcos y muchas casas blancas presentí lo mucho que iba a disfrutar los meses que venían por delante. No me equivoqué. Agradezco a Yannis Kopsinis y Manu Morante la acogida que me dieron en el Departamento de Telecomunicaciones de la KAPA y lo mucho que me enseñaron sobre procesamiento de señal.

Pude visitar la Universidad Nacional Autónoma de México gracias a Marni Pazos, de quien valoro mucho que en todo momento me hiciera sentir como en casa. Recuerdo con mucho cariño a otras personas de allí, como Arturo e Irene, que me recibieron con entusiasmo y me presentaron la Ciudad de México y el observatorio de Coeneo. Agradezco al Instituto de Geofísica de Michoacán la invitación a su seminario y su interés en aprender sobre nuestras investigaciones.

En el IRAP de Toulouse tuve el privilegio de aprender sobre la magnetosfera y de investigar con mediciones de satélites, bajo la supervisión de Sergio Toledo. A Sergio le agradezco su interés en mi trabajo, sus explicaciones, su trato genial y su capacidad para resolver mis dificultades de programación en unos pocos segundos. Fue muy agradable trabajar contigo y con mis compañeras: Andrea, Naïs y el resto.

En definitiva, ha merecido la pena cada esfuerzo realizado durante estos años. La palabra "gracias" se me queda pequeña para expresar lo que siento hacia todas las personas extraordinarias que han sido protagonistas de esta etapa.

Esta tesis doctoral ha recibido financiación del Ministerio de Educación, Ciencia y Deporte, a través de la beca FPU15/04291, del programa de Formación de Profesorado Universitario, y del Ministerio de Economía y Competitividad, a través de los proyectos de investigación FIS2013-44975-P, FIS2017-90102-R y PID2020-112805GA-I00. También agradezco al IRAP de Toulouse y a la Asociación Universitaria Iberoamericana de Posgrado las ayudas económicas prestadas para mis estancias.

Resumen

Esta tesis está dedicada al estudio de las Resonancias de Schumann (RS) medidas en la estación de Sierra Nevada (Granada, España). Las RS se forman en la cavidad delimitada por la superficie de la Tierra y por la ionosfera, que es excitada principalmente por la actividad eléctrica atmosférica. Estas resonancias pertenecen a la banda de frecuencia extremadamente baja (ELF) del espectro electromagnético, y ocurren aproximadamente a las frecuencias de 8 Hz, 14 Hz, 20 Hz, 26 Hz, etc. Cada resonancia queda caracterizada por tres parámetros: su amplitud, su frecuencia central y su anchura.

Las RS están afectadas por las condiciones de la atmósfera a una escala global, y a través de su medida, en una estación situada en cualquier punto del planeta, se pueden extraer conclusiones sobre la evolución de los principales núcleos de actividad tormentosa del planeta y sobre el estado de la ionosfera. La investigación sobre estas resonancias comenzó en los últimos años del siglo XX, y ha estado vinculada al estudio de fenómenos atmosféricos, climáticos y espaciales. En la actualidad, el seguimiento de la actividad eléctrica atmosférica despierta un gran interés para el estudio del clima. Numerosos proyectos y acciones de investigación están destinados a mejorar la colaboración internacional entre infraestructuras de investigación en el campo de los fenómenos eléctricos atmosféricos.

Pocos años antes del comienzo de esta tesis, se diseñó y construyó una estación de medida de las componentes horizontales, Norte-Sur y Este-Oeste, del campo magnético en la banda ELF en Sierra Nevada (Granada, España), con el objetivo de contribuir a la investigación en el campo de las RS con nuevas medidas y con propuestas sobre el procesamiento de los datos y la interpretación de los resultados.

En esta tesis se discute la conveniencia de tener en cuenta y de indicar explícitamente la metodología utilizada para extraer los parámetros de las RS a partir de las medidas de campo magnético registradas en las estaciones. Para llevar a cabo dicha discusión, se propone una metodología de procesado que es aplicada para extraer los parámetros de las tres primeras RS de las medidas de la estación de Sierra Nevada, y es utilizada como ejemplo para estudiar cómo la elección de las diferentes opciones y parámetros que configuran la metodología

influye en los valores finales obtenidos para los parámetros de las RS. No es una práctica habitual en la literatura dar cuenta de la metodología empleada para obtener los parámetros de las RS, sin embargo, dado que su influencia sobre los resultados resulta ser sensible, consideramos conveniente indicarla de la forma más explícita posible de modo que los resultados obtenidos por distintos grupos de investigación puedan ser comparados con rigor.

La metodología propuesta para obtener los parámetros de las RS a partir de las medidas de la estación de Sierra Nevada consta de cuatro partes. En la primera, se calculan los espectros de amplitud de cada intervalo de medidas de campo magnético de 10 minutos de duración utilizando el método de Welch. En la segunda parte, se aplica un filtro para detectar y eliminar el ruido antropogénico que afecta a las medidas. Se describen las características de dicho ruido antropogénico. Para eliminar el ruido se emplea la técnica de interpolación lineal, en lugar de técnicas estadísticas que son más complejas y menos reproducibles. En la tercera parte se realiza un ajuste lorentziano sobre los espectros de amplitud. Se exploran diferentes métodos de minimización para llevar a cabo el ajuste, así como distintas formas de establecer los valores iniciales del ajuste y la banda de ajuste. En la cuarta parte, se calculan los parámetros de las RS a partir de la curva de ajuste. Los valores obtenidos para los parámetros de las RS se guardan con un formato específico para su posterior análisis. Se realiza un estudio cuantitativo de las diferencias en los valores de los parámetros de las RS causados por las diferentes opciones exploradas en todas las partes de la metodología propuesta.

El material empleado para aplicar esta metodología, consistente en una amplia colección de códigos, funciones, notebooks y programas desarrollados principalmente en el lenguaje de programación Python, se ha diseñado bajo el principio de máxima adaptabilidad a las medidas provenientes de otras estaciones ELF. Este material, junto con las medidas experimentales de campo magnético de la estación ELF de Sierra Nevada, se ha puesto a disposición de la comunidad científica.

Una vez obtenidos los parámetros de las RS, para realizar un estudio de sus variaciones regulares es necesario descartar o enmascarar los valores que corresponden a intervalos de medida para los que algún parámetro muestra un valor absurdo o inaceptable, para que estos no afecten demasiado a la tendencia. Para

determinar el intervalo de valores aceptables para cada parámetro de las RS, se realiza un estudio estadístico.

Para llevar a cabo el estudio de las variaciones de los parámetros de las RS, se ha creado una amplia colección de versátiles notebooks en Jupyter, que ayudan a analizar rápida y cómodamente las variaciones a distintas escalas temporales: diurna (intradía), diaria (a lo largo de varios días), mensual, estacional y anual. Se incluye en el análisis otra información aparte de los parámetros, como la saturación, la integral del espectro de potencia o la chi cuadrado. Estos notebooks tienen dos objetivos: generar gráficos diversos que permitan una rápida visualización de las variaciones de los parámetros las RS y exportar esa información en un formato conveniente para un análisis posterior. Se han ideado para ser adaptables a las necesidades del investigador que los utilice, pues incluyen varios parámetros para determinar distintas opciones para realizar el análisis y para modificar la apariencia de los gráficos. La colección de notebooks junto a una explicación detallada de los mismos, ejemplos de su uso y los datos de los parámetros de las RS, son puestos a disposición de la comunidad científica.

El estudio de las variaciones regulares de los parámetros de las RS obtenidos a partir de las medidas de campo magnético en la estación ELF de Sierra Nevada, haciendo uso de los notebooks anteriores, se ha realizado desde marzo de 2013 hasta febrero de 2017. Los resultados se comparan con los obtenidos en trabajos previos, en los que se investiga la relación de las variaciones de las RS con fenómenos atmosféricos, medioambientales y espaciales, como los patrones de evolución diurna y estacional de los principales núcleos tormentosos del planeta (Asia, África y América), la oscilación Sur "El Niño" o los ciclos de actividad solar. La mayoría de los resultados presentados en esta tesis están en línea con los de trabajos previos, si bien hay algunas discrepancias que requieren más investigación.

También se ha aplicado la técnica conocida como *Singular Spectrum Analysis* a las series temporales de los parámetros de las RS con el fin de obtener las componentes principales de dichas series. Para aplicar este análisis se ha implementado un esquema para rellenar los huecos en los que no hay disponibles datos experimentales. Entre las componentes principales de prácticamente todos los parámetros se han hallado la componente anual y la semianual.

Los espectros de amplitud de algunos de los intervalos de medida muestran diferentes anomalías, como picos extraños en algunas frecuencias, una amplitud inusualmente alta para la parte de bajas (o altas) frecuencias del espectro, demasiado ruido, dificultad para observar las RS, etc. Se ha realizado un registro visual y una clasificación de las anomalías detectadas en los espectros de amplitud de las medidas de la estación de Sierra Nevada entre marzo y julio de 2013, y se ha desarrollado un conjunto de funciones para estudiar si afectan a los valores de los parámetros de las RS.

Abstract

This thesis is devoted to the study of the Schumann Resonances (SRs) measured at the Sierra Nevada station (Granada, Spain). The SRs occur in the cavity delimited by the Earth's surface and the ionosphere, which is mainly excited by the atmospheric electric phenomena. These resonances belong to the Extremely Low Frequency (ELF) band of the electromagnetic spectrum, and their approximate frequencies are 8 Hz, 14 Hz, 20 Hz, 26 Hz, etc. Each resonance is defined by three parameters: its amplitude, its central frequency and its width.

The SRs are affected by the atmospheric conditions at a global scale, and their measurements in a station, located at any point of the globe, allow to obtain conclusions on the evolution of the main lightning centers of the globe and on ionospheric concerns. The research on these resonances began in the last years of the twentieth century, and has been linked to the study of atmospheric, climatic and space phenomena. Nowadays, the monitoring of the lightning activity arises great interest for climatic studies. Many projects and actions are committed to enhancing international collaboration among different groups and infrastructures in the field of atmospheric electricity.

A few years before the beginning of this thesis, a new ELF measurement station was designed and deployed at Sierra Nevada (Granada, Spain), to record the horizontal (North-South and East-West) components of the magnetic field. The aim was to contribute to the research in the area of the SRs with new measurements and with proposals on the processing methodology and the interpretation of the results.

The convenience to explicitly indicate the methodology used to extract the SR parameters from the raw ELF magnetic field measurements is discussed in this thesis. With that purpose, a processing methodology has been proposed and applied to extract the parameters of the three first SRs from the measurements at the Sierra Nevada station. This methodology is used as an example to study how the choice of the different options and parameters that configure the methodology affects the values obtained for the parameters. In the literature, it is not usual to account for the processing methodology used to extract the SR parameters; however, as its influence on the results is found to be noticeable, we

consider that it is convenient to specify the methodology as explicitly as possible so that the results obtained by different research groups can be compared with rigor.

The proposed methodology to obtain the SR parameters from the Sierra Nevada measurements consists of four stages. In the first one, the amplitude spectra of each 10 min interval of recordings are calculated making use of the Welch method. In the second one, a filter is applied to detect and eliminate the anthropogenic noise that affects the measurements. The features of the anthropogenic noise in Sierra Nevada are presented. The linear interpolation technique is applied to eliminate the noise, instead of statistical techniques that are more complex and less reproducible. In the third stage, a Lorentzian fit is performed on the spectra. Different options for the minimization method, the initial values and the fitting band are explored. In the fourth stage, the SR parameters are defined and calculated from the fitting curve. The values obtained for the SR parameters are stored with a specific format for a latter analysis. A quantitative study of the differences in the values of the parameters caused by the different choices explored in the methodology is carried out.

The material used to apply this methodology, which consists of a wide range of codes, functions, notebooks and programs developed mainly in Python language, has been designed under the principle of maximum adaptability to the recordings from other ELF stations around the world. This material, together with the experimental magnetic field measurements from the Sierra Nevada station, has been made available to the scientific community.

Once the SR parameters are obtained, we perform a study of their regular variations. To do this, we need to mask or disregard the values that correspond to time intervals for which any parameter shows an absurd or unacceptable value so that they do not largely affect the trends. To decide the range of acceptable values for each parameter, a statistical study is performed.

For the study of the regular variations of the SR parameters, a wide collection of versatile Jupyter notebooks have been created to comfortably study their variations at different temporal scales: diurnal, daily, monthly, seasonal and annual. Other information apart from the parameters, such as the saturation rate, the power spectrum amplitude or the chi square, is analyzed. The notebooks have

two main purposes: to generate diverse charts that allow a fast visualization of the variations of the SR parameters and to export that information in a convenient format for a later quantitative analysis. They are devised to be adaptive to the user, as they have many parameters that determine some options to perform the analysis and also to modify the graphical configuration of the charts. The collection of notebooks together with a detailed explanation of their features, some examples of their use and the SR parameters data are made available to the scientific community.

A study of the regular variations of the SR parameters extracted from the Sierra Nevada station magnetic field recordings from March, 2013, to February, 2017, is presented making use of the mentioned notebooks. The results are compared with previous works on the relation of the SR variations and atmospheric, environmental and space phenomena, such as the diurnal and seasonal patterns of the main global tropical thunderstorm centers (Asia, Africa and America), "El Niño" Southern Oscillation, and the cycles of solar activity. Most of the features observed in previous works are confirmed in the results of this thesis, although there are some discrepancies that demand future research.

The principal components of the evolution of the time series of the SR parameters are also obtained, using the Singular Spectrum Analysis. With that purpose, a scheme to fill the blanks in the experimental magnetic field recordings has been implemented. The annual and the semiannual components are found among the principal components of the time series of almost all the parameters.

For some time intervals, the amplitude spectra show different anomalies, such as strange peaks at certain frequencies, an unusually high amplitude for low (or high) frequencies, too much noise, difficulty to see the SRs, etc. These anomalies are recorded and classified, and a collection of functions is presented to study whether or not they affect the values of the SR parameters. The anomalies detected in the amplitude spectra of the Sierra Nevada recordings from March to July, 2013, are studied.

Publications

Papers:

- **Rodríguez-Camacho, J.**, Fornieles, J., Carrión, M.C., Portí, J.A., Toledo-Redondo, S., and Salinas, A. (2018).
  On the Need of a Unified Methodology for Processing Schumann Resonance Measurements.
  Journal of Geophysical Research: Atmospheres, 123, 13,277–13,290.
  https://doi.org/10.1029/2018JD029462
  Impact factor (JCR 2018): 3.633.
  Q1, 17/86 in Meteorology and Atmospheric Sciences.
  (Chapter 3)

- Salinas, A., **Rodríguez-Camacho, J.**, Portí, J., Carrión, M.C., Fornieles, J., and Toledo-Redondo, S. (2022).
  Schumann resonance data processing programs and four-year measurements from Sierra Nevada ELF station.
  Computers and Geosciences, 105148.
  https://doi.org/10.1016/j.cageo.2022.105148
  Impact factor (JCR 2021): 5.168.
  Q1, 33/202 in Geosciences, Multidisciplinary.
  (Chapter 5)

- **Rodríguez-Camacho, J.**, Salinas, A., Carrión, M.C., Portí, J., Fornieles, J., and Toledo-Redondo, S. (2022).
  Four Year Study of the Schumann Resonance Regular Variations Using the Sierra Nevada Station Ground-Based Magnetometers.
  Journal of Geophysical Research: Atmospheres, 127, e2021JD036051.
  https://doi.org/10.1029/2021JD036051
  Impact factor (JCR 2021): 5.217.
  Q1, 22/94 in Meteorology and Atmospheric Sciences.
  (Chapter 7)

Conference proceedings:

- **Rodríguez-Camacho, J.**, Blanco-Navarro, D., Gómez-Lopera, J.F., and Carrión, M.C. (2021).
  Application of the singular spectrum analysis to the time variations of the amplitude of schumann resonance measurements.
  2020 28th European Signal Processing Conference (EUSIPCO), 2215–2219.
  https://doi.org/10.23919/EUSIPCO.2018.8553019

- **Rodríguez-Camacho, J.**, Lopera, J.F.G., Salinas, A., Fornieles-Callejón, J., Portí, J., Blanco-Navarro, D., Carrión, M.C., and Camba, E.N. (2019).
  Graphical schemes designed to display and study the long-term variations of Schumann resonance.
  2019 27th European Signal Processing Conference (EUSIPCO), 1–5.
  https://doi.org/10.23919/EUSIPCO.2019.8903030

- **Rodríguez-Camacho, J.**, Fornieles-Callejon, J., Gomez-Lopera, J.F., Salinas, A., Portí, J., Blanco, D., and Carrión, M.C. (2019).
  An approach for long-term study of Schumann Resonances.
  Geophysical Research Abstracts, 21.
  https://meetingorganizer.copernicus.org/EGU2019/EGU2019-7708.pdf

- **Rodríguez-Camacho, J.**, Blanco-Navarro, D., Gómez-Lopera, J. F., Fornieles-Callejón, J., and Carrión, M.C. (2018).
  Separation of anthropogenic noise and extremely low frequency natural magnetic field using statistical features.
  2018 26th European Signal Processing Conference (EUSIPCO), 2405–2409.
  https://doi.org/10.23919/EUSIPCO.2018.8553019

- **Rodríguez-Camacho, J.**, Blanco, D., Gómez-Lopera, J. F., Fornieles-Callejón, J., and Carrión, M. C. (2017).
  A new method for anthropogenic noise removal in the ELF band based on ICA technique.
  2017 Computing and Electromagnetics International Workshop (CEM), 23–24.
  https://doi.org/10.1109/CEM.2017.7991868

Contents

Chapter 1. Introduction

The Schumann Resonances (SRs) are global natural electromagnetic (EM) resonances within the cavity formed by the Earth's surface and the ionosphere, which is excited mainly by lightning events. An illustration of this phenomenon is shown in Figure 1.1.

Figure 1.1. Illustration of the Earth-ionosphere cavity, and the SRs generated by lightning activity. The scheme is not scaled. From NASA, 2013. https://www.nasa.gov/mission_pages/sunearth/news/gallery/schumann-resonance.html.

The SRs belong to the Extremely Low Frequency (ELF) band of the EM spectrum, with approximate frequencies of 8 Hz, 14 Hz, 20 Hz, 26 Hz, etc. These resonances exhibit a global behavior and contain information about the ionospheric conditions and the stormy activity around the whole Earth. Some theoretical concerns about the SRs as well as previous works on the main features of the global lightning activity are shown in section 1.1.

One of the main applications of the study of the SRs is the monitoring of atmospheric, climatic and space phenomena. Some of the most relevant publications on the relation of the SRs with these phenomena are mentioned in section 1.2. At present, there is growing interest in the study of lightning for climatic purposes. Research agencies are putting forward strategies for global collaboration on this topic.

There are currently several ELF measurement stations at different locations around the world that measure the SRs. A new ELF measurement station was designed and deployed in Sierra Nevada (Granada, Spain) by the research group in which this

thesis has been carried out. The experimental data used to study the SRs in this thesis has been measured at that station from 2013 to 2017, and its relevant details are explained in section 1.3.

An overview of the current situation of the research on SRs is presented in section 1.4, outlining the major difficulties that must be addressed in the field to enhance international collaboration between different infrastructures. The motivation of this thesis is also presented in this section.

1.1. The Earth-ionosphere cavity as a waveguide. The lightning activity as its excitation

The Earth can be seen as a well-conducting sphere covered by a dielectric atmosphere. The thickness of the atmosphere is small compared the Earth's radius. The conductivity of the atmosphere gradually increases up to 6 magnitude orders, generating the ionosphere. This rapid increase in the atmospheric conductivity allows for treating the atmosphere as a dielectric layer between two relatively good conductors. This model is valid from arbitrary small frequencies to 10 MHz. When the radio frequency exceeds 10-20 MHz, the ionosphere becomes transparent (Nickolaenko & Hayakawa, 2014). Then, a spherical cavity is formed where the low frequency band waves propagate. We can consider that the approximate height of the lower ionosphere is 60 km during the day and 90 km during the night (Toledo-Redondo, 2012).

Although some scientists like Nikola Tesla in 1905 came up with the idea of the propagation of radio waves in this cavity, it was Schumann (1952) and Köning who first proposed the existence of a natural resonance inside this cavity excited by the planetary lightning activity. Schumann considered the terrestrial waveguide as an ideal one, made of two perfectly conducting concentric spheres separated by a height much smaller than the Earth's radius, a. Then, taking into account the reduced height of the atmosphere, Schumann obtained the following formula (Equation 1.1) for the eigenfrequencies of the Earth–ionosphere cavity (Nickolaenko & Hayakawa, 2014).

$$(ka)^2 = n(n+1), \quad n = 1, 2, 3... \tag{1.1}$$

where $k = \omega/c$ is the free space wave number, a is the Earth's radius, c is the light velocity in vacuum, $\omega = 2\pi f$ is the angular wave frequency, and n is the mode number. In this equation, if k is cleared, we can obtain the frequencies for the SRs as shown in Equation 1.2.

$$f_n = \frac{c}{2\pi a}\sqrt{n(n+1)}, \quad n = 1, 2, 3... \tag{1.2}$$

The values obtained for the first resonance frequencies are: f_1 = 10.6 Hz, f_2 = 18.3 Hz, f_3 = 26.0 Hz, etc.

Schumann and Köning tried to experimentally measure the resonant frequencies of the SRs. They could distinguish a waveform with a strong sinusoidal character with a frequency of about 9 Hz (Besser, 2007). But the results were dubious and unsatisfactory (Nickolaenko & Hayakawa, 2014). The experimental confirmation of the existence of the SRs arrived in 1960, with the work of Balser and Wagner (1960). They used more powerful spectral analysis techniques: they applied the Fourier transform to 10 minute long measurement series, and the resonant frequencies obtained did not match the predictions based on the formula given by Schumann (Equation 1.2). The approximate values for the first SRs were 8 Hz, 14 Hz, 20 Hz, etc. This difference can be explained because the assumptions of an ideal spherical waveguide made by Schumann were not realistic. The ionosphere height is not perfectly defined, the EM waves reflect at different altitudes as conductivity increases (Toledo-Redondo, 2012). Also, there are losses due to the finite ionosphere conductivity, and it causes that the resonant frequencies decrease. The spherical symmetry of the waveguide is not perfect: the day-night asymmetry, the non-uniform Earth magnetic field or the polar cap absorption are examples of this (Price, 2016).

A detailed synopsis of the historical development of the concept of SRs can be found in Besser (2007), which shows a review of relevant works about the physical and mathematical concerns of the SRs, especially about the obtention of the formula of the Equation 1.1.

The Earth-ionosphere cavity is mainly excited by lightning discharges, originating thus the SRs. For a single lightning event, with no horizontal extension, the electric and magnetic fields corresponding to the three first SR modes are shown in Figure 1.2, assuming the hypothesis of ideality of the Earth-ionosphere waveguide.

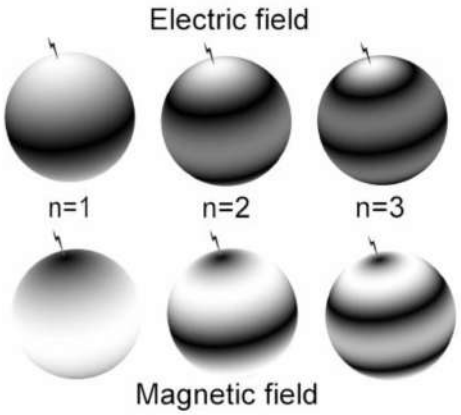

Figure 1.2. Electric and magnetic fields for the first three SR modes. White shading implies field maximum, and black shading implies field minimum. From Price (2016).

The electric field has a maximum at the position of the lightning event and at the antipode, while the magnetic field (orthogonal to the electric) has a minimum at the same locations, regardless of the mode. The analytical expression for the vertical electric field of the SRs assuming ideality conditions is given in Price (2016). The meaning of this result is that the amplitude of the SRs measured in a specific location depends on the intensity or the current momentum of the discharge and also on the relative distance between the lightning source and the observer.

The actual picture of the lightning activity in the atmosphere differs much from the previous hypothesis of one single vertical discharge with no horizontal extension. The real lightning discharges are not completely vertical or have zero horizontal extension. In addition, many events happen at different locations in a small period of time, so what we have is a superposition of EM fields generated by different sources, each one in a different location of the globe. A map showing the global distribution of lightning events is shown in Figure 1.3.

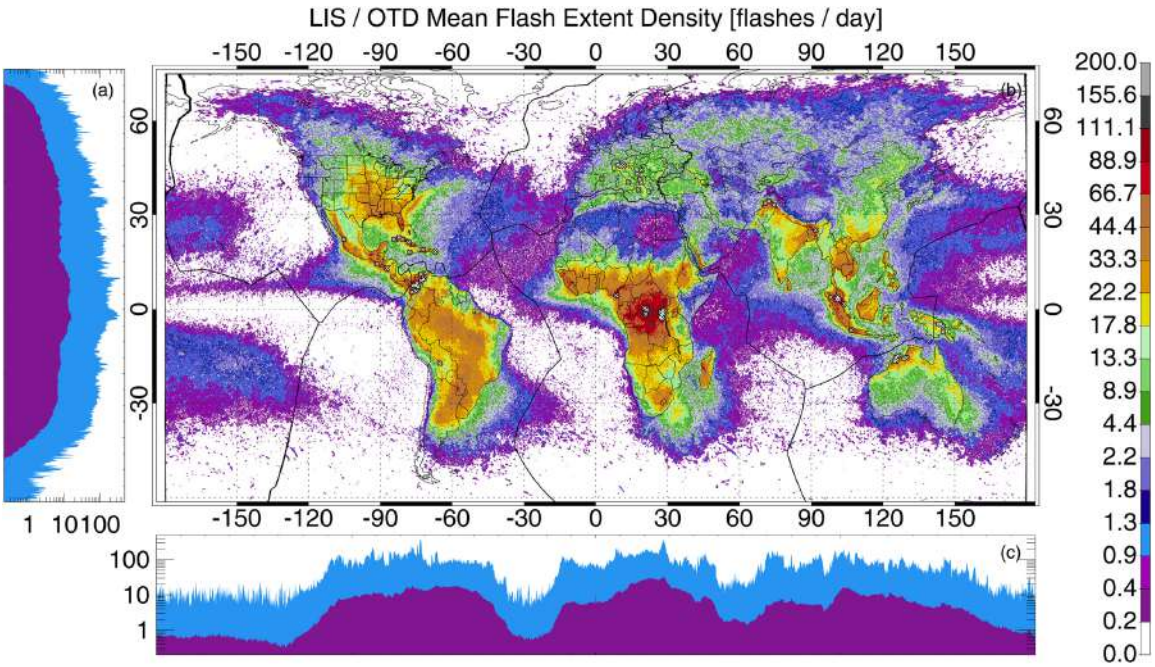

Figure 1.3. Global distribution of lightning flash rate in units of $km^{-2}yr^{-1}$. The lightning events have been detected with the Lightning Imaging Sensor (LIS) and the Optical Transient Detector (OTD) satellites. Mean (purple) and maximum (blue) values for each latitude and longitude are also shown on the left and below the map. From Peterson et al. (2021).

The activity of these three main centers follows a strong diurnal variation, with maximum activity in the local late afternoon (4pm - 5pm) and minimum activity in the local late morning (8am - 9am). This is shown in Figure 1.4. The African center is observed to be the most intense, followed by America and Asia (Blakeslee et al., 2014).

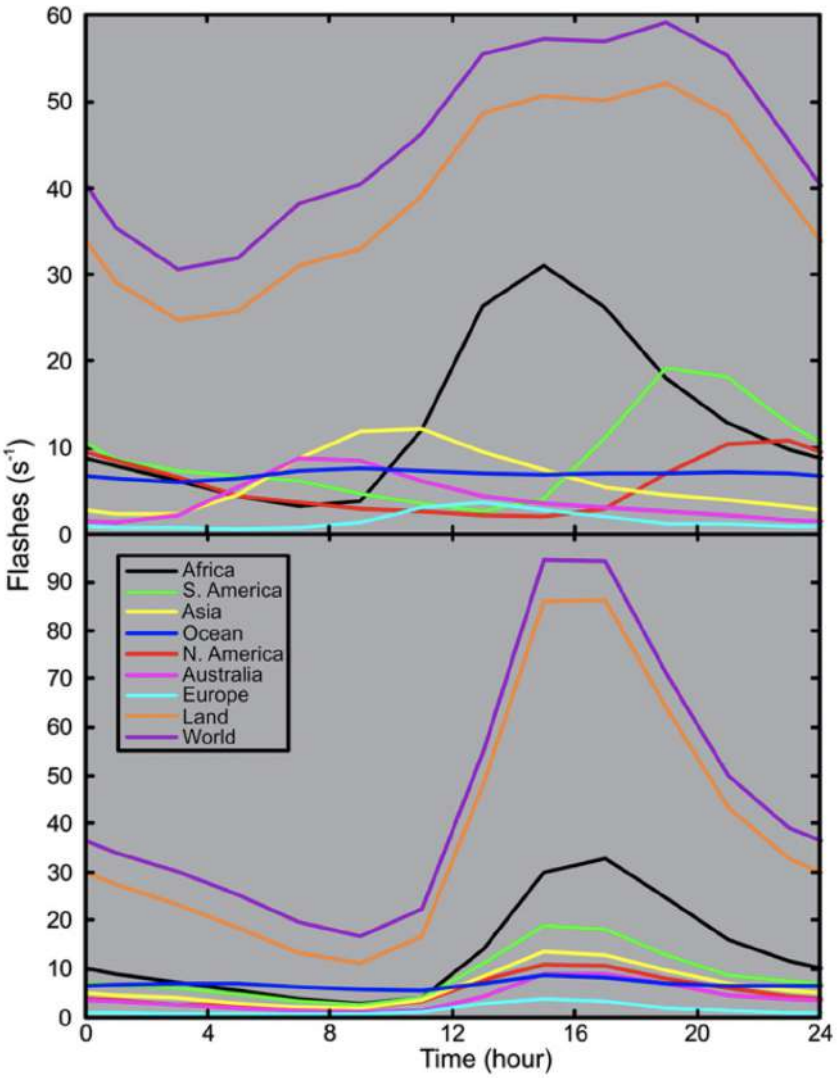

Figure 1.4. Diurnal patterns of the evolution of the lightning flash rate for the three main lightning centers, in UTC (above) and in the local time for each center location (below). Also, the flash rate at other locations and for land/ocean lightning flash rates are shown. From Blakeslee et al. (2014)

The lightning activity of the principal centers also follows a seasonal variation, as explained in Blakeslee et al. (2014), where we can see that in the boreal summer the world lightning rate is maximum, whereas it is minimum in the boreal winter. The data about the lightning event occurrence are obtained from the Optical Transient Detector and from the Lightning Imaging Sensor satellites in that work. The diurnal and seasonal variations of the lightning activity cause the same patterns of variations in the recorded SRs.

In addition to the lightning events produced in thunderstorms, there are other phenomena that may contribute to the SRs, such as the transient luminous events (TLEs), which are believed to be related to many of the SR transients (Q-bursts). The TLEs can be defined as large scale optical phenomena that occur above the

troposphere, in the mesosphere, the stratosphere or the lower ionosphere. These phenomena are closely related to the electrical activity in underlying thunderstorms (Pasko, 2010). Information on the features of the most common TLEs can be found in Chen et al. (2008), Geem et al. (2006), and Invernón (2018). There is growing interest in TLEs, and research agencies have recently launched missions devoted to the observation and study of these phenomena (Invernón, 2018).

1.2. Application of the SRs to the study of atmospheric, climatic and space phenomena

The research on the SRs has been linked to atmospheric, climatic and space phenomena since many years ago.

The correlation between the monthly variations of the SR parameters and the average temperature in the tropics is studied in Williams (1992), where the temperature is found to affect the SRs through the lightning flash rate, which increases nonlinearly with temperature.

Füllekrug and Fraser-Smith (1997) studied the connection between the magnetic field variations in the lower ELF range and the mean tropical temperature measured on a seasonal scale. The authors extended the relationship between the ELF magnetic field variations and the tropical temperature anomalies to a seasonal scale, where a semi-annual variation of the SRs was predicted before by Williams (1994). The long term monitoring of global lightning activity is presented to provide a thermometer-independent measure of temperature.

In Sekiguchi et al. (2006), the Principal Component Analysis is applied to the NS component of the horizontal magnetic field recorded at Moshiri (Japan) from November, 1998, to May, 2002, to extract the annual, the semiannual, and the interannual components of its variation. The components are also extracted for the global surface temperature averaged for different latitude ranges. The results show that there is a relation between the annual variations of the SR intensity and those of the global temperature. The greatest cross-correlation coefficient is 0.95, and corresponds to the case when the global surface temperature is averaged not only for the tropical region but for the latitude range that covers from 80^oN to 80^oS.

The relation between lightning –the main SRs source– and upper tropospheric water vapour is addressed in Price (2000), and the conclusion is that good agreement is

found between both series of data: "the ELF maxima and minima often precede the water-vapour maxima and minima on a daily basis".

As the EM field caused by a discrete lightning discharge (source) at a specific point (observer) of the world depends on the source-observer distance (see Figure 1.2), one of the main causes of the SR variations measured at a station is the spatial drift of the lightning discharges that occur around the globe. Both the amplitudes and the central frequencies of the SRs are closely related to the relative source-observer distance.

In Nickolaenko and Rabinowicz (1995), the diurnal frequency range (i.e., the difference between the maximum and the minimum values for each day of recordings) for the SR1 central frequency was extracted from the vertical electric field recorded at Kyoto (Japan) between February, 1967, and January, 1968. It was correlated with optical lightning observations. The authors conclude that the diurnal frequency range for the SR1 central frequency is an estimator for the area covered by the global lightning.

In Sátori and Zieger (1999), the central frequencies of the three first SRs (SR1, SR2 and SR3) measured at Nagycenk (Hungary) from 1994 to 1998 are correlated with the Southern Oscillation Index (which is related to the latitude at which the American lightning events occur). The central frequencies of SR1 and SR2 are found to be slightly higher when the American lightning events occur more southward (which corresponds to El Niño warm episodes). The central frequency of SR3 is observed to be much more sensitive to the location of the discharges. The explanation could be that the EM field generated by a single lightning event varies faster in the spatial scale for the frequencies close to the SR3 than for the frequencies close to the SR1 and SR2.

Belyaev et al. (1999) use the horizontal components of the magnetic field and the vertical component of the electric field, measured at Lehta (Karelia, Russia), in July and August, 1998, to calculate the Poynting vector. This vector is used for the study of the space-time dynamics of the global thunderstorm activity from a single station. A night-time peak of activity in the African thunderstorm activity is revealed at around 2-3 UT, which reaches about 1/3 of the regular afternoon activity. The diurnal and seasonal variations of the SRs measured at this station from August, 1999, to March, 2005, are analyzed in Yatsevich et al. (2008).

In a more recent work (Sátori et al., 2009), data from the lighting observation by the LIS Satellite reveal that the land lightning activity increases and moves southwards during the El Niño periods (December 1997 - February 1998). The ocean lightning

activity decreases but its contribution to the global activity is smaller. Unexpectedly, the mean SR intensities measured at Nagycenk are observed to be lower during two El Niño periods than during two La Niña periods. According to the authors, the changes observed in the SR intensities can be explained as a combination of two factors: the changes in the lightning discharge intensities and the changes in the relative distance between the discharges and the station. The second factor would explain the results observed.

The SRs recorded at many different ELF stations around the world show an increase in intensity during the transition months that precede the super El Niño episodes in 1997-1998 and 2015-2016, which reveals an increase in the lightning activity, as shown in Williams et al. (2021). Independent observations from the Optical Transient Detector and the World Wide Lightning Location Network also exhibit increased lightning activity in those transition months. The main conclusion remarked by the authors is that the variations in the intensity of the SRs may serve as a precursor for these extreme climate events.

In Simões et al. (2012), a detailed review of the low frequency EM wave phenomena related to the tropospheric-ionospheric coupling mechanisms is performed. The authors remark that plenty of scientific disciplines (atmospheric electricity, atmospheric dynamics and chemistry, space plasma physics, meteorology, electromagnetic wave propagation, chemistry, etc) are involved. The authors state that the research on ULF-VLF wave propagation contributes to the understanding of the Earth atmospheric environment. Some of the most important topics to be studied are listed. One of them is to "identify possible correlations between long term Schumann resonance variability and climate trends".

The influence of the solar cycle on the SRs has also been addressed in the literature. An intense solar activity may cause changes in the magnetosphere and in the ionosphere, which could imply a change the EM behavior of the Earth-ionosphere cavity and thus in the SRs.

The NS component of the ELF magnetic field has been recorded at the ELF station in the Bieszczady Mountains (South-East of Poland) irregularly for 6 years in Kulak et al. (2003). These measurements were carried out both during the maximum and the minimum of the solar cycle 23. The relation between the SR1 central frequency and the solar flux (both in the X-ray and in the radio ranges) is analyzed. The SR1 central frequency is found to increase from 7.75 Hz at the minimum solar activity of the cycle to 7.95 Hz when solar activity is maximum. Also, the global attenuation rate at 8 Hz is observed to decrease from 0.31 dB/Mm at the minimum solar activity of the cycle to 0.26 dB/Mm at the maximum.

An experimental study evidences that there exists a solar X-ray modulation of the Earth–ionosphere waveguide in Sátori et al. (2005). Data from three different stations are used: the vertical electric field from Nagycenk (Hungary) and the horizontal magnetic field from the Rhode Island (USA) and the Arrival Heights (Antarctica) stations. Combining the three stations, a 14 year series of data is available (from 1988 to 2001), which covers the maxima of the solar cycles 22 and 23 and the minimum in between. For the central frequencies of the first seven SRs, SR1-7, an increase is observed during the maxima and a minima is observed during the minima. A similar behavior is observed in the quality factors of the three first SRs. This is valid for all the field components studied. These variations can be attributed to the X-ray-induced modification of the conductivity profile of the outer dissipation layer of the atmosphere.

Similar conclusions are obtained from the vertical electric field measured at Modra (Slovakia) in Ondrášková et al. (2011). The central frequencies and the quality factors of the SR1 and the SR2 decrease from the solar cycle maximum in 2001–2002 to the anomalous solar cycle minimum in 2008–2009. The decrease observed in these parameters is greater than it was in Sátori et al. (2005). Furthermore, the variation of the diurnal frequency range, i.e., the difference between the maximum and the minimum value for a certain parameter during a day, is studied in order to estimate the diameter of the lightning source region. This source diameter was found to be greater in the northern hemisphere summer from 2002 to 2007. However, the difference in the source diameter between summer and winter almost disappeared in the solar cycle minimum (2008-2009).

A different duration for each one of the 'electromagnetic seasons' is proposed in Nickolaenko et al. (2015). In this work, also the normalized intensity and the central frequencies of the SR1 are monitored and compared with the solar activity. Regular horizontal (NS and EW) magnetic field recordings at the "Akademik Vernadsky" Ukrainian Antarctic station (2002-2011) were used for this study. The variation of the central frequencies from 2002 (maximum solar activity) to 2009 (minimum solar activity) could be explained by a reduction of 1 km of the effective height of the lower ionosphere. To explain the variation in that period for the field intensity, a 10 km reduction of the height of the lower ionosphere is needed. The authors consider that the most realistic interpretation of these variations may combine two factors: the changes in the effective height of the lower ionosphere and a latitudinal drift of the thunderstorms.

The SRs obtained from the the horizontal (NS and EW) magnetic field measured at two different ELF stations: the Ukrainian Antarctic station "Akademik Vernadsky" (2002-2019) and the Svalbard station in the Arctic (2013-2019) are studied in Koloskov et al. (2020). The SR1 peak intensities and central frequencies are studied together with the solar activity 10.7 index. For the intensities, the seasonal variations are observed to be in-phase in the Arctic and in the Antarctic stations, whereas for the central frequencies, the seasonal variations are observed to be in opposite phase in both locations. Also, the variation of the SR1 parameters follow an interannual variation that is quite related to the changes in the solar activity. The peak intensities and the central frequencies increase in the maximum of the solar cycle activity. The authors conclude that the seasonal changes are mainly caused by the latitudinal drift of the global thunderstorm centers, that covers up to $\pm(18^o–26^o)$, and the interannual changes are due to global changes in the lower ionosphere. If the ionospheric changes are attributed to variations of the upper (magnetic) characteristic height of the ionosphere, with a constant lower (electric) characteristic height, then the results are explained by an increase of ~2–3 km (for quiet solar activity years, this height is about 98 km). By contrast, if the ionospheric changes are attributed to variations in the lower characteristic height with a constant upper height, the results correspond to an increase of ~1–1.5 km (for quiet solar activity years, this height is about 55 km) (Koloskov et al., 2020).

The effect of the solar terminator on the SR parameters is also addressed in the literature. The terminator effect consists of strong gradients produced in the Earth's ionosphere when the day-to-night transition or the night-to-day transition happen. Strong changes in many magnitudes (for example, in the total electron concentration) are observed in this region at all heights of the atmosphere. The horizontal magnetic components recorded at the ELF station at Hollister (California, USA), together with the horizontal magnetic components and the vertical electric field recorded at the ELF stations in Rhode Island (USA), Mitzpe Ramon (Israel) and Nagycenk (Hungary), are used in Melnikov et al. (2004) to study if they are influenced by the terminator effect. The conclusion is that the vertical electric field shows this influence in all the three stations where it is measured, however, the magnetic field components are affected only in the station at Hollister. The rapid variations of the amplitudes, central frequencies and widths occur during approximately one hour at dawn and dusk.

1.3. The Sierra Nevada ELF station

Many ELF measurement stations around the world have been mentioned in the previous section. Both the vertical component of the electric field and the horizontal (NS and EW) components of the magnetic field can be recorded at an ELF station. This is due to the hypothesis of the Earth-ionosphere cavity being delimited by two perfect conductors, so that in the surface on the Earth only the horizontal magnetic field and the vertical electric field would be different from zero (Price, 2016). In some stations, only some of these components are recorded.

The most usual devices used to measure the horizontal magnetic field components in the ELF band are induction search coil magnetometers. Typically, the ELF stations will have two magnetometers, oriented in the NS and the EW magnetic directions, respectively, to measure the NS and the EW components of the magnetic field. Vertical antennas are used to measure the vertical electric field. An antenna basically consist of a conductor (that is usually a sphere) elevated at a certain altitude from the ground. The voltage of the sphere, with respect to the ground, is recorded to obtain the vertical electric field.

The ELF observatories must be placed in very low anthropogenic noise areas, as the natural EM resonances have a very low intensity in the ELF band. For that reason, they are usually located in rural areas or natural parks, far from the traffic, the industry, the power generators or other sources of noise (Price, 2016).

Most of this thesis is aimed at studying the SR recordings at the ELF station "Juan Antonio Morente", located at Sierra Nevada (37^{o}02'N, 3^{o}19'W), a protected natural park in the province of Granada (Spain) at an altitude of 2500 m above the sea level. The station was designed and built in 2012 by some members of the research group in which this thesis has been developed, but the first data available are from March, 2013. A map indicating the location of the station is shown in Figure 1.5. Before deciding the final placement of the station, different measurement campaigns were carried out in remote areas of the province of Granada in order to find the place with the less influence of local noise (Fornieles-Callejón et al., 2015).

The station measures the two components (NS and EW) of the horizontal magnetic field using two induction search coils with a ferromagnetic core, that are buried at 1 m depth, about 100 m away from the central unit of the station. The vertical component of the electric field is not measured. The sampling frequency is f_s = 256 Hz, and for this frequency the total power consumption is 10 W. The source of power consists of two solar panels, and the gel batteries can store energy for a period of approximately 3 weeks. The station also has an antenna to remotely send the

Figure 1.5. Map showing the city of Granada (orange circle), the Mediterranean coast and the location of the Sierra Nevada ELF station (red globe). Adapted from Google Maps.

recordings to the University of Granada, though they are also stored in a memory device at the station. The station is shown in Figure 1.6.

Figure 1.6. Photography of the Sierra Nevada ELF measurement station, taken in March, 2013. From Fornieles-Callejón et al. (2015).

The magnetometers were specifically designed to measure the first three SRs with a good SNR, and are optimized for frequencies in the band 6 to 25 Hz. The technical

features of the station and the magnetometers are explained in Fornieles-Callejón et al. (2015), where we can see that the magnetometer coils have 980 000 turns, their length is 925 mm and their outer diameter is 62 mm. Inside the coils, there is a ferromagnetic core made of a material called NILOMAG alloy 77, that has a relative magnetic permeability between 60 000 and 300 000. The core has a length of 1250 mm and a diameter of 22 mm.

A magnetic field in the range of some pT induces a voltage of some mV in each coil. This voltage goes through a 1 m long coaxial cable to a preamplifier that amplifies the signal around 34 dB (equivalent to a gain of 50). After that, the signal travels again through a coaxial cable to the central unit (for a distance of about 100 m), where it is amplified again (34 dB) and low pass filtered, using a Butterworth of tenth order filter, to get rid of the 50 Hz noise produced by the electric lines (Fornieles-Callejón et al., 2015). After that, the signal is digitized using 16 bits for quantization (15 for the absolute value and 1 for the sign). Finally, this digital voltage is stored in the central unit of the station and remotely sent to the University of Granada. The minimum and maximum values for the digitized voltage are -10 V and +10 V, respectively, so a saturation will occur every time that a sample of the recordings is out of this range before the digitization. This scheme is shown in Figure 1.7.

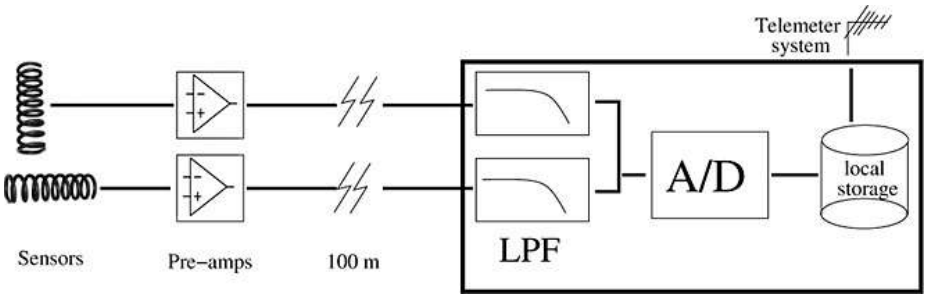

Figure 1.7. Measurement process at the Sierra Nevada ELF station, from the induction of voltage in the coils (sensors) by the ELF magnetic field to the storage and dispatch of the recordings. From Fornieles-Callejón et al. (2015).

1.4. Present situation of the research on SRs. Thesis motivation and structure

At present, the relevance of monitoring the lightning activity is arousing more interest for the study of the climate. The aim to enhance international collaboration among research infrastructures in order to address global environmental challenges can be found in the European Strategy Forum on Research Infrastructures, where we can find numerous European research projects. One of these projects is "Coopera-

tion of Research Infrastructures to Address Global Challenges in the Environmental Field" (COOP+, http://www.coop-plus.eu). The global, interdisciplinary collaboration among research infrastructures requires a large effort on common practices, including the access and sharing of data.

Also, the "European Cooperation in Science and Technology" (COST) is a European program that promotes the exchange of scientific knowledge and collaboration through interdisciplinary research networks. The COST program is structured in different specific actions. Each action is carried out by a working group.

One of the working groups of the COST program is the WG1-Atmospheric Electricity Network (http://www.atmospheric-electricity-net.eu/working-group-1). Its purpose is to establish a European network of measurements of atmospheric electric fields, which includes the SRs. One of the tasks of this working group is to standardize measurement procedures, data collections, and archiving procedures.

Currently, the raw data are not usually made public, and they could be exploited to obtain additional results by other researchers. The methodology for extracting the SRs from ELF station raw measurements is only superficially treated in the specialized literature. Plenty of different procedures and data formats are used by the researchers. Also, many relevant details to compare the SRs obtained from different station measurements are frequently omitted.

The existence of a common format for the data, as well as a unified procedure, is desirable. At least, the information about the station and the methodology should be given in enough detail so that the results from different ELF stations can be adequately compared.

Some years before the beginning of this PhD thesis, the Sierra Nevada ELF station was deployed with the intention to be part of the network of atmospheric EM field stations. It has been working from 2013 until now, although the data analyzed in this thesis comprise only four years of recordings: from March, 2013 to February, 2017. After February, 2017, the station suffered a technical failure and there are no recordings for the following two months. Moreover, the quality of the recordings is not optimal for the months after.

The station had a double purpose. First, the SR parameters were to be obtained from the raw magnetic field measurements and compared with previous results and with atmospheric/space data. Secondly, the recordings were to be shared with the scientific community. The data and the results have been shared at three different levels. The first level corresponds to the raw magnetic field data recorded at the station. The second level corresponds to an intermediate part of the process, which may be useful

to carry out different studies by the scientific community. The third level corresponds to the values obtained for the SR parameters, as well as the processing programs, functions and notebooks, which are also shared with the scientific community.

The present PhD thesis began in the context described in the paragraphs above, and it develops the two purposes for which the Sierra Nevada station was developed.

By means of the development of this two purposes, this thesis contributes to the task of the WG1 to standardize measurement procedures, data collections, and archiving procedures, and thus works towards the aim to enhance international collaboration among research infrastructures.

The thesis is structured as follows. The objectives of the thesis are listed in chapter 2. Chapter 3 addresses the need to specify the procedure used to obtain the SR parameters from the raw field measurements. A methodology to obtain the SRs from the Sierra Nevada measurements is explained, and the change in the SR parameters values caused by the different choices in the procedure is analyzed. This chapter has been published as a scientific paper. Chapter 4 is an extension of the explanation of some aspects of the methodology: the anthropogenic noise elimination and the definition of the SR parameters.

Chapter 5 details the software that has been designed to apply the procedure to the measurements. The different programs that make up the software are offered for download, together with the raw data and intermediate data. This chapter has been published as a scientific paper.

A scheme to study the SR regular variations is presented in chapter 6. A wide collection of notebooks designed to study different scale variations of the SRs is offered for download.

The study of the variations of the SR parameters, their comparison with previous results and their relation with some atmospheric and space phenomena has been made in chapter 7, which has also been published as a scientific paper.

Chapter 8 shows the extraction of the principal components of the temporal variations of some SR parameters making use of the Singular Spectrum Analysis, and also contains an identification and a study of the anomalies observed in the SR amplitude spectra from March to July, 2013. Finally, chapter 9 contains the conclusions of this thesis.

Chapter 2. Objectives and methodology

This thesis has three main objectives:

1. Discuss the need to explicitly indicate the methodology used to extract the SR parameters from the raw ELF measurements.
   - Design a processing methodology to obtain the calibrated amplitude spectra of the Sierra Nevada ELF station magnetic field recordings, and the quantitative value for the amplitudes, central frequencies and widths of the three first SRs.
   - Estimate how much the values obtained for the SR parameters may change depending on the choices for the different options and parameters involved in the processing methodology.

2. Create an adequate set of codes (functions, programs and notebooks) that enables to analyze, visualize and export the SR parameters (amplitudes, central frequencies and widths), as well as other relevant information (saturations of the magnetometers, out-of-range parameter values, etc), in a useful, fast and comfortable way. These codes are to be shared with the scientific community.
   - Develop a set of processing programs to extract the SR parameters.
   - Propose a storage format to save the parameter values and other relevant information. Both the codes and the storage format are to be shared with the scientific community.
   - Establish a wide set of diverse tools that allow the researchers to automatically obtain, study, export or visualize the information or results in a desired format.

3. Analyze the long-term variations of the SRs measured at the Sierra Nevada ELF station, compare them with those from other stations and correlate them with atmospheric, climatic and space phenomena.
   - Obtain the variations of the SR parameters for different time scales: diurnal, daily, seasonal, monthly, annual.
   - Compare the variations obtained with previous results from other stations. Correlate the variation with atmospheric, climatic and space phenomena.
   - Extract the principal components of the temporal variations of the parameters (annual, semiannual...).
   - Keep a record of the anomalies observed in some amplitude spectra, classify them and supervise their influence on the value of the SR parameters.

This thesis is framed in the development of two research projects, in which the PhD candidate has participated:

- Experimental and Numerical Study of Natural Electromagnetic Phenomena for Environmental Diagnostic. (FIS2013-44975-P).
- Numerical and experimental study of the Troposphere-Magnetosphere-Ionosphere coupling by means of Schumann Resonance analysis. Application to climate and Space Weather. (FIS2017-90102-R).

Both projects have been financed by the Ministerio de Economía y Competitividad of the Government of Spain, and co-financed with FEDER funds of the European Union. The three objectives of this thesis are a contribution to the objectives of the two projects above.

The two projects above are structured around two general objectives. One of them is related to the experimental study of the SRs contained in the magnetic field recorded at the Sierra ELF station. The other one is related to the numerical study of the ionosphere using the Transmission-Line Matrix (TLM) method. The three objectives of this thesis largely contribute to the first objective of the projects, while the second objective of the projects will not be addressed in this thesis.

The methodology of this thesis is explained below:

- The objective 1 is addressed in chapters 3 and 4. The proposed methodology will be divided into steps and described in detail, providing examples of its application to the Sierra Nevada recordings. Different options will be analyzed and an estimation of the differences in the SR parameter values will be provided.
- The objective 2 is addressed in chapters 5 and 6. The codes will be divided into those used to extract the SR parameters from the raw data (chapter 5), following the processing methodology explained in chapters 3 and 4, and those used to study, export and visualize the results and the variations of those SR parameters (chapter 6).
- The objective 3 is addressed in chapters 7 and 8, where the diurnal, daily and seasonal variations will be analyzed and a correlation with atmospheric phenomena will be performed. The principal components of the time variations of the components will be obtained using PCA and results anomalies observed in some spectra will be exposed.

Chapter 3. On the Need of a Unified Methodology for Processing Schumann Resonance Measurements

This chapter has been published in the paper:

On the Need of a Unified Methodology for Processing Schumann Resonance Measurements

Authors: **J. Rodríguez-Camacho**[1], J. Fornieles[2], M.C. Carrión[1], J. A. Portí[1], S. Toledo-Redondo[3] and A. Salinas[2] (2018).

[1]Department of Applied Physics, University of Granada, Granada, Spain,
[2]Department of Electromagnetism and Matter Physics, University of Granada, Granada, Spain,
[3]Science Directorate, European Space Agency, ESAC, Villanueva de la Cañada, Spain

Correspondence to: A. Salinas, asalinas@ugr.es

Journal of Geophysical Research: Atmospheres, 123, 13,277–13,290.

https://doi.org/10.1029/2018JD029462

Impact factor (JCR 2018): 3.633.
Q1, 17/86 in Meteorology and Atmospheric Sciences.

Key Points:

- We obtain Schumann resonances from ELF station measurements
- We define the analysis process of raw time domain data and likely influence of possible alternatives in the final Schumann resonance values
- A format for sharing Schumann resonance-based data is proposed

Abstract

The monitoring of natural electromagnetic activity in the extremely low frequency range is considered as a means of obtaining global information on the lightning activity and other parameters concerning the state of the Earth's atmosphere. In this sense, the possible application of the study of Schumann resonances (SRs) to environmental monitoring systems has already been proposed in the recent past. However,

the usual lack of details existing in the literature concerning the process of extracting SR parameters hinders the development of global networks intended for environmental purposes. In this paper, the methodology used to extract SR information from data measured at the Sierra Nevada extremely low frequency station, Spain, is described in detail. The process is split in three main parts: the determination of the amplitude spectrum from the low-amplitude noisy signal measured, the anthropogenic noise elimination and, finally, the calculation of an analytical function to fit the filtered amplitude spectrum from which SR parameters can be precisely defined. Some different options in the method are considered, and their effect on the SR results has been quantified. Significant differences in the final results have been observed in some of the options considered. As a conclusion of this work, it becomes clear that, if data from different research groups are to be shared and quantitatively compared, a standardization of the process is required or, at least, some details on the station and this process should be provided together with the SR results.

3.1. Introduction

SRs are global electromagnetic resonances that take place in the cavity formed by the Earth's surface and the ionosphere, mainly excited by lightning activity. The SR frequencies correspond to the extremely low frequency (ELF) band of the electromagnetic spectrum, 8, 14, and 20 Hz being approximate values for the first three resonance modes, respectively. The existence of SRs was first predicted in 1952 by Schumann (1952) and later measured by Balser and Wagner (1960). The SRs exhibit a global behavior and contain information concerning the storms and lightning activity at the whole Earth. It is for this global characteristic that SRs turn to be a useful tool to determine lightning activity throughout the Earth (Nickolaenko & Hayakawa, 2014; Sekiguchi et al., 2006; Shvets et al., 2010), and, therefore, to extract information on climate and its variations (Dyrda et al., 2014; Füllekrug & Fraser-Smith, 1997; Rycroft et al., 2000; Simões et al., 2012).

Price and Rind (1992) were the first to propose that climate changes in the Earth may cause an increase in the lightning activity of the planet. Williams (1992) showed the link between the average temperature in the tropic surface and monthly variations in the SR parameters. A similar study was later published by Füllekrug and Fraser-Smith (1997). The connection between different layers of the Earth's atmosphere is discussed in Price (2000). Atmospheric electricity and the SRs are strongly influenced by the lightning activity over the Earth, which in turn affects important parameters concerning the global climate, such as surface temperatures, tropical convections, and

water vapor at the higher troposphere (Rycroft et al., 2000; Williams, 2009). The advantage in measuring with terrestrial ELF stations relies on the fact that they allow continuous and long-term measurements, in contrast to data obtained from satellite observations, which present a relatively short lifetime. The global electric circuit, and therefore the SRs, is a means of obtaining global climate information out of local measurements, hence the importance of having a network of ELF stations sharing results (Rycroft et al., 2000). In order to compare measurements from different stations, local contributions must be removed from global ones (Greenberg & Price, 2004; Pechony & Price, 2006; Sentman & Fraser, 1991). The importance of simultaneously measuring SRs with different ELF stations spread throughout the Earth is justified in Greenberg and Price (2007), Nickolaenko et al. (2011), and Pechony and Price (2006).

The analysis of environmental phenomena through SRs is addressed in numerous works. A characterization of the main African thunderstorm center in basis of the signal spectrum including seven SRs is carried out in Dyrda et al. (2014). Ondrášková et al. (2011) identify a reduction in the SR frequencies coinciding with a minimum in the solar cycle. El Niño phenomenon is also studied in terms of its relationship with variations in SR frequencies (Sátori, 1996; Sátori & Zieger, 1999). SR studies based on long-term measurements taken by different stations can be found in Kulak et al. (2014), Ondrášková and Ševćík (2013, 2014), Ouyang et al. (2015), Roldugin et al. (2004), and Roldugin et al. (2006), Zhou et al. (2013).

The procedure for obtaining SRs from ELF station measurements is only superficially addressed in the specialized literature, and, when it has been done, many data and/or procedures which may be relevant to carry out a sound comparison of different station measurements are almost completely omitted. Assuming that it would be convenient that different ELF stations around the world are able to share data, the existence of a common format as well as a unified procedure is needed, or at least, there should be enough particular information concerning the station and the method used to process the interchanged data before any comparison is carried out. In this context, the European Cooperation in Science and Technology is a European program devoted to promote scientific exchange and collaboration through interdisciplinary research networks. The program is structured in working groups with different specific European Cooperation in Science and Technology actions. The aim of the working group called WG1-Atmospheric Electricity Network is establishing a European network of measurements of atmospheric electric fields, which includes parameters such as SRs. Some of the tasks in this group are the standardization of measurement procedures, data collections, and archiving procedures

(http://www.atmospheric-electricity-net.eu/working-group-1). The work presented in this paper is concerned with this need.

The interest of extending international collaboration between research infrastructures in order to be able to address global environmental challenges can be found in the European Strategy Forum on Research Infrastructures through European research projects, such as Cooperation of Research Infrastructures to Address Global Challenges in the Environment Field (COOP+, http://www.coop-plus.eu). The cross-disciplinary and global collaboration among research infrastructures that is required to address these challenges implies a significant effort on common practices, including access and sharing of data.

In the recent past, the authors of this paper designed and deployed an ELF station at the Sierra Nevada Natural Park in Granada, Spain, which has been continuously measuring the natural magnetic field since 2013 (Fornieles-Callejón et al., 2015). As expected, the raw data recorded by the station do not present any SR signature. They simply look like a noisy signal not containing any valuable information. A complex processing stage must be previously applied before SRs can be identified in such a noisy and low-amplitude signal. But this complex processing method is far from being uniquely defined. Each stage implies several possibilities and the effect on the final result is not always neither clear nor negligible. In this context, the possibility that processed results from different stations may be affected in a different manner due to different methods undermines the objective value of the processed data, since they cannot be directly compared to other authors' data.

This work describes some of the possible alternatives considered in the method used to analyze the data registered by the station at Sierra Nevada. The influence of these choices on the SR results is studied and discussed. Some options will be shown to play a minor role on SRs, but, on the contrary, other choices will have a relevant impact on the processed results. This fact may be interpreted as a clear sign that a standardization of the procedure should be established if data from different groups and stations are to be compared. The aim of this work is not to establish neither the data interchange protocol nor the method to extract the SRs from the time domain data, but to note the need of defining a common procedure regarding this topic and launch some initial proposals in order to the scientific community may study, improve and complete them.

3.2. The Procedure Used in the ELF Station at Sierra Nevada

The ELF station at Sierra Nevada, Granada, Spain, is equipped with two magnetometers, north-south (N-S) and east-west (E-W) oriented. The signal detected by these magnetometers is amplified, digitized, and registered directly in the time domain. The station is provided with a data acquisition system with a sampling frequency of f_s = 256 Hz, which means that the time step between successive samples is around 3,906 μs. The time domain measurements are stored in files with 921,600 samples, approximately corresponding to 1-hr register. The size of each file is 1.8 MB, and the storage requirements for 1-month measurements is 2.7 GB, approximately, including the files containing data for both sensors and also files with additional information. These storage requirements are perfectly affordable for present storage systems; therefore, a direct data interchange between ELF stations is feasible. Nevertheless, although time domain signal may provide valuable information, the relevance of the data in Geophysical Research studies is considerably increased by extracting SR information from them. In this sense, it seems preferable to share SR information rather than raw time domain data, provided the process to obtain SR data is commonly agreed by the scientific community. The format proposed in this work for the final file has a size about 50 MB per month and sensor.

The frequency response of the magnetometers ranges from a few tenths of a hertz to 45 Hz. Frequencies from 6 to 25 Hz have been calibrated, thus including the first three SR modes, located around 8, 14, and 21 Hz, which are the aim of the Sierra Nevada ELF station. The analog to digital converter uses 16 bit to digitize samples in the range ±10 V. The system minimum resolution is therefore $10/2^{15} = 3.052 \cdot 10^{-4}$ V. Saturation limits are fixed at ±9.990 V. Identifying the saturated measurements caused, for instance, by local phenomena, and extracting them from the regular and nonsaturated response is a preliminary step in the signal processing method. In order to do so, the number and temporal position of the saturated samples is identified in each 1-hr file data.

3.2.1. Determination of the Amplitude Spectrum

The procedure starts with the estimation of the power spectrum contained in the data recorded by the magnetometers. The scientific community reports 10-min periods, hereinafter referred to as the time series, as the minimum intervals required for the resonant behavior of the cavity to be observed, incorporating the effect of a

statistically significant number of lightning strokes during the processed time period. This time interval allows monitoring the evolution of the SRs in the presence of phenomena such as solar storms (e.g., Nickolaenko and Hayakawa, 2014; Ouyang et al., 2015; Salinas et al., 2016; Zhou et al., 2013).

The discrete Fourier transform (DFT) of the time series is not a good spectral estimator, since its variance at a given frequency does not reduce when the sample size increases. To overcome this drawback, Bartlett (1948) method splits the time series into smaller time intervals containing m data, hereinafter referred to as time windows, to which the DFT is applied. The final spectrum for the time series is the average of the partial spectrums at each time window. The benefit of this average is that variance reduces by a factor equal to the number of time windows into which the time series is split.

Welch method is an improved version of Bartlett method which includes two minor modifications Welch (1967). First, a certain time swapping between adjacent time windows is applied. Second, the algorithm also uses a function to smooth the effect of abrupt ends on both sides of each time window. In this work, the swapping corresponds to one half of the time window size and a Hann window has been used to smooth the tail series, which, for the nth out of m samples, is defined by (Oppenheim & Shafer, 2009)

$$h(n) = 1 - \cos^2\left(\frac{(n-1)\pi}{m}\right). \tag{3.1}$$

With the aim of keeping the original spectrum amplitude independent on the amount of data, m, the above function must be normalized, resulting

$$\tilde{h}(n) = \frac{h(n)}{\sqrt{\Sigma_{k=1}^{m} h(k)^2/m}}. \tag{3.2}$$

In order to carry out a DFT in its fast version, fast Fourier transform (FFT), the number of samples, N, should be a power of 2. According to appropriate time durations reported in the specialized literature, the use of 10, 15, 20, and 30 s for the duration of the time windows has been considered. Each one of these values corresponds to a number of samples in the time window of m equal to 2,560; 3,840; 5,120; and 7,680, respectively. The lower power of 2 that is able to deal with all these cases is $N = 2^{13} = 8192$. To meet the condition on $N = 8192$, a zero padding on both sides of the time series is applied for each time window.With this choice, the frequency step for the FFT data obtained does not depend on the window time length, which for the specific case considered in this work is $\Delta f = f_s/N = 0.03125$ Hz.

Slightly different definitions of the DFT can be found in the specialized literature. The following definition for a series of N samples, h_k, will be used in this work (Press et al., 1992):

$$H_n = \sum_{k=0}^{N-1} h_k e^{j2\pi kn/N}, \tag{3.3}$$

which provides the transformed value, H_n, corresponding to the frequency $f_n = n\Delta f$, for $n = 0, 1, ..., N/2$.

The amplitude spectrum of the signal for each time series is obtained by using the following procedure. First, the square module of the DFT for each time window is calculated. Equation (3.3) only describes positive frequencies; values corresponding to negative frequencies ($n = -1, \ldots, -N/2+1$) are taken into account by incorporating a factor of 2 in the corresponding positive frequency. Second, in order to define the discrete amplitude spectrum, the transformed series is divided by the product of the sampling frequency, f_s, and the number of samples used before applying the zero padding, m. This normalization makes the result independent on the amount of information, that is, the value of m, which is a remarkable property. Third, the resulting square module spectra for all the windows are then averaged. The square root of this quantity is the average amplitude spectrum for that specific time series, usually in $\mathrm{V/Hz^{1/2}}$ units.

As previously mentioned, an important fact to be taken into account is the possibility that measurements may be out of scale. If a saturated sample is detected in a time window, this period is eliminated from the time series average. There must be a certain balance in the length of the time window to obtain appropriate results. Longer durations make the time windows more significant from the statistical point of view, but it then may occur that a significant number of time windows are eliminated, since the probability of detecting a saturating event increases. In this sense, together with other values directly concerning the SRs, we think that some information quantifying the saturation level for each time series should be included in the information provided for each ELF station. To this end, the saturation level has been defined as the ratio of saturated time windows (therefore, eliminated from the average) to the number of the total time windows in the full 10-min time series under study.

The data calibration required is specific for each station used to carry out the measurements. As regards the Sierra Nevada ELF station, calibration is described by the following equation:

$$B(f) = S_c(f)V(f), \tag{3.4}$$

where $B(f)$ stands for the amplitude spectrum of the magnetic field, expressed in $T/Hz^{1/2}$ units, $V(f)$ is the amplitude spectrum of the measured voltage per square root frequency obtained in the previous step, and $S_c(f)$ is the calibration function, details of which can be found in Fornieles-Callejón et al. (2015).

3.2.2. Anthropogenic Noise Elimination

The station is located far from the main anthropogenic noise sources, such as power lines, electrical machinery, and transport systems based on electrical motors, as well as from villages or public roads. During the period in which a proper site was being looked for, measurements of the anthropogenic noise conditions were carried out. Due to logistic, preservation, and maintenance reasons, the station is located near a mountain hut. The electrical needs at the hut are reduced to a few appliances and lighting, which are supplied by an electric power system consisting of an electric generator (alternator), a battery pack, a battery charger, and an inverter.Measurements taken during the search of the appropriate site did not show anthropogenic noise; however, human-created noise was detected later in well-defined narrow frequency bands. It seems clear that the principal source responsible for the anthropogenic noise is the mountain hut, but, due to its ELF, other more distant sources (power plants, train signal, ...) cannot be disregarded. It is worth noting that this disturbances only happen at certain non-regular time periods. The signal at 50 Hz, corresponding to electric power lines, does not constitute a problem due to the distant location of these lines and to the effect of a filtering stage consisting of a Butterworth filter of the tenth order, which precedes the analog to digital converter.

The bands at which anthropogenic noise has been detected correspond to (14.6 and 15 Hz), (15 and 15.4 Hz), and (16.4 and 16.9 Hz), which we will refer to as human noisy bands (HNBs). The amplitude at the central frequency of these bands may reach values 1 order of magnitude higher than the natural electromagnetic signal to be measured. Figure 3.1 is a plot of the amplitude spectrum of a 10-min time series including human activity. The anthropogenic noise can be observed as three narrow peaks located around 15 and 16.5 Hz. Two alternative fitting curves for the signal that will be discussed below are also included.

Due to the fact that this noise appears in the spectrum as very narrow spikes, the undesired signal is filtered by simply fitting a straight line to the limit points of each

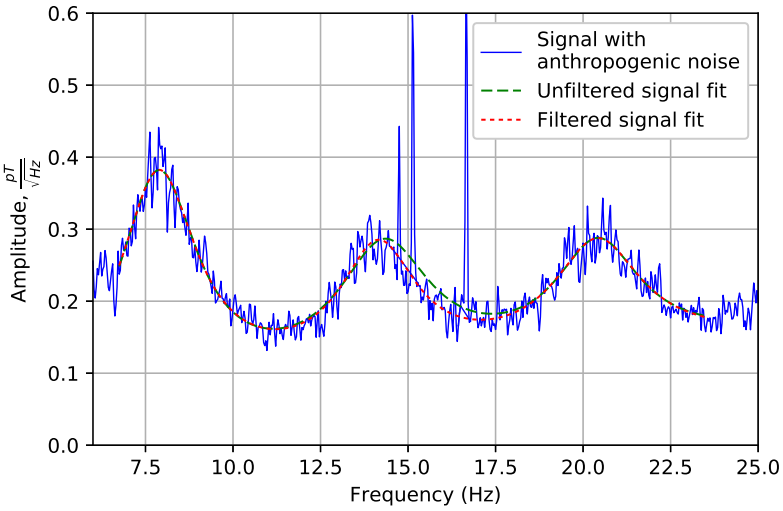

Figure 3.1. Amplitude spectrum for a 10-min time series with anthropogenic noise (blue line). Fitting curve before (green dashed) and after filtering (red dotted) the anthropogenic noise.

frequency band mentioned above. This filtering process should only be automatically carried out if required, that is, if human noise is detected. The procedure used in this work is carried out in the frequency domain for each 10-min series as follows. For each HNB to be filtered, we will consider a nearby band with a similar bandwidth, which is used for reference purpose. These bands depend on the particular ELF station, in our case, the following reference bands have been chosen: (14.1 and 14.5 Hz), (15.5 and 15.8 Hz), and (15.8 and 16.34 Hz). The maximum and the minimum of the difference between the measurement and the value fitted by the straight line are identified at the reference band. The average of both values is then calculated. Since there is no human noise in the reference band, both differences are expected to have similar amplitude but opposite sign; therefore, the expected average is close to 0. Identical procedure is applied to the HNB to be filtered. In the absence of anthropogenic noise, the average is similar to that obtained for the reference band. On the contrary, in the case of presence of anthropogenic noise, the average is considerably larger than that in the reference band. The criterion for automatically applying the filtering process is that the ratio of the average at the HNB to the average at the reference band is greater than a certain threshold value. Numerical studies have been carried out, showing that three is a good empirical threshold value to ensure a proper human noise detection capability. The influence of the anthropogenic noise filtering process on the SR values will be shown in section 3.3, devoted to numerical results.

3.2.3. Curve Fitting

Since the natural electromagnetic noise is permanently affected by a stochastic component, a nonlinear fit of the spectrum must be carried out, which minimizes the mean square error (SE) between the measured data and an analytical function. The original rippled spectrum after applying Bartlett method and the smoothed curves after a fitting process can be clearly seen in Figure 3.1. The curve fitting process allows determining quantitative parameters concerning SRs. This is the most decisive stage of the process, since the SR values may be directly determined from the fitting function. The main options to be taken into account in the fitting process are (i) the type of functions used; (ii) the optimization method; (iii) the initial values chosen for the function parameters, since an iterative algorithm is used; and (iv) the frequency band inside the calibrated frequency zone where the fit is applied.

As regards the type of adjusting functions, due to the resonant behavior expected, a fit using Lorentzian functions, combined with a straight line to allow taking into account a possible slope in the spectrum, is often used (Mushtak and Williams, 2009; Nickolaenko and Hayakawa, 2002, and references therein). The Lorentzian fit for adjusting three resonances is given by

$$L(f) = \sum_{i=1}^{3} \frac{A_i}{\left(\frac{f-f_i}{\sigma_i}\right)^2 + 1} + Bf + C, \tag{3.5}$$

where A_i stands for the amplitude of the ith mode, resonating at frequency f_i and with a bandwidth of σ_i, while parameters B and C correspond to the straight line.

In addition to Lorentzian ones, testing other fitting functions seems also appropriate at this methodology definition stage as well. Gaussian functions are present in many natural phenomena, and, due to its apparent similarity to the spectrum observed, they turn into good candidates to carry out the fitting process. The general form for a fit in terms of Gaussian functions combined with a straight line for three modes is given by

$$G(f) = \sum_{i=1}^{3} A_i^{-\left(\frac{f-f_i}{\sigma_i}\right)^2} + Bf + C, \tag{3.6}$$

where the parameters in the above equation define the same magnitudes as in the Lorentzian case. In this work, a comparison of SR values obtained using both types of fitting functions has been carried out. The linear terms are proposed in Roldugin et al. (2006) to describe the decreasing with frequency noise from input electronic

circuits, with $B < 0$. Another possible origin for the linear terms is that, despite higher order modes are not present in the calibrated region, the effect of their low-frequency tails cannot be disregarded. The coefficients B and C would correspond to a linear approximation of these tails and would explain positive values for B. In this sense, the linear terms could help minimize the differences observed when a spectrum is adjusted using different number of modes. Some results of this study will be shown in the next section.

With respect to the optimization method, determining the appropriate value for the different parameters in (3.5) and (3.6) is an optimization problem concerning minimizing or maximizing functions for which there exist very efficient methods. Newton method, gradient or maximum slope method, conjugate gradient (CG) method, or quasi-Newton (QN) method are some examples. For the case of the nonlinear modeling of a data set which involves us, Levenberg-Marquardt (LM) is considered as the standard method (Press et al., 1992). An estimate of the differences in the final values for the fitting parameters obtained using different methods will be shown in the results section.

The third aspect is related to the fitting process. It involves using nonlinear iterative techniques to determine the parameters for each time series, which requires defining seed or initial values for each parameter in (3.5) or (3.6). Nonlinearity makes the convergence of the method to be highly dependent on an appropriate estimate of the initial value for the parameters to be calculated. Let A_{i0}, f_{i0}, σ_{i0}, B_0, and C_0 be the initial values for A_i, f_i, σ_i, B, and C, respectively. In this work, a two-stage procedure for the choice of the initial parameters is proposed. First, values A_{i0}, f_{i0} and σ_{i0} are taken from Toledo-Redondo et al. (2010) to approximately match the experimental results. Initial values for the straight line terms, B_0 and C_0, are chosen to be 0. Using these initial values, the fit of the monthly average spectrum corresponding to a specific time of the day is calculated. As a result, we have monthly averaged amplitudes, frequencies, and bandwidths, A_i, f_i, σ_i, respectively, together with average values for B and C, which gather monthly information at each time interval of the day. Second, in order to obtain a particular fitting curve for each time period of a specific day, a new fitting process is applied to that spectrum. The initial parameters used for this second fitting process are the monthly averaged values obtained in the first step: $f_{i0} = f_i$, $\sigma_{i0} = \sigma_i$, $B_0 = B$, $C_0 = C$, except for the amplitudes that are taken to be $A_{i0} = A(f_i)$, that is, the amplitude of the particular spectrum under study at the average frequency f_i. The reason for this different choice for defining A_{i0} is that the frequency values are very similar for different days at a specific hour, but this is not the case for the amplitudes; however, a first approximate is easily obtained from the spectrum value at frequency f_i.

Finally, another variable that must be defined in the nonlinear fitting procedure is the frequency band for which the best fit is obtained in the calibrated frequency band, which for the Sierra Nevada station ranges from 6 to 25 Hz. Due to the shape of both Lorentzian and Gaussian functions, the leading and trailing part of the data series may significantly affect the final values of the parameters. Thus, it is important to establish an adjusting frequency band to ensure a good convergence of the nonlinear fitting algorithm and also to allow a sound comparison of data from different stations.

The software developed for this procedure is based on Lmfit package, an extension of the Python package Optimize, which provides a high level interface to solve optimizing and curve fitting problems. It is a free software package with Open Source License, a project currently under development (Newville et al., 2014). A study of the influence of the bandwidth on the fitting results is carried out and discussed in the next section.

3.2.4. Definition of the SR values

The definition of the value for the SRs, amplitudes, resonance frequencies, and bandwidths, in terms of the adjusting curve is not clearly specified in the literature. Three possible definitions for the amplitude and resonance frequency may be considered as reasonable basing on the results from the fitting functions:

1. The values that are directly obtained from the fitting procedure. The SR amplitudes and frequencies correspond to the fitting parameters, A_i and f_i, respectively

2. Other possibility is that SR frequencies correspond to the frequency fitting parameters, f_i, as in the previous case. As regards the SR amplitudes, instead of directly using the fitting parameters A_i, the SR amplitudes are defined as the value of the fitting function at f_i, that is, $P_i = L(f_i)$ or $P_i = G(f_i)$ in (3.5) or (3.6), respectively. This criterion takes into account the shift that may occur in the amplitude at the frequency at which each individual maximum occurs when all the modes and the linear term are simultaneously considered.

3. A third possibility is to use the fitting procedure as a first step to substitute the noisy experimental function by the smooth adjusted one. The maximum values of this fitted function, P_i' , and their corresponding frequencies, f_i' , define the SR amplitudes and frequencies, respectively. It is worth mentioning that the P_i' values do not necessarily coincide neither with A_i nor with P_i. Similarly, the

fitting frequencies, f_i, do not necessarily coincide with the maximum frequencies, f_i', of the adjusted curve.

To easily and unambiguously identify each amplitude in the rest of the paper, amplitudes A_i will be named individual mode amplitudes, P_i will be termed global mode amplitudes, and P_i' will be referred to as local maximum amplitudes. Frequencies f_i will be named resonance frequencies, while f_i' will be called local maximum frequencies.

As regards the bandwidth for each resonance mode, the fitting parameters σ_i are directly considered as defining the bandwidth of each resonance mode, regardless which of the three options has been chosen for the amplitudes and frequencies.

Although results are likely to be qualitatively similar, significant quantitative differences may arise. Next section discusses differences and similarities among these parameters. In order to carry out a comparative analysis of the measurements for different ELF stations, it seems convenient that the information provided is constrained to the adjusting parameters, since it is more clearly and objectively reproducible. However, present storage media allow dealing with additional information, which may be highly valuable in future research. For this reason, as final result of the process, a file containing at least the following data should be generated for each month and sensor: saturation level, spectrum of the measurements, spectrum of the fitted signal, bandwidths, adjusting parameters, and UTC hour for the initial interval of that month. A possible format is that generated by Numpy, a Python-based package (http://www.numpy.org). The file read would be directly carried out through Numpy arrays, keeping the structure with which they were written. This would avoid the need of a great deal of information to describe how data were registered in the files, which would be simply reduced to enumerate the Numpy arrays, instead. The file size would be approximately of 50 MB per month and sensor, a manageable size, with a binary format which would allow fast write/read access.

3.3. Results and Discussion

This section includes a number of examples showing how the different options discussed in the previous section influence the SR results obtained from the raw time domain data measured by the ELF station located at Sierra Nevada, Spain. The quantitative analysis consists on a comparison of the parameters for the nonlinear fit obtained using the different possibilities. As a general rule in this study, the comparison between two options will be used. In the case of more than two possibilities, the

comparison will be carried out by considering one of them as the reference option. It is convenient to define a parameter describing the monthly average difference with respect to a reference value. In this sense, let Q_i stand for the value of a certain parameter, Q, for the ith time interval in that specific month and option of one of the possible methods described in the previous section. If the corresponding reference value is denoted as Q_{ir}, its mean relative difference (MRD) is defined as

$$\Delta Q = \frac{1}{N} \sum_{i=1}^{N} \frac{|Q_i - Q_{ir}|}{0.5\,(|Q_i + Q_{ir}|)}, \tag{3.7}$$

where the sum is carried out over the N time series in the specific month under study.

Another important point to be taken into account to carry out a long-term monitoring of SRs is defining which values are acceptable to obtain a correct and meaningful average. In addition and equally important, identical criteria should be used in the studies carried out by different research groups or based on different station measurements if a proper comparison is to be done. The definition of a standard mask for filtering unacceptable data is beyond the scope of this work, but it seems clear that, at least, the long-term studies published should not only include the SR data but also the particular mask used for filtering invalid data. The mask values used in this work are shown in Table 3.1. No conditions are imposed on the linear terms B and C.

Table 3.1
Valid Ranges for the Fitting Parameters Under Regular Behavior

Valid range
$0 \leq A_i \leq 2$
$0 \leq \sigma_i \leq 6$
$7 \leq f_1 \leq 8.5$
$13 \leq f_2 \leq 15.5$
$19 \leq f_3 \leq 23.5$

Results shown in this work correspond to December 2013. This particular month has been chosen due to the fact that it is a relatively quiet period in terms of both local and global lightning activity, thus allowing a fairly good definition of the SRs, even though their amplitude is considerably lower than in the summer season. The SR amplitude spectrograms for the N-S and E-W sensors corresponding to the measurements made in December 2013 are shown in Figure 3.2.

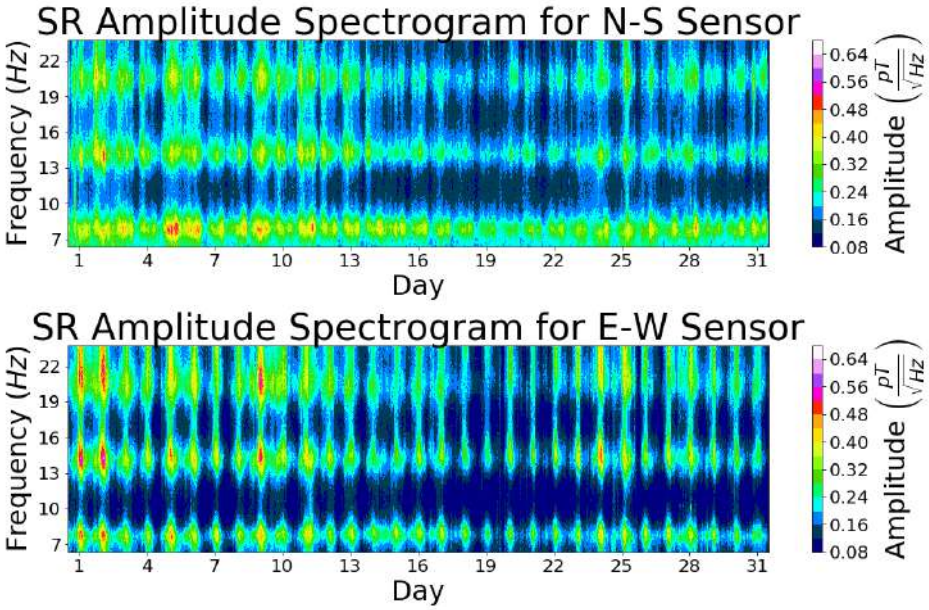

Figure 3.2. Amplitude spectrograms for the N-S and E-W sensors during December 2013. SR = Schumann resonance.

3.3.1. Estimation of the Amplitude Spectrum

The influence of the duration of the time window to which the FFT is applied in the procedure of spectrum estimation is the first alternative to be studied. The parameters obtained for a Lorentzian fit for December 2013 using time windows of 10 and 30 s are compared in Figure 3.3, showing the MRD between the most usually considered SR values obtained for both time windows. Namely, Figure 3.3 plots the fitting parameters of the individual mode amplitudes, A_i, the resonance frequencies, f_i, and the bandwidths, σ_i, values, together with the global mode amplitudes, P_i, of the complete function at f_i. It can be observed that the differences in the frequencies and global mode amplitudes are lower than 2%, approximately; however, individual mode amplitudes and bandwidths may differ by up to 6%.

Regarding the linear coefficients B and C, their values are not usually reported by the specialized literature. In our case, B is around 0.005 $\frac{\mathrm{pT}}{\mathrm{Hz}^{3/2}}$ and C is around 0.05 $\frac{\mathrm{pT}}{\sqrt{\mathrm{Hz}}}$. The positive value for B indicates that the linear term adjusts the tail of the fourth and higher modes, although this could be different for other stations. Their values are highly dependent on the specific procedure chosen. Their MRD may even be higher than 100%, although the global effect on the fit is of second order, not having a great influence on the frequencies and global amplitudes. These considerations on B and C are valid for the rest of cases studied in this paper and will not be mentioned hereinafter.

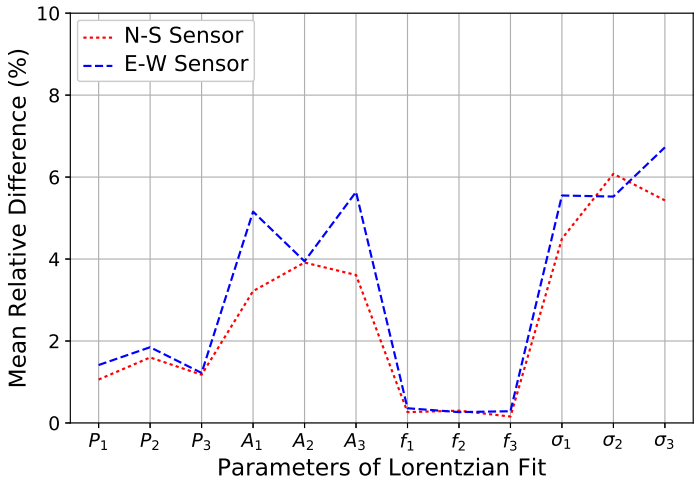

Figure 3.3. Mean relative difference for 10- and 30-s time widow size of the individual mode amplitudes, A_i, resonance frequencies, f_i, and bandwidths, σ_i, together with global mode amplitudes, P_i. The values correspond to a Lorentzian fit.

The use of 10-s time windows has the advantage of considerably reducing the number of saturation periods. This is clearly appreciated in Figure 3.4, which is a plot of the saturation level at each time series for both time windows. This behavior can be explained by the fact that it is more likely that saturation occurs for 30-s than for 10-s windows. Furthermore, the increase in the number of time intervals for each time series has the added benefit of reducing variance when calculating the spectrum average, thus providing less noisy results. The use of 20-s time windows has also been considered. Results, not shown in this work for the sake of brevity, describe an intermediate case.

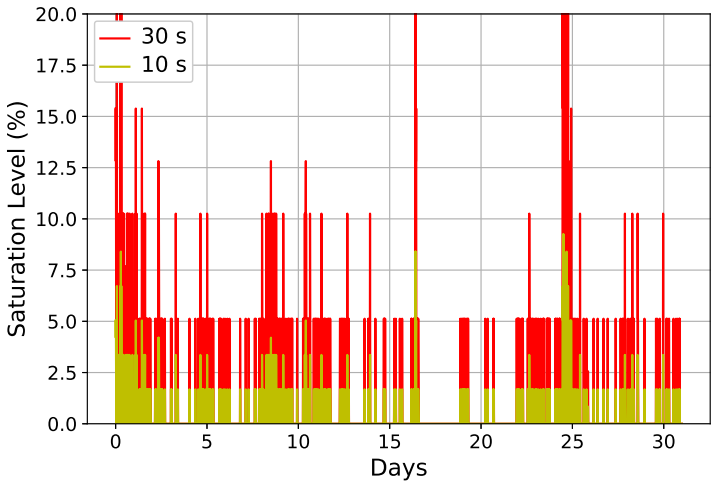

Figure 3.4. Saturation level for 10- and 30-s time window size at the N-S sensor during December 2013.

3.3.2. Anthropogenic Noise Filtering Results

As previously mentioned, measurements of the Sierra Nevada station are affected by anthropogenic noise. The filter described in section 3.2.2, consisting on substituting the undesired narrow peaks by straight lines, is simple and efficient since the anthropogenic noise presents disturbances with narrow bandwidths at fixed positions. In order to study the effect of the anthropogenic filter in the spectrum, two cases are considered. First, the spectrum has only been filtered at the HNBs when a certain threshold value is exceeded, as described in section 3.2.2. Second, the straight line filter is applied for all cases, even if the human noise is not present. Figure 3.5 is a plot of the MRD between both cases for the E-Wand N-S sensors when the threshold value used is three. It can be observed that the most significant differences occur again for A_i and σ_i, but they are now below 3%, while f_i and P_i deviate less than 1%. As regards the MRD for the global amplitudes, the greatest value corresponds to the second mode. This is most likely due to the effect of the anthropogenic noise filtering, since the HNBs are close to the second mode. The differences are not negligible and information on the filtering process, including bandwidths affected, and possible use of thresholds should be provided together with the data.

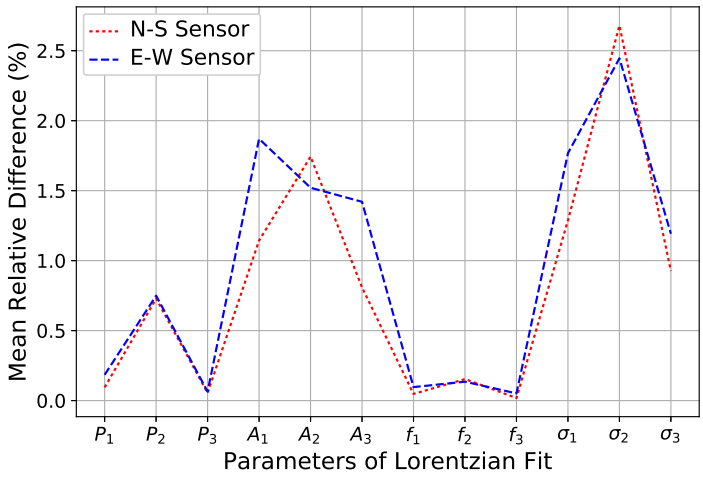

Figure 3.5. Mean relative difference of the individual mode amplitudes, A_i, resonance frequencies, f_i, and bandwidths, σ_i, together with global mode amplitudes, P_i, when the human noise at the human noisy bands is filtered in all cases or only when a threshold value of three is exceeded. The values correspond to a Lorentzian fit for the two sensors at the extremely low frequency station.

The effect of the anthropogenic noise elimination on the fitting curve can be observed in Figure 3.1. The fitting before filtering process deviates from the experimental signal due to the presence of three high amplitude peaks. This undesired effect disappears once the human noisy peaks have been removed.

3.3.3. Curve Fitting Results

So far, previous figures have shown results concerning resonances and making reference to the adjusting parameters, but no mention has been done on the adjusting process itself. In fact, some necessary results have already been used for obtaining them, nevertheless, the discussion has been left to this moment.

Lorentzian fitting functions are often used in the optimization process, although some authors state that the curves are not strictly Lorentzian (Nickolaenko & Hayakawa, 2002). Ondrášková and Ševčík (2014) compare the results obtained using the Lorentzian fit and the complex demodulation method. In this paper, the differences between Lorentzian and Gaussian fits are considered. In order to explore the convenience of these types of fitting functions, a study of the degree of adaptation of the spectrum when using one or other type of functions has been carried out. Figure 3.6 is a plot of the SE between the measured and the adjusted data using Lorentzian and Gaussian fitting functions during December 2013. The SE value is directly provided by the Lmfit package, defined as the sum of the squared difference between the measured and fitted values. Figure 6 clearly shows that errors generated by the Lorentzian fit are significantly lower than those produced by Gaussian functions.

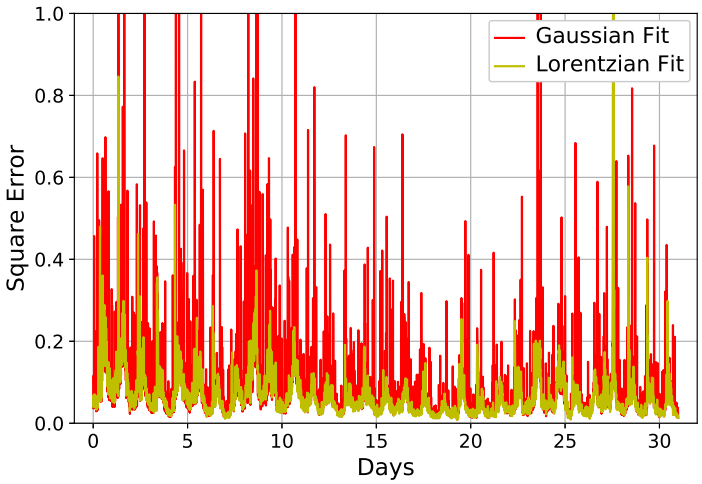

Figure 3.6. Square error between the fitting curves and measured amplitude spectrum using Gaussian and Lorentzian functions for each time series at the N-S sensor during December 2013.

It is also interesting to note that the Gaussian fit sometimes provides values out of the expected range. As mentioned above, data outside these suitable ranges are filtered according to an estimate of acceptable values. This task is implemented by applying a mask to the data set, which in this work corresponds to the upper and lower limits summarized in Table 3.1 for each parameter. Figure 3.7 shows the evolution of the resonance frequency for the first SR mode during some days of December 2013 for

both Gaussian and Lorentzian fit. Values outside the acceptable ranges in Table 3.1 have not been plotted and correspond to the discontinuities appearing in the Gaussian represented in Figure 3.7. A clear difference between both fits can be easily observed, but what is almost more important is that the Gaussian fit produces significant periods of time during which the adjusted results are outside the acceptable ranges. This undesired effect is less frequent in the case of the Lorentzian fit.

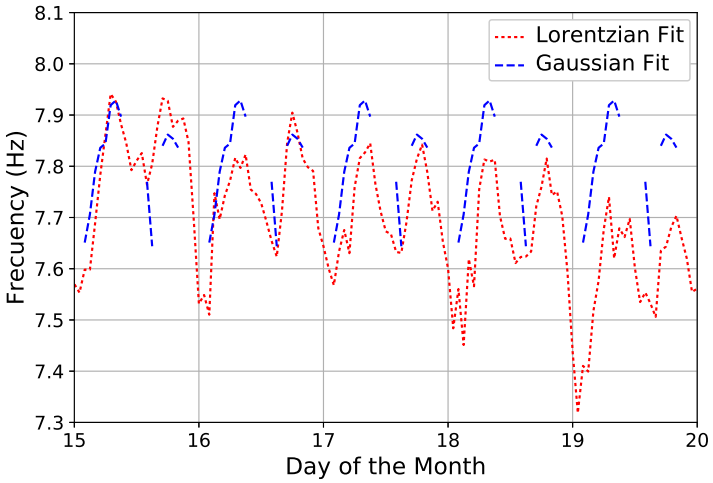

Figure 3.7. First mode resonant frequencies for several days during December 2013, obtained using Lorentzian and Gaussian fits.

Next, the effect of the method used for the nonlinear optimization required for obtaining the fitting parameters is studied. LM is the most commonly accepted method in the specialized literature for dealing with this type of problems, but it seems advisable at this point to carry out a study of the behavior of the fitting parameters obtained using other different methods. Figure 3.8 plots the SE between the experimental spectrum and the spectrum adjusted using LM, CG, and QN methods. It can be concluded from this figure that CG method produces the highest values for the SE, while LM and QN methods provide lower and very similar error values, indistinguishable most of the time. In addition, an important fact to be taken into account is that LM method is almost one order of magnitude faster than QN method. In this sense and only concerning the LM and QN methods, Figure 3.9 is a plot of the MRD of the fitting parameters for both methods in the data measured by the N-S and E-W sensors. Important differences are again observed suggesting that information on the method used should be provided. Parameters such as individual mode amplitudes and resonance bandwidths present deviations up to 30%, although these differences are reduced to less than 2% for global mode amplitudes, which combine the effect of the three individual modes and the linear term.

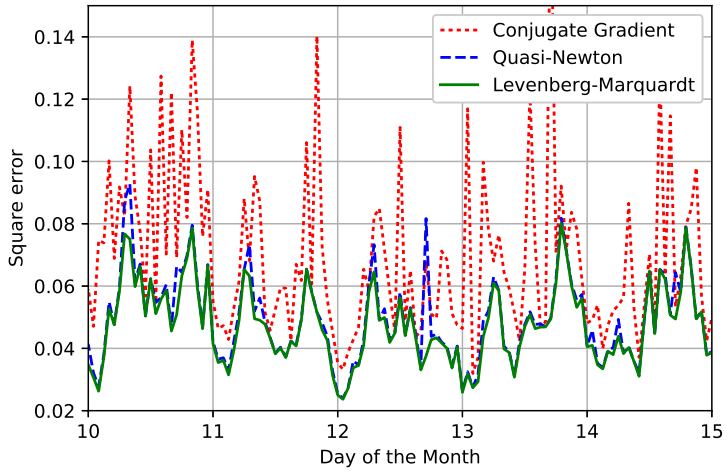

Figure 3.8. Square error between the fitting curves and measured amplitude spectrum using different methods for the fitting process at the N-S sensor between 10 and 15 December 2015.

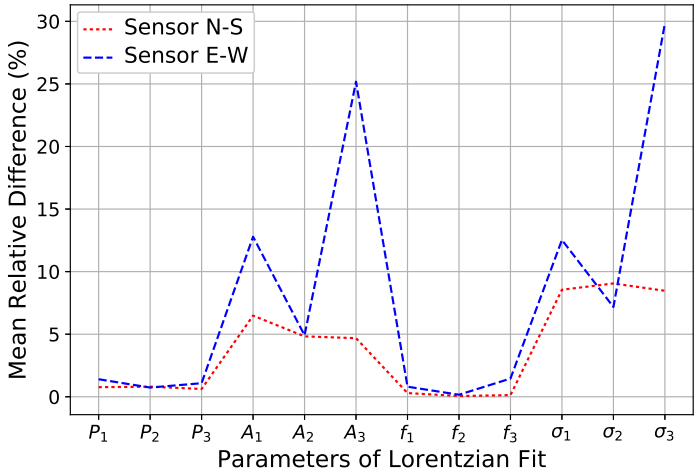

Figure 3.9. Mean relative difference between Levenberg-Marquardt and quasi-Newton methods of the individual mode amplitudes, A_i, resonance frequencies, f_i, and bandwidths, σ_i, together with global mode amplitudes, P_i.

The fitting bandwidth is another variable to be taken into account in the least squares adjustment method used for the Lorentzian fit. The choice of an adjusting band inside the calibrated frequency range, 6 to 25 Hz, may affect the obtained results, especially for the resonances near the band limits. A comparison of the adjusting parameters using Lorentzian functions with different bandwidths is plotted in Figure 3.10. The bandwidth [6.35 and –23.75 Hz] has been chosen as reference band due to the fact that it presents a lower number of parameters outside the acceptable range described in Table 3.1. According to Figure 3.10, differences up to 8% can be obtained depending on the bandwidth used; therefore, it seems that SR values provided by a specific ELF station should be accompanied by the frequency bandwidth used for the curve fitting.

This bandwidth should be maintained for the different measurements of a given ELF station. It would also be desirable that a standardization of this bandwidth is carried out to be generally used by different ELF stations if a sound comparison between the results from different stations is to be expected.

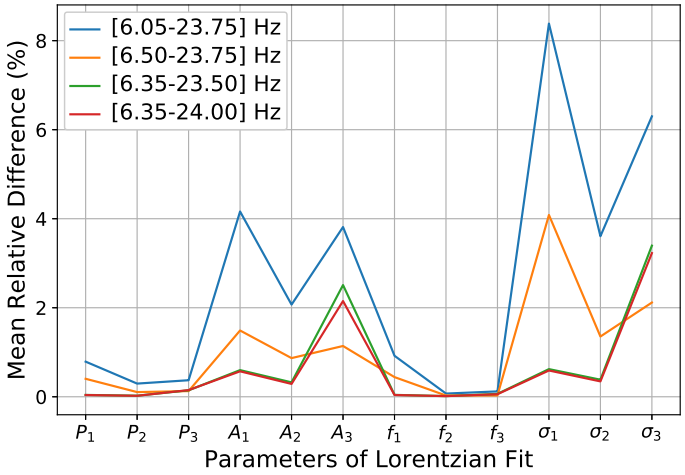

Figure 3.10. Mean relative difference for different fitting bandwidths of individual mode amplitudes, A_i, resonance frequencies, f_i, and bandwidths, σ_i, together with global mode amplitudes, P_i.

The last point considered in the study is again concerned with the definition of SR values. The figures presented above describe the effect of different choices on parameters directly obtained from the fitting process, namely, individual mode amplitudes, A_i, resonance frequencies, f_i, and bandwidths, σ_i. The more stable behavior of the global mode amplitudes, P_i, has also been shown in the figures to test the influence of the different choices in the final result if all the modes are simultaneously considered. It remains to be studied if the local maximum amplitudes and frequencies, P_i' and f_i' , directly obtained from the maxima at the adjusted curve, may be considered as a good definition of SR amplitudes and frequencies. Figure 3.11 shows the MRD between P_i and P_i' and between frequencies f_i and f_i', for the first three resonance modes. Only slight differences can be appreciated, which means that both sets of parameters could be used to define SR parameters. Nevertheless, differences exist and it would be convenient to unify definitions or, at least, specify which of the possible definitions for SR parameters has been used if data are to be shared and compared among different research groups or ELF stations.

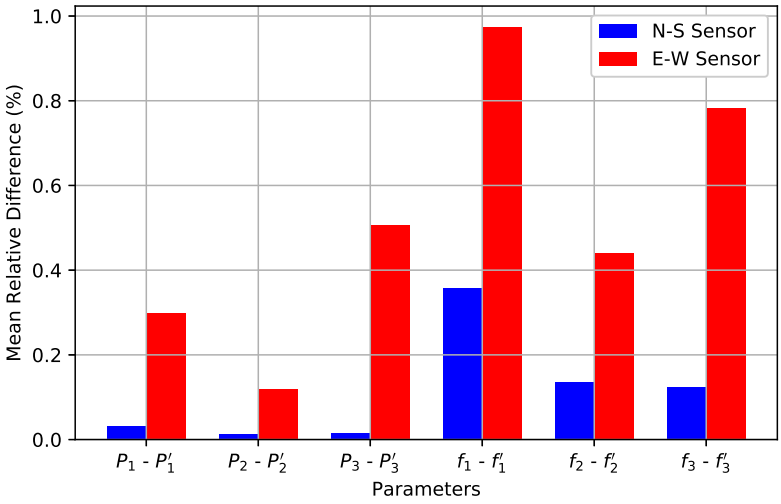

Figure 3.11. Mean relative difference between global mode amplitudes, P_i, and local maximum amplitudes, P'_i , and between resonance frequencies, f_i, and local maximum frequencies, f'_i.

3.4. Conclusions

This work starts from the hypothesis that it is highly convenient to share research techniques and results concerning natural electromagnetic phenomena in a more general sense. Closely related to this aim, it should be necessary to define the procedure to obtain SR parameters from the raw data measured by the different ELF stations around the world. Concerning this particular topic, this work describes in detail a possible procedure to extract SR parameters. Some of the alternatives appearing at critical stages of the process are discussed, together with its effect on the final results.

The procedure is divided into three main stages: the calculation of the amplitude spectrum, the anthropogenic noise elimination, and the curve fitting and SR related parameters definition.

As regards the first stage, the amplitude spectrum for ten minute time series has been obtained using Welch method with a normalized Hann window. Three different time windows, of 10-, 20-, and 30-s duration, have been considered. The MRD of the results may reach 6%, depending on the window size. Since any local phenomena may cause the digitizing system to saturate during certain time windows, these saturated time windows are eliminated from the time series. A quantification of the saturation events, the saturation level, has been defined. It seems that using 10 s time windows is more appropriate than 20 or 30 s ones, since they are still statistically significant but, in addition, its shorter duration causes that saturation events are less likely to occur.

Concerning the second stage, the effect of the human noise is highly dependent on each ELF station; therefore, in order to share SR results, information should be provided on the noise presence, its characteristics, and the filtering procedure used to eliminate it. As regards the ELF station at Sierra Nevada, the anthropogenic noise appears as three very narrow peaks located at specific frequencies near the second SR mode. The noise is filtered by substituting the peaks at this specific noise bands by straight lines connecting the signal at adjacent frequencies. The filtering process may be applied only when a relevant peak is observed or in all cases, even of no human noise is detected. In any case, the difference between both filtered signals is below 2%.

Concerning the third stage, the curve fitting process, several aspects have been addressed. First, the type of fitting functions to be used. Lorentzian and Gaussian functions combined with a linear term are commonly used by scientists. The comparison of adjusted data to experimental ones shows lower errors for the case of Lorentzian fit. In addition, curve fitting using Gaussian functions is more susceptible to yield results out of the expected range, which forces using a mask to filter those values outside an acceptable range. Closely related to curve fitting is the non-linear optimization process used to perform it. A study of the behavior of the CG, QN, and LM methods has been carried out. The comparison to experimental results is better for QN and LM methods, almost indistinguishable most of the time; however the LM method is 1 order of magnitude faster. Finally, the influence of the bandwidth chosen to perform the curve fitting process is also studied. A comparison of several bandwidths to the results obtained using a reference band shows that deviations in the adjusting parameters may reach up to 10% of the reference value in individual mode amplitudes and bandwidths, while differences are sensibly lower for global mode amplitudes and resonance frequencies.

Finally, an important question naturally arises associated to the use of fitting functions to adjust experimental results to an analytical function. Which quantities define the SR parameters? Three possibilities have been considered in this work: (i) directly, the parameters obtained from the fitting process, referred to as the individual mode amplitudes and resonance frequencies; (ii) the global mode amplitudes, which define the amplitude at resonance frequencies simultaneously taking into account all the terms in the adjusting series; and, finally, (iii) the local maximum amplitudes and frequencies, directly obtained from the adjusted curve. The different options considered through this work show stable results for resonance frequencies and global mode amplitudes, but relevant differences, up to 25%, may appear for individual mode amplitudes and bandwidths. As regards considering the adjusted curve, differences below 1% have been found between global mode amplitudes and local maximum am-

plitudes and their corresponding frequencies. This different behavior allows directly using frequencies obtained from the fitting process but this is not so evident to define the SR amplitudes. It seems desirable to unify concepts in order to always compare identical quantities or, at least, provide specific information on the parameters used to define SR properties.

Summarizing, at the moment, the process of extracting information from ELF station measurements is far from being uniquely defined. The existence of a future global network of ELF stations capable of monitoring the natural electromagnetic activity in the Earth's atmosphere and the possibility of using collected data for environmental purposes has been proposed by scientific community in different occasions. Nevertheless, some decisions on the methodology used to obtain SR parameters should be addressed before, in order to define a standardization of the processing method.

Acknowledgements

This work has been supported by the investigation research project FIS2017-90102-R, of the Ministry of Economy and Competitiveness (MINECO) co-financed by the Fund European Regional Development (FEDER), and the Ministry of Education, Science and Sport of Spain through the FPU grants for PhD studentship (reference: FPU15/04291). This manuscript has been developed in the context of the cooperation threads created by COOP+ project (European Union's Horizon 2020 research and innovation program: grant agreement 654131). S. T. R. holds an ESA research fellowship and acknowledges support from the ESA science faculty of the European Space Astronomy Centre (ESAC). We are grateful to Parque Nacional Sierra Nevada for providing support to the project. The data set of this paper is available from http://hdl.handle.net/10481/53032.

References

Balser, M., & Wagner, C. A. (1960). Observations of Earth-ionosphere cavity resonances. *Nature*, *188*, 638–641. https://doi.org/10.1038/188638a0

Bartlett, M. S. (1948). Smoothing periodograms from time series with continuous spectra. *Nature*, *161*, 686–687. https://doi.org/10.1038/161686a0

Dyrda, M., Kulak, A., Mlynarczyk, J., Ostrowski, M., Kubisz, J., Michalec, A., & Nieckarz, Z. (2014). Application of the Schumann resonance spectral decomposition in characterizing the main African thunderstorm center. *Journal of Geophysical Research: Atmospheres*, *119*, 13, 338–13, 349. https://doi.org/10.1002/2014JD022613

Fornieles-Callejón, J., Salinas, A., Toledo-Redondo, S., Portí, J., Méndez, A., Navarro, E. A., Morente-Molinera, J. A., Soto-Aranaz, C., & Ortega-Cayuela, J. S. (2015). Extremely low frequency band station for natural electromagnetic noise measurement. *Radio Science*, *50*, 191–201. https://doi.org/10.1002/2014RS005567

Füllekrug, M., & Fraser-Smith, A. C. (1997). Global lightning and climate variability inferred from ELF magnetic field variations. *Geophysical Research Letters*, *24*(19), 2411–2414. https://doi.org/10.1029/97GL02358

Greenberg, E., & Price, C. (2004). A global lightning location algorithm based on the electromagnetic signature in the Schumann resonance band. *Journal of Geophysical Research: Atmospheres*, *109*, D21111. https://doi.org/10.1029/2004JD004845

Greenberg, E., & Price, C. (2007). Diurnal variations of ELF transients and background noise in the Schumann resonance band. *Radio Science*, *42*, RS2S08. https://doi.org/10.1029/2006RS003477

Kulak, A., Kubisz, J., Klucjasz, S., Michalec, A., Mlynarczyk, J., Nieckarz, Z., Ostrowski, M., & Zieba, S. (2014). Extremely low frequency electromagnetic field measurements at the Hylaty station and methodology of signal analysis. *Radio Science*, *49*, 361–370. https://doi.org/10.1002/2014RS005400

Mushtak, V. C., & Williams, E. R. (2009). An improved Lorentzian technique for evaluating resonance characteristics of the Earth-ionosphere cavity. *Atmospheric Res.*, *91*(2), 188–193.

Newville, M., Stensitzki, T., Allen, D. B., & Ingargiola, A. (2014). LMFIT: Non-linear least-square minimization and curve-fitting for Python. https://doi.org/10.5281/zenodo.11813

Nickolaenko, A. P., & Hayakawa, M. (2002). *Resonances in the Earth-Ionosphere Cavity*. Dordrecht, Netherlands: Kluwer Academy.

Nickolaenko, A. P., & Hayakawa, M. (2014). *Schumann Resonance for Tyros*. Springer, Japan.

Nickolaenko, A. P., Yatsevich, E. I., Shvets, A. V., Hayakawa, M., & Hobara, Y. (2011). Universal and local time variations deduced from simultaneous Schumann resonance records at three widely separated observatories. *Radio Science*, *46*, RS5003. https://doi.org/10.1029/2011RS004663

Ondrášková, A., Ševčík, S., & Kostecký, P. (2011). Decrease of Schumann resonance frequencies and changes in the effective lightning areas toward the solar cycle minimum of 2008-2009. *Journal of Atmospheric and Solar-Terrestrial Physics*, *73*(4), 534–543. https://doi.org/10.1016/j.jastp.2010.11.013

Ondrášková, A., & Ševčík, S. (2013). The determination of Schumann resonance mode frequencies using iterative procedure of complex demodulation. *Contributions to Geophysics and Geodesy*, *43*(4), 305–326. https://doi.org/10.2478/congeo-2013-0018

Ondrášková, A., & Ševčík, S. (2014). The iterative complex demodulation applied on short and long Schumann resonance measured sequences. *Contributions to Geophysics and Geodesy*, *44*(4), 313–328. https://doi.org/10.1515/congeo-2015-0008

Oppenheim, A., & Shafer, R. W. (2009). *Discrete-Time Signal Processing, Prentice Hall Signal Processing Series* (3rd ed.). NJ: Prentice Hall.

Ouyang, X. Y., Xiao, Z., Hao, Y. Q., & Zhang, D. H. (2015). Variability of Schumann resonance parameters observed at low latitude stations in China. *Advances in Space Research*, *56*(7), 1389–1399. https://doi.org/10.1016/j.asr.2015.07.006

Pechony, O., & Price, C. (2006). Schumann resonances: Interpretation of local diurnal intensity modulations. *Radio Science*, *41*(2), RS2S05. https://doi.org/10.1029/2006RS003455

Press, W., Flannery, B., Teukolsky, S., & Vetterling, W. (1992). *The art of scientific computing*. New York: Cambridge University Press.

Price, C., & Rind, D. (1992). A simple lightning parameterization for calculating global lightning distributions. *Journal of Geophysical Research: Atmospheres*, *97*(D9), 9919–9933. https://doi.org/10.1029/92JD00719

Price, C. (2000). Evidence for a link between global lightning activity and upper tropospheric water vapour. *Nature*, *406*(6793), 290–293. https://doi.org/10.1038/35018543

Roldugin, V. C., Maltsev, Y. P., Vasiljev, A. N., Schokotov, A. Y., & Belyajev, G. G. (2004). Diurnal variations of Schumann resonance frequency in NS and EW magnetic components. *Journal of Geophysical Research: Space Physics*, *109*, A08304. https://doi.org/10.1029/2004JA010487

Roldugin, V. C., Vasiljev, A. N., & Ostapenko, A. A. (2006). Comparison of the Schumann resonance parameters in horizontal magnetic and electric fields according to observations on the Kola Peninsula. *Radio Science*, *41*(2), RS2S07. https://doi.org/10.1029/2006RS003475

Rycroft, M. J., Israelsson, S., & Price, C. (2000). The global atmospheric electric circuit, solar activity and climate change. *Journal of Atmospheric and Solar-Terrestrial Physics*, *62*(17), 1563–1576. https://doi.org/10.1016/S1364-6826(00)00112-7

Salinas, A., Toledo-Redondo, S., Navarro, E. A., Fornieles-Callejón, J., & Portí, J. A. (2016). Solar storm effects during Saint Patrick's Days in 2013 and 2015 on the Schumann resonances measured by the ELF station at Sierra Nevada (Spain). *Journal of Geophysical Research: Space Physics*, *121*, 12, 234–12, 246. https://doi.org/10.1002/2016JA023253

Sátori, G. (1996). Monitoring Schumann resonances-II. Daily and seasonal frequency variations. *Journal of Atmospheric and Terrestrial Physics*, *58*(13), 1483–1488. https://doi.org/10.1016/0021-9169(95)00146-8

Sátori, G., & Zieger, B. (1999). El Niño related meridional oscillation of global lightning activity. *Geophysical Research Letters*, *26*(10), 1365–1368.

Schumann, W. O. (1952). Über die stralungslosen Eigenschwingungen einer leitenden Kugel die von einer Luftschicht und einer Ionospärenhle umgeben ist. *Zeitschrift für Naturforschung*, *7a*, 149–154. https://doi.org/10.1515/zna-1952-0202

Sekiguchi, M., Hayakawa, M., Nickolaenko, A. P., & Hobara, Y. (2006). Evidence on a link between the intensity of Schumann resonance and global surface temperature. *Annales Geophysicae*, *24*(7), 1809–1817. https://doi.org/10.5194/angeo-24-1809-2006

Sentman, D. D., & Fraser, B. J. (1991). Simultaneous observations of Schumann resonances in California and Australia: evidence for intensity modulation by the local height of the D region. *Journal of Geophysical Research: Space Physics*, *96*(A9), 15973–15984. https://doi.org/https://doi.org/10.1029/91JA01085

Shvets, A. V., Hobara, Y., & Hayakawa, M. (2010). Variations of the global lightning distribution revealed from three-station Schumann resonance measurements. *Journal of Geophysical Research: Space Physics*, *115*(A12), A12316. https://doi.org/10.1029/2010JA015851

Simões, F., Pfaff, R., Berthelier, J.-J., & Klenzing, J. (2012). A review of low frequency electromagnetic wave phenomena related to tropospheric-ionospheric coupling mechanisms. *Space Science Reviews*, *168*(1-4), 551–593. https://doi.org/10.1007/s11214-011-9854-0

Toledo-Redondo, S., Salinas, A., Portí, J., Morente, J. A., Fornieles, J., Méndez, A., Galindo-Zaldívar, J., Pedrera, A., Ruiz-Constán, A., & Anahnah, F. (2010). Study of Schumann resonances based on magnetotelluric records from the western Mediterranean and Antarctica. *Journal of Geophysical Research: Atmospheres*, *115*(D22114). https://doi.org/10.1029/2010JD014316

Welch, P. (1967). The use of fast Fourier transform for the estimation of power spectra: A method based on time averaging over short, modified periodograms. *IEEE Transactions on Audio and Electroacoustics*, *15*(2), 70–73. https://doi.org/10.1109/TAU.1967.1161901

Williams, E. R. (2009). The global electrical circuit: A review. *Atmospheric Research*, *91*, 140–152. https://doi.org/10.1016/j.atmosres.2008.05.018

Williams, E. R. (1992). The Schumann Resonance: A global tropical thermometer. *Science*, *256*(5060), 1184–1187. https://doi.org/10.1126/science.256.5060.1184

Zhou, H., Yu, H., Cao, B., & Qiao, X. (2013). Diurnal and seasonal variations in the Schumann resonance parameters observed at Chinese observatories. *Journal of Atmospheric and Solar-Terrestrial Physics*, *98*, 86–96. https://doi.org/10.1016/j.jastp.2013.03.021

Chapter 4. Additional concerns to the unified methodology for processing Schumann Resonance measurements

4.1. The anthropogenic noise patterns at the Sierra Nevada ELF station and different elimination schemes

As mentioned in chapter 3, the area where the Sierra Nevada ELF station is located is affected by the presence of anthropogenic noise despite being a natural park. This noise appears as three high, narrow, intermittent peaks in the amplitude spectra at the frequencies of 14.85 Hz, 15.25 Hz and 16.67 Hz.

It is convenient to get rid of these peaks to continue with the next steps of the methodology. Let us discuss in more depth some aspects of this important point.

4.1.1. Pattern of the anthropogenic noise peak at 16.67 Hz

The peak at 16.67 Hz follows a surprisingly regular pattern: it appears for 15 minutes every 45 minutes. This evolution does not depend on the time of the day or the season of the year, and can be seen in Figures 4.1 and 4.2.

The source of this noise is not completely clear. As its frequency is a submultiple of the frequency of the alternating current carried by the power lines (50 Hz), this noise could be caused by the power lines. Another peak is observed in some spectra at the frequency of 32.33 Hz (out of the calibrated band of the magnetometers). Another possibility, pointed out by some researchers (Ondrášková et al., 2007), is that this noise comes from the Austrian railway driving frequency.

4.1.2. Pattern of the anthropogenic noise peaks at 14.85 Hz and 15.25 Hz

As regards the other two peaks at 14.85 Hz and 15.25 Hz, they are caused by a power generator that is near the ELF station. This generator supplies electrical power to

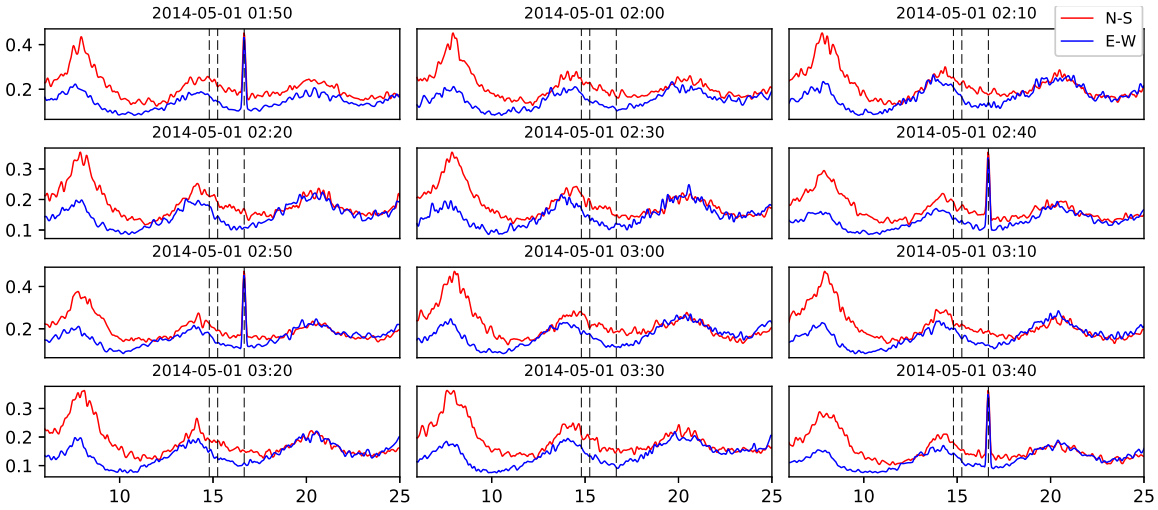

Figure 4.1. Evolution of the anthropogenic noise peak at 16.67 Hz, from 01:50 to 03:40 (Universal Time), 1st of May 2014. The x-axis is the frequency (Hz) and the y-axis is amplitude ($\frac{pT}{\sqrt{Hz}}$).

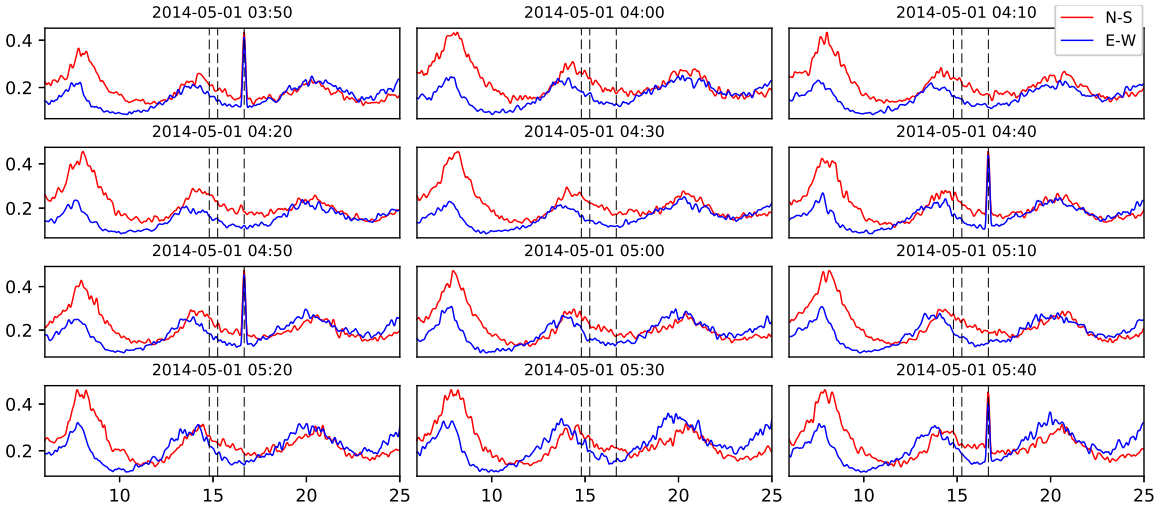

Figure 4.2. Evolution of the anthropogenic noise peak at 16.67 Hz, from 03:50 to 05:40 (Universal Time), 1st of May 2014. The x-axis is the frequency (Hz) and the y-axis is amplitude ($\frac{pT}{\sqrt{Hz}}$).

the mountain hut "Refugio del Poqueira" and is placed next to it, at approximately 200 m of the station as show in Figure 4.3. The distance from the power generator to the magnetometers is a bit greater than 200 m because they are buried approximately 100 m away from the station.

These two peaks at 14.85 Hz and 15.25 Hz follow a diurnal pattern, which repeats day after day with little variation. The peaks appear in the spectra only during the local morning and early afternoon, with their amplitudes varying during the day. This diurnal pattern is shown in Figures 4.4 and 4.5. The x-axis shows the Universal Time.

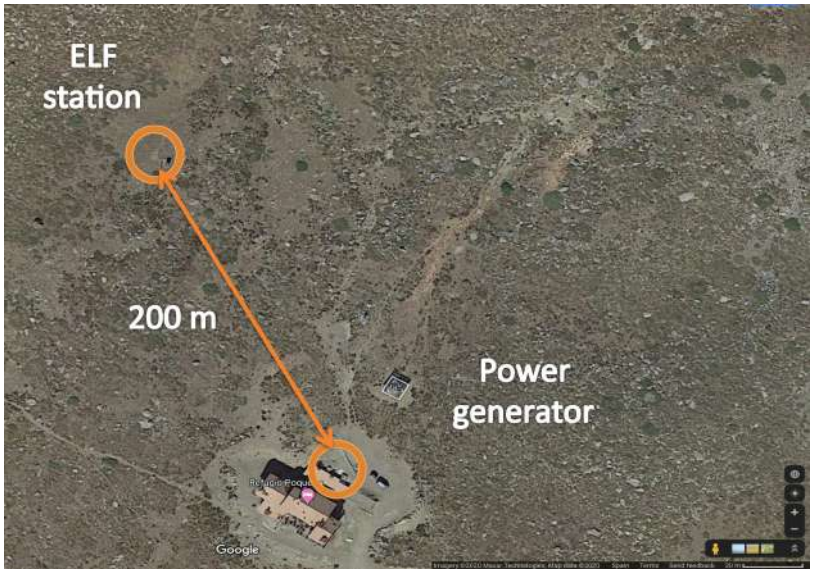

Figure 4.3. Relative position of the Sierra Nevada ELF station and the mountain hut "Refugio del Poqueira", obtained from Google Maps.

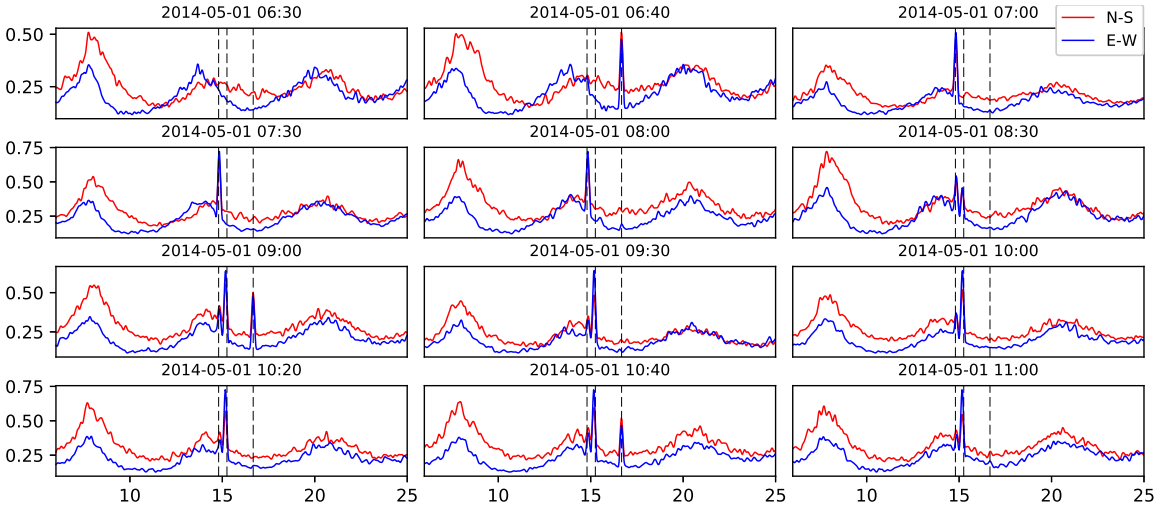

Figure 4.4. Evolution of the anthropogenic noise peaks at 14.85 Hz and 15.25 Hz, from 06:30 to 11:00 (Universal Time), 1st of May 2014. The x-axis is the frequency (Hz) and the y-axis is amplitude ($\frac{pT}{\sqrt{Hz}}$).

4.1.3. Different strategies to detect and remove the anthropogenic noise

At this point we need to eliminate the anthropogenic noise to continue with the proposed methodology. Otherwise, the next step (the Lorentzian fit) would not provide the desired fitting curve parameters as they would be considerable affected by the presence of the noise. The problem of detecting the noise peaks must also be taken into consideration. The detection and elimination of the noise can be addressed, generally speaking, following two different strategies:

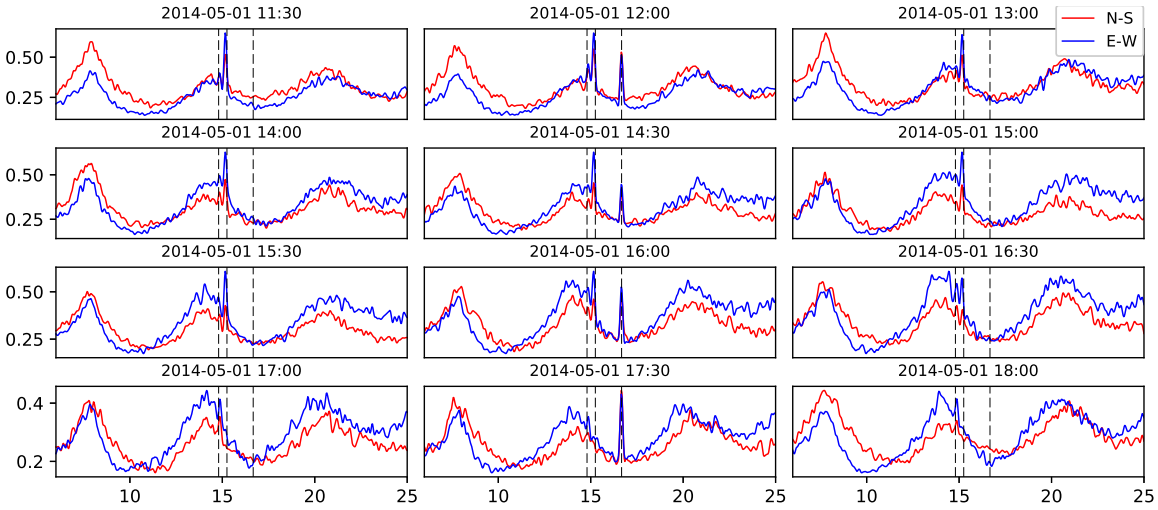

Figure 4.5. Evolution of the anthropogenic noise peaks at 14.85 Hz and 15.25 Hz, from 11:30 to 18:40 (Universal Time), 1st of May 2014. The x-axis is the frequency (Hz) and the y-axis is amplitude ($\frac{pT}{\sqrt{Hz}}$).

– Using a statistical technique to detect and separate the noise from the natural magnetic field in the Time Domain (TD) raw recordings. If the performance of the statistical technique is optimum and the separation of the noise and the natural signal is good, this strategy has the advantage of removing the noise in a more exact and precise way, and it is the only way to obtain the TD SR recordings without noise if we are interested in studying them. The Independent Component Analysis (ICA) has been applied to the raw measurements of the Sierra Nevada station in Rodríguez-Camacho et al. (2017). Also, a method consisting of finding the rotation of the two original directions of the magnetometers (North-South and East-West) that maximizes the value of a certain statistical parameter has been performed on the Sierra Nevada measurements in Rodríguez-Camacho et al. (2018b), and the results obtained have been discussed. However, these techniques can be theoretically complex, due to a non-linear effect on the recordings and depend on a few parameters that must be fixed, and also require considerably long computational periods. The results would also be more difficult to reproduce as they depend a lot on small variations in the data or in the parameters of the separation method.

– Detecting the noise peaks in the spectra and removing them with a technique based on linear interpolation. This option requires implementing an algorithm that detects a peak in the spectra and substitutes it for a straight line. This method is explained in section 5.5, as well as the computational code used to apply the algorithm. The linear interpolation method is illustrated in Figure 4.6.

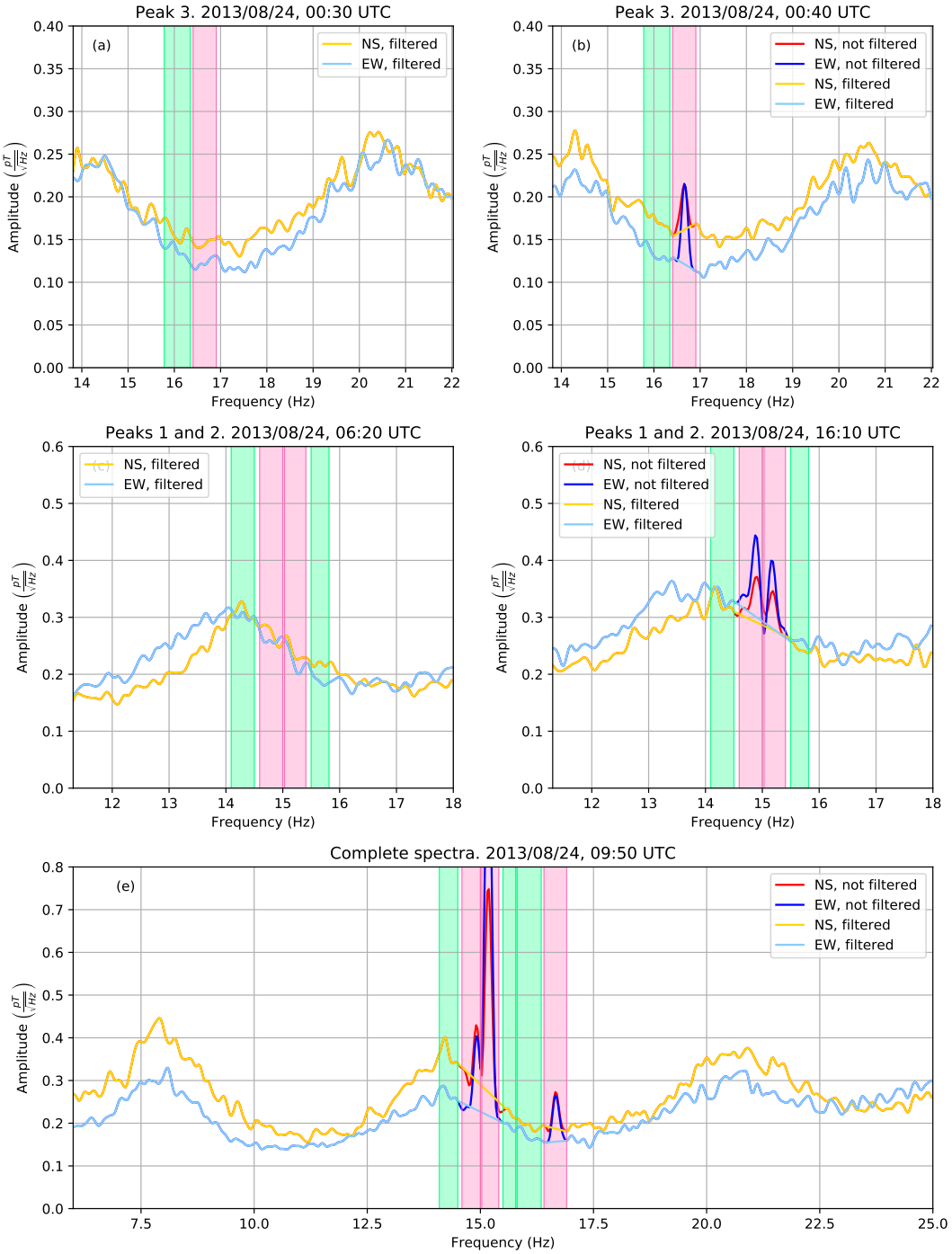

Figure 4.6. Illustration of the linear interpolation method to detect and remove the anthropogenic noise with five real spectra. The noisy bands are shadowed in red, and the reference bands, in green. The detection of the presence of noise peaks in the spectra is based on the comparison between the noise band and the reference band. If the noisy band shows a peak that is considerably higher than the fluctuations observed in the reference band, then there is presence of anthropogenic noise in the spectrum. This process is similar to the way how a human supervisor would determine the presence of noise. If noise is detected, it must be removed by a linear interpolation (straight line) between the edges of the noisy band.

4.2. Different options to define the SR parameters

The precise definition of the SRs parameters is not completely specified in the literature. The following reasonable options to define the amplitude and the central frequency of the i-th resonance will be studied, and we will justify which one is most convenient:

- As the individual mode amplitude (a_i) and the individual mode central frequency (f_i) of the i-th lorentzian function. These are the values directly obtained from the lorentzian fit.
- As the i-th local maximum of the global fitting function (the sum of the three lorentzian functions plus the linear term), and the frequency at which that maximum is reached. We call these values local maximum amplitude (p_i) and local maximum frequency (fp_i).
- Another possibility is to define the central frequency as the individual mode central frequency (f_i) and the amplitude as the value of the fitting curve for that frequency (as_i). This amplitude will be called global mode amplitude.

An illustration of the different definition of the individual mode amplitude, a_i, and the local maximum amplitude, p_i, is shown in Figure 4.7.

The fitting parameter σ_i is directly considered as the definition of the width of i-th resonance, regardless which of the three options has been chosen for the amplitudes and frequencies. This definition for the width is equivalent to the resonance peak width at half maximum, i.e., the distance from the f_i at which the amplitude of the i-th individual mode is a half of the individual mode amplitude ($a_i/2$), as shown in Equation 4.1:

$$l_i(f) = \frac{a_i}{1+\left(\frac{f-f_i}{\sigma_i}\right)^2} \implies l_i(f_i \pm \sigma_i) = \frac{a_i}{1+\left(\frac{(f_i \pm \sigma_i)-f_i}{\sigma_i}\right)^2} = \frac{a_i}{1+\left(\frac{\pm\sigma_i}{\sigma_i}\right)^2} = \frac{a_i}{1+1} = \frac{a_i}{2} \quad (4.1)$$

To decide which definition for the amplitudes and the central frequencies is the best, the following concerns will be considered:

- We can observe that the total fitting function $L(f)$ adapts reasonably well to the experimental spectra. It can be observed by visual inspection or calculating the χ^2 values for the fits. However, the individual lorentzian functions do not stick to the experimental spectra.

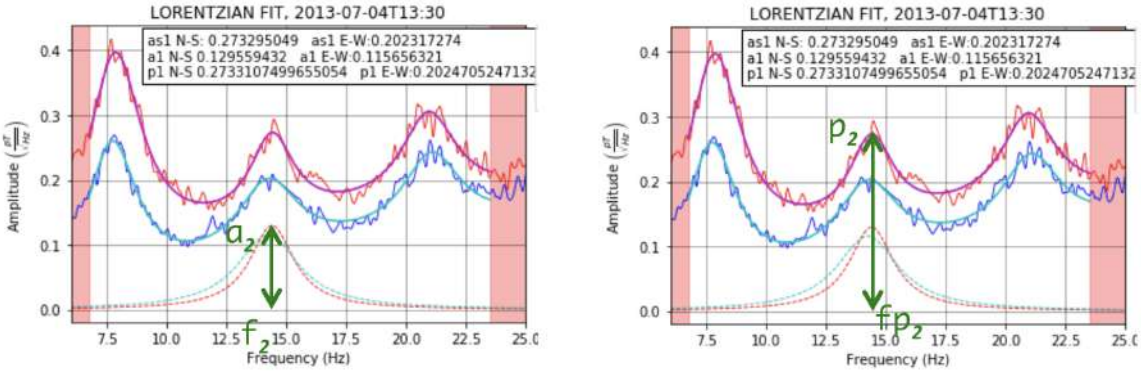

Figure 4.7. The 2nd lorentzian function of the fit (dashed lines) is shown together with the global fitting function and the spectra (solid lines). On the left, the individual mode amplitude, a_2, and the individual central frequency, f_2, are shown. On the right, the local maximum amplitude (p_2) and the local maximum amplitude (fp_2) is shown. The second resonance mode has been taken as an example.

- There may be several combinations of three lorentzian functions and a linear term that yield very similar fitting curves, because differences in the individual mode parameters can compensate to give similar global functions.

- The parameters p_i and fp_i, obtained from the fitting curve, are much more stable and robust than the individual parameters a_i and f_i, as less unacceptable values are obtained after the fit for p_i and fp_i than for a_i and f_i.

It may happen that one or more than one parameters among the individual mode amplitudes (a_1, a_2, a_3), the individual mode central frequencies (f_1, f_2, f_3), the widths (σ_1, σ_2, σ_3), the slope and intercept of the linear part of the fitting curve are anomalous, but the total fitting curve, i.e., the sum of the three lorentzian functions and the linear part, could still fit the spectrum, thus being the global parameters p_1, p_2, p_3, fp_1, fp_2 and fp_3 acceptable.

The amplitude spectra and their lorentzian fits for two different time intervals are shown in Figure 4.8. The values of a_1, a_2, a_3; p_1, p_2, p_3; f_1, f_2, f_3; fp_1, fp_2 and fp_3 are displayed in the figure. We can observe that the global function actually fits to the experimental spectra, whereas the individual mode lorentzian functions do not fit.

In order to prove that p_i and fp_i are more stable than a_i and f_i, the Figure 4.9 is shown. The temporal evolution of the different definitions of the parameters is shown for the third SR, SR3, from the 10th of June to the 20th of June. This is observed for the three SR parameters and for all the days recorded at the station.

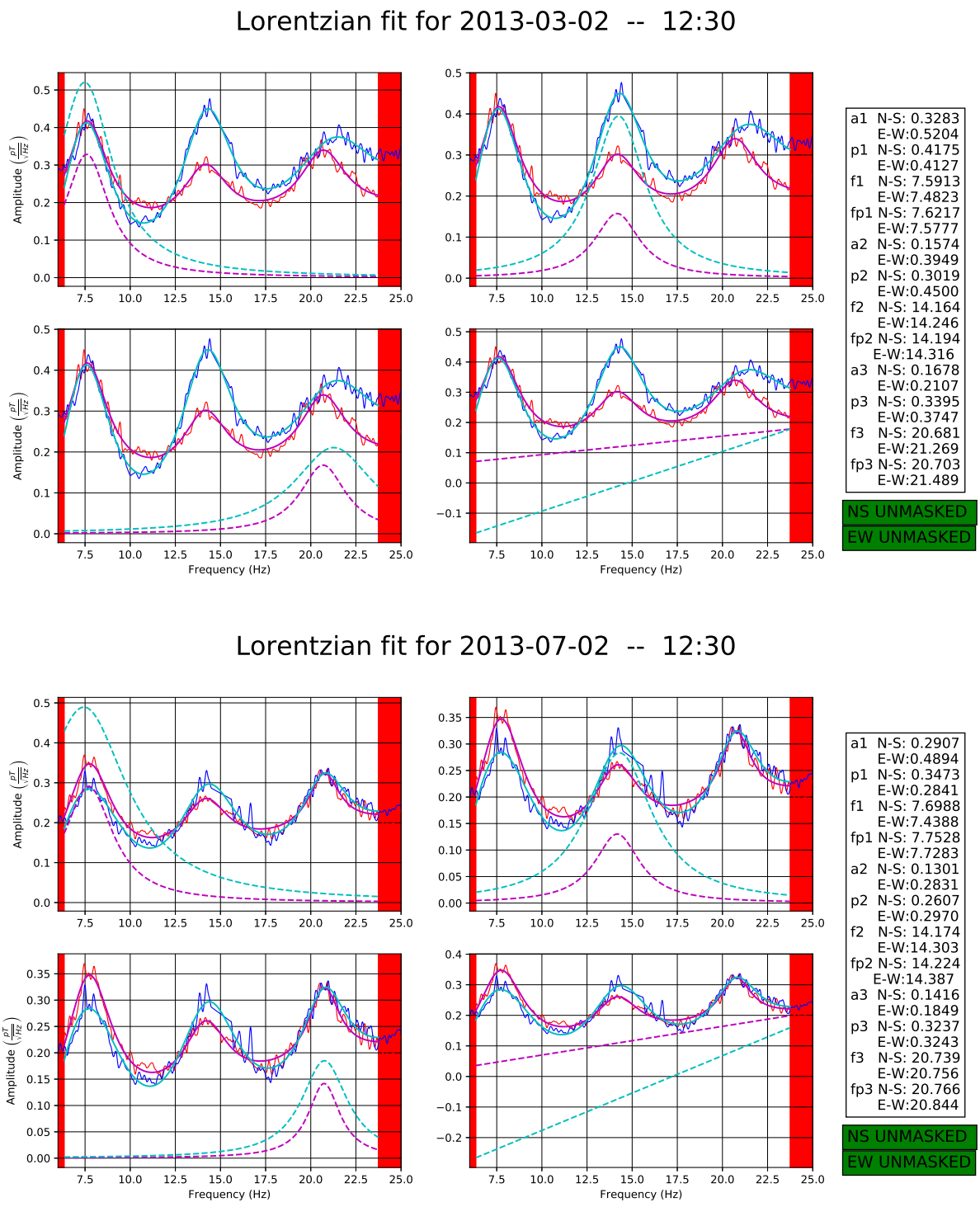

Figure 4.8. The contributions of the 1st mode (upper left), the 2nd mode (upper right), the 3rd mode (lower left) and the linear part to the global fitting curve can be observed separately. It is clear that the global fitting curve is much more meaningful than the individual mode contributions. This trend is observed over all the recordings available.

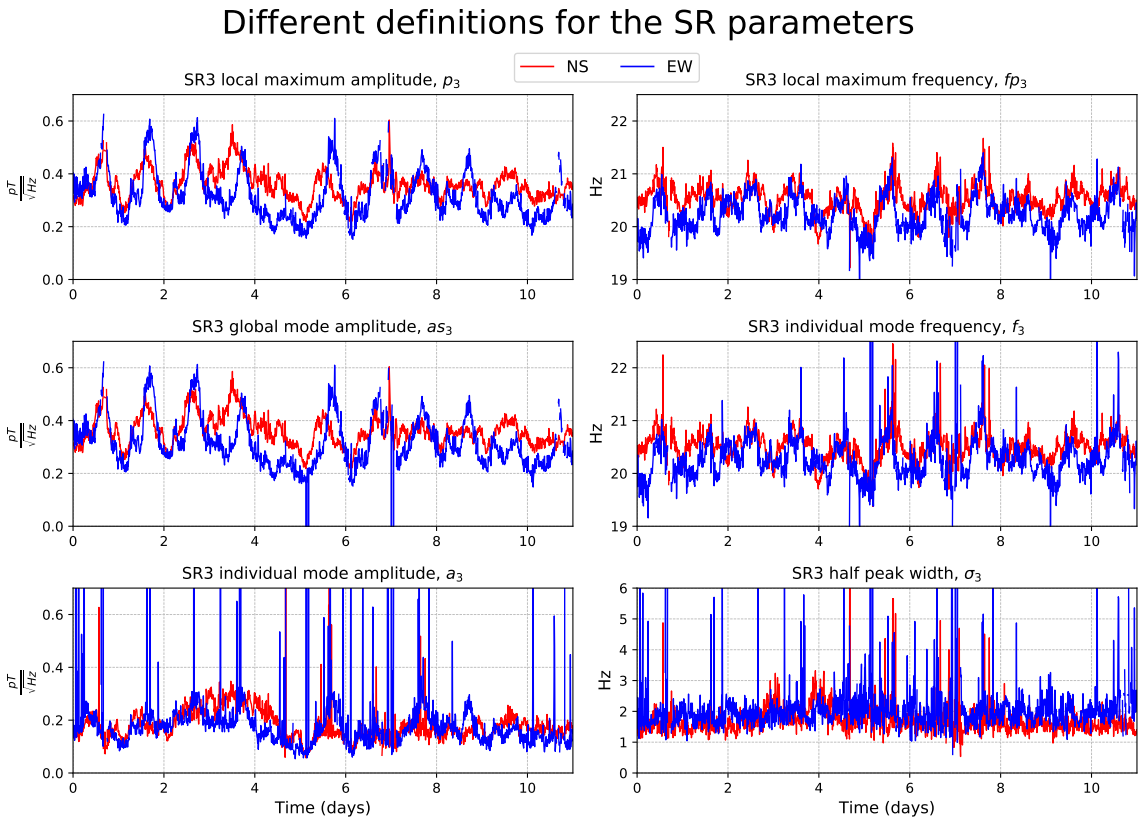

Figure 4.9. Values obtained for p_3, as_3, a_3, f_3, fp_3 and σ_3 for each 10 minute time interval from 10th June (day 0 in the charts) to 20th June (day 10 in the charts), 2014. The parameters p_3 and fp_3 are clearly more stable than as_3, a_3 and f_3.

Then, the SR parameters considered for the long term analysis of the SRs will be the local maximum amplitudes (p_1, p_2, p_3), the local maximum frequencies, (fp_1, fp_2, fp_3) and the half peak widths (σ_1, σ_2, σ_3). These parameters are observed to have acceptable values if the fitting curve has a usual shape and fits to the experimental amplitude spectra.

A part of the discussion shown in this section was presented in Castro et al. (2017) and Rodríguez-Camacho et al. (2019a).

Chapter 5. Schumann resonance data processing programs and four-year measurements from Sierra Nevada ELF station

This chapter has been published in the paper:

Schumann resonance data processing programs and four-year measurements from Sierra Nevada ELF station

Authors: A. Salinas[a,*], **J. Rodríguez-Camacho**[b], J. Portí[b], M.C. Carrión[b], J. Fornieles-Callejón[a], S. Toledo-Redondo[c] (2022).

[a]Department of Electromagnetism and Matter Physics, University of Granada, Granada, Spain
[b]Department of Applied Physics, University of Granada, Granada, Spain
[c]Department of Electromagnetism and Electronics, University of Murcia, Murcia, Spain

* Corresponding author.
E-mail address: asalinas@ugr.es (A. Salinas).

Computers and Geosciences, 105148.

https://doi.org/10.1016/j.cageo.2022.105148

Impact factor (JCR 2021): 5.168.
Q1, 33/202 in Geosciences, Multidisciplinary.

Article info

Keywords:
Schumann resonances
Data processing
ELF station

Abstract

In this work, we present to the scientific community the measurements taken during four years, from March 2013 to February 2017 inclusive, by the Extremely Low Frequency Sierra Nevada station, Spain, together with the data processing programs

developed in Python (version 3.8) to extract the Schumann resonance (SR) parameters (i.e., amplitudes, resonant frequencies, resonance widths) in 10 min time periods from these records. The measurements correspond to the voltage induced by the atmospheric electromagnetic field at the north-south and east west oriented magnetometers of the station. The process comprises four stages. The spectrum, calibrated in the frequency band ranging from 6 Hz to 25 Hz, is obtained at the first stage using the Welch method with Hann windows. The second step eliminates the anthropogenic noise generated by different undesired sources. Next, a non-linear fit of the measured spectrum combining Lorentzian functions together with a linear term is carried out in order to identify the presence of SRs and quantitatively characterize them. This third step is carried out using the Python package Lmfit, which implements the Levenberg-Marquad algorithm. Finally, a compact and easy-to-read output is generated at the fourth stage, using the power of the Numpy arrays and the npz format. In addition, four Jupyter notebooks with the description of the code and the possibility of their use in interactive mode are presented as supplementary material with this paper.

5.1. Introduction

The Earth's electromagnetic cavity consists of the good dielectric atmosphere, limited by two conducting boundaries: the planet surface and the lower ionosphere. The main electromagnetic source of this cavity is the lightning activity, mainly produced by storms. The Earth's electromagnetic cavity has eigenfrequencies around 8, 14, and 21 Hz, for the first three modes, respectively. Lightning produces a broadband electromagnetic spectrum that reaches the MHz band, but, due to the conductivity of the atmosphere at these frequencies, only Extremely Low Frequency (ELF) components, up to ~50 Hz, are capable of completing various turns around the planet before they almost completely attenuate and become undetectable. Multiple lightning sources are active at any time around the globe, exciting ELF modes which are known as Schumann Resonances (SRs) (Schumann, 1952). SRs were predicted in 1952, and first detected by Balser and Wagner (1962). A historical review on the progress of SR studies can be found in (Besser, 2007).

There is plenty of specialized scientific literature on Atmospheric Electrodynamics in general and on SRs in particular. Worthy examples are the books (Nickolaenko & Hayakawa, 2002, 2014) and the reviews (Price, 2016; Simões et al., 2012; or Sátori et al., 2013). The SRs constitute the AC part of the Global Electric Circuit (GEC) (Rycroft et al., 2008) and their variations have been linked to the average temperature of the surface near tropical latitudes (Williams, 1992) and to the global lightning

activity (Füllekrug & Fraser-Smith, 1997; Prácser et al., 2019; Toledo-Redondo et al., 2010; Williams et al., 2014). SRs are also a powerful tool to monitor global climate phenomena, such as El Niño (Williams et al., 2021) and also to study fluctuations in the ionosphere at the scale of years, (e.g., Bozóki et al. 2021; Koloskov et al. 2020; Nickolaenko et al. 2015).

SRs on Earth are a very faint signal, of the order of a few pT for the magnetic field components, i.e., roughly six orders of magnitude below the geo-magnetic field strength at the Earth's surface. Therefore, in order to measure and characterize them, the detectors must have high sensitivity and must be optimized to provide a good signal to noise ratio (Fornieles-Callejón et al., 2015). Most ELF stations devoted to measure SRs typically comprise two magnetometers which lie in the plane of the surface, plus one vertical electric antenna (e.g., Nickolaenko and Hayakawa, 2014). Nowadays, there are several SR stations spread all around the globe and various studies benefit from multi-point observations (Roldugin et al., 2004; Schlegel & Füllekrug, 2000; Sentman & Fraser, 1991; Shvets & Hayakawa, 2011). Despite the interest in ELF station global networks to share data and findings, the actual situation is that each research group usually works with their own data, since details on the data measured, the signal processing techniques and the codes to implement them are not usually available for the scientific community.

In this sense, two contributions are introduced in this work with regards to previous studies on SR measurements which may be of interest for those research groups that are working or want to start research on SRs and related problems such as the GEC. It can also be useful for those research groups in Atmospheric Sciences and Space Weather to make correlations between different measurements. The first contribution is that the scientific community is granted access to four years of raw and processed data from the Sierra Nevada ELF station measurement records. It seems reasonable to think that providing the data is of high interest to pursue a common goal set by the SR research community in particular, and by the atmospheric electrodynamics research community, in general, as it is the creation of a shared database with records of the different worldwide ELF stations. Our intention is not to set a standard for the processing and the format of the data but to propose a starting point. The second contribution of this work is concerned with the presentation of the codes for obtaining the SR parameters and other related results from these data. The analysis of the four year long records may demand a huge amount of code lines, which can make it difficult to fully understand the algorithms and, therefore, may hinder their use by other researchers. For this reason, the Jupyter notebooks (Granger & Perez, 2021) are presented together with this paper in the supplementary material, containing the Python code, as well as the explanations needed to understand the processing of the

data. Providing the data and the self-explanatory Jupyter notebooks focuses on the concepts and tools behind reporting modern data analyses in a reproducible manner: any supposed scientific achievement must be verified and must serve as a basis for building new achievements. In this sense, the notebooks from Jupyter project allow to publish data analyses in a single document that permit other researchers to easily carry out the same analysis to obtain the same results for the provided data and comparable results for their own measurements.

This paper is structured as follows. Section 5.2 describes the main characteristics of the Sierra Nevada ELF station and the structure of the data in the different repositories. Section 5.3 gives the skeleton of the programs and the blocks in which they are structured. In Sections 5.4 to 5.7, a detailed description of each block mentioned above is presented. Finally, Section 5.8 summarizes the main conclusions of this work.

5.2. The station and the data

5.2.1. The station

The ELF measurement station is located at the heart of the Sierra Nevada National Park, at 2500 m above sea level, in the area surrounding the mountain hut, *Refugio del Poqueira* (37^{o}02'N, 3^{o}19'W) and it has two magnetometers, North-South (NS) and East-West (EW) oriented. The magnetometers have been optimized with the specific purpose of measuring the first three SRs with a very high signal-to-noise ratio (28 dB for a time-varying signal of 1 pT in the band from 6 Hz to 25 Hz).

The station data acquisition system works at a sampling frequency of f_m = 256 Hz and generates a raw data file for each sensor and hour. The sampling time interval is 3906 μs, which is slightly less than $1/f_m$. In 1 h file, a total of 921,600 samples are taken, so the time length of measurements of each file is 3599.7696 s, instead of 3600 s, which implies a delay of 0.2304 s every hour. For this reason, the time of the first date of each hour file is different to the next hour, and so on.

The measurements correspond to the output of the sensor, including the amplification and digitization system. Measurements are taken between ±10 V limits, greater values produce saturation. The digitization system employs 16 bits equally distributed. The amplification system uses a Butterworth filter of tenth order to dampen the effect of the 50 Hz network signal. Due to the specific characteristics of the designed filter,

it is very inaccurate to obtain the phase of the transfer function. That's why the scaling function shown below only defines the amplitude.

The magnetometers have been calibrated for frequencies between 6 Hz and 25 Hz. Considering the equivalent circuit of the magnetometers, (Fornieles-Callejón et al., 2015), their frequency response corresponds to an RLC circuit that exhibits an almost flat response for frequencies below 25 Hz, approximately, which defines the upper bandwidth limit. In order to avoid the $1/f$ noise, the lower bandwidth limit has been established to 6 Hz. To convert the voltage induced in the sensors into a magnetic field, the calibration function must be defined for each frequency of the spectrum. Previously, it is necessary to pass the measurements from the time domain to the frequency domain using the Fourier transform. From the theorical RLC model of the magnetometers, the calibrated magnetic field is given by:

$$B(f) = S_c(f)V(f), \tag{5.1}$$

with f in the (6 Hz, 25 Hz) interval. $B(f)$ is the magnetic field (in $T/\sqrt{Hz}$), $V(f)$ is the transformed voltage amplitude and $S_c(f)$ is the calibration coefficient for each frequency f. As mentioned above, the specific design of the Butterword filter presents difficulties in accurately measuring the phase, therefore, we only apply the calibration function to the amplitude of the Fourier transformed voltage and all the quantities in (5.1) are to be understood as the amplitude of the corresponding quantity.

The function $S_c(f)$ is given by:

$$S_c(f) = \frac{1}{2500}\ \frac{1}{1.9\cdot 10^6}\ \frac{1}{f}\sqrt{\left(1-\left(\frac{f}{f_0}\right)^2\right)^2+\left(2\delta\frac{f}{f_0}\right)^2}, \tag{5.2}$$

where 1/2500 is the amplification factor, $1/(1.9\cdot 10^6)$ is the magnetometer sensitivity, $1/f$ is given by Faraday's induction law. Finally, f_0 and δ are the resonance frequency and dumping factor of the equivalent RCL of the measurement system, respectively, and they can be calculated from:

$$f_0 = \frac{1}{2\pi\sqrt{LC_T}}, \quad \delta = \frac{R}{2}\sqrt{\frac{C_T}{L}}, \tag{5.3}$$

where $R = 320$ kΩ is the magnetometer resistance, $L = 298$ kH is the magnetometer inductance and $C_T = 40$ pF is the magnetometer capacitance. The technical char-

acteristics of the station are described in more detail in (Fornieles-Callejón et al., 2015).

5.2.2. The data

The Sierra Nevada ELF station was deployed on July 17, 2012 and has been operating almost continuously since March 2013. The measurement period made available with this paper runs from March 2013 to February 2017. The days for which no measurements are available are: 2014, July 2 and 3 and November 5 to 18; 2016, from July 4 to 6.

The raw data of the station corresponding to the aforementioned measurement periods can be downloaded from the following Zenodo repositories (Salinas et al., 2022a, 2022b, 2022c, 2022d). Each repository corresponds to one year of measurements except the first one that contains the data for the years 2013 (from March) and 2017 (January and February).

Each data folder is named with the four digits corresponding to the specific year, e.g., 2014. Each year contains folders for each month, named with the four digits corresponding to the year and month, e.g., 1412 stands for the raw data during December 2014. Within each month folder, the data and information files for each sensor and each hour are available. Data are stored in files containing measurements corresponding to a time period of approximately 1 h. The filenames begin with a common part, "smplGRTU1_sensor_", followed by a specific part to denote the sensor used (0 for the NS orientation and 1 for the EW orientation), the date and the initial time of the measurements recorded. For example, smplGRTU1_sensor_0_1412010430 stands for data measured by the NS-oriented magnetometer, during the year 2014, month 12, day 01, hour 04, and starting minute 30. The information file has the same name but ends with _info.txt. Each information file, among other data, contains the specific time in which the first sample of the corresponding data file is taken. The starting time for each file is determined using GPS signals and has a resolution of milliseconds. Since this time of the first sample in each file is variable and part of the filename, the filenames in each month folder are not completely determined a priori. For this reason and to ease the task of the different programs used, each month folder includes two files, 'ficheros0' and 'ficheros1', for sensor NS and EW respectively, that contain the set of filenames for that specific month. Therefore, for each normally measured day, we have 24 data files and also 24 information files for each sensor. Each hour data file occupies 1.8 MB, so each month has roughly a data volume of 2.6 GB.

The data in each 1 h data file is in 16-bit binary format and its conversion to voltage involves multiplying by a factor defined by $10/2^{15}$, to describe the ±10 V saturation limits and the use of a 16-bit of the A/D system, one bit for the sign and 15 bits for amplitude.

5.3. The code: an overview

The software codes to extract the SR parameters presented with this work are programmed in Python (version 3.8) using the modules Numpy,[1] Matplotlib,[2] Lmfit,[3] and Interact[4] (this one is only used in notebooks).

The main blocks and programs developed are the following:

1. 'Reading_Fourier.py'. It reads the raw data in the time domain and obtains the amplitude spectrum in the calibrated band of the measurement system.

2. 'Anthropo.py'. When present, this program eliminates the anthropogenic noise in the amplitude spectrum of the previous step.

3. 'Lorentz_Lmfit.py'. The program applies a non-linear fit using the 'Lmfit' module of Python to generate a Lorentzian fitted spectrum together with its corresponding error parameters.

4. 'Packaging.py'. This program carries out a final storage of the relevant data. The program generates a file for each month and sensor that allows a direct reading and recovering of the structure (arrays of the Numpy package of Python) of all the processed data generated by the previous packages for subsequent analysis purposes.

The full set of four programs may be of interest to those researchers who are interested in the direct measurements of the Sierra Nevada station or in processing their own raw data. They are welcome to use the program of block 1 using the ELF station raw data that can be downloaded from the Zenodo repositories (Salinas et al., 2022a, 2022b, 2022c, 2022d) as mentioned above. But the code is developed in modular form, thus, as regards those researchers interested in working with the different phases of the spectrum, with or without anthropogenic noise, with the spectrum fitted

[1] https://numpy.org/.
[2] https://matplotlib.org/.
[3] https://lmfit.github.io/lmfit-py/.
[4] https://pypi.org/project/interact/.

or not, they can use the output files from programs in block 2 or 3. There are several repositories that can help in this task. The University of Granada repositories http://hdl.handle.net/10481/73978 and http://hdl.handle.net/10481/73978 contain all the files of the complete process (blocks 1 to 4) corresponding to December 2014 and March 2015 respectively. They have the same structure of years and months as the raw data folder. Within each month, output files for each step of the processing can be found. The code files, notebooks and one day (March 1, 2015) input/output files can be downloaded from the GitHub repository https://github.com/asalinas62/Sierra_Nevada_SR.

If the researcher's interest is exclusively concentrated in the use of the final results of the analysis, they can directly use the files resulting from block 4. These files can be downloaded from the University of Granada repository https://digibug.ugr.es/handle/10481/71563. This folder stores the final SR results of the raw data processing from the period of time between March 2013 to February 2017. These files have been used to carry out the Schumann resonance long-term analysis presented in (Rodríguez-Camacho et al., 2022), where a first analysis of the data provided with this work can be found.

The input and output files associated to the programs used for each intermediate processing stage are:

1. 'Reading_Fourier.py': the amplitude spectra and related information generated by this program are stored in the following files (December 2014 is used as an example):
   - SR1412_media_0,1: it contains the amplitude spectra within the calibrated band of the magnetometers (6 Hz–25 Hz), for the NS sensor (sensor 0) and for the EW sensor (sensor 1), respectively. The writing format is ASCII in one column.
   - SR1412_satper_0,1: it stores the percentage of those 10 s intervals that show saturation within each 10 min interval. There is a file for each sensor. The writing format is ASCII in one column.
2. 'Anthropo.py': the anthropogenic noise detected in the measurements is eliminated from the spectrum. The following output file is generated:
   - SR1412_mediaNA_0,1: similar to SR1412_media_0,1 but with the anthropogenic noise filtered from the amplitude spectra. The writing format is ASCII in one column.
3. 'Lorentz_Lmfit.py': a Lorentzian fitting of the amplitude spectrum is made. The output files for this step are:

- SR1412_mediaLO_0,1: it contains the parameters of the Lorentzian adjustment of the spectra in amplitude for each 10 min interval and sensor. The writing format is ASCII in one column.
- SR1412_mediaLOC_0,1: it includes the fitting error parameter of the χ^2 function in each spectrum. The writing format is ASCII in one column.
- SR1412_mediaLOE_0,1: it contains the errors that the fitting program assigns to each calculated fitting parameter. The writing format is ASCII in one column.

As a summary of the whole process, for each month of measurements (December 2014 and NS sensor is used as an example) and each sensor the procedure is as follows. The raw data from the station is arranged in files 1 h long. The 'Reading_Fourier.py' program calculates the amplitude spectrum for the frequency band (6 Hz–25 Hz) and the saturation index for each 10 min interval and they are saved in two files, SR1412_media_0 and SR1412_satper_0, respectively. The first file is used to filter the anthropogenic noise with the 'Anthropo.py' program and the output spectra are stored in the file SR1412_mediaNA_0. This file in turn serves as input for the 'Lorentz_Lmfit.py' program, which returns the parameters of the Lorentzian fit. Finally, selected outputs of each block are stored.

The general procedure for processing data from an ELF station with the code presented in this work may have many particularities that must be taken into account if it is to be adapted to data from other stations. Nevertheless, we can establish the following general inputs to the programs that can be adapted to each particular ELF station:

1. Define the measurement interval generated by the station: in our case, one month is divided in 1 h data files.

2. Define the characteristics of the A/D system: sampling frequency, measurement range and number of bits.

3. Define the calibration function to convert voltage into magnetic field. In the case of the Sierra Nevada ELF station and due to the characteristics of the sensors, this step can only be taken in the frequency domain.

4. In case there is anthropogenic noise with characteristics similar to those found in Sierra Nevada: define the frequency bands with possible anthropogenic noise.

A more detailed description of the programs corresponding to this overview is carried in the following sections.

5.4. Signal processing step 1: the Reading_fourier.py program

This program reads the raw data and obtains the amplitude spectrum for each component of the horizontal magnetic field. The code and details of this stage are described in the notebook 'Reading_Fourier_docu.ipynb'.

The data for each hour and sensor is processed in 10 min intervals. Since the noise level is large due to the low power of SRs, in order to get a natural stabilization of the SR spectra, we apply the Welch method to improve the signal to noise ratio. The 10 min time signal is divided into 10 s segments, overlapped by 5 s, and a Fast Fourier Transform (FFT) is calculated for each of them after applying a Hann window. Following Nickolaenko and Hayakawa, 2002, pg. 170, the resulting power spectra are then averaged, and the calibration function is applied to the obtained amplitude spectrum, see also (Price & Melkinov, 2004), providing physical units of $pT/\sqrt{Hz}$.

To apply Welch's method, the FFT of a set of n data is made, taken in groups of m data and with a shift of p data. The number of intervals generated from n, m and p is $[(n-m)/p]+1$, where '[ ]' stands for the integer part. The value of n corresponds to the amount of data in a 10 min interval. The value of m = 2560 corresponds to the number of measurements in a 10 s sub-interval and p corresponds to a 5 s shift interval, which means that consecutive FFTs have and overlap of 5 s.

As mentioned above, we use the Hann's window with m samples that is defined by:

$$h(i) = 1 - \cos^2(\pi(i-1)/m) \tag{5.4}$$

for $i = 1, \ldots, m$, with the normalizing factor $\sqrt{\sum_{i=1}^{m} h(i)^2/m}$. The m data window is expanded with zeros to 10^{23} samples. This new window size and the sampling frequency define a frequency increment of 31.25 mHz.

The FFT is done with the Numpy subroutine 'fft.rfft' that takes advantage of the real character of the data. The Hann window and Welch method have been easily implemented using Numpy arrays.

In the analysis of each 10 min interval through the FFT of the 10 s sub-intervals, each 10 s time span including saturated signals is eliminated and not considered in the average for its corresponding 10 min interval. According to the number of 10 s time portions eliminated, the percentage of saturation for each 10 min span is defined.

This saturation level may be indicative of the presence of transient sources in the ELF band. Due to the large size of the Earth's electromagnetic cavity, it is likely that its influence in global quantities is not relevant but may be indicative and interesting to detect local phenomena. The study of the possible correlation of this percentage of saturation with global or local variations of the different parameters associated with the SRs, amplitudes, resonance frequencies and resonance widths is a pending task which is beyond the scope of this work.

The following directory tree is considered in this program. The input files for this code contain the raw data measured at the station, which are stored in a folder named 'S_N_Data' (Sierra Nevada Data). The output files are located in the folder named 'S_N_FD' (Sierra Nevada, Frequency Domain) which contains another sub-folder with the month under study in a scheme which resembles that of the 'S_N_Data' folder. As previously mentioned, the 'Reading_Fourier.py' code generates two output files: one stores the spectrum and the other includes the percentage of saturation for each 10 min interval in that specific month. There are independent files for each magnetometer. The output file is organized as one column data using ASCII format. As regards the spectrum, the file includes an amplitude value for each frequency between 6 Hz and 25 Hz with a frequency resolution of 31.25 mHz, while there is a unique value of the saturation level for each 10 min interval.

Fig. 5.1 shows an example of the raw data measured by one of the sensors, at 256 samples/s, which is the input for program 'Reading_Fourier.py'. The ordinate axis represents volts at the magnetometers due to the fact that the calibration function $S_c(f)$ required to translate to magnetic field values is defined in the frequency domain and the data are shown in time domain. Fig. 5.2 shows an example of the amplitude spectra for the two sensors obtained as output of the program 'Reading_Fourier.py' for a specific 10 min interval spectrum, such as that shown in Fig. 5.1. The three SR peaks can be clearly distinguished at roughly 8, 14, and 20 Hz. In addition, there are fluctuations of the spectra due to the low energy of the signal (below 0.4 pT/$\sqrt{Hz}$ for the whole 6 Hz–25 Hz band). As stated before, the electromagnetic field energy that can travel few turns around the cavity is very small, due to the losses caused by the conductivity of the Earth's atmosphere.

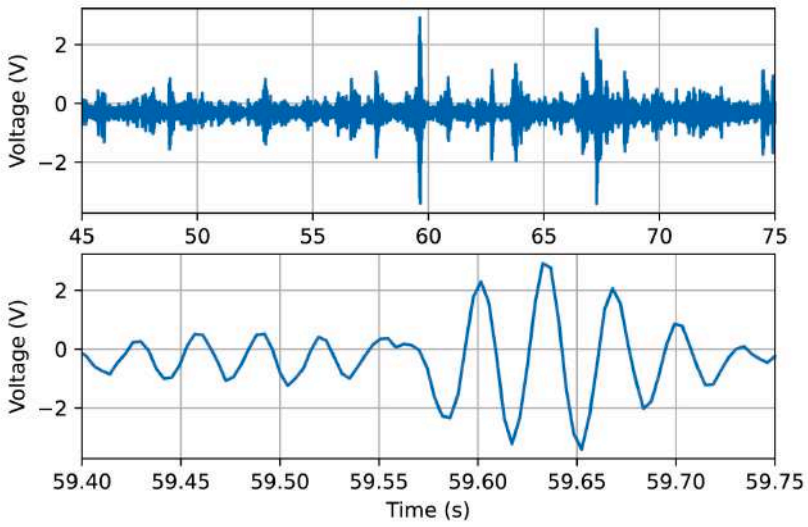

Figure 5.1. Example of the raw data generated by the station data system. The signal corresponds to voltage in the time domain recorded by the NS-oriented magnetometer at a rate of 256 samples/s. The upper plot corresponds to the time interval after 45 s from the instant 00:49 UTC on March 1, 2015. The lower plot shows in more detail the time interval ranging from 59.4 s to 59.75 s.

5.5. Signal processing step 2: elimination of the anthropogenic noise

Despite the site to set the Sierra Nevada ELF station was carefully chosen to avoid human activity, an increase of this activity occurred in the vicinity of the station soon after its deployment, and, since then, the appearance of anthropogenic signals could be detected in the measurements at certain hours. This noise is not observed in the example of Fig. 5.2 but in other 10 min intervals, such as in the example shown in the top of Fig. 5.3, the amplitude spectrum of the signal includes clear narrow peaks with an amplitude much higher than that of the natural signal. These peaks are fundamentally observed in three bands, (14.7 Hz, 15.00 Hz), (15.00 Hz, 15.48 Hz), and (16.45 Hz, 16.90 Hz), which have an anthropogenic origin. The first two peaks are closely located and appear while a diesel generator that supplies electricity to a mountain hut near the station is running. The third peak contains the operating frequency of the Central European train network. The appearance of this anthropogenic noise does not follow a fixed hourly pattern, so its elimination requires a detection process to avoid filtering in time intervals for which there is no noise. Furthermore, the presence of noise in the different bands is neither simultaneous nor permanent. Thus, there are some 10 min intervals for which the three peaks can be observed, only one or two peaks are present in another intervals, while other periods do not present any anthropogenic signal at all. Due to the proximity of the two lower

bands, the combined frequency band (14.55 Hz, 15.35Hz) has been considered to deal with the anthropogenic noise originated by the diesel generator of the hut.

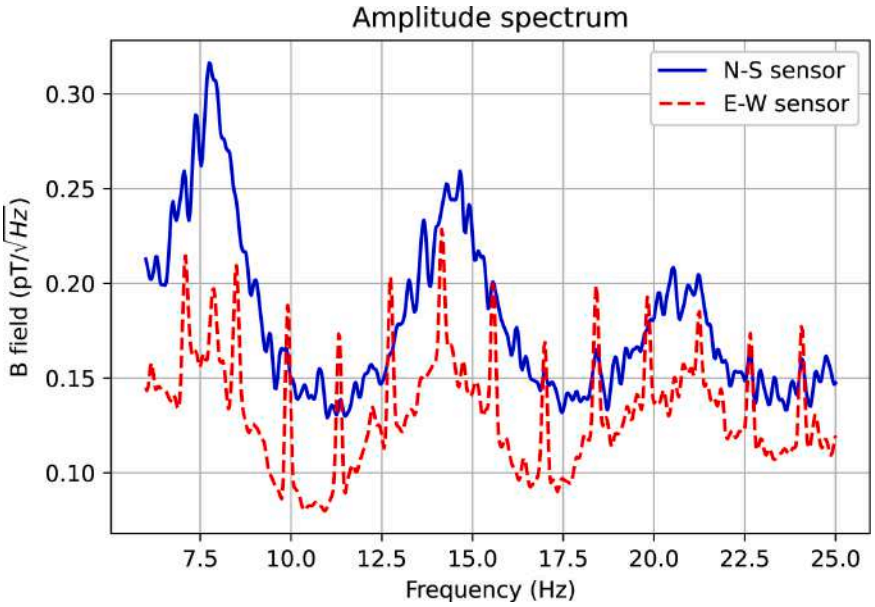

Figure 5.2. Example of output from the program 'Reading_Fourier.py', which shows the typical amplitude spectrum for the two sensors during a given 10 min interval. The signal corresponds to the 10 min interval associated to the time 00:49:34 UTC of March 1, 2015.

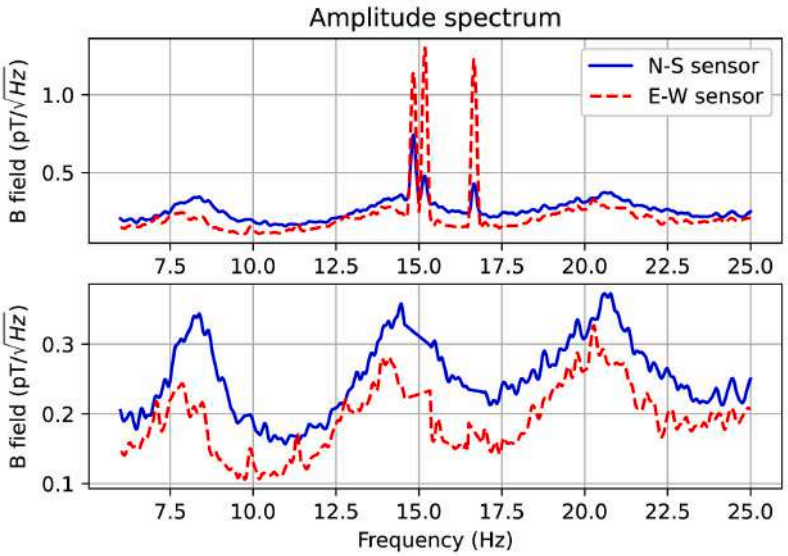

Figure 5.3. Example of application of anthropogenic noise filtering. (Top) Amplitude spectrum generated by the program 'Reading_Fourier.py' for a 10 min time period in which anthropogenic noise is present. Blue and red lines correspond to the NS and EW sensors, respectively. (Bottom) The spectra in the top panel are processed with the program 'Antropo.py'. The resulting spectra are plotted showing that the anthropogenic noise has been removed. The signal corresponds to the 10 min interval associated to the 17:10 UTC of March 29, 2015.

If an anthropogenic signal exists in the corresponding noisy band, a straight line is fitted between these limits. That is to say, for a set of n noisy measurements of the magnetic field in this band, $B_N(i)$, at a frequency $f_N(i)$, where $i = 1, ..., n$,

with $i = 1$ and $i = n$ define the lower and upper limits of the band, respectively, the filtering process consists of substituting the actual measurements, $B_N(i)$, by the filtered values, $B_{FN}(i)$ corresponding to $f_N(i)$ for the straight line connecting the noisy band limits, $f_N(1)$ and $f_N(n)$:

$$B_{FN}(i) = \frac{B_N(n) - B_{Ni}(1)}{f_N(n) - f_N(1)}(f_N(i) - f_N(1)) + B_N(1). \tag{5.5}$$

The problem raised is determining if the anthropogenic noise is present or not to avoid filtering a signal unaffected by this type of noise. To this aim, a neighbor band at which anthropogenic noise has never been detected is used as reference. At this band, the set of reference measured magnetic field, $B_R(i)$, at the reference frequencies, $f_R(i)$, $i = 1, \ldots, n$, helps in detecting the anthropogenic noise presence. To do so, interpolated values $B_{FR}(i)$ at the reference frequencies for the straight line connecting the reference band limits are calculated through the expression:

$$B_{FR}(i) = \frac{B_R(n) - B_R(1)}{f_R(n) - f_R(1)}(f_R(i) - f_R(1)) + B_R(1). \tag{5.6}$$

Then, quantities d_N and d_R to compare interpolated and original values are defined for both the anthropogenic noise band and the reference one in the following manner:

$$d_{N,R} = \text{Max}\left\{\frac{B_{N,R}(i) - B_{FN,FR}(i)}{B_{FN,FR}(i)}\right\} + \text{Min}\left\{\frac{B_{N,R}(i) - B_{FN,FR}(i)}{B_{FN,FR}(i)}\right\}, \tag{5.7}$$

where the N and R subscripts refers to the noise and the reference bands, respectively. The way in which d_N and d_R allow detecting the presence of anthropogenic noise is as follows. In the absence of anthropogenic noise in the considered band and due to the fact that the ELF signal detected at the station includes a natural noise component, measurements will be randomly distributed above and below the straight line and the sum of the positive maximum and negative minimum terms in (5.7) tend to compensate. This also applies in the reference band, which is defined close to the band with anthropogenic noise to preserve a similar behavior. In contrast, when anthropogenic noise is present, the maximum positive term in (5.7) will be considerable higher and will not be cancelled by the minimum negative value which will not be substantially affected. For this reason, detecting a value of d_N clearly higher than that of d_R indicates the presence of anthropogenic noise and the noise filter must be applied, and the actual measurements $B_N(i)$ are substituted by the filtered ones, $B_{FN}(i)$ at each frequency measured.

More detailed explanations are given in 'Antropo_Docu.ipynb'. The process is automatic, but the singularity of the noise advises including the possibility of a second and direct correction if the filtered signal is not as good as expected after this first automatic filtering process. To this end, the notebook allows carrying out a visual inspection of the signal to apply a second-stage filtering. To perform this task, the 'Interact' package within the Python module 'ipywidgets'[5] is used.

Fig. 5.3 shows an example of the anthropogenic noise removal. The top panel shows the output of the program 'Reading_Fourier.py' for a 10 min period time with anthropogenic noise. Three large spikes can be clearly observed, two around 15 Hz and one around 16.5 Hz. The bottom panel shows the same spectra after being processed with the program 'Antropo.py'. The anthropogenic noise has been removed. As a final result of this step, we have a file with the signal amplitude spectrum for each sensor and month, which is free of anthropogenic noise within the calibrated band of the magnetometers. In Fig. 5.2 and for the EW sensor, a somehow regular spike sequence can be also observed but their amplitude is comparable to that of the measured signal. These peaks are a result of the noisy nature of the ELF signal received and they do not require the application of a filtering process as it is the case of the anthropogenic peaks of much higher amplitude observed at the top of Fig. 5.3.

The input files for 'Antropo.py' program are the output files of 'Reading_Fourier.py' program, i.e., the amplitude spectrum for each 10 min interval of the month under study and its percentage of saturation. The output of 'Antropo.py' is a file containing the spectrum without anthropogenic noise but maintaining the structure of the input file, that is to say, ASCII format and one column. In case this filtering stage is not required, it will suffice changing the name of the output file of program 'Reading_Fourier.py' or, alternatively, to change the name of the input file of program 'Lorenzt_Lmfit.py' of the next step.

5.6. Signal processing step 3: curve fitting using Lorentzian functions

Once the two previous steps have been applied, the amplitude spectrum of the horizontal magnetic field components, free of anthropogenic noise, is available for each 10 min interval. Unfortunately, this spectrum shows important fluctuations due to its low amplitude with respect to the amplitude of the environmental and instrumental noises, as it can be seen in Figs. 5.2 and 5.3. The bandwidth of the magnetometers at

[5] https://pypi.org/project/ipywidgets/.

the Sierra Nevada station allows the measurement of the first three SRs. Each mode is quantitatively defined through three parameters: amplitude or local maximum value of the spectrum, frequency at which this maximum is observed, and bandwidth of each resonance. These parameters are difficult to define in the noisy spectra of stages 1 and 2. To overcome this difficulty, we can adjust the noisy spectrum to an analytical function that allows defining them with the least possible ambiguity. The resonant behavior expected is in the origin of the Lorentzian fit first proposed in (Sentman, 1987). Since then, a fit combining Lorentzian functions, plus a straight line to allow taking into account a possible slope in the spectrum, is often used by other authors (Mushtak and Williams, 2009; Nickolaenko and Hayakawa, 2002, and references therein). The comparison of Lorentzian fits with Gaussian ones is considered in (Rodríguez-Camacho et al., 2018), which confirms lower errors between the adjusted and experimental data for the case of the Lorentzian fit.

Therefore, the goal of this part of the process is to fit the noisy spectrum provided by step 2 for each 10 min interval using a Lorentzian function for each peak in the frequency interval within the calibrated bandwidth of the magnetometers. The code and notebook associated with this step is 'Lorentz_Lmfit.py' and 'Lorentz_Lmfit_docu.ipynb' respectively.

The Lorentzian fit for adjusting the signal corresponding to three modes used in this stage consists in minimizing the mean square error between the experimental spectrum and the function defined by:

$$L(f) = \sum_{i=1}^{3} \frac{A_i}{1 + \left(\frac{f - f_i}{\sigma_i}\right)^2} + Bf + C, \tag{5.8}$$

where A_i stands for the amplitude of the i-th mode, resonating at frequency f_i and with a bandwidth of σ_i, while parameters B and C correspond to an added linear adjusting term in the frequency spectrum.

In addition to these 11 parameters, we can define a global mode amplitude, P_i, as the value of the fitting function at the resonance frequencies, f_i. Namely:

$$P_i = L(f_i) \tag{5.9}$$

These values describe the amplitude of each resonance peak and takes into account the simultaneous effect of the three Lorentzian terms combined with the correcting effect of the linear term.

The procedure therefore consists in minimizing a function χ^2 that accounts for the difference between the data and the model by varying the parameters of the fitting:

$$\chi^2 = \sum_{i=1}^{N} (F(f_i) - L(f_i))^2, \tag{5.10}$$

where $F(f_i)$ is the value of the measured spectrum for the frequency f_i, L is the fitting function, namely, the sum of Lorentzian functions and a linear term, also for the frequency f_i, and N is the total number of samples of the spectrum to be analyzed. Therefore, the function χ^2 is a scalar function that depends on 11 parameters and the optimization problem results in finding the vector with the values of the 11 parameters for which function χ^2 has a minimum value.

In the developed code, we use the packages 'numpy', 'lmfit.minimize', and 'lmfit.Parameters'. The module 'lmfit'[6] is not installed by default within Python. This module provides a high-level interface for performing non-linear adjustments in Python. It is an extension of 'scipy.optimize', the first optimization module developed for this language. We chose the Levenberg-Marquardt fit algorithm, which provides good results with less computing demands than other methods (Rodríguez-Camacho et al., 2018).

In order to carry out the fit, the method needs the estimation of a seed, or initial value, for each one of the 11 parameters. The seeds are chosen as follows for each 10 min interval:

1. We start from preset values for the central frequencies, width of each of the first three resonances and the linear term. This choice is based on averaged measurements of these quantities. Details can be found in (Rodríguez-Camacho et al., 2018).

2. The initial guesses for peak amplitudes are determined by averaging the month of data and taking the average amplitude at the predefined central frequency. This choice of initial amplitudes is a simplification of the process described in (Rodríguez-Camacho et al., 2018), but providing similar results.

The code executes the following steps:

1. Reading of the output spectra of the 'Anthopo.py' program of block 2, i.e., the calibrated frequency band for each 10 min interval.

[6] https://lmfit.github.io/lmfit-py/model.html.

2. Definition of the spectrum for the range of fitting frequency band that is contained in the range of calibrated frequency interval. The bandwidth (6.35 Hz – 23.75 Hz) has been chosen because it produces a lower number of parameters outside the acceptable range described in Table 1 in (Rodríguez-Camacho et al., 2018) when compared to other possible frequency regions defined inside the calibrated bandwidth of the station magnetometers.

3. Call to 'lmfit' function and determination of 11 fitting parameters for each 10 min interval of the month.

4. Evaluation of the three global mode amplitude.

5. Output of the results obtained.

The outputs of program 'Lorentz_Lmfit.py' for each 10 min interval of the month and sensor are:

1. A list of 14 fitting parameters.

2. A list of the 11 errors associated with the Lorentzian fitting.

3. A list of the mean square errors (χ^2 function) of the fitting.

The error parameters are outputs of program Lmfit. The study of the correlation of these errors with variations of the parameters associated with the SRs is still pending.

Fig. 5.4 shows the results of fitting an amplitude spectrum using three Lorentzian fits. The signal in red line shows the anthropogenic noise filtered spectrum obtained after applying the program 'Anthropogenic.py' at stage two. This signal is the input for the program 'Lorentz_Lmfit.py' of stage three, which provides the fit shown with blue-dashed line.

5.7. Step 4: Data packaging

In the final part of the process, a file is generated in numpy format (npz[7]) with all the information for the month. This is the file that could be shared between ELF stations, containing all the information necessary for the study of the SRs for each month. Information about the beginning in universal time of each 10 min interval of the month is also incorporated.

For each 10 min interval, the following readings from the previous steps are done:

[7] https://numpy.org/doc/stable/reference/generated/numpy.savez.html.

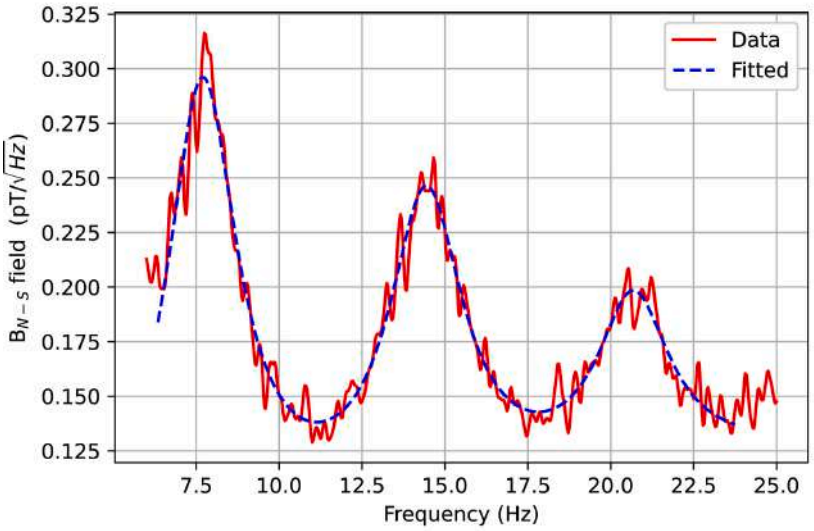

Figure 5.4. Example of fitted amplitude spectrum, using three Lorentzian curves plus a linear term. The red line shows the output of stage two, program 'Anthropo.py', and the blue line shows the fitted spectrum resulting from applying program 'Lorentz_Lmfit.py' of stage 3. The signal corresponds to the 10 min interval associate to time 00:49 UTC of March 21, 2015.

- Percentage of saturation.
- Amplitude spectrum.
- Parameters of the Lorentzian fitting.
- Value of the χ^2 function.
- Value of the error in the fitting for each parameter.

In addition, six new parameters associated with the Lorentzian fitting are obtained from the fitted spectra. They correspond to the maximum amplitude values for each mode and corresponding frequencies for each resonance. The maximum values of this fitted function, the local maximum amplitudes, and their corresponding frequencies, local maximum frequencies, also could define the SR amplitudes and frequencies, respectively. This calculation has been included in this part in order to make it optional with respect to the Lorentzian fitting made in the previous step.

The output file has npz format for writing/reading data. The file is in binary format, but it maintains the numpy array structure so that its reading and the recovery of the structure of each array is immediate. This makes that the size of each file is considerably reduced and, in addition, that no specific program is required to relate data with each output array. As a drawback, the reading depends on Python language and the Numpy package.

There is a file for each month of measurements and for each sensor. The filename makes reference to the year, month and sensor used. The name for December 2014 and sensor NS is SN_1412_0.npz, for instance. Each file has a size of 43.3 MB, therefore, all the months can be stored in the same directory in order to facilitate the reading for a later analysis. The list of saved arrays is:

- 'sat': saturation percentage,
- 'fre': list of frequencies in the calibrated band,
- 'freajus': list of frequencies in the adjustment band,
- 'rs': spectra obtained from the measurements,
- rs_LO: spectra obtained from the fitting process,
- PARLO: parameters obtained from the adjustment (peaks, amplitudes, frequencies, widths, slope, and ordinate at the origin of the linear term),
- parLOC: χ^2 function,
- parLOE: error in the parameters,
- pr: maximum values for each resonance,
- time: date and time of the beginning of each 10 min interval of the month.

5.8. Conclusions

Measuring the natural ELF electromagnetic field in the atmosphere is a complicated task. The ELF stations around the Earth are scarce and the techniques to extract the SRs from them are also complex. Sharing these measurements, procedures and codes may help to spread the findings of a particular research group to the rest of scientific community and to establish a global network to study SRs and their applications.

In this work, we present the algorithms that allow characterizing each SR mode starting from the raw data measured by the ELF station at Sierra Nevada, Spain, recorded between March 2013 and February 2017. This software is written in Python language (version 3.8), because it allows easy access to the different stages of the procedure and, therefore, it facilitates obtaining intermediate results as well as including modifications, adaptations and even improvements of the method. A detailed and comprehensive description of the code is given through several Jupyter notebooks that are provided as supplementary material. In addition, the time raw data series

measured by the Sierra Nevada station during a four year period are provided in this paper as well as the outputs of the different parts of the procedure.

The procedure starts from the time series raw data measured by the ELF station and ends with the obtention of three parameters to quantitatively describe each resonance: peak amplitude, central frequency and resonance width. The code is divided into four stages, which can be run independently in order to optimize the results of each stage without affecting the other. Each block can be run on a personal computer requiring a CPU time of a few minutes.

The programs and basic tasks carried out in each stage are the following:

1. First, 'Reading_Fourier' reads the raw data obtained by the stations and generates an initial spectrum for each 10 min period of each month.

2. The program 'Anthropo.py' is applied to filter the human noise present in some of the spectra obtained at the first stage.

3. In the third stage, a Lorentzian fit is obtained through the program 'Lorentz_Lmfit'.

4. Finally, the last program, 'Packaging.py', generates an output file in 'npz' format with all the results.

Authorship contribution statement

All authors conceived the idea, provided software supervision and participated in essential manuscript reviews and editing. The code has been developed mainly by A. Salinas and J. Rodríguez-Camacho. The original manuscript has been written by A. Salinas and J. Portí. S. Toledo-Redondo, J. Fornieles-Callejón and M.C. Carrión provided project resources and contributed to data curation and analysis.

Code availability section

Name of the code/library: Sierra_Nevada_SR
Contact: asalinas@ugr.es; +34 958242312.
Hardware requirements: Laptop or PC running Linux, Mac or Windows operating systems.
Program language: Python (version 3.8).
Software required: Python and Jupyter notebooks.
Program size: 27 kB (total for the four programs).
The source codes, Jupyter notebooks and one day of data (March 1, 2015) can be found at: https://github.com/asalinas62/Sierra_Nevada_SR.

The Sierra Nevada ELF raw data station from the period March 2013 to February 2017 can be downloaded from the Zenodo repositories (Salinas et al., 2022a, 2022b, 2022c, 2022d).

The final proceeded data from the previous raw data using the program 'Packaging.py' in npz format can be download from the University of Granada repository http://hdl.handle.net/10481/71563.

The raw data, intermediate proceeded and final data of the December 2014 and March 2015 can be download from the University of Granada repositories http://hdl.handle.net/10481/73978 and http://hdl.handle.net/10481/73977 respectively.

Declaration of competing interest

The authors declare that they have no known competing financial interests or personal relationships that could have appeared to influence the work reported in this paper.

Acknowledgments

This work has been supported by the investigation research project FIS2017-90102-R, of the Ministry of Economy and Competitiveness (MINECO) co-financed by the Fund European Regional Development (FEDER), and the Ministry of Education, Science and Sport of Spain through the FPU grants for PhD studentship (reference: FPU15/04291). We acknowledge support of the Ministry of Science and Innovation of Spain (grant PID2020-112805GA-I00). We are grateful to Parque Nacional Sierra Nevada for providing support to the project.

Appendix A. Supplementary data

Supplementary data to this article can be found online at https://doi.org/10.1016/j.cageo.2022.105148.

References

Balser, M., & Wagner, C. A. (1962). On frequency variations of the Earth-ionosphere cavity modes. *Journal of Geophysical Res.*, *67*(10), 4081–4083. https://doi.org/10.1029/JZ067i010p04081

Besser, B. P. (2007). Synopsis of the historical development of Schumann resonances. *Radio Science*, *42*(2), RS2S02. https://doi.org/10.1029/2006RS003495

Bozóki, T., Sátori, G., Williams, E., Mironova, I., Steinbach, P., Bland, E. C., Koloskov, A., Yampolski, Y. M., Budanov, O. V., Neska, M., Sinha, A., Rawat, R., Sato, M., Beggan, C., Toledo-Redondo, S., Liu, Y., & Boldi, R. (2021). Solar cycle-modulated deformation of the earth–ionosphere cavity. *Frontiers in Earth Science*, *9*, 735. https://doi.org/10.3389/feart.2021.689127

Fornieles-Callejón, J., Salinas, A., Toledo-Redondo, S., Portí, J., Méndez, A., Navarro, E. A., Morente-Molinera, J. A., Soto-Aranaz, C., & Ortega-Cayuela, J. S. (2015). Extremely low frequency band station for natural electromagnetic noise measurement. *Radio Science*, *50*, 191–201. https://doi.org/10.1002/2014RS005567

Füllekrug, M., & Fraser-Smith, A. C. (1997). Global lightning and climate variability inferred from ELF magnetic field variations. *Geophysical Research Letters*, *24*(19), 2411–2414. https://doi.org/10.1029/97GL02358

Granger, B., & Perez, F. (2021). Jupyter: Thinking and storytelling with code and data. *Computer Science and Engineering*, *23*(2), 7–14. https://doi.org/10.1109/MCSE.2021.3059263

Koloskov, A. V., Nickolaenko, A. P., Yampolsky, Y. M., Hall, C., & Budanov, O. V. (2020). Variations of global thunderstorm activity derived from the long-term Schumann resonance monitoring in the Antarctic and in the Arctic. *Journal of Atmospheric and Solar-Terrestrial Physics*, *201*, 105231. https://doi.org/10.1016/j.jastp.2020.105231

Mushtak, V. C., & Williams, E. R. (2009). An improved Lorentzian technique for evaluating resonance characteristics of the Earth-ionosphere cavity. *Atmospheric Res.*, *91*(2), 188–193.

Nickolaenko, A. P., & Hayakawa, M. (2002). *Resonances in the Earth-Ionosphere Cavity*. Dordrecht, Netherlands: Kluwer Academy.

Nickolaenko, A. P., & Hayakawa, M. (2014). *Schumann Resonance for Tyros*. Springer, Japan.

Nickolaenko, A. P., Koloskov, A. V., Hayakawa, M., Yampolski, Y. M., Budanov, O. V., & Korepanov, V. E. (2015). 11-year solar cycle in Schumann resonance data as observed in Antarctica. *Sun and Geosphere*, *10*(1), 39–49.

Prácser, E., Bozóki, T., Sátori, G., Williams, E., Guha, A., & Yu, H. (2019). Reconstruction of global lightning activity based on Schumann resonance measurements: Model description and synthetic tests. *Radio Science*, *54*(3), 254–267. https://doi.org/10.1029/2018RS006772

Price, C., & Melkinov, A. (2004). Diurnal, seasonal and inter-annual variations in the Schumann resonance parameters. *Journal of Atmospheric and Solar-Terrestrial Physics.*, *66(13-14)*, 1179–85. https://doi.org/10.1016/j.jastp.2004.05.004

Price, C. (2016). ELF electromagnetic waves from lightning: the Schumann resonances. *Atmosphere*, *7*(9), 116. https://doi.org/10.3390/atmos7090116

Rodríguez-Camacho, J., Fornieles, J., Carrión, M. C., Portí, J. A., Toledo-Redondo, S., & Salinas, A. (2018). On the need of a unified methodology for processing Schumann resonance measurements. *Journal of Geophysical Research: Atmospheres*, *123*(23). https://doi.org/10.1029/2018JD029462

Rodríguez-Camacho, J., Salinas, A., Carrión, M. C., Portí, J., Fornieles-Callejón, J., & Toledo-Redondo, S. (2022). Four year study of the Schumann resonance regular variations using the Sierra Nevada station ground-based magnetometers. *Journal of Geophysical Research: Atmospheres*, *127*(6), e2021JD036051. https://doi.org/10.1029/2021JD036051

Roldugin, V. C., Maltsev, Y. P., Vasiljev, A. N., Schokotov, A. Y., & Belyajev, G. G. (2004). Diurnal variations of Schumann resonance frequency in NS and EW magnetic components. *Journal of Geophysical Research: Space Physics*, *109*, A08304. https://doi.org/10.1029/2004JA010487

Rycroft, M. J., Harrison, R. G., Nicoll, K. A., & Mareev, E. A. (2008). An overview of Earth's global electric circuit and atmospheric conductivity. *Space Science Reviews*, *137*, 83–105. https://doi.org/10.1007/978-0-387-87664-1_6

Salinas, A., Rodríguez-Camacho, J., Portí, J., Carrión, M. C., Fornieles-Callejón, J., & Toledo-Redondo, S. (2022a). Four-year measurements from Sierra Nevada ELF station. Zenodo. Year 2014 [Data set]. https://doi.org/10.5281/zenodo.6348691

Salinas, A., Rodríguez-Camacho, J., Portí, J., Carrión, M. C., Fornieles-Callejón, J., & Toledo-Redondo, S. (2022b). Four-year measurements from Sierra Nevada ELF station. Zenodo. Year 2015 [Data set]. https://doi.org/10.5281/zenodo.6348773

Salinas, A., Rodríguez-Camacho, J., Portí, J., Carrión, M. C., Fornieles-Callejón, J., & Toledo-Redondo, S. (2022c). Four-year measurements from Sierra Nevada ELF station. Zenodo. Year 2016 [Data set]. https://doi.org/10.5281/zenodo.6348930

Salinas, A., Rodríguez-Camacho, J., Portí, J., Carrión, M. C., Fornieles-Callejón, J., & Toledo-Redondo, S. (2022d). Four-year measurements from Sierra Nevada ELF station. Zenodo. Years 2013, p.2017 [Data set]. https://doi.org/10.5281/zenodo.6348930

Sátori, G., Rycroft, M., Bencze, P., Märcz, F., Bór, J., Barta, V., Nagy, T., & Kovács, K. (2013). An overview of thunderstorm-related research on the atmospheric electric field, Schumann resonances, sprites, and the ionosphere at Sopron, Hungary. *Surveys in Geophysics*, *34*(3), 255–292. https://doi.org/10.1007/s10712-013-9222-6

Schlegel, K., & Füllekrug, M. (2000). Diurnal harmonics in Schumann resonance parameters observed on both hemispheres. *Geophysical Research Letters*, *27*(17), 2805–2808. https://doi.org/10.1029/2000GL003774

Schumann, W. O. (1952). Über die stralungslosen Eigenschwingungen einer leitenden Kugel die von einer Luftschicht und einer Ionospärenhle umgeben ist. *Zeitschrift für Naturforschung*, *7a*, 149–154. https://doi.org/10.1515/zna-1952-0202

Sentman, D. D. (1987). Magnetic elliptical polarization of Schumann resonances. *Radio Science*, *22*(4), 595–606. https://doi.org/10.1029/RS022i004p00595

Sentman, D. D., & Fraser, B. J. (1991). Simultaneous observations of Schumann resonances in California and Australia: evidence for intensity modulation by the local height of the D region. *Journal of Geophysical Research: Space Physics*, *96*(A9), 15973–15984. https://doi.org/https://doi.org/10.1029/91JA01085

Shvets, A., & Hayakawa, M. (2011). Global lightning activity on the basis of inversions of natural ELF electromagnetic data observed at multiple stations around the world. *Surveys in Geophysics*, *32*(6), 705. https://doi.org/10.1007/s10712-011-9135-1

Simões, F., Pfaff, R., Berthelier, J.-J., & Klenzing, J. (2012). A review of low frequency electromagnetic wave phenomena related to tropospheric-ionospheric coupling mechanisms. *Space Science Reviews*, *168*(1-4), 551–593. https://doi.org/10.1007/s11214-011-9854-0

Toledo-Redondo, S., Salinas, A., Portí, J., Morente, J. A., Fornieles, J., Méndez, A., Galindo-Zaldívar, J., Pedrera, A., Ruiz-Constán, A., & Anahnah, F. (2010). Study of Schumann resonances based on magnetotelluric records from the western Mediterranean and Antarctica. *Journal of Geophysical Research: Atmospheres*, *115*(D22114). https://doi.org/10.1029/2010JD014316

Williams, E., Bozóki, T., Sátori, G., Price, C., Steinbach, P., Guha, A., Liu, Y., Beggan, C., Neska, M., Boldi, R., et al. (2021). Evolution of global lightning in the transition from cold to warm phase preceding two super El Niño events. *Journal of Geophysical Research: Atmospheres*, *126*(3), e2020JD033526.

Williams, E. R. (1992). The Schumann Resonance: A global tropical thermometer. *Science*, *256*(5060), 1184–1187. https://doi.org/10.1126/science.256.5060.1184

Williams, E. R., Mushtak, V. C., Guha, A., Boldi, R. A., Bor, J., Nagy, T., Satori, G., Sinha, A. K., Rawat, R., Hobara, Y., et al. (2014). Inversion of multi-station Schumann resonance background records for global lightning activity in absolute units. *AGU Fall Meeting Abstracts*, *2014*, 1, AE24A–08.

Chapter 6. Design of algorithms, functions and notebooks aimed at the automatic visualization of relevant SR long term analysis features

The previous chapters are devoted to the design and the description of a methodology to process the Sierra Nevada ELF SR measurements. In this chapter, the main objective is to present the collection of codes, functions and programs that will be used in the following chapter for the study of the long term SR variations. This material will be public and available for the reader to use, together with the data, as one of the goals of this thesis is to enable the reader to quickly and easily perform their own customized study of the SRs. This material offers an option for designing the computer architecture that will be used to complete the entire processes of extraction and analysis of the SRs from the ELF magnetic field raw data. The principle of these codes to be adaptive to measurements from other ELF stations has been followed. This system of codes, functions and programs is completely open to suggestions and improvements by the scientific community, as many options to organize each step of the methodology and the variations study may exist.

6.1. Time arrangement of the 10 min intervals

The starting point in this chapter is the `npz` file described at the end of section 5.5 for each month and sensor (NS/EW). This file contains the mentioned information for each 10 min time interval of that month and sensor. The starting time for each interval of a month is different, which is due to two reasons:

- The sampling time interval is 3906 μs, which is slightly less than $1/f_m = 1/256$, and this causes a shift of 0.2304 s every hour (equivalently, 5.53 s every day or 2 min 46 s every month).
- There are some gaps in the recordings due to sporadic technical failures in the station or problems with the transfer and storage of the data. Although it is unusual, sometimes the station stops recording data and after a random period of time (a few minutes, hours or days), starts working again.

In order to clarify and systematize the later analysis of the recordings, the central time (the average of the starting and final times) of each 10 min interval will be approximated to the closest 10 min division of the hour. For example, if the central

time of an interval is 08:37:12, this central time is approximated to 08:40:00, and if the central time is 21:04:42, it is approximated to 21:00:00.

The time arrangement of the 10 min intervals is illustrated in Figure 6.1. Each cell of the table corresponds to a certain day and time, and contains all the relevant information concerning that interval (the parameter values, the power spectrum integral, the saturation ratio, etc). The time arrangement process is needed to calculate the diurnal (or daily) variations of the SRs, which implies averaging the parameter values over all the intervals corresponding to the same time of different days (i.e., to the same column of the table), or to the same day (i.e., to the same row of the table).

	00:00 (j=0)	00:10 (j=1)	00:20 (j=2)	00:30 (j=3)	...	...	23:40 (j=142)	23:50 (j=143)
2013-03-01 (i=0)	2013-03-01 00:00	2013-03-01 00:10	2013-03-01 00:20	2013-03-01 00:30	...	...	2013-03-01 23:40	2013-03-01 23:50
2013-03-02 (i=1)	2013-03-02 00:00	2013-03-02 00:10	2013-03-02 00:20	2013-03-02 00:30	...	...	2013-03-02 23:40	2013-03-02 23:50
2013-03-03 (i=2)	2013-03-03 00:00	2013-03-03 00:10	2013-03-03 00:20	2013-03-03 00:30	...	...	2013-03-03 23:40	2013-03-03 23:50
...	...	...	...	...	...	...	...	...
...	...	...	...	...	...	...	...	...
2017-09-26 (i=1670)	2018-08-30 00:00	2018-08-30 00:10	2018-08-30 00:20	2018-08-30 00:30	...	...	2018-08-30 23:40	2018-08-30 23:50
2017-09-27 (i=1671)	2018-08-30 00:00	2018-08-30 00:10	2018-08-30 00:20	2018-08-30 00:30	...	...	2018-08-30 23:40	2018-08-30 23:50

Figure 6.1. Illustration of the time arrangement procedure for the 10 min intervals. The time intervals are placed in the corresponding cell of the table, according to their date and the 10 min division of the day that is closest to the central time of the interval.

The SR parameters extracted from any ELF station can be structured in a similar way to that explained above disregarding the processing methodology followed to obtain them, so the set of codes, functions and programs shown in this chapter can be used to analyze the information from other stations even if the previous processing methodology differs from that used with the Sierra Nevada measurements.

The script `time_arrange` places each 10 min interval in its corresponding cell of the table in Figure 6.1. To find the corresponding row and column of the table, this script loads the first time stamp of each 10 min of recordings from the `npz` files (in a loop) and does the following operations:

1. Adding a delta time of 10 min to the starting date of the time interval (`fec`):

```
inte = np.timedelta64(10,'m')
fec_ = fec + inte
```

2. Calculating the difference with respect to the 00:00 of the first day of measurements (2013-03-01):
   `dife = fec_ - np.datetime64('2013-03-01')`

3. Taking the integer part of the division of the previous result by a time delta of 1 day:
   `i = (dife/np.timedelta64(1,'D')).astype(int)`

4. Extracting the hours and minutes of the time difference:
   `hours = dife - i*np.timedelta64(1,'D')`

5. Dividing those hours and minutes by 10 min and taking the integer part:
   `j = (hours/inte).astype(int)`

The row and the column that correspond to the time interval are, respectively, `i` and `j`.
For example, for the interval that starts on 2014-07-01 at 14:38:41, the script would run as follows:

```
First interval starting time: 2014-07-01T14:38:41.195000
1.Adding a delta time of 10min: 2014-07-01T14:48:41.195000
2.Calculating the difference with respect to the 00:00 of the first day of measurements: 421
30121195000 microseconds
3.Taking the integer part of the division of the previous result by a time delta of 1 day: 4
87
4.Extracting the hours and minutes of the time difference: 53321195000 microseconds
5.Dividing those hours and minutes are divided by the duration of a subinterval and taking t
he integer part: 88
The 10-min multiple time corresponding to that cell is: 2014-07-01T14:40
What is right since the central time of the interval is: 2014-07-01T14:43:41.195000
```

6.2. Masks

The SR parameter values for some intervals are anomalous, i.e., they are considerably different from the usual values observed in the recordings. This can be due to:

- The occurrence of strong phenomena such as lightning events, Q-bursts, TLE or similar at any location around the globe.
- Lightning events near the recording station.
- Some local disturbance, such as people or animals walking near the station.
- A bad performance of the anthropogenic noise removal scheme, which would leave some peak of noise in the filtered spectra.
- A bad performance of the Lorentzian fitting scheme which could provide a fitting curve that does not fit the spectrum.

The two first reasons do not imply that the recorded spectra and the anomalous parameter values obtained are wrong, but also in these cases we are interested in studying the long-term global variations of the SR disregarding singular or local phenomena that could have a temporary impact on the recordings. In order to conduct this long term study, we need to take these few intervals out from the analysis. Otherwise the anomalous values obtained for a few intervals would largely influence the averages and trends that we attempt to study.

It is critical for the analysis to set the criteria to decide whether a 10 min interval is anomalous or not, given its parameter values. First of all, the parameters that will be considered for that decision are the local maximum amplitudes p_1, p_2 and p_3 and the local maximum frequencies, fp_1, fp_2 and fp_3, defined in section 4.2. As mentioned in section 4.2 and illustrated in Figures 4.8 and 4.9, these parameters are the most meaningful and the most stable to study the spectra.

The methodology followed in this chapter consists of disregarding only those time intervals for which any of the global parameters are unacceptable. We admit a time interval if all its global parameters are acceptable, even if one or more than one individual mode parameters are not acceptable but they compensate so that the global parameters are acceptable, since this would not imply a problem or a cause of disruption in our study.

A parameter concerning the sum of the square residuals of the fit –the sum of the squares of the differences between the spectrum and the fitting curve– could have been included but it has been considered unnecessary as the global fitting line hardly ever differs much from the spectrum for typical situations. In addition, the residuals would largely depend on the level of fluctuation of the spectrum, which is higher during the afternoon than during the night, for example, which would add a difficulty to deal with that parameter.

In order to set the range of values of the SR parameters for which we will consider that an interval is acceptable, a statistical study is performed on the values of each parameter. This statistical study is performed for the NS and for the EW components separately, as there are differences between the recordings at both sensors. The statistical distributions of the values of other parameters are also shown, although they will not be relevant for the design of the mask.

Looking at the statistical distributions of the parameters, we define the acceptable range for each parameter as a range containing a vast majority of the values of that parameter. The acceptable ranges for the parameters have been defined as shown in Tables 6.1 and 6.2.

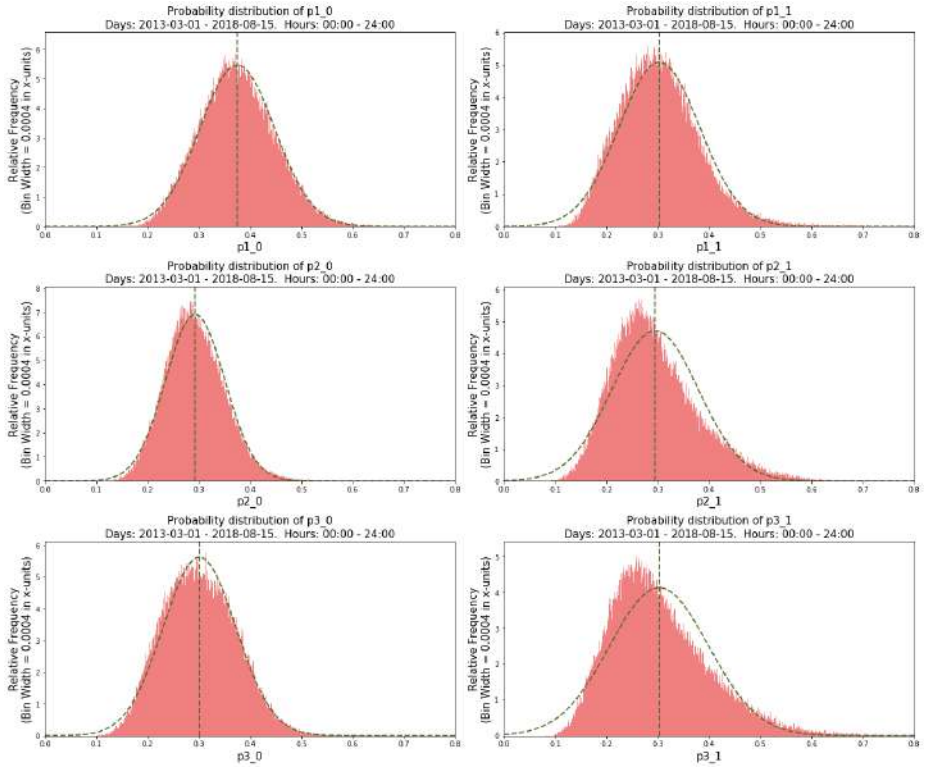

Figure 6.2. Statistical distributions of the local maximum amplitudes of the 1st mode (first row), the 2nd mode (second row) and the 3rd mode (third row), for the NS magnetic field component (left) and the EW magnetic field component (right).

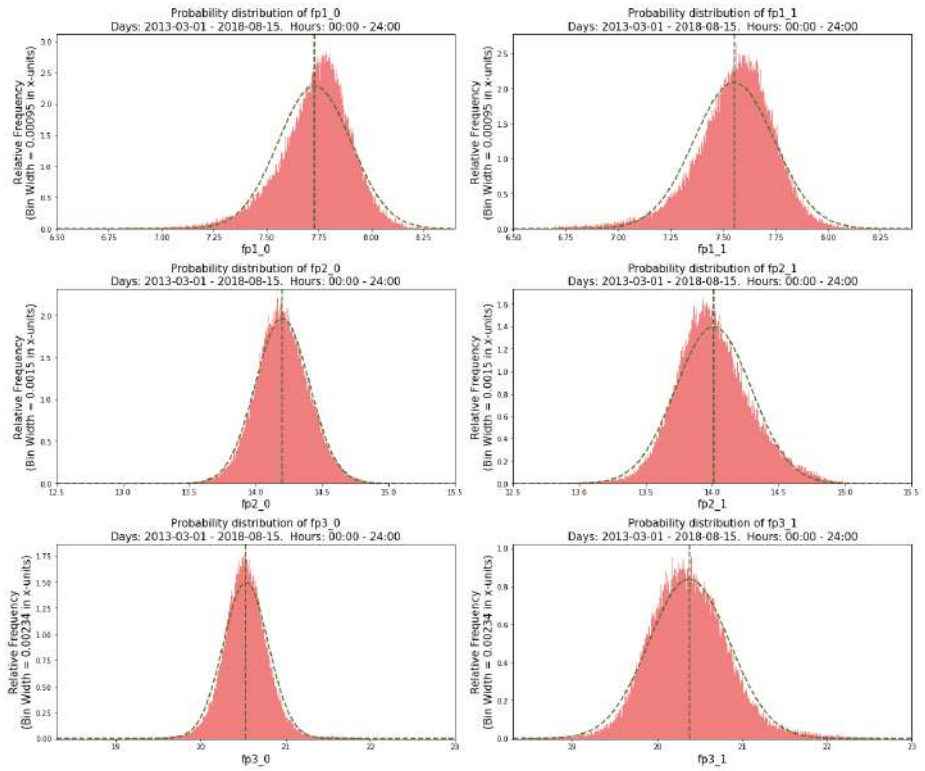

Figure 6.3. Statistical distributions of the local maximum central frequencies of the 1st mode (first row), the 2nd mode (second row) and the 3rd mode (third row), for the NS magnetic field component (left) and the EW magnetic field component (right).

NS comp	p1_0	fp1_0	p2_0	fp2_0	p3_0	fp3_0
Lower limit	0.13	6.80	0.10	13.18	0.08	19.15
Higher limit	0.80	8.35	0.80	15.19	0.80	21.98

Table 6.1. Range of acceptable values for each fitting parameter, for the NS component.

EW comp	p1_1	fp1_1	p2_1	fp2_1	p3_1	fp3_1
Lower limit	0.10	6.70	0.08	12.82	0.08	18.40
Higher limit	0.80	8.22	0.80	14.98	0.80	22.60

Table 6.2. Range of acceptable values for each fitting parameter, for the EW component.

Some masked (removed) and unmasked (accepted) intervals are shown in Figure 6.4. It can be clearly seen that the intervals are masked when strange peaks appear that make it impossible to distinguish the resonances in the spectra. Also, some intervals are masked because of other anomalies, such as an increase in the amplitude or the central frequency of the 3rd mode. A deeper characterization of other anomalous spectra that are observed for some time intervals is performed in section 8.1.

In Figures 6.5 and 6.6 we can see that there are big differences in the results depending on whether the automatic masking scheme is applied or not. The results are noisier and more chaotic when the mask is not applied. However, the option of analyzing the parameter values with or without applying the masking scheme will be possible in all the functions and notebooks presented in this work, for the sake of versatility.

We are also interested in revising how many 10 min intervals are masked, because if too many intervals are taken off from the long term analysis, that could cause a loss of significance of our results. For this purpose, we have designed a function to plot the masked time intervals, that will be presented in subsection 6.3.12.

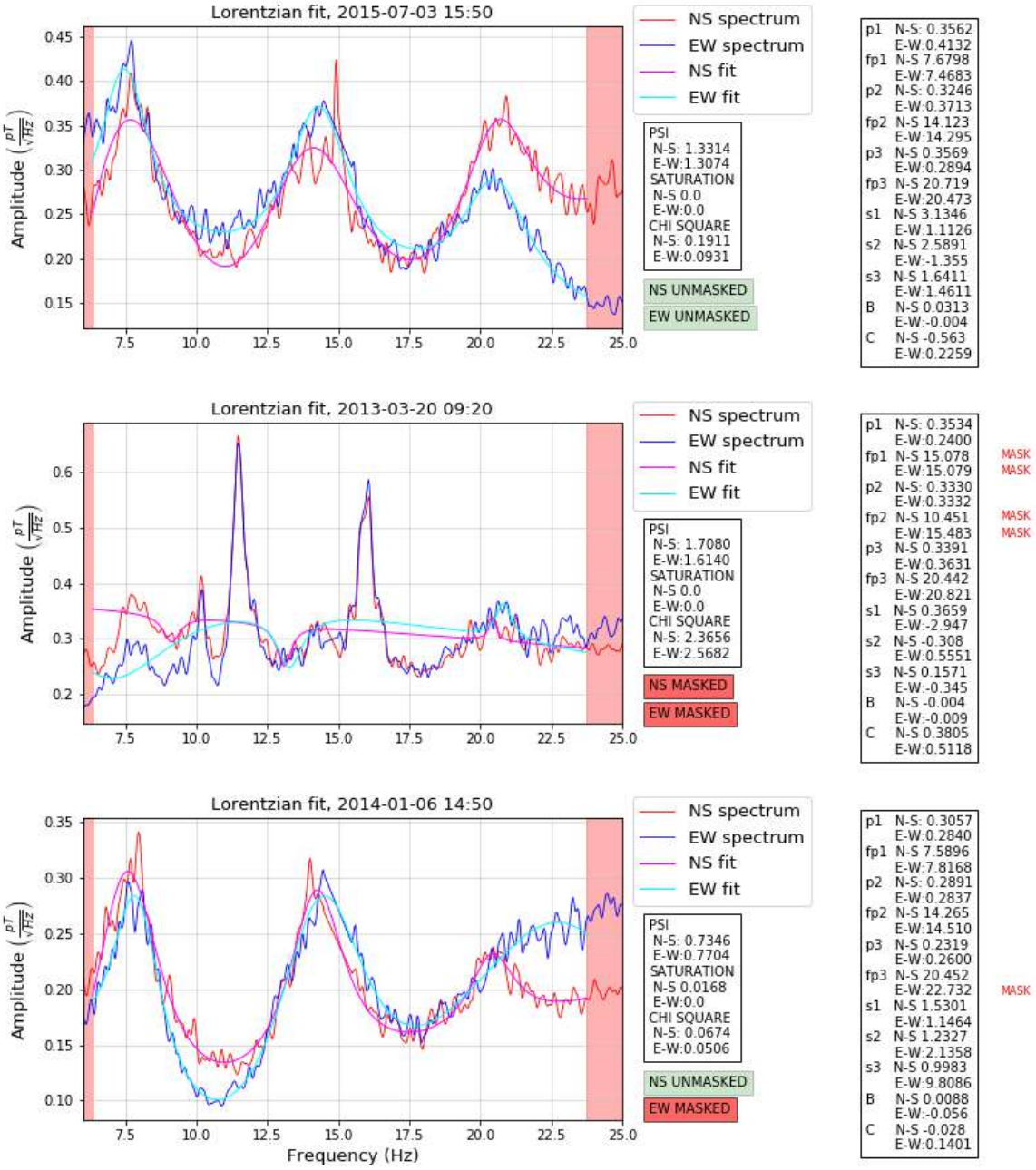

Figure 6.4. Examples of masked and unmasked spectra. The NS and the EW spectra in the first plot are both unmasked because the values of the local maximum amplitudes and the local maximum central frequencies are within the ranges of acceptable values specified in Table 6.1 for the NS component and in Table 6.2 for the EW component. In the second plot, both the NS and the EW spectra are masked because the values for the SR1 and the SR2 local maximum central frequencies are out of the ranges of acceptable values. In the third plot, the NS spectrum is unmasked but the EW spectrum is masked due to an unacceptable value of the SR3 local maximum central frequency.

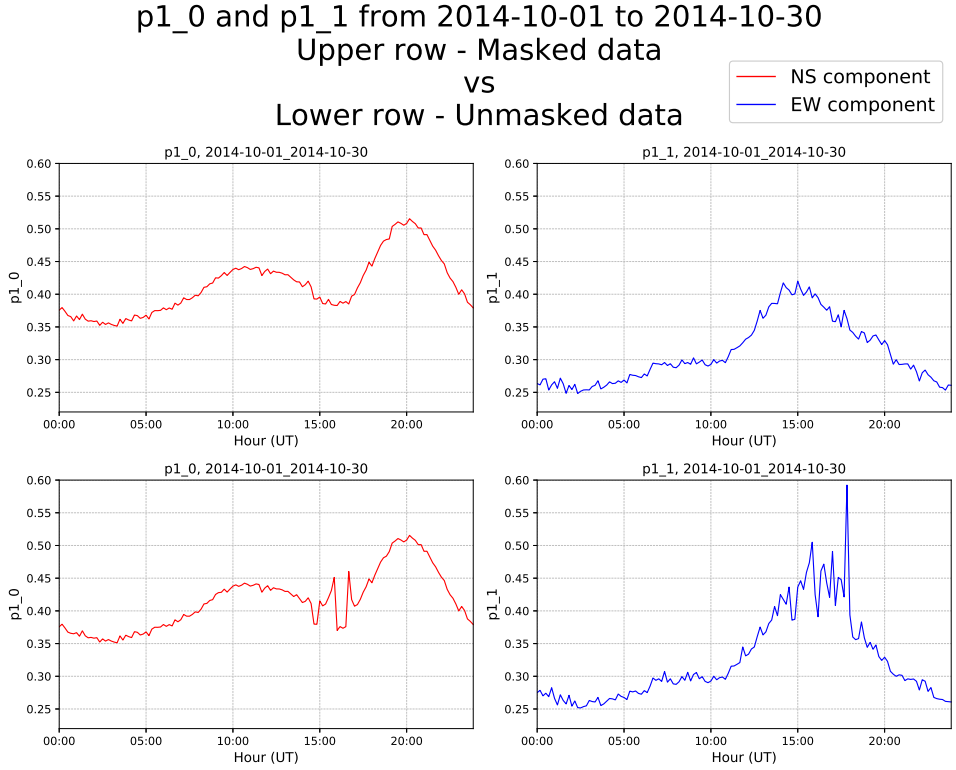

Figure 6.5. Visualization of the variation of the SR1 local maximum amplitude for the NS (left) and the EW (right) components, when the masked intervals are removed (above) vs. when they are included in the chart (bottom).

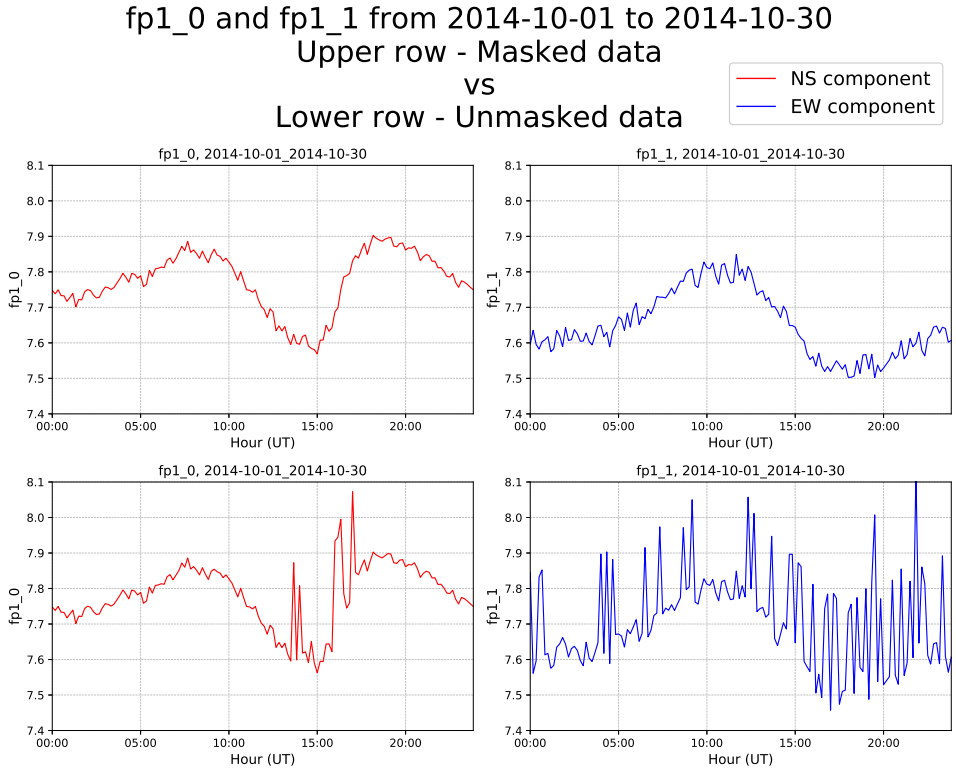

Figure 6.6. Visualization of the variation of the SR1 local maximum central frequency for the NS (left) and the EW (right) components, when the masked intervals are removed (above) vs. when they are included in the chart (bottom).

6.3. Design of functions and notebooks aimed at the automatic visualization of relevant SR long term analysis features

One of the most important objectives of this thesis is to offer a wide range of computational tools that allow the researchers to obtain, export, visualize and study all the information related to the SR parameters. This objective has been presented in Rodríguez-Camacho et al. (2019a), Rodríguez-Camacho et al. (2019b) These computational tools are presented in the form of a collection of Jupyter notebooks, available for download (together with the SR parameters values extracted from the Sierra Nevada ELF recordings) in the link below:

https://hdl.handle.net/10481/78097

In the link above, we can download a folder with 17 different notebooks, the folder `Data`, a file called `Variations.py` and a specific notebook called `Explanations.ipynb`. Each notebook has been designed to study a specific feature or variation of the SRs. For that purpose, it uses a function, with the same name as the notebook, that is defined in the file `Variations.py`. The function contains the algorithms to process the data and to pass them to the notebook, while the notebook provides a comfortable environment to customize the specific settings that are suitable for the analysis and the visual options desired for the charts.

All the notebooks are completely ready to be used, they are configured to automatically load the SR parameters and other relevant data from the folder `Data`. The user can change the input arguments that are used by default in the notebooks, and thus generate different plots containing the relevant information with a desired format. The different possibilities for the input arguments, for each notebook, are listed and explained in detail in the notebook `Explanations.ipynb`, together with an explanation of each notebook. The notebooks are totally able to deal with SR parameters and information obtained from other ELF stations, as long as they are stored with with the format of one sample every regular time interval of the day.

The abbreviations or codes of the different SR parameters will be slightly different in this chapter in comparison to the previous chapters, in order to avoid subscripts in the notebooks and include the component (NS or EW) in the code of each parameter. The SR parameter will be named in this chapter as explained below:

- `p1`, `p2` and `p3` are the local maximum amplitudes, i.e., the three first local maxima of the global Lorentzian fitting curve (of the sum of the three Lorentzian functions and the linear part).

- `fp1`, `fp2` and `fp3` are the frequencies corresponding to the local maximum amplitudes, i.e., the frequencies at which the amplitudes `p1`, `p2` and `p3` are reached in the global Lorentzian fitting curve.

- `s1`, `s2` and `s3` are the half peak widths of each one of the three Lorentzian functions of the fitting curve.

- `as1`, `as2` and `as3` correspond to the fitting curve evaluated in `f1`, `f2` and `f3`, i.e., the sum of the three Lorentzian functions and the linear part in those frequencies.

- `a1`, `a2` and `a3` are the individual mode amplitudes of each one of the three Lorentzian functions of the fitting curve.

- `f1`, `f2` and `f3` are the individual mode central frequencies of each one of the three Lorentzian functions of the fitting curve.

Also, the following information about the SRs can be studied:

- `a` and `b` are the slope and the intercept, respectively, of the straight line used in the Lorentzian fit to account for the electronic noise and the left queue of the fourth SR.

- `psi` is the power spectrum integral, i.e., the energy under the power spectrum within the fitting band, 6.35 – 23.75 Hz.

- `sat` is the fraction of saturation for each 10-minute measurement interval.

- `chi` is the chi square value for the Lorentzian fits.

Every code is followed by `_0` to refer to the recordings in the NS sensor or by `_1` to refer to the recordings in the EW sensor.

In the next subsections, the different notebooks will be presented and their utility to study, visualize and export the SR parameters and other relevant information will be explained, together with some examples of graphs obtained using them. Their most important input and output arguments will be presented. All the input and output arguments of the notebooks as well as more examples of its use can be found in each notebook itself. The vast majority of the notebooks include, among their most important input arguments, the following temporal arguments:

- `date_i`: a `str` containing the date and time of the first recording that we want to consider. Examples: `'2013-03-01T00:00'`, `'2014-02-01T23:10'`, `'2014-02-01'`, `'2014-02'`. If only the date is given and the time is missing, the time is set to `00:00` by default. If the day and/or the month are missing, they are set to `'01'` by default.

- `date_f`: a `str` containing the date and time of the last recording that we want to consider. Examples: `'2013-03-01T00:00`, `'2014-02-01T23:10'`, `'2014-02-01'`, `'2014-02'`. If only the date is given and the time is missing, the time is set to `'00:00'` by default. If the day and/or the month are missing, they are set to `'01'` by default.

- `hi`: a `str` with the format `'hh:mm'`, containing the first time interval of the day that we want to include in our analysis. Examples: `'00:00'`, `'10:00'`, `'13:10'`. It is set to `'00:00'` by default.

- `hf`: a `str` with the format `'hh:mm'`, containing the last time interval of the day that we want to include in our analysis. Examples: `'08:00'`, `'20:40'`, `'24:00'`. It is set to `'24:00'` by default.

Other input arguments, that are common to many notebooks and are mainly used to customize the appearance of the charts, will be listed at the end of this section. In addition to plot the charts, the notebooks return some output arguments that can be useful for a quantitative study of the SR parameters variations. The most important ones are presented in this section for each notebook.

6.3.1. Samples

The notebook `Samples.ipynb` is the simplest notebook that will be used to analyze the temporal evolution of the SR parameters. In this notebook, we must select one or several parameters to visualize their evolution between two chosen dates and times. For each one of the parameters chosen, one sample for each time interval (i.e., 1 sample every 10 minutes) is used to plot its evolution. The most important input arguments, apart from the temporal ones, are:

- `lpar`: a list of `str` values containing the codes of the parameters that we want to visualize. Examples: `['p1_0']`, `['p1_0','p1_1']`, `['fp1_0','fp2_0','fp3_0']`.

- `scale`: a `str` that can be equal to `'hours'` or to `'days'`. If it is equal to `'hours'`, the x-axis unit is hours. If it equal to `'days'`, the x-axis unit is days. It is set to `hours` by default.

The output arguments of this notebook are:

- `xti`: a `np.array` of `float` values containing the x-axis values of the hours or days (depending on the value of `scale`) taken into consideration to generate the plot.
- `sd_all`: a `np.array` of `float` values with `len(lpar)` rows which contain, each one, the series of values of each one of the parameters in `lpar`.

Two examples of graphs obtained with this notebook are shown in Figures 6.7 and 4.9. In the latter, we can compare the effect, on the graph, of choosing `scale='hours'` (left) or `scale='days'`. It can be observed that there is a period of missing data, probably due to a technical failure at the ELF station, the 2nd and 3rd of July 2014.

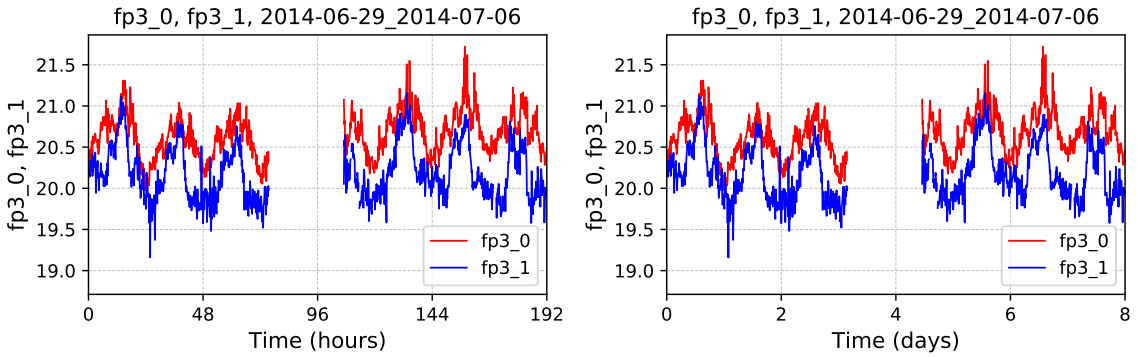

Figure 6.7. Evolution of the SR3 local maximum central central frequency from the NS and the EW components, `fp3_0` and `fp3_1`, obtained using the notebook `Samples.ipynb`. There is a blank in the data on 2nd and 3rd July.

6.3.2. Diurnal variation

This notebook is specifically designed to deal with the diurnal variations of the SR parameters. As explained in the introduction, the diurnal pattern of variation of the SRs is tightly bonded to the global pattern of lightning activity around the globe, which occurs mainly in three lightning centers, located in Africa and Madagascar (African center), South and Central America and the Caribbean Sea (American center), and South-East Asia and Indonesia (Asian center), as shown in Figure 1.3. The activity of each center is maximum in the local noon and minimum in the late morning, as seen in Figure 1.4. Since the intensity of the discharge and also the distance from each center to our ELF station vary along the day, the SR parameters will show a primary diurnal pattern of variation.

The function `diurnal_variation` is widely explained, including some examples, in the notebook `DiurnalVariation.ipynb`. One of its most important input arguments,

apart from the temporal ones, is `lpar` (it is similar to the previous notebooks). The output arguments of the function are:

- `hours`: a `np.array` of `float` values containing the time intervals (x-axis values) of the plot.
- `medh`: a `np.array` of `float` values with `len(lpar)` rows which contain, each one, the diurnal average (y-axis values) of each one of the parameters in `lpar`.
- `counth`: a `np.array` of `int` values containing the number of unmasked samples taken into consideration to calculate the average for each time of the day.

Some examples of charts obtained using this notebook are shown in Figures 6.8, 6.9, 6.10 and 6.11. The diurnal variations shown in these figures have been averaged in the period 2013-03-01 to 2016-12-31.

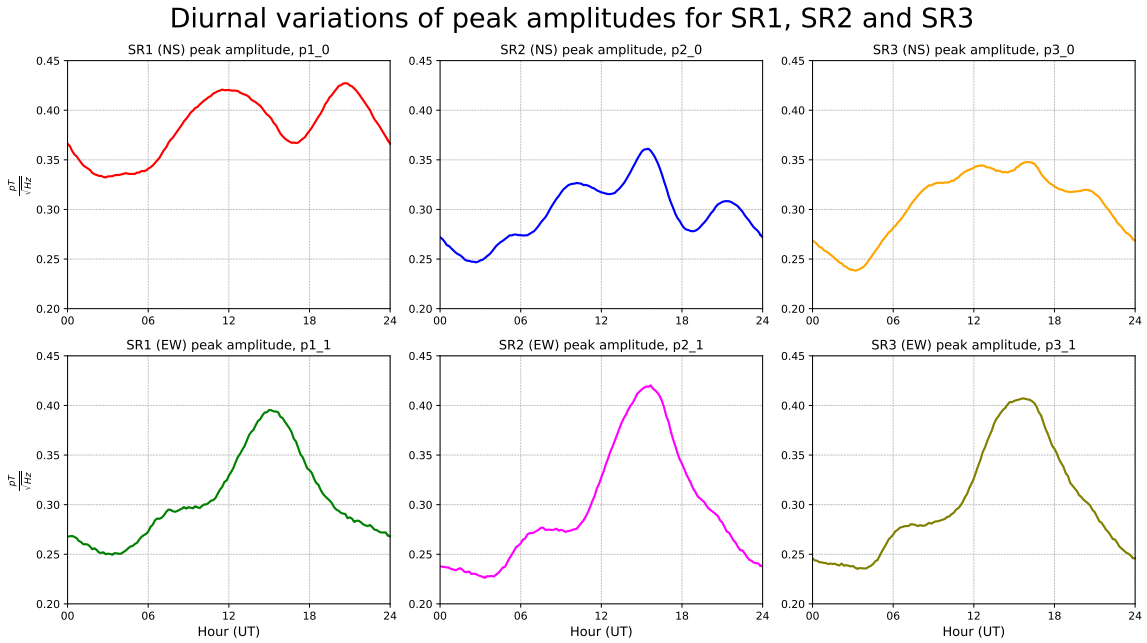

Figure 6.8. Diurnal variation of the local maximum amplitudes for SR1, SR2 and SR3 - `p1, p2, p3`, respectively, for the NS component - `_0` - (up) and for the EW component - `_1` - (down).

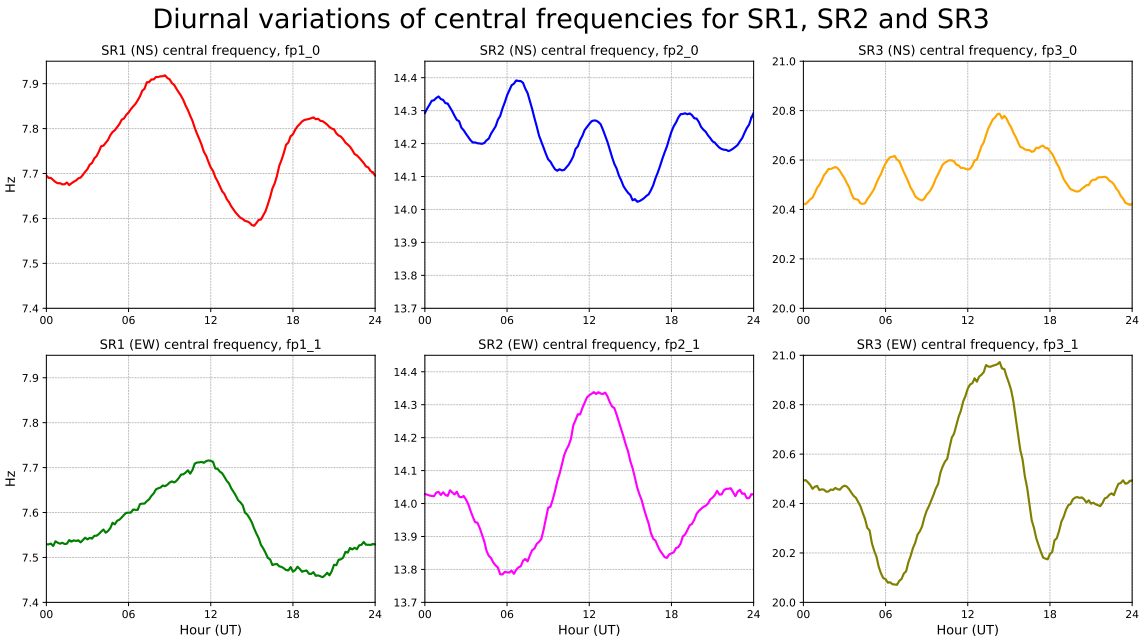

Figure 6.9. Diurnal variation of the local maximum central frequencies for SR1, SR2 and SR3 - `fp1, fp2, fp3`, respectively, for the NS component - `_0` - (up) and for the EW component - `_1` - (down).

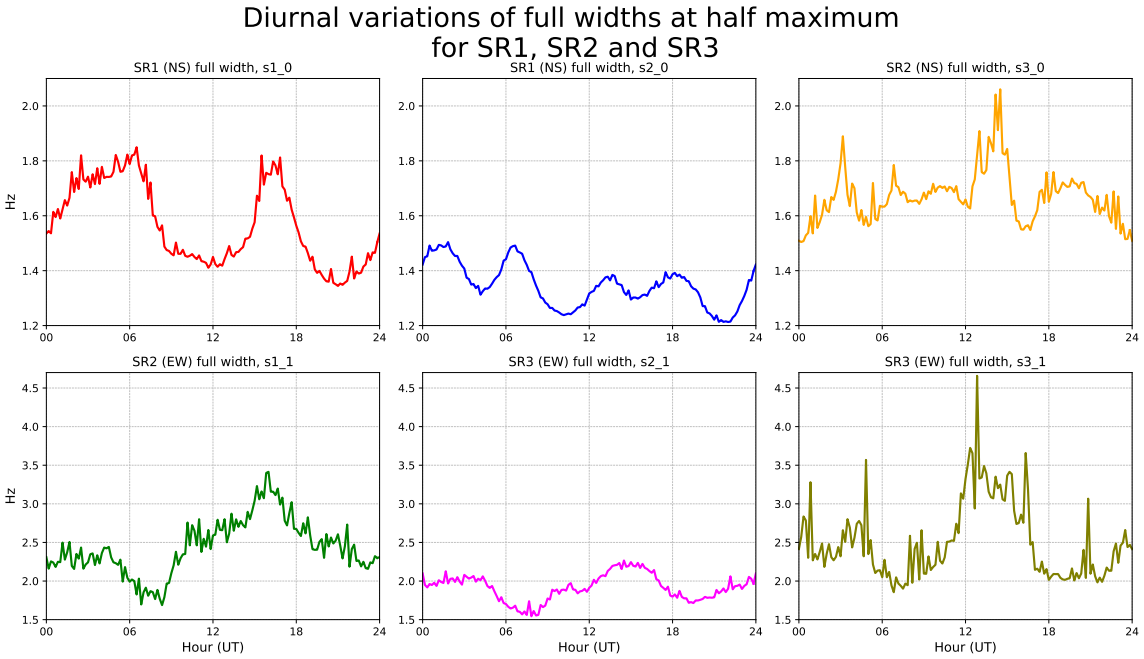

Figure 6.10. Diurnal variation of the widths at half maximum for SR1, SR2 and SR3 - `s1, s2, s3`, respectively, for the NS component - `_0` - (up) and for the EW component - `_1` - (down).

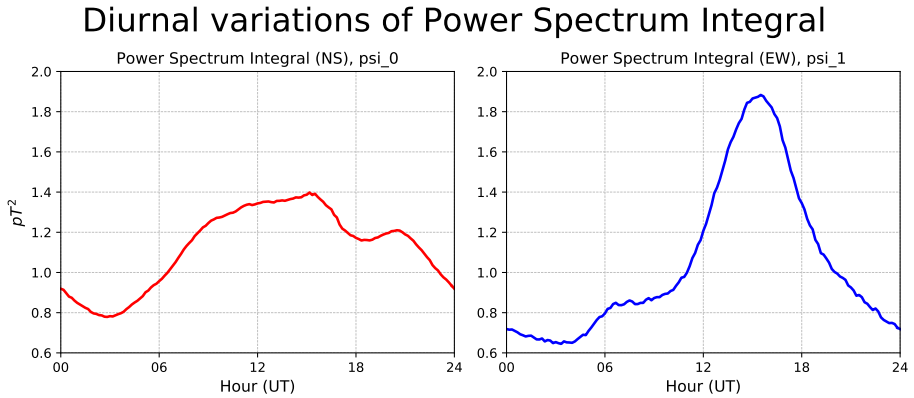

Figure 6.11. Diurnal variation of the power spectrum integral - `psi` for the NS component - `_0` - (left) and for the EW component - `_1` - (right).

6.3.3. Daily variation

The notebook `Daily_Variation.ipynb` has been created to trace the variations in the SR parameters within a period of some days. To perform this study, we need to take a representative value for each day in order to get rid of the diurnal variations. This representative value is the daily average. Using this notebook we can analyze the variations of the daily averaged values of the SR parameters. This is useful as a first approach to observe if the SR parameters show any seasonal trend, or if they have any particular behavior before or after an atmospheric event. An explanation and the list of all its arguments can be found in the notebook. The first example of its use is shown in Figure 6.12.

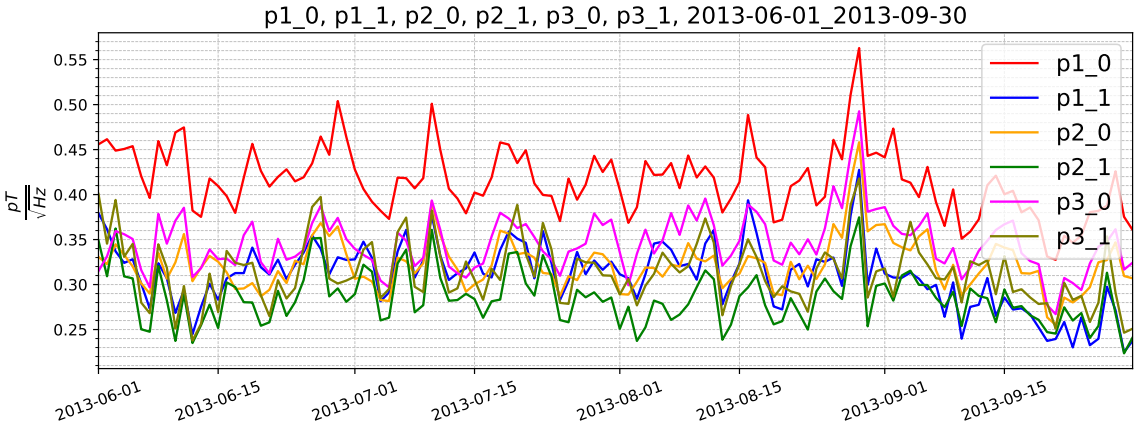

Figure 6.12. Daily variation of the local maximum amplitudes for SR1, SR2 and SR3 - `p1, p2, p3`, respectively, for the NS component - `_0` - and for the EW component - `_1`.

The most important input arguments of this notebook are `lpar` (similar to the previous notebook) and `softd`. The parameter `softd` allows to average the SR parameters over a period of more than one day using the parameter `softd`, if we are interested

in reducing the fluctuation (or stochastic component) of the graph. For example, if `softd=7`, the function will divide the total amount of days between the initial and the final dates into groups of 7 consecutive days, and for the fourth day of each group (the day in the middle) it will plot the averaged value of the parameter over the 7 days. The parameter `softd` is set to 1 by default. Using `softd=7`, some examples of graphs obtained using the function are in Figures 6.13, 6.14, 6.15 and 6.16.

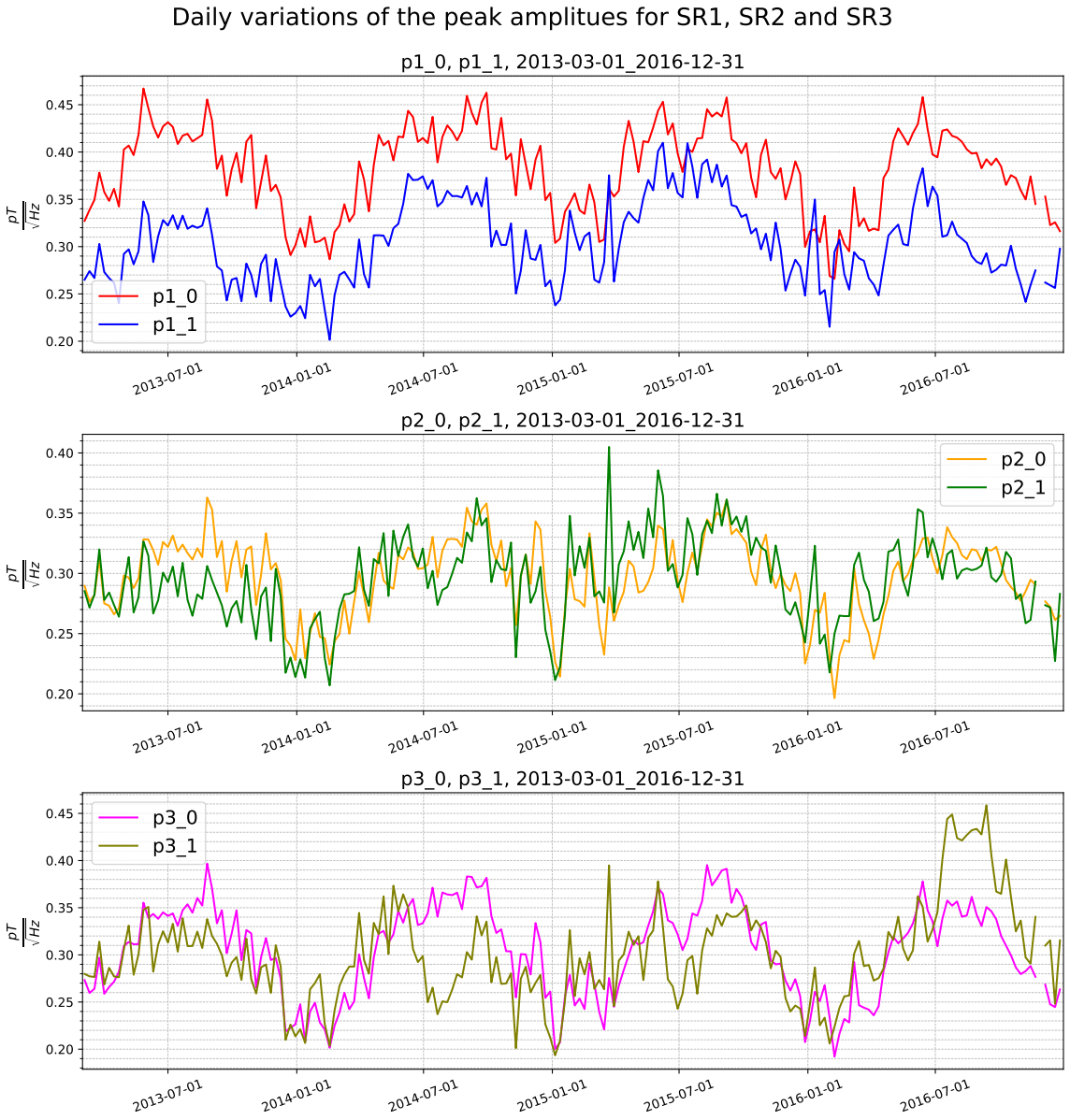

Figure 6.13. Daily variation of the local maximum amplitudes for SR1 (up), SR2 (middle) and SR3 (down) - `p1, p2, p3`, respectively, for the NS component - `_0` - and for the EW component - `_1` - from March, 2013 to December, 2016.

– `days`: a `np.array` of `float` values containing the days (x-axis values) taken into consideration to generate the plot.

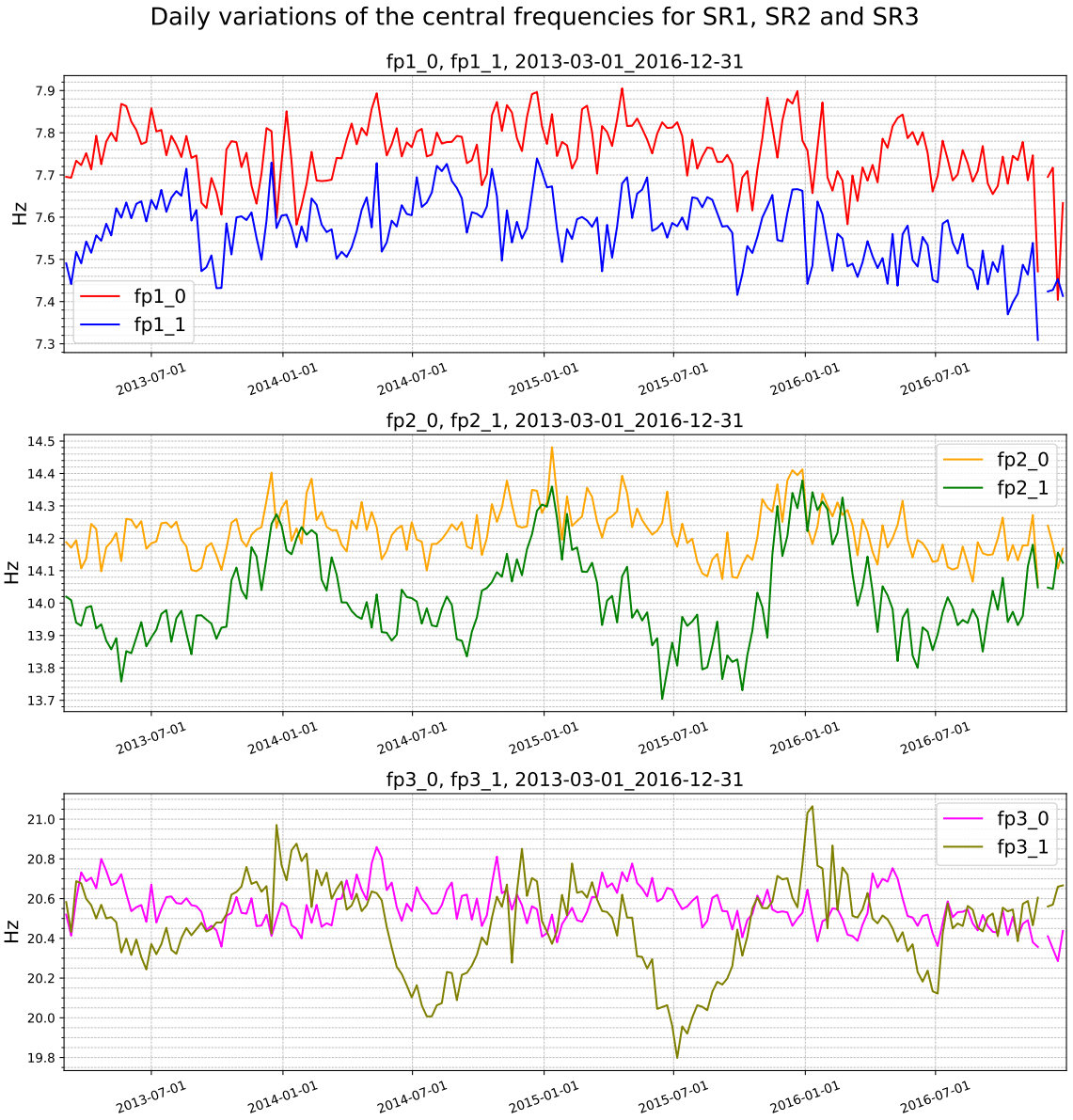

Figure 6.14. Daily variation of the local maximum central frequencies for SR1 (up), SR2 (middle) and SR3 (down) - `fp1, fp2, fp3`, respectively, for the NS component - `_0` - and for the EW component - `_1` - from March, 2013 to December, 2016.

- `medd`: a `np.array` of `float` values with `len(lpar)` rows which contain, each one, the daily average value of each one of the parameters in 'lpar' (y-axis values).
- `countd`: a `np.array` of `int` values containing the number of unmasked samples taken into consideration to calculate the average for each day taken into account.

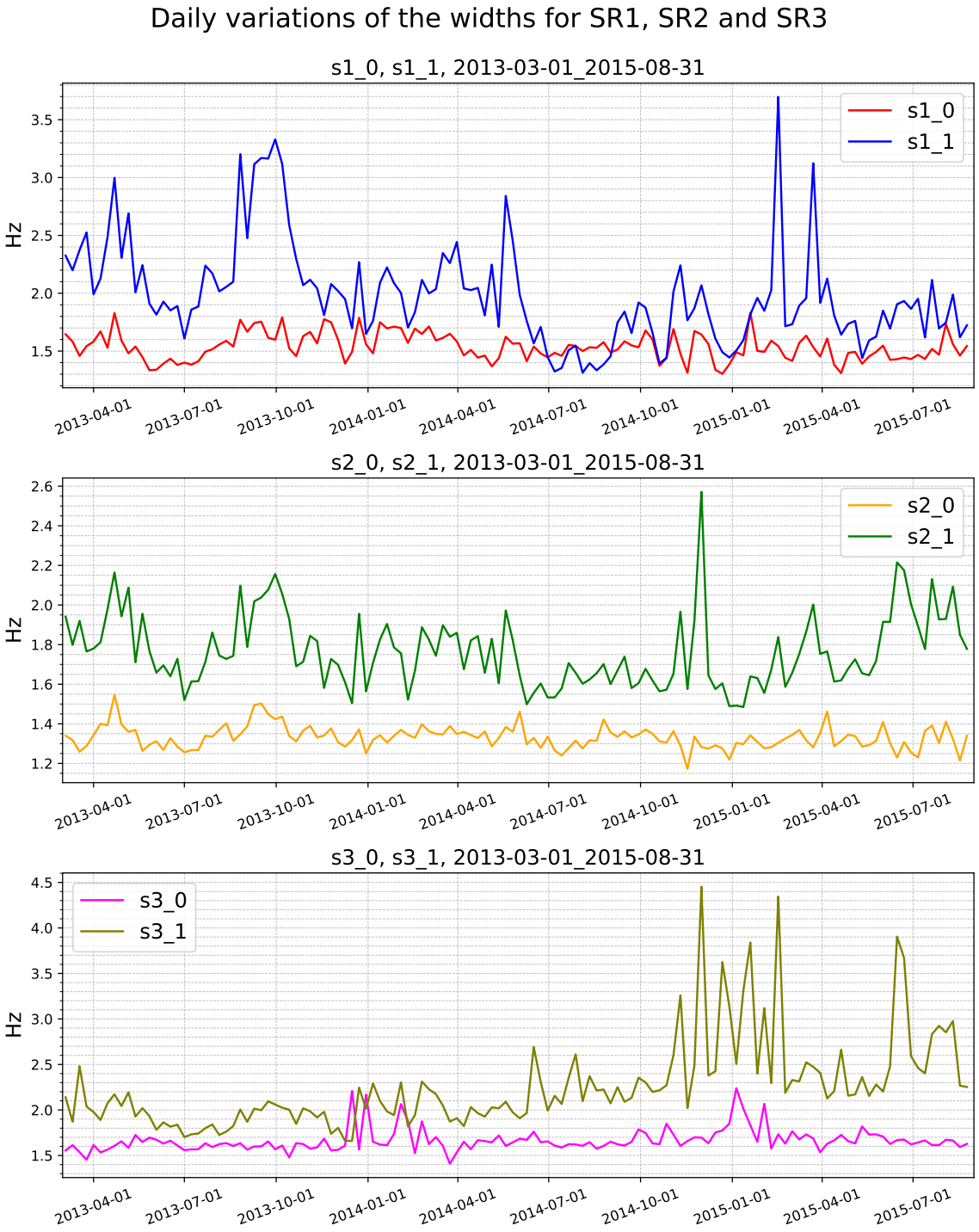

Figure 6.15. Daily variation of the widths at half maximum for SR1 (up), SR2 (middle) and SR3 (down) - `s1, s2, s3`, respectively, for the NS component - `_0` - and for the EW component - `_1` - from March, 2013 to August, 2015.

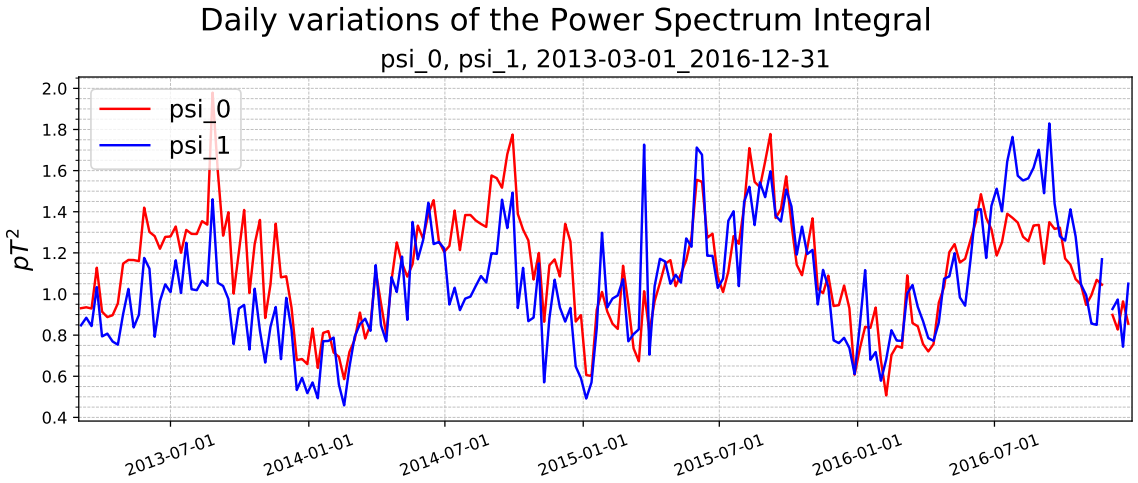

Figure 6.16. Daily variation of the power spectrum integral, for the NS component - `_0` - and for the EW component - `_1` - from March, 2013 to December, 2016.

6.3.4. Daily amplitude

The daily amplitude of a SR parameter in a day is the amplitude of its diurnal variation in that day, i.e., the difference between its maximum value and its minimum value in that day. The variation of the daily amplitude is used in Ondrášková et al. (2011) (as the diurnal frequency range) to estimate the diameter of the lightning source regions.

The notebook `Daily_Amplitude.ipynb` is very similar to `Daily_Variation.ipynb`, with the only difference that the daily amplitude, instead of the daily average, is returned and plotted.

The input argument `softd` has the same meaning as in `Daily_Variation.ipynb`, and the output parameter `medd` is substituted by `ampl_d`, a `np.array` of `float` values with `len(lpar)` rows which contain, each one, the amplitude of the daily variation of each one of the parameters in `lpar` (the y-axis values of the chart).

Two examples of plots obtained using this notebook are shown in Figures 6.17 and 6.18.

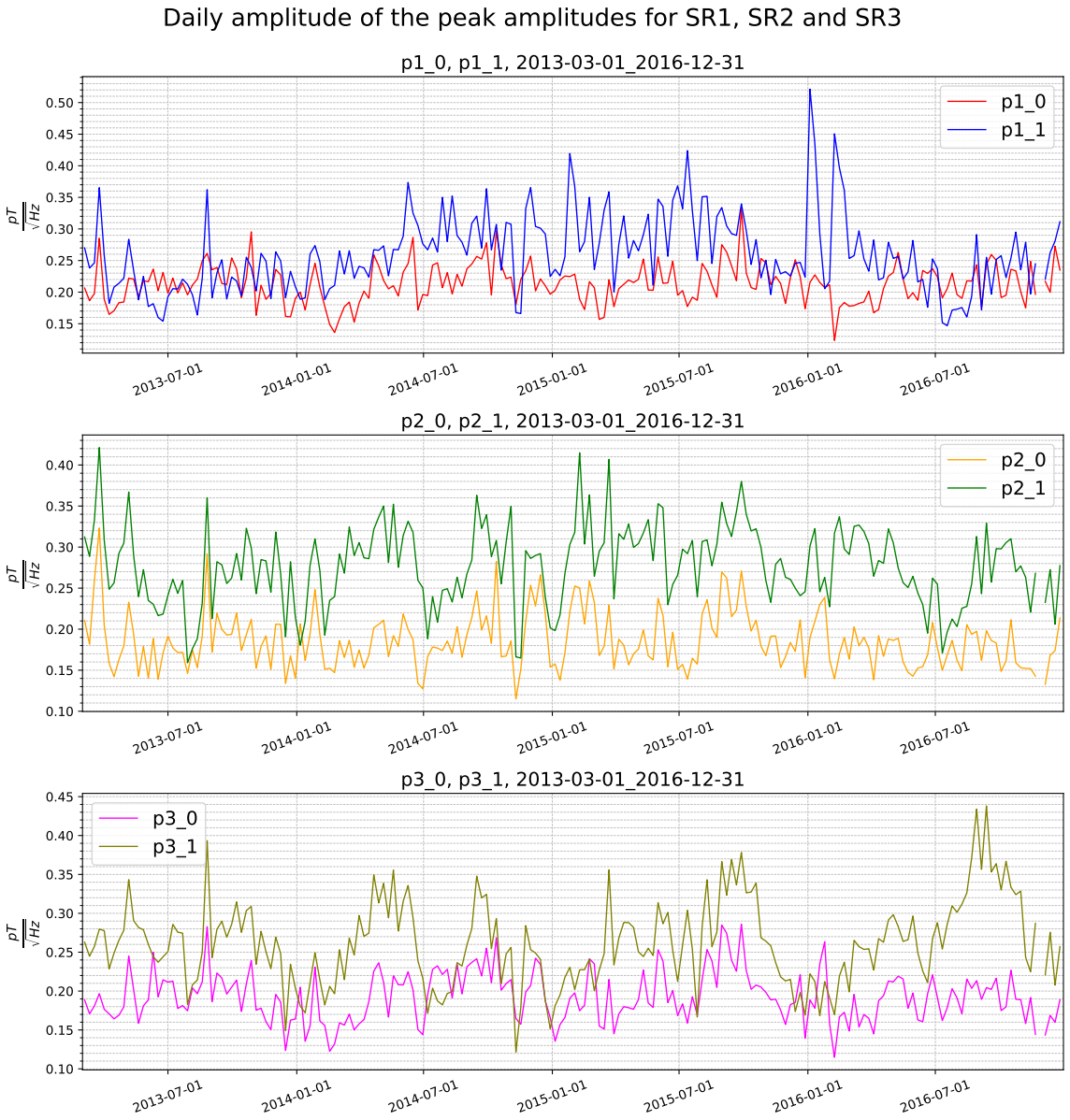

Figure 6.17. Daily amplitude of the variation of the local maximum amplitudes for SR1 (up), SR2 (middle) and SR3 (down) - `p1, p2, p3`, respectively, for the NS component - `_0` - and for the EW component - `_1` - from March, 2013 to December, 2016.

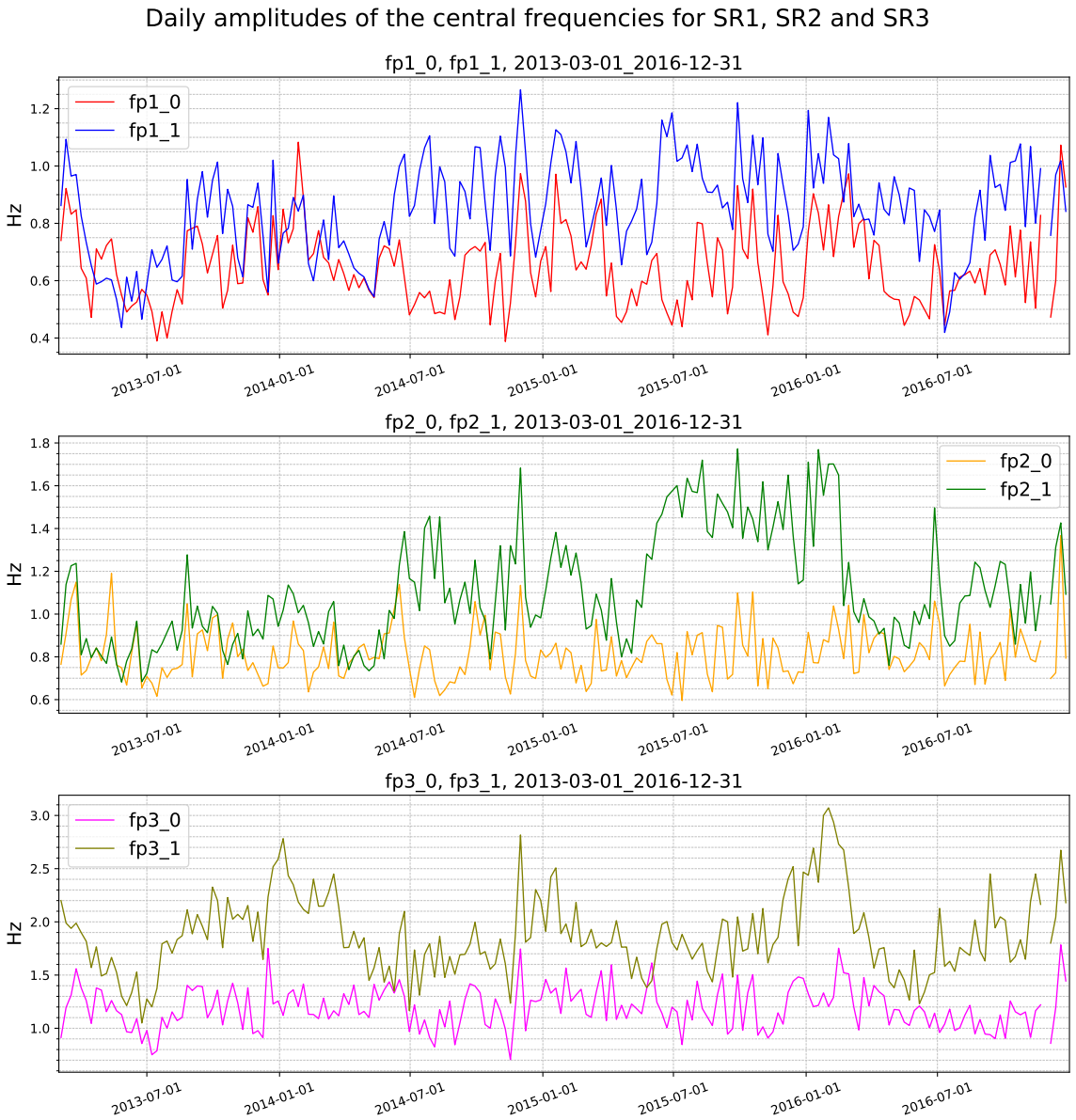

Figure 6.18. Daily amplitude of the variation of the local maximum central frequencies for SR1 (up), SR2 (middle) and SR3 (down) - `fp1, fp2, fp3`, respectively, for the NS component - `_0` - and for the EW component - `_1` - from March, 2013 to December, 2016.

6.3.5. Diurnal pattern

For a given parameter, the notebook `Diurnal_Pattern.ipynb` plots a color mesh with the values of the parameter for each day (x-axis) and each hour (y-axis) of recordings. With this plot we can simultaneously visualize the diurnal and the daily variations of a parameter. It is useful to see how the diurnal variations of the SR parameters change for the different months of recordings.

This function is also useful to analyze the terminator effect. During the sunset and the sunrise, important variations in the temperature and the electron/ion concentrations take place in all the layers of the atmosphere, especially in the ionosphere, where the total electron concentration increases by an order of magnitude or more at sunrise (Melnikov et al. 2004 and references therein). In the patterns of the SR amplitudes, we could expect to see an increase after the sunrise and a decrease a bit before the sunset, as observed in the recordings from Mitzpe-Ramon and Nagycenk analyzed in Melnikov et al. (2004).

Two of the most important input arguments, apart from the temporal ones, are:

- `par`: a `str` value containing the code of the parameter to visualize. Examples: `'p1'`, `'fp2'`, `'psi'`.
- `sunline`: a `logical` value. If `sunline=True`, two lines showing the sunrise and the sunset times, respectively, will be shown on the plot. If `sunline=False`, these lines will not be shown.

The output arguments of the function are:

- `x`: a `np.array` of `float` values containing the days (x-axis values) taken into consideration to generate the plot.
- `y`: a `np.array` of `float` values containing the hours (y-axis) of the day taken into consideration to generate the plot.
- `data_ma_0`: a `np.array` of `float` values with `len(hours)` rows and `len(days)` columns containing the values of the parameter for each hour and day of the plot for the NS sensor.
- `data_ma_1`: a `np.array` of `float` values with `len(hours)` rows and `len(days)` columns containing the values of the parameter for each hour and day of the plot for the EW sensor.

The diurnal patterns for the local maximum amplitudes and the local maximum central frequencies, for SR1, SR2 and SR3, are shown in Figure 6.19.

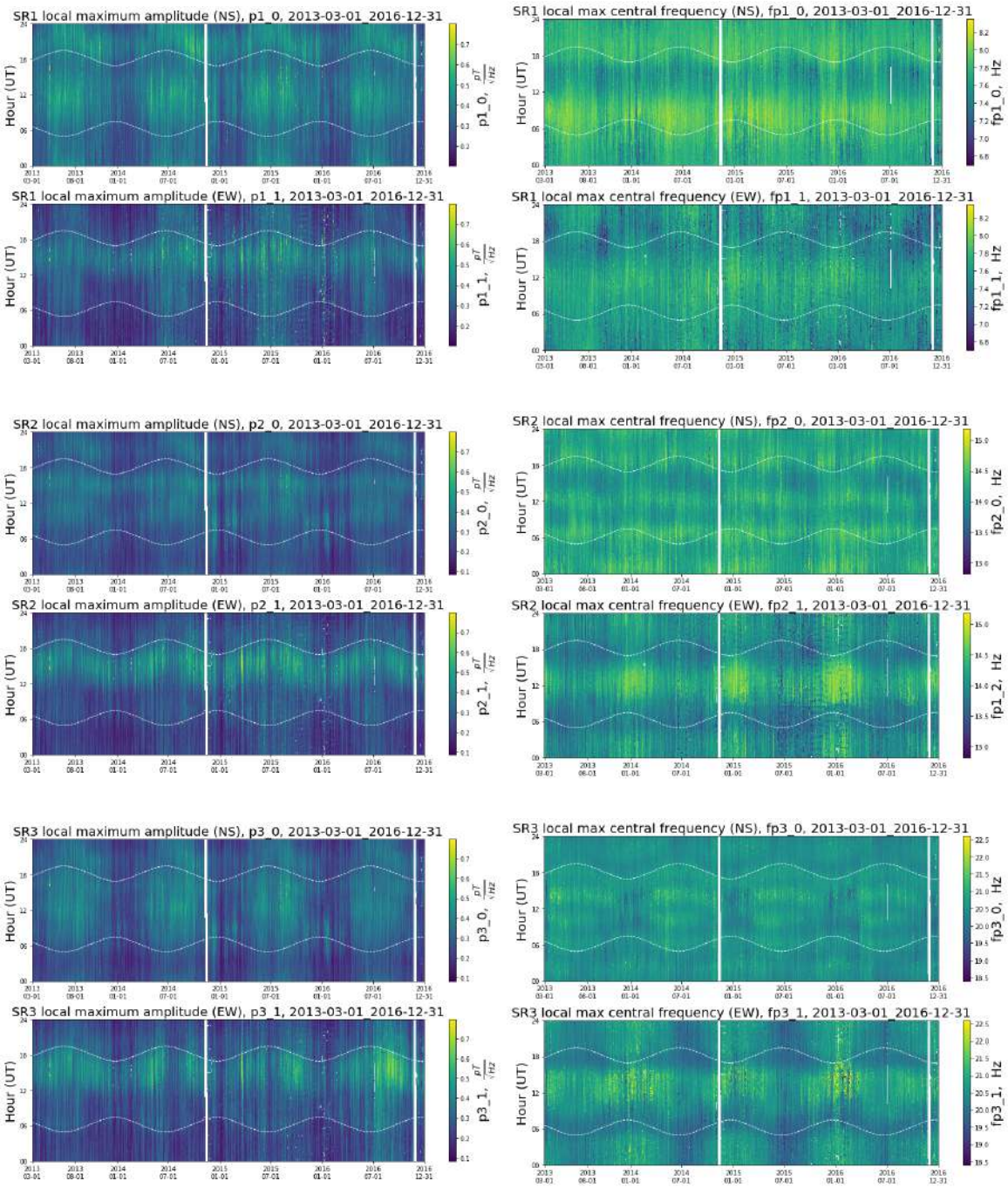

Figure 6.19. Diurnal pattern for SR1 local maximum amplitude, `p1` (upper left), SR1 local maximum central frequency, `fp1` (upper right), SR2 local maximum amplitude, `p2` (middle left), SR2 local maximum central frequency, `fp2` (middle right), SR3 local maximum amplitude, `p3` (down left), and SR3 local maximum central frequency, `fp3` (down right). The sunrise and sunset times are plotted as a grey dashed line. The x-axis is the day and y-axis is the UT hour. For each parameter, the NS component (up) and the EW component (down) are shown.

6.3.6. Seasonal variation

As observed in the figures shown in the previous sections, the SRs clearly show a seasonal behavior. This is due to the seasonal changes in the global lightning activity (Blakeslee et al., 2014). The changes of the SRs in the different seasons of the year have been studied in previous works (Nickolaenko et al., 2015).

The notebook `Seasonal_Variation.ipynb` allows to automatize the study of the seasonal variations of the SRs, by plotting the diurnal variation of a given SR parameter for each season of the year. This notebook allows us to define as many different seasons as desired within the year, and set their starting dates freely.

One option is to use the astronomical seasons (the spring goes from March, 20 to June, 20; the summer goes from June, 21 to September, 21; the autumn goes from September, 22 to December, 20; and the winter goes from December, 21 to March, 19). A second option is to set only two seasons (winter and summer), and a third option is to use the EM seasons proposed by Nickolaenko et al. (2015) (the winter is set to last from February, 1 until March, 31; the spring goes from April, 1 to May, 31; the summer is set to last from June, 1 to September, 30; and the autumn goes from October, 1 to January, 31).

Two of the most important input arguments, apart from the temporal ones, are:

- `par`: a `str` value containing the code of the parameter to visualize. Examples: `'p1'`, `'fp2'`, `'psi'`.
- `fest_red`: a list containing the dates corresponding to the first day of each one of the seasons in which we want to split the year up. The format has to be `'mm-dd'` for each date. Examples: `['03-20','06-21','09-22','12-21']`, `['04-15','10-15']`, `['03-01','04-30','09-22']`.

There are two output arguments:

- `hours`: a `np.array` of `float` values containing the hours (x-axis values) of the day taken into consideration to generate the plot.
- `med_est`: a `np.array` of `float` values with `len(fest_red)` rows which contain, each one, the diurnal average variation of `par` for each season (y-axis values).

The seasonal variations for the astronomical seasons have been obtained for the SR local maximum amplitudes, the local maximum central frequencies, the widths at half maximum and the power spectrum integral (Figures 7.2, 7.3, 7.4 and 7.5, respectively).

The seasonal variations using the EM seasons are shown in Figures 6.20, 6.21 and 7.5. These results are discussed in chapter 7.

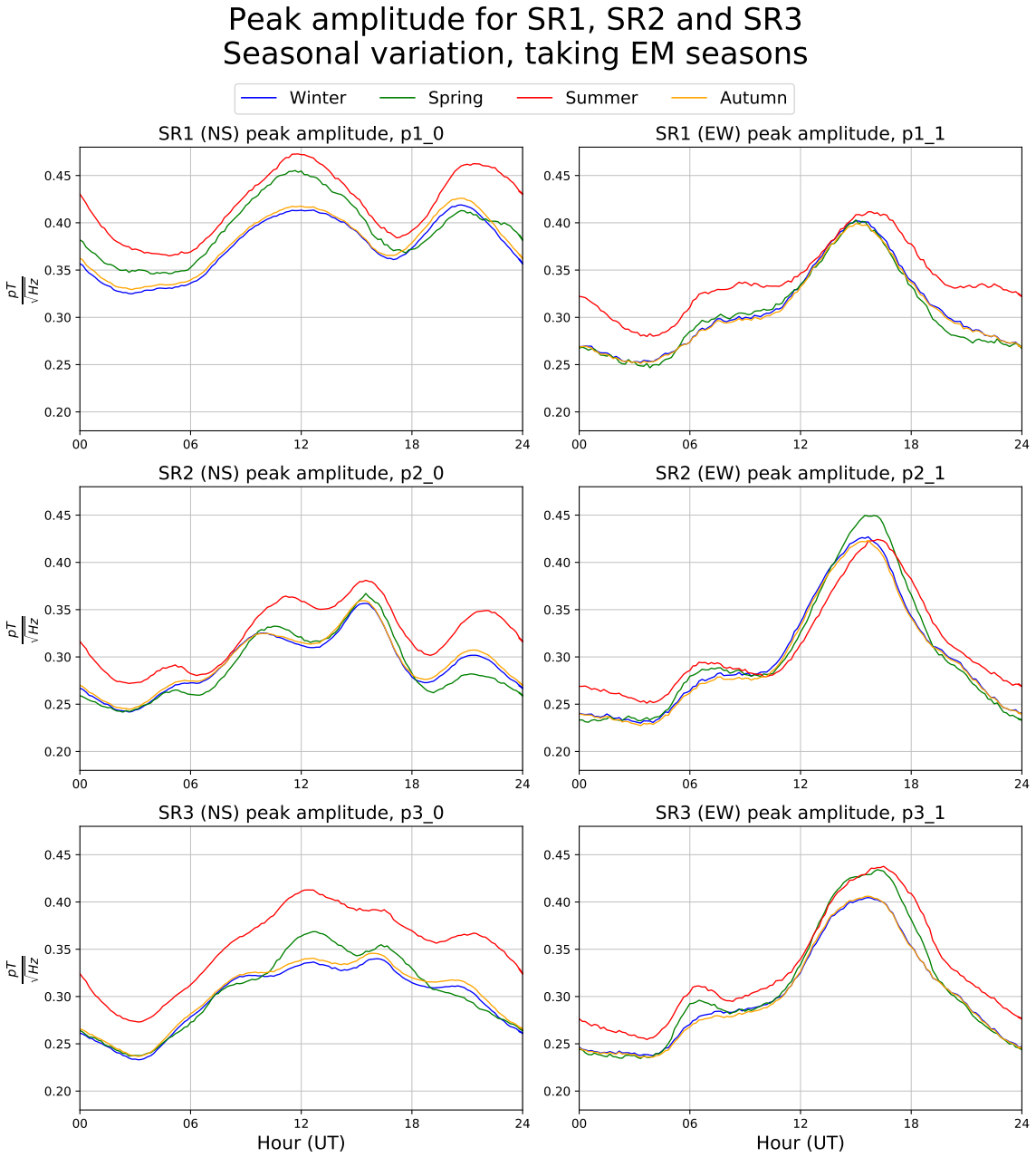

Figure 6.20. Seasonal variations for the SR1 (up), SR2 (middle) and SR3 (down) local maximum amplitudes -`p1`, `p2` and `p3`, respectively- for the NS (left) and the EW (right) components - `_0` and `_1`, respectively. The days used for the study of these variations go from 1st March 2013 to 31st December 2016. The EM seasons defined in Nickolaenko et al. (2015) have been used: winter (February, 1 to March, 31), spring (April, 1 to May, 31), summer (June, 1 to September, 30) and autumn (October, 1 to January, 31).

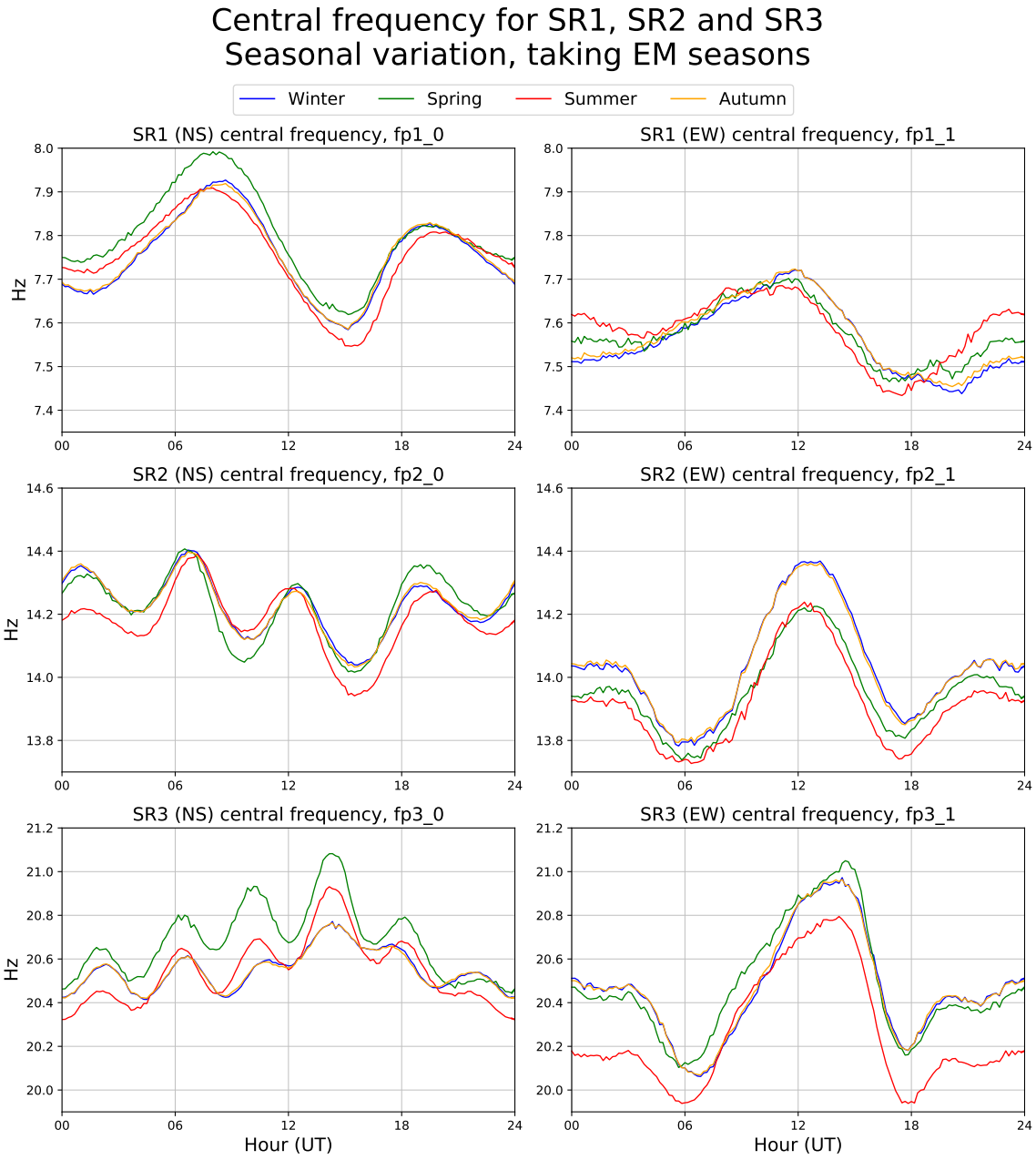

Figure 6.21. Seasonal variations for the SR1 (up), SR2 (middle) and SR3 (down) local maximum central frequencies -`fp1`, `fp2` and `fp3`, respectively- for the NS (left) and the EW (right) components - `_0` and `_1`, respectively. The days used for the study of these variations go from 1st March 2013 to 31st December 2016. The EM seasons defined in Nickolaenko et al. (2015) have been used: winter (February, 1 to March, 31), spring (April, 1 to May, 31), summer (June, 1 to September, 30) and autumn (October, 1 to January, 31).

6.3.7. Annual variation

The notebook `Annual_Variation.ipynb` has been created to visualize the diurnal variation of a given parameter for each one of the 12 different months of the year.

It has two main functionalities:

- It allows to observe if there exists a transition between a 'winter type' to a 'summer type' (and back to the 'winter type') in the diurnal variations of the parameters due to latitudinal movements of the sources during the year (Ondrášková et al., 2011). It helps us also establish the seasons of the year in terms of the SR behavior.
- We can compare the behavior of the diurnal variation of a given parameter in the same month for different years, which is a way of studying if the SR behave anomaly in a certain month with respect to that month for other years.

For each month, the average diurnal variation of the chosen parameter is plotted in a different color. A line showing the average trend of the diurnal variation of the parameter, over all the years considered, is also plotted.

The most important input argument is the parameter, `par`, to be plotted. Four elements are given as output:

- `hours`: a `np.array` of `float` values containing the time intervals of the day taken into consideration to generate the plot.
- `promedh`: a `np.array` of `float` values that contains the average diurnal variations for every month (axis 0).
- `medh`: a `np.array` of `float` values that contains the diurnal variations classified for every month (axis 1) of every year (axis 0).
- `conth`: a `np.array` of `float` values that contains the number of available unmasked values to average for each every month (axis 1) of every year (axis 0).

The annual variations of the global peak amplitudes and the global peak central frequencies of SR1, SR2 and SR3, for the NS and for the EW components, are shown in Figures 6.22 to 6.33. The annual variations of the PSI are shown in Figures 7.8 and 7.9. The annual variations of the widths at half maximum can be found in the notebook.

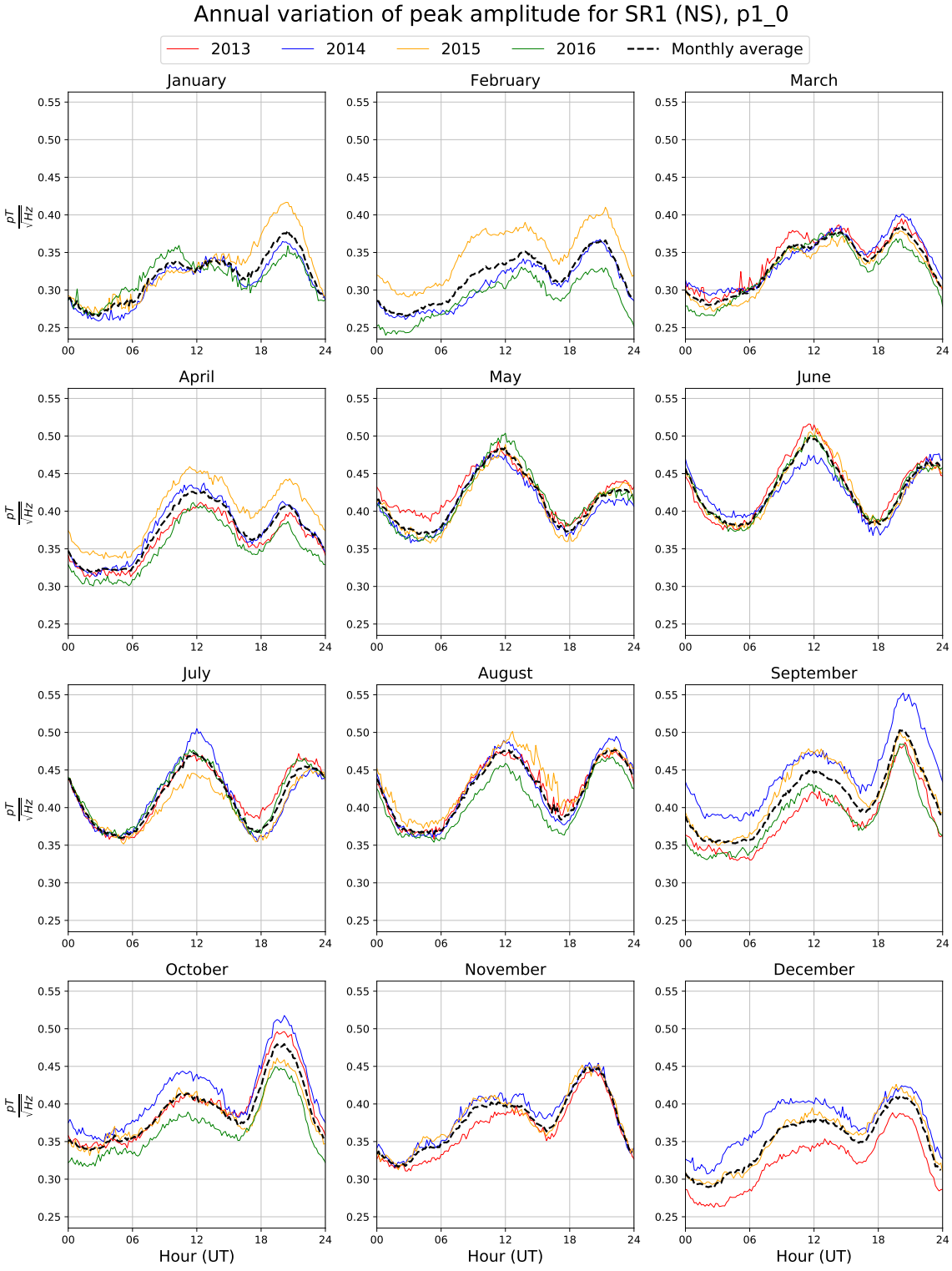

Figure 6.22. Annual variation for the SR1 (NS component) local maximum amplitude, p1_0.

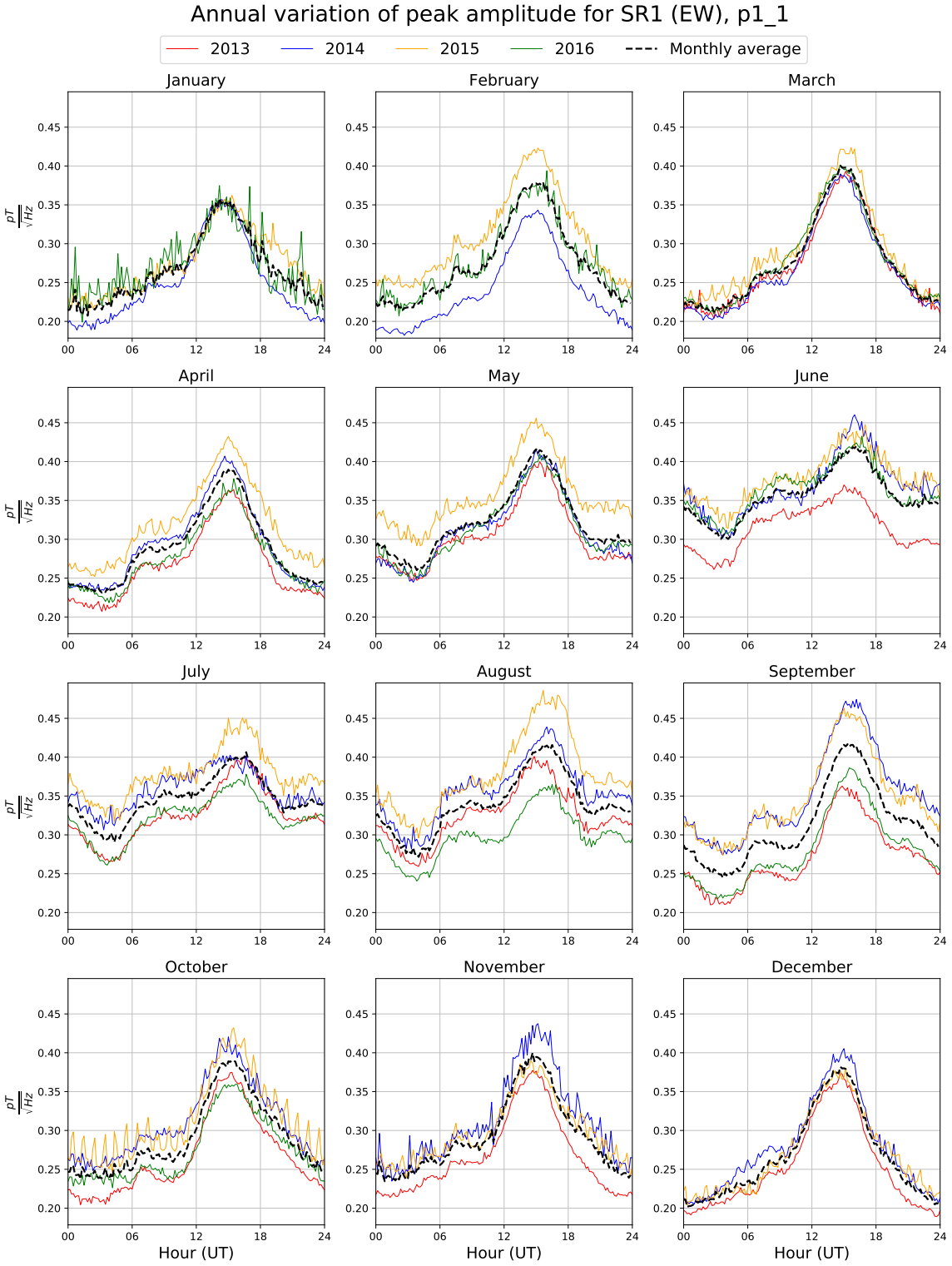

Figure 6.23. Annual variation for the SR1 (EW component) local maximum amplitude, p1_1.

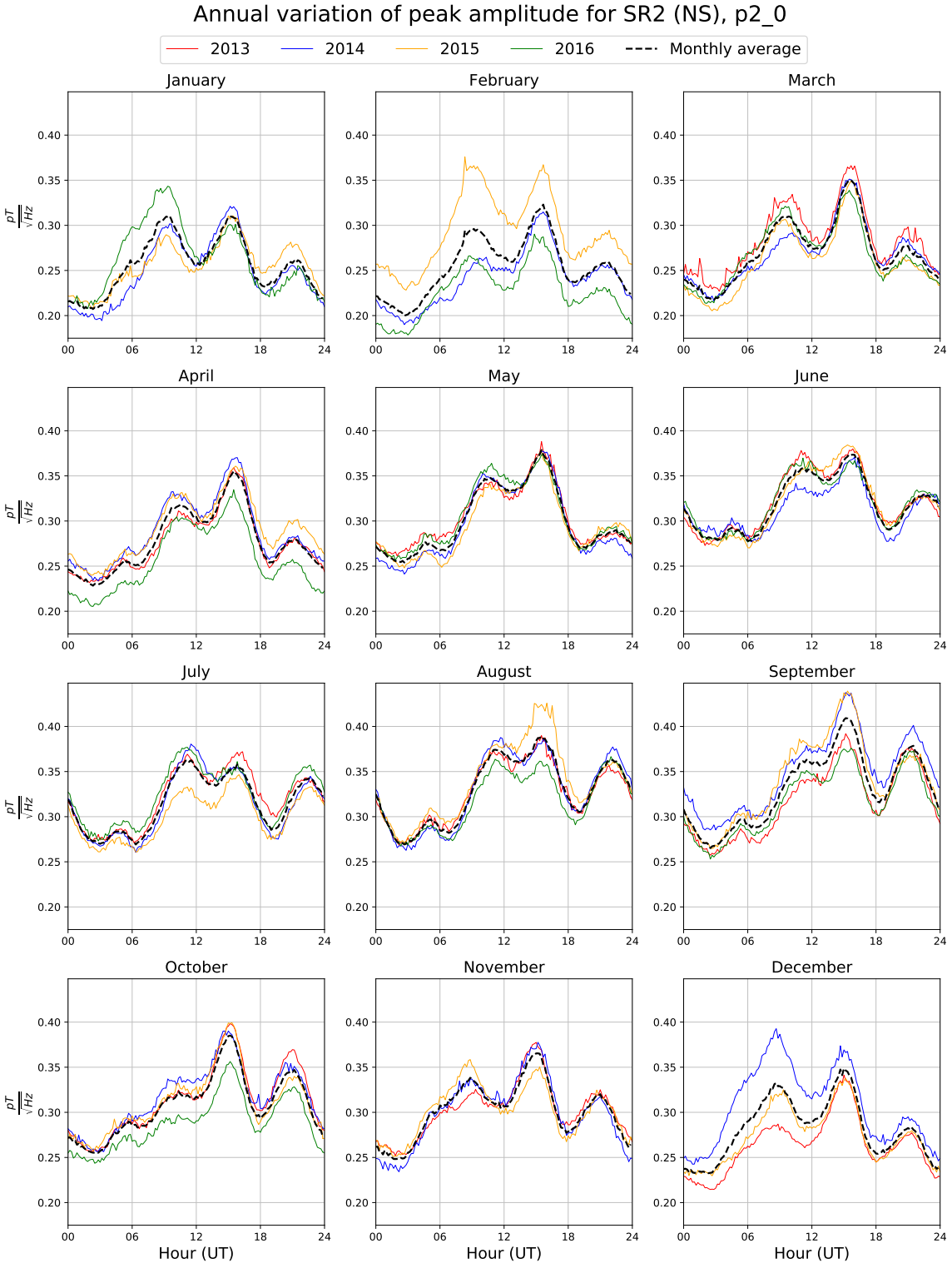

Figure 6.24. Annual variation for the SR2 (NS component) local maximum amplitude, p2_0.

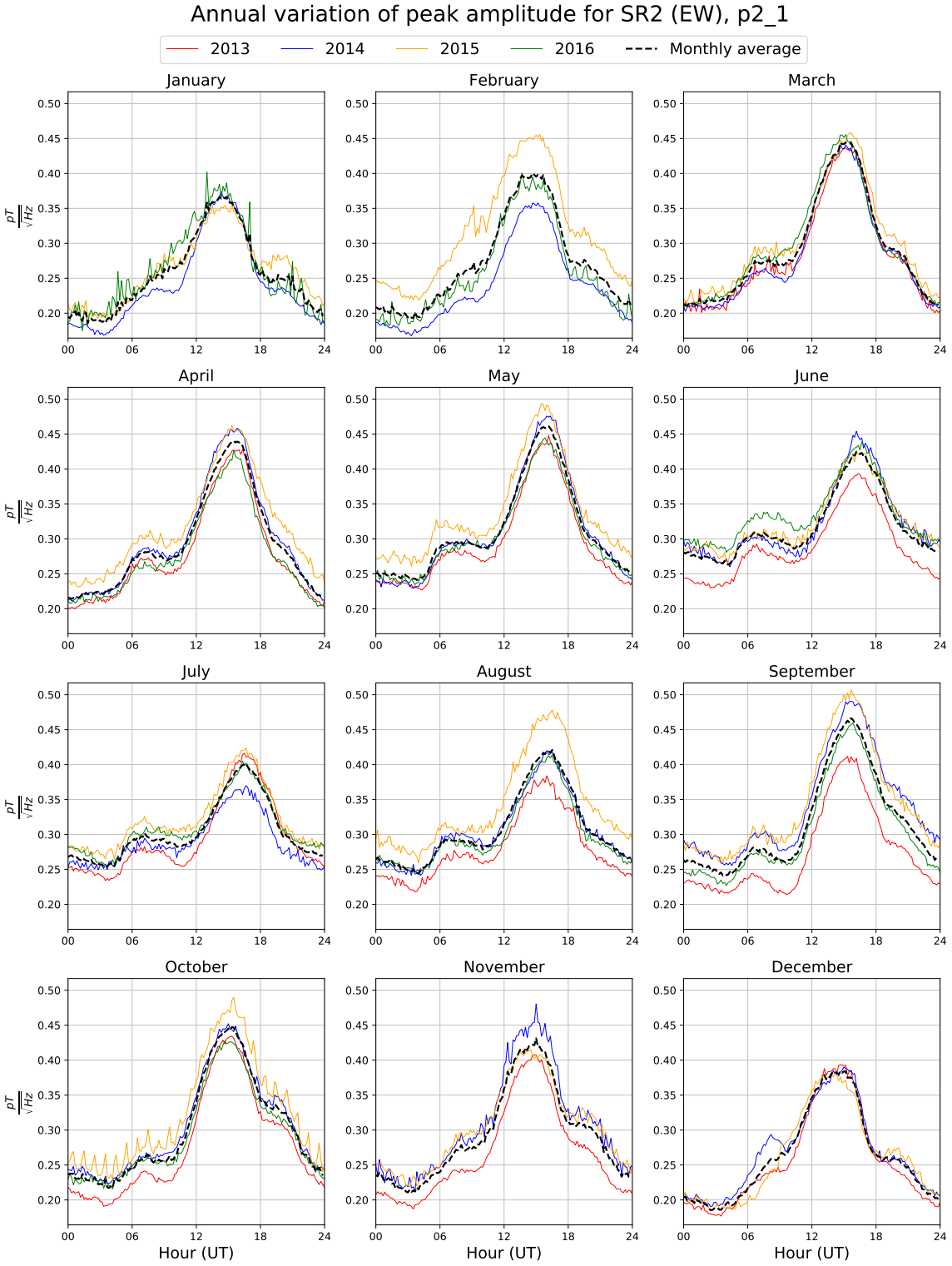

Figure 6.25. Annual variation for the SR2 (EW component) local maximum amplitude, p2_1.

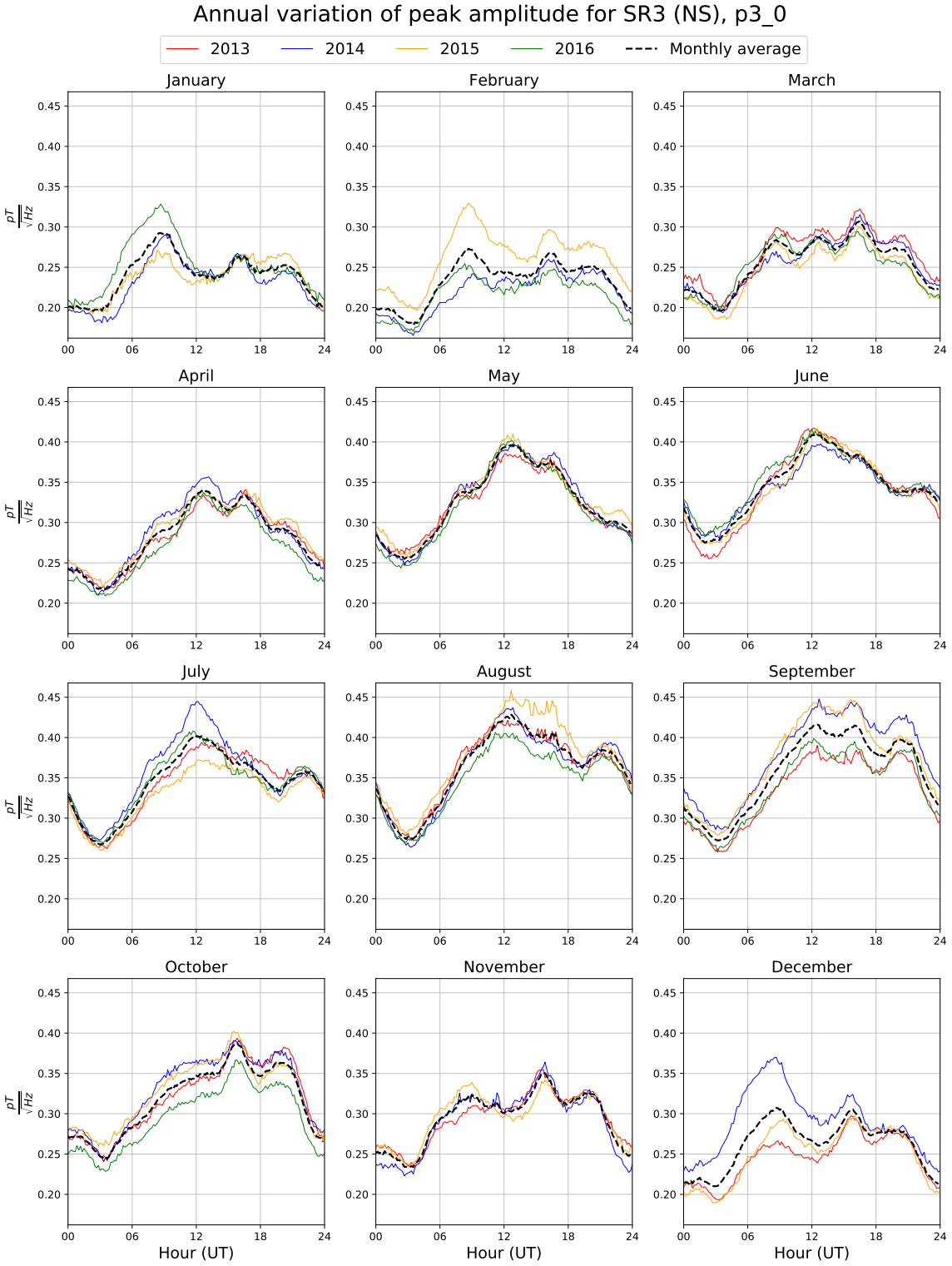

Figure 6.26. Annual variation for the SR3 (NS component) local maximum amplitude, p3_0.

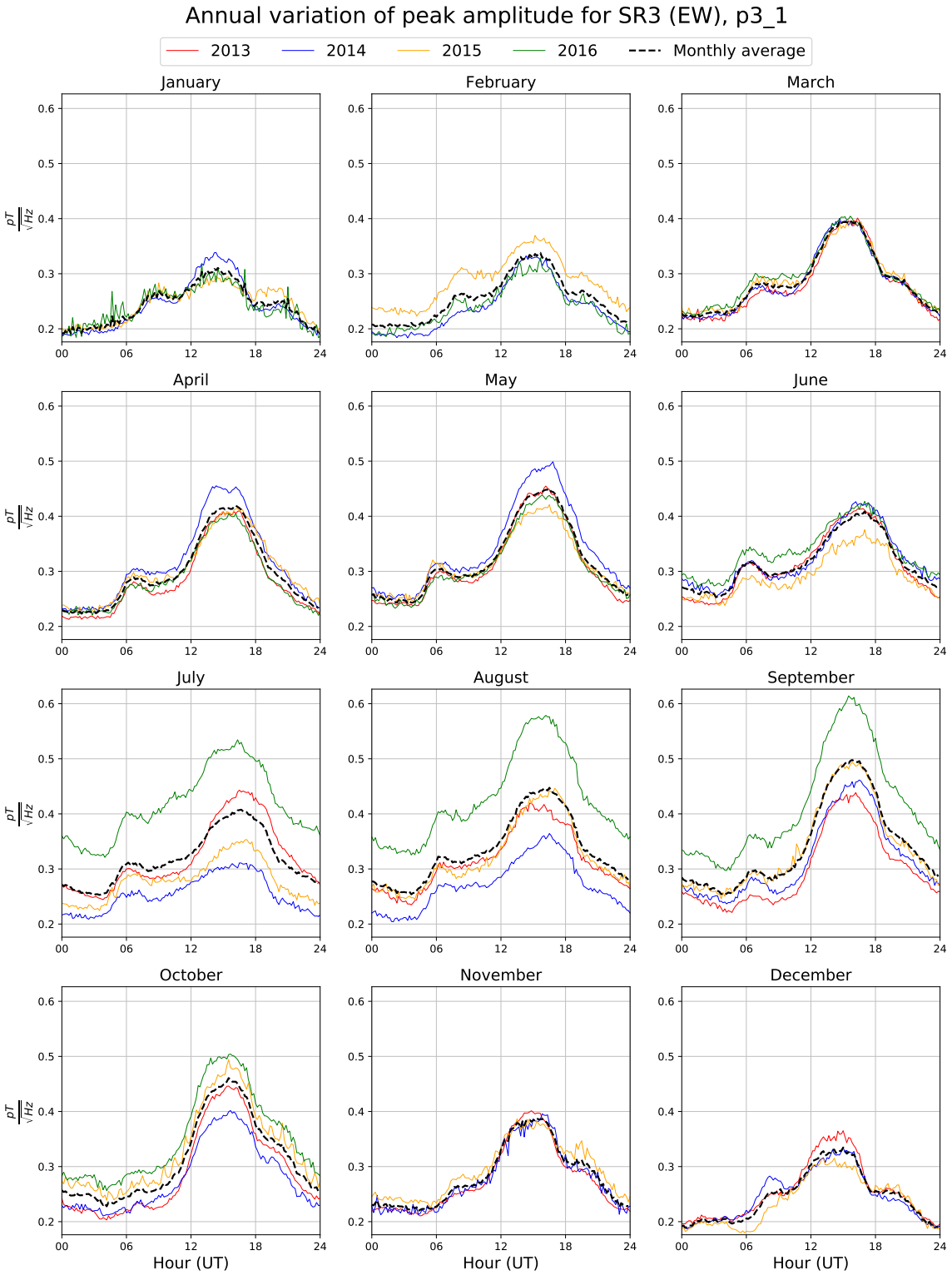

Figure 6.27. Annual variation for the SR3 (EW component) local maximum amplitude, p3_1.

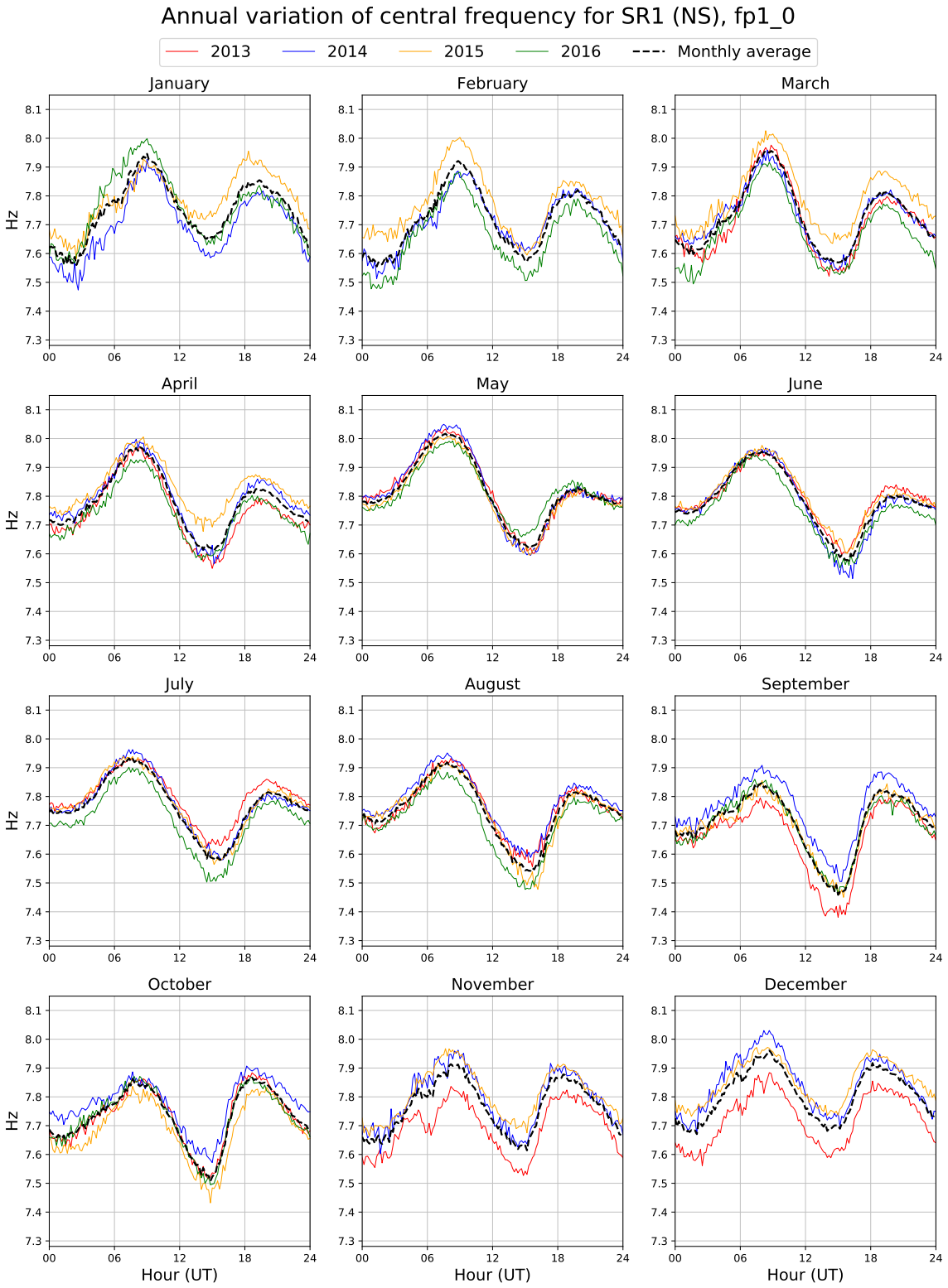

Figure 6.28. Annual variation for the SR1 (NS component) local maximum central frequency, `fp1_0`.

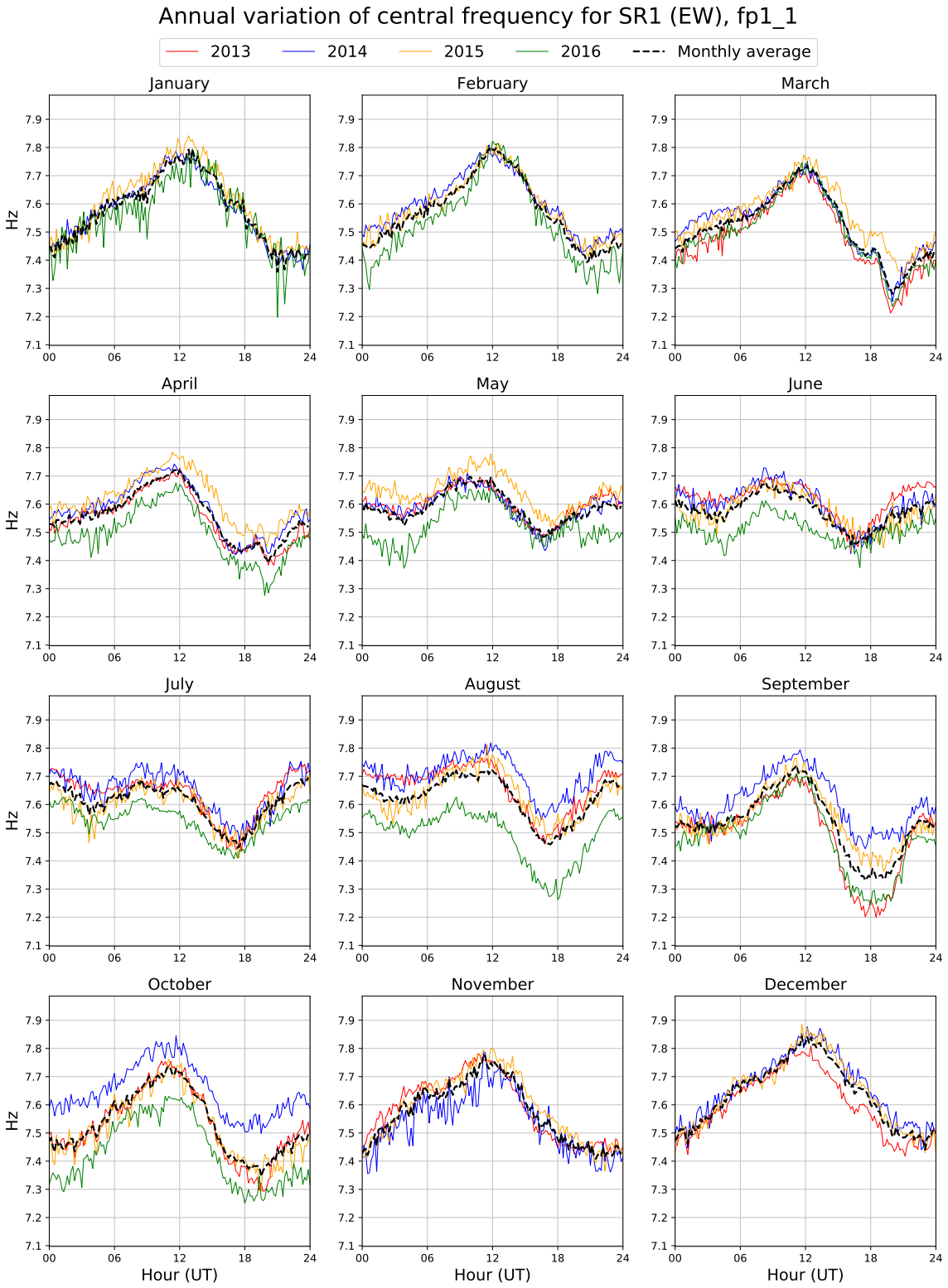

Figure 6.29. Annual variation for the SR1 (EW component) local maximum central frequency, `fp1_1`.

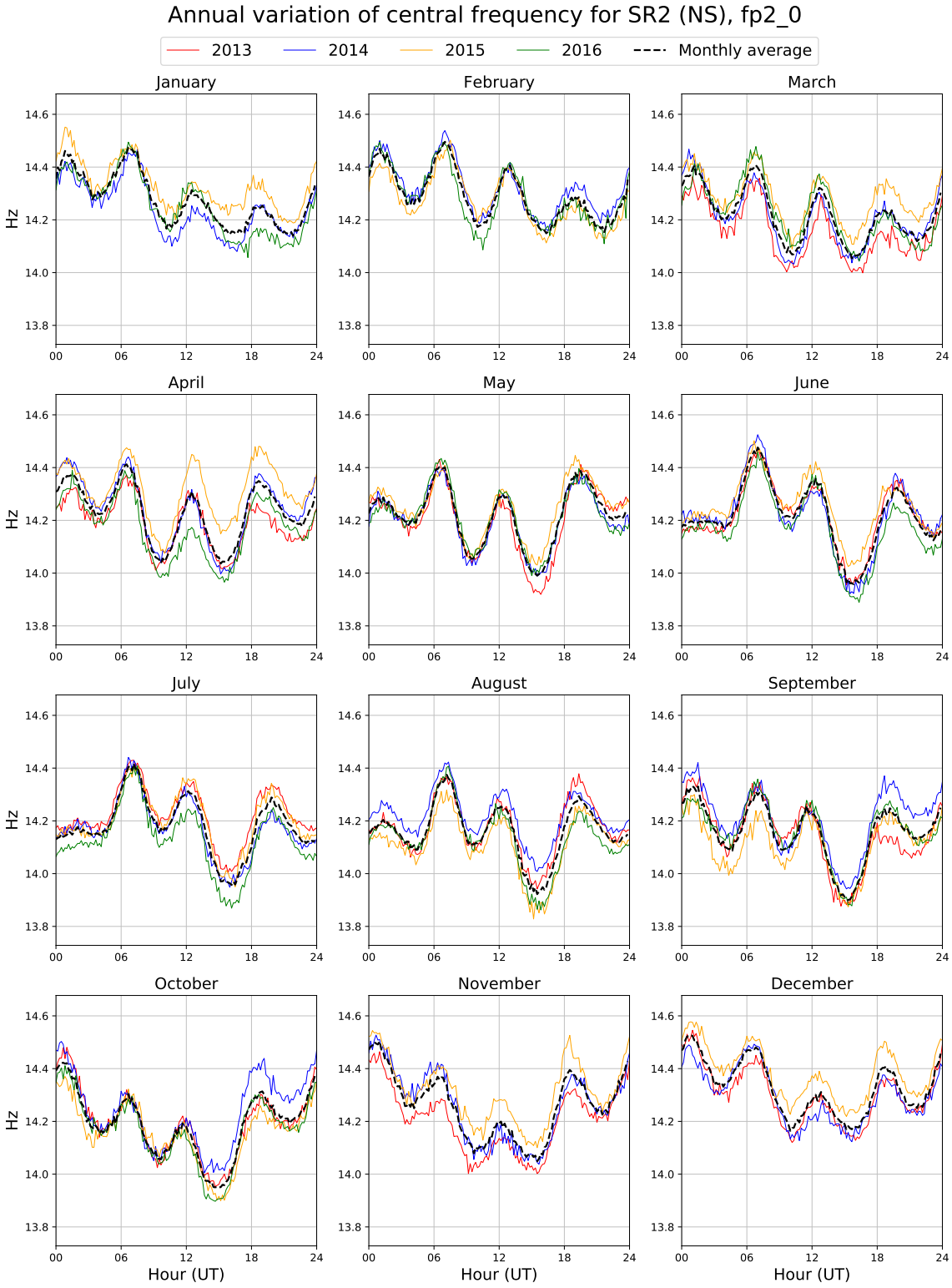

Figure 6.30. Annual variation for the SR2 (NS component) local maximum central frequency, `fp2_0`.

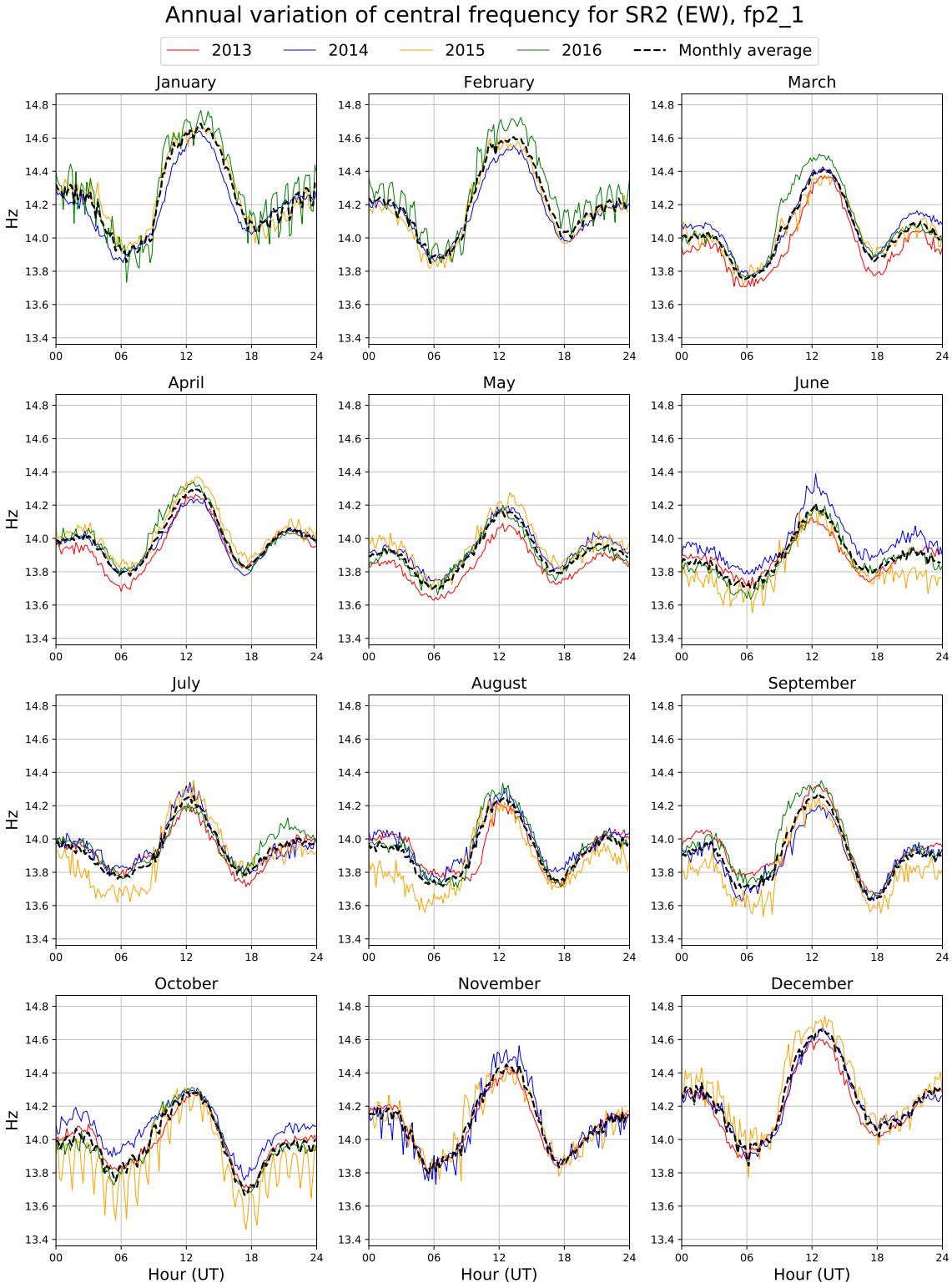

Figure 6.31. Annual variation for the SR2 (EW component) local maximum central frequency, `fp2_1`.

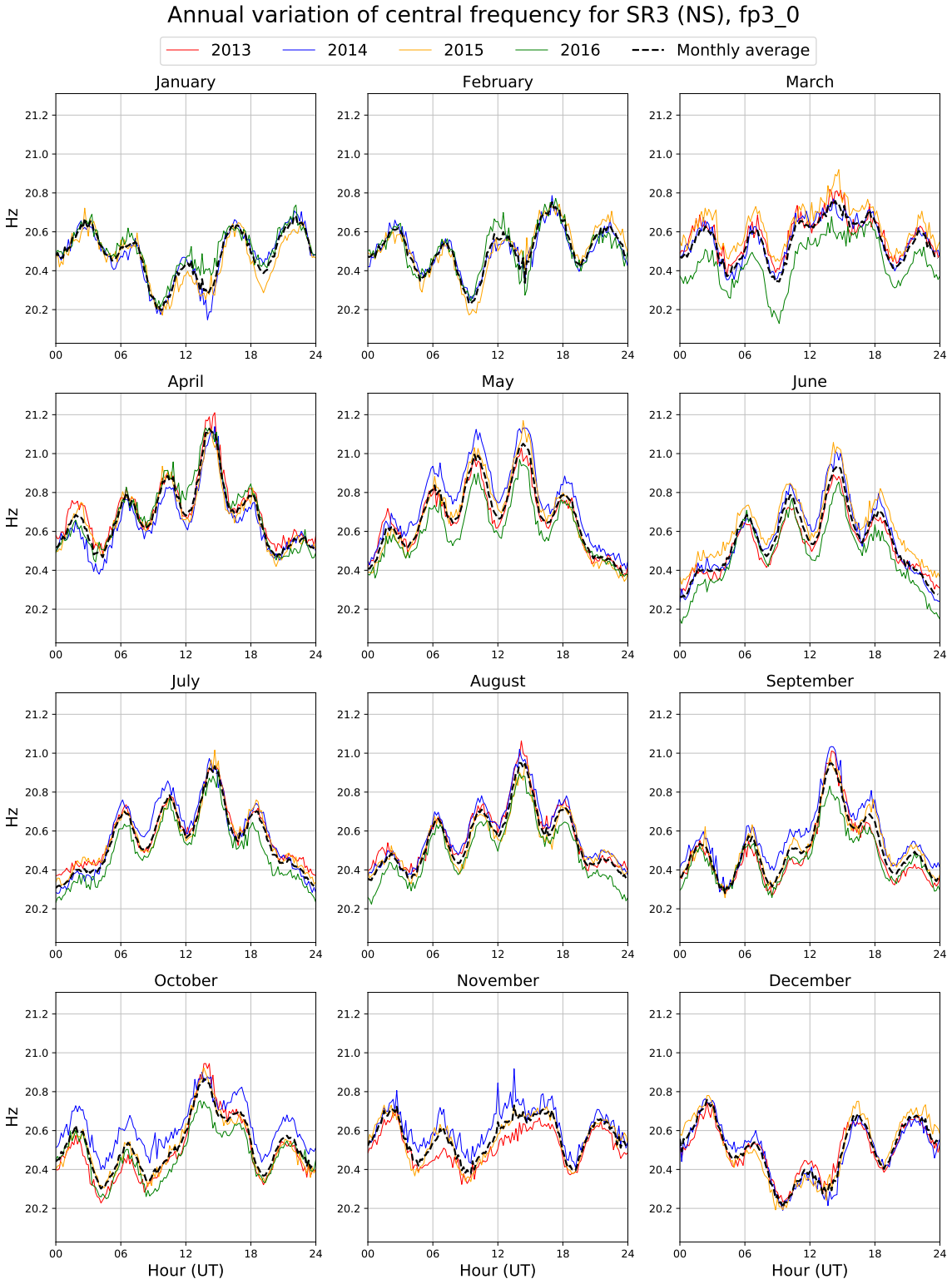

Figure 6.32. Annual variation for the SR3 (NS component) local maximum central frequency, `fp3_0`.

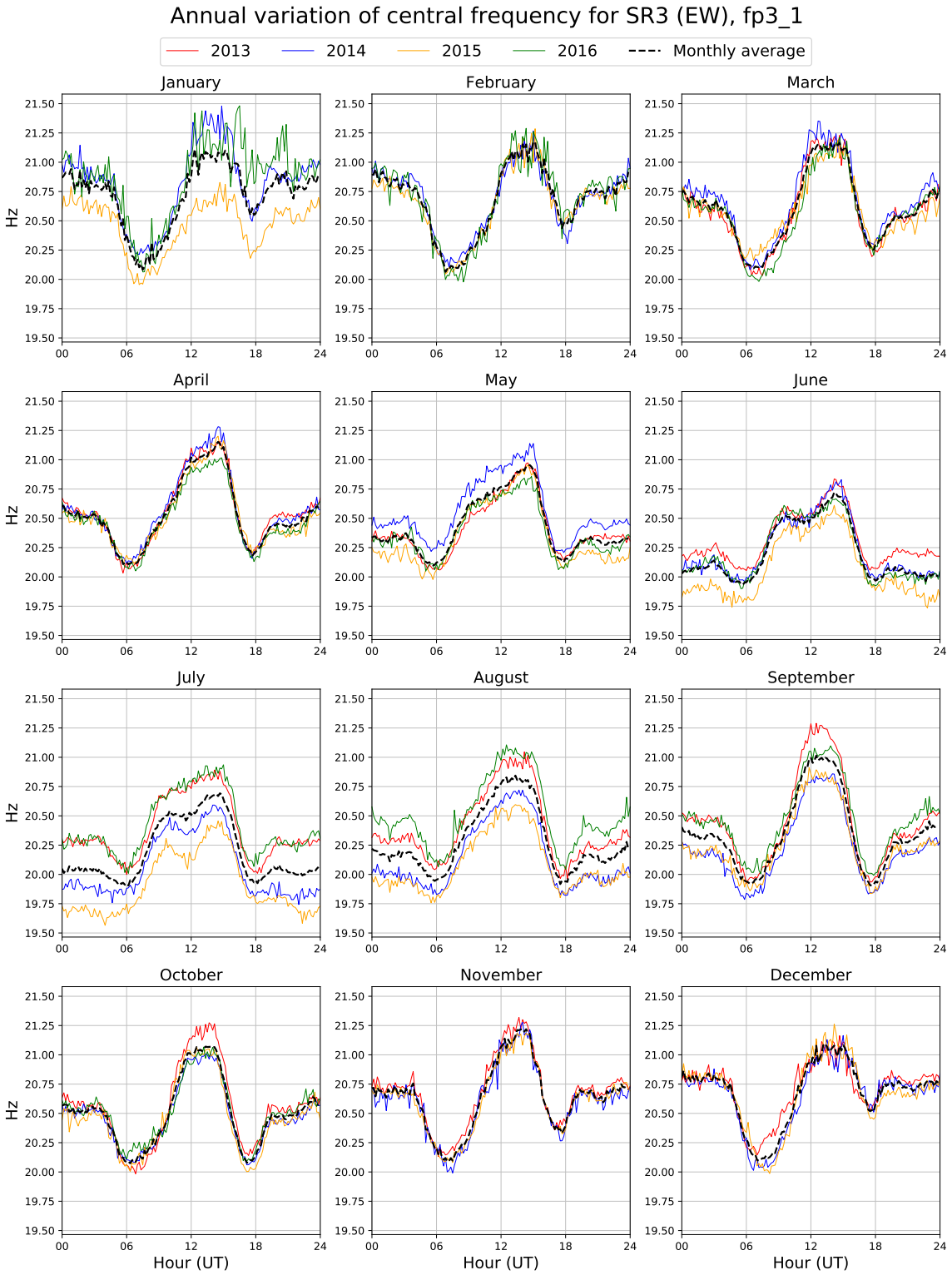

Figure 6.33. Annual variation for the SR3 (EW component) local maximum central frequency, `fp3_1`.

6.3.8. Month plots

The notebook `Month_Plots.ipynb` plots the diurnal variation of a series of parameters for a series of specific months that we want to study. It is useful to compare the diurnal variations with those obtained at other ELF stations in specific months, or to look for a relation between the SRs and climatic phenomena in certain months.

Two input arguments of this notebook are:

- `lpar`: a list of `str` values containing the codes of the parameters that we want to visualize.
- `months`: a list containing the months that we want to visualize. Examples: `['2014-01','2014-02','2014-03','2014-04']`, `['2016-01', '2016-06']`, `['2015-05','2015-07','2015-09','2015-11','2016-01','2016-03']`.

The output arguments of this notebook are:

- `hours`: a `np.array` of `float` values containing the hours of the day taken into consideration to generate the plot.
- `medh`: a `np.array` of `float` values with `len(lpar)` rows which contain, each one, the diurnal average variation of each one of the months in `months`.

In Figure 6.34, we can see an example of use of this notebook. Another example is Figure 7.7.

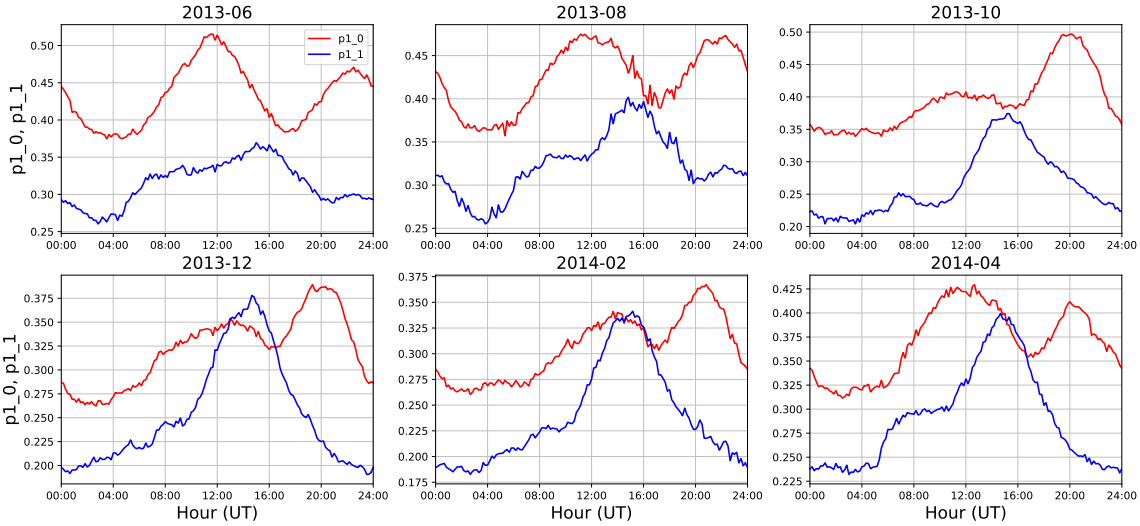

Figure 6.34. Diurnal variation of the global peak amplitude for SR1, for the NS component (`p1_0`) and for the EW component (`p1_1`), for the months 13-06, 13-08, 13-10, 13-12, 14-02 and 14-04.

6.3.9. Mask plot

The notebook `Mask_Plot.ipynb` has been designed to quickly visualize the 10 min time intervals that are masked and thus removed from the long term analysis of the SR variations. It is convenient to control the number of intervals that are taken out from the analysis since a large amount of masked intervals could make the results less meaningful. It is optional to display a text box (if the input argument `text` is set to `true`) with the total number of samples recorded and the amount of them that are masked, as well as the ratio of masked intervals. The rest of the input and output arguments are explained in detail in the notebook.

In Figure 6.35, the masked intervals from March, 2013 to October, 2016 are shown. The rate of masked intervals is higher (about three times) for the EW component than for the NS component. The station presents two periods for which there are no recordings available. Figure 6.36 is a zoom-in on the dates from July 1st to July 5th, 2014, in which a failure took place at the station and no recordings are available for a period of about one day.

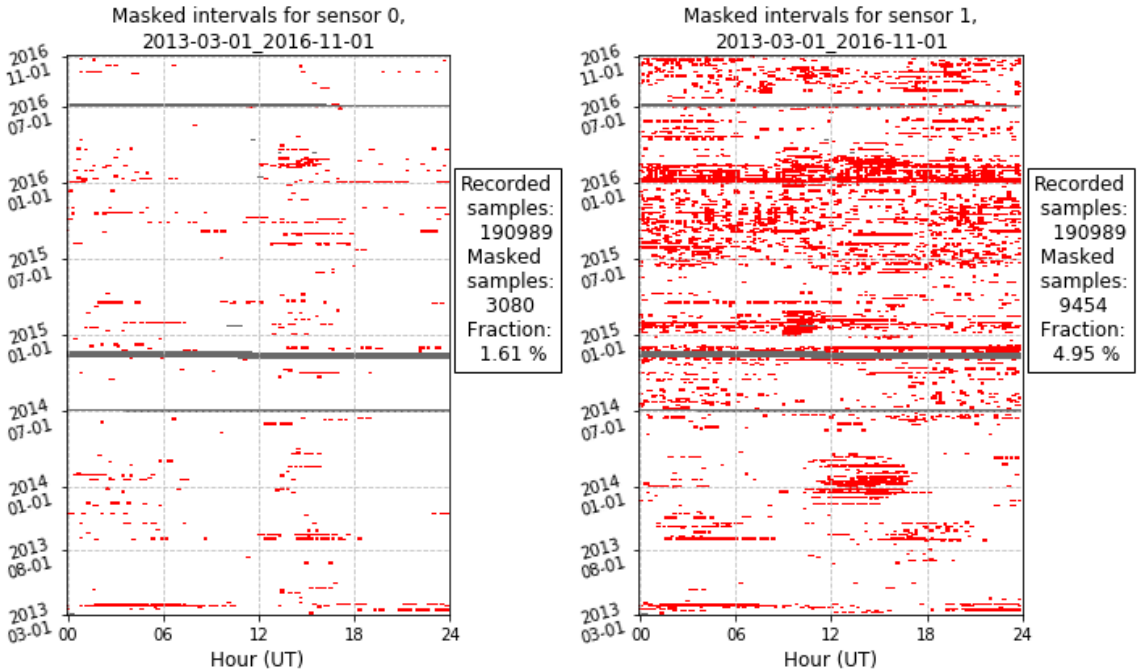

Figure 6.35. Masked intervals from March, 2013 to October, 2016, for the NS component (left) and the EW component (right). The 10 min intervals for which there are no recordings available are plotted in gray, while the 10 min intervals for which the SR parameters show an unacceptable value are plotted in red.

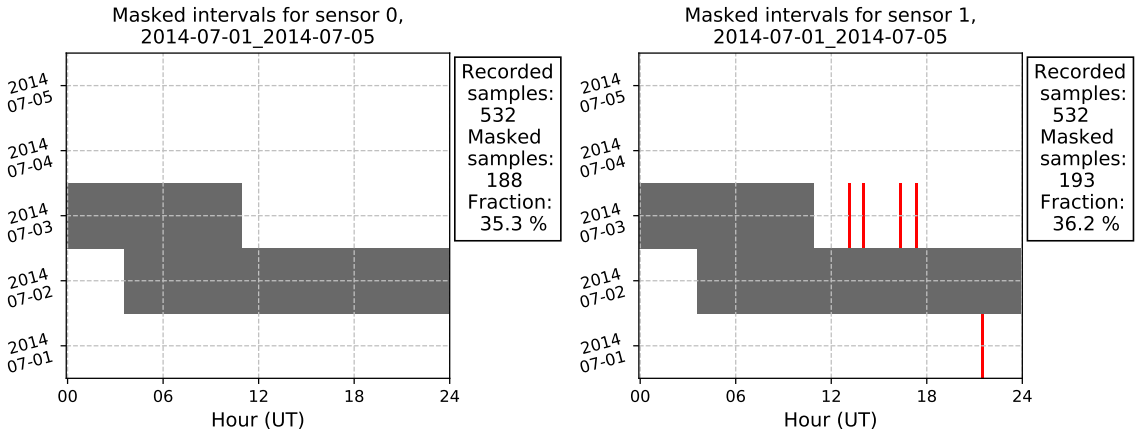

Figure 6.36. Masked intervals from July 1st to July 5th, 2014, for the NS component (left) and the EW component (right). The 10 min intervals for which there are no recordings available are plotted in gray, while the 10 min intervals for which the SR parameters show an unacceptable value are plotted in red.

6.3.10. Saturation Plot

The notebook `Saturation_Plot.ipynb` has been designed to display the fraction of saturated 10 s windows for each 10 min time interval of recordings. The rate of saturation might be related to the ratio of local lightning events or other phenomena. It is also convenient to keep track of the saturation because a high amount of saturated windows would imply less meaningful results. The input and output arguments are explained in detail in the notebook.

In Figure 6.37, we can observe that the maximum ratio of saturated windows is around $0.16 = 16\%$, however this maximum value is rarely observed, the typical saturation ratio is below 4%.

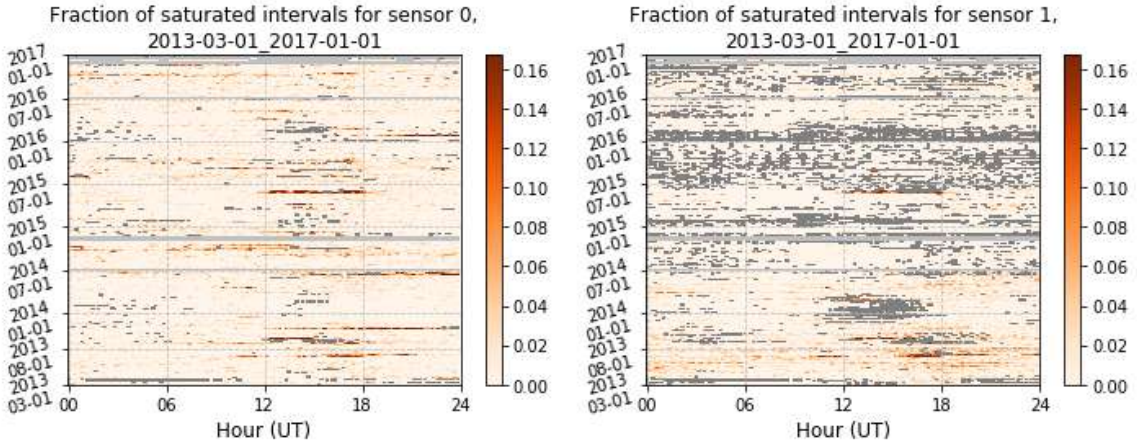

Figure 6.37. Fraction of saturated 10 s windows for each 10 min time interval, from March, 2013 to December, 2016, for the NS (left) and the EW (right) components.

6.3.11. Chi plot

The notebook `Chi_Plot.ipynb` traces the value of the χ^2 for the lorentzian fit for all the 10 min time intervals. The values for χ^2 for all the 10 min time intervals are shown in Figure 6.38. The value of χ^2 is clearly higher for the EW than for the NS component, which indicates that the lorentzian fitting function adapts better (with less square error) to the the NS component. Again, the value of χ^2 might be related to the significance of the results.

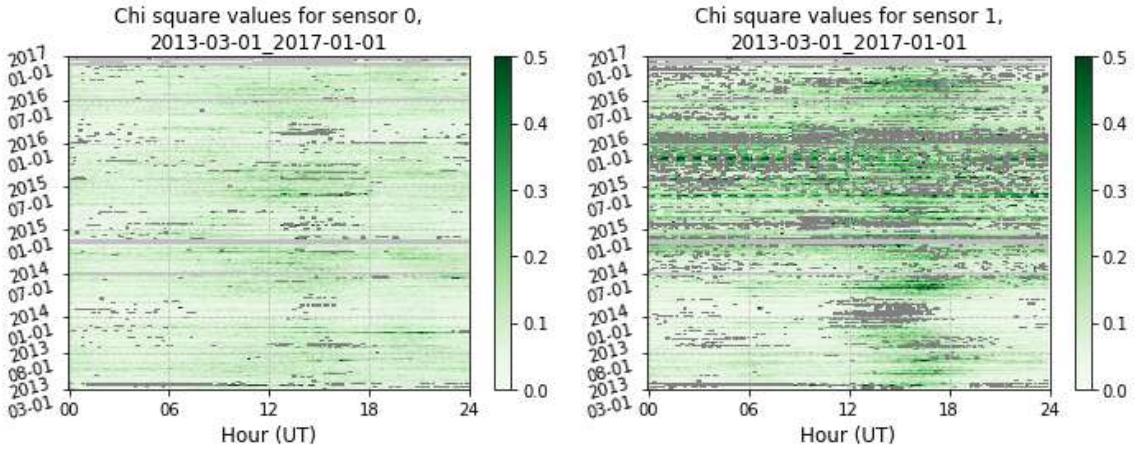

Figure 6.38. Value of χ^2 for the lorentzian fit of each 10 min time interval, from March, 2013 to December, 2016, for the NS (left) and the EW (right) components.

6.3.12. Study Mask

The notebook `Study_Mask.ipynb` plots a color mesh where we can analyze if a given parameter has an out-of-range value and so cause the masking of each time interval. The masked time intervals for which the value of that parameter, `par`, is too high are plotted in a color `color[0]`, the masked intervals for which the value of `par` is too low are plotted in a color `color[1]`, the masked intervals for which the value of `par` is not anomalous are plotted in a color `color[2]`, and the time intervals for which there are no recordings available are plotted in `color[3]`. In figures 6.39 and 6.40, we can observe several plots obtained with this notebook.

The most important input arguments, apart from the temporal ones, are:

- `par`: a `str` parameter code among `'p1_0'`, `'p2_0'`, `'p3_0'`, `'fp1_0'`, `'fp2_0'`, `'fp3_0'`, `'p1_1'`, `'p2_1'`, `'p3_1'`, `'fp1_1'`, `'fp2_1'`, `'fp3_1'`.
- `colors`: a 4 `str` list containing four valid matplotlib color codes.

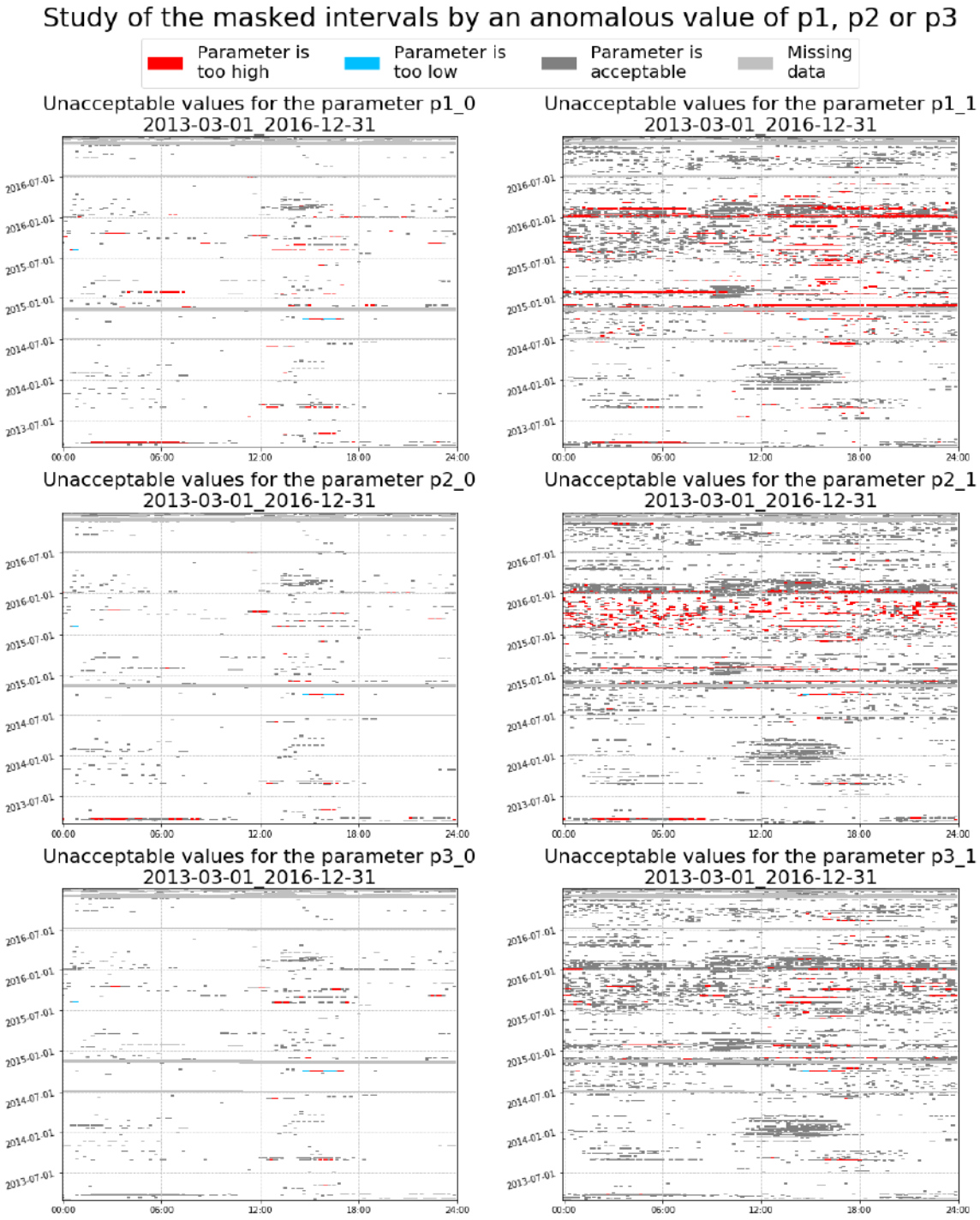

Figure 6.39. Time intervals that have been masked due to unacceptable values for `p1_0` (upper left), `p1_1` (upper right), `p2_0` (middle left), `p2_1` (middle right), `p3_0` (lower left), and `p3_1` (lower right). If the parameter value is too high for a time interval, it is shown in red. If the parameter value is too low for a time interval, it is shown in blue. Dark grey indicates that the time interval is masked due to an anomalous value for another parameter. Light grey indicates no recordings available for that time interval.

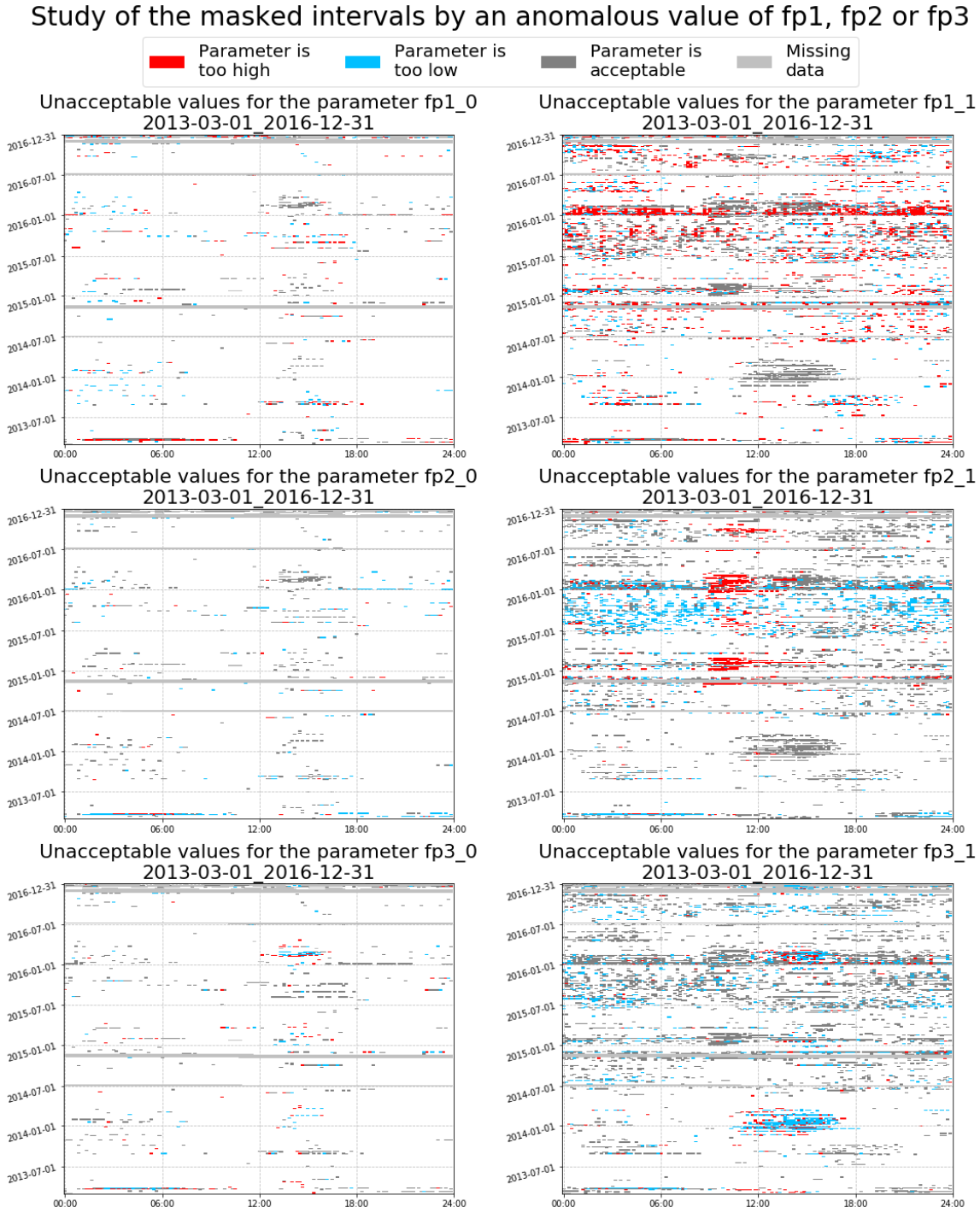

Figure 6.40. Time intervals that have been masked due to unacceptable values for `fp1_0` (upper left), `fp1_1` (upper right), `fp2_0` (middle left), `fp2_1` (middle right), `fp3_0` (lower left), and `fp3_1` (lower right). If the parameter value is too high for a time interval, it is shown in red. If the parameter value is too low for a time interval, it is shown in blue. Dark grey indicates that the time interval is masked due to an anomalous value for another parameter. Light grey indicates no recordings available for that time interval.

And the output parameters are:

- `hours`: a `np.array` of `float` values containing the hours of the day taken into consideration to generate the plot.
- `days`: a `np.array` of `float` values containing the days taken into consideration to generate the plot.
- `Ma_pa_sup`: a 2-dim `np.array` of `logical` values containing the time intervals for which the parameter `par` is too high.
- `Ma_pa_inf`: a 2-dim `np.array` of `logical` values containing the time intervals for which the parameter `par` is too low.
- `Ma_s`: a 2-dim `np.array` of `logical` values containing the masked intervals.
- `Ma_t`: a 2-dim `np.array` of `logical` values containing the intervals for which there are not recordings available.

6.3.13. Spectra

It is needed to be able to visualize the NS and the EW amplitude spectra, together with their respective lorentzian fits, to visually check how the fits adapt to the spectra. Also, some time intervals show amplitude spectra with certain particularities or anomalies, and we are interested in studying them. For both purposes, the notebook `Spectra.ipynb` has been created. It allows to display the amplitude spectra of as many 10 min intervals as we want. Three examples of graphs obtained using this function are given in Figure 6.41.

The most important input arguments, apart from the temporal ones, are:

- `date_strs`: a list of `str` values, each one of them accounting for one date and time with the format `'YYYY-MM-DDThh:mm'`. Examples: `['2013-03-01T00:40', '2013-03-04T15:40']`, `['2018-08-13T12:00']`, `['2015-05-09T10:00', '2015-05-09T10:10','2015-05-09T10:20','2015-05-09T10:30']`.
- `text`: a logical value. It `text=True`, a text box on the right of each plot containing information about it is shown.
- `shadow`: a logical value. If `shadow=True`, the frequency range out of the fitting band appears shadowed in red.

This notebook does not return any output argument. If the input argument `text` is set to `True`, this notebook displays the values of the SR local maximum amplitudes,

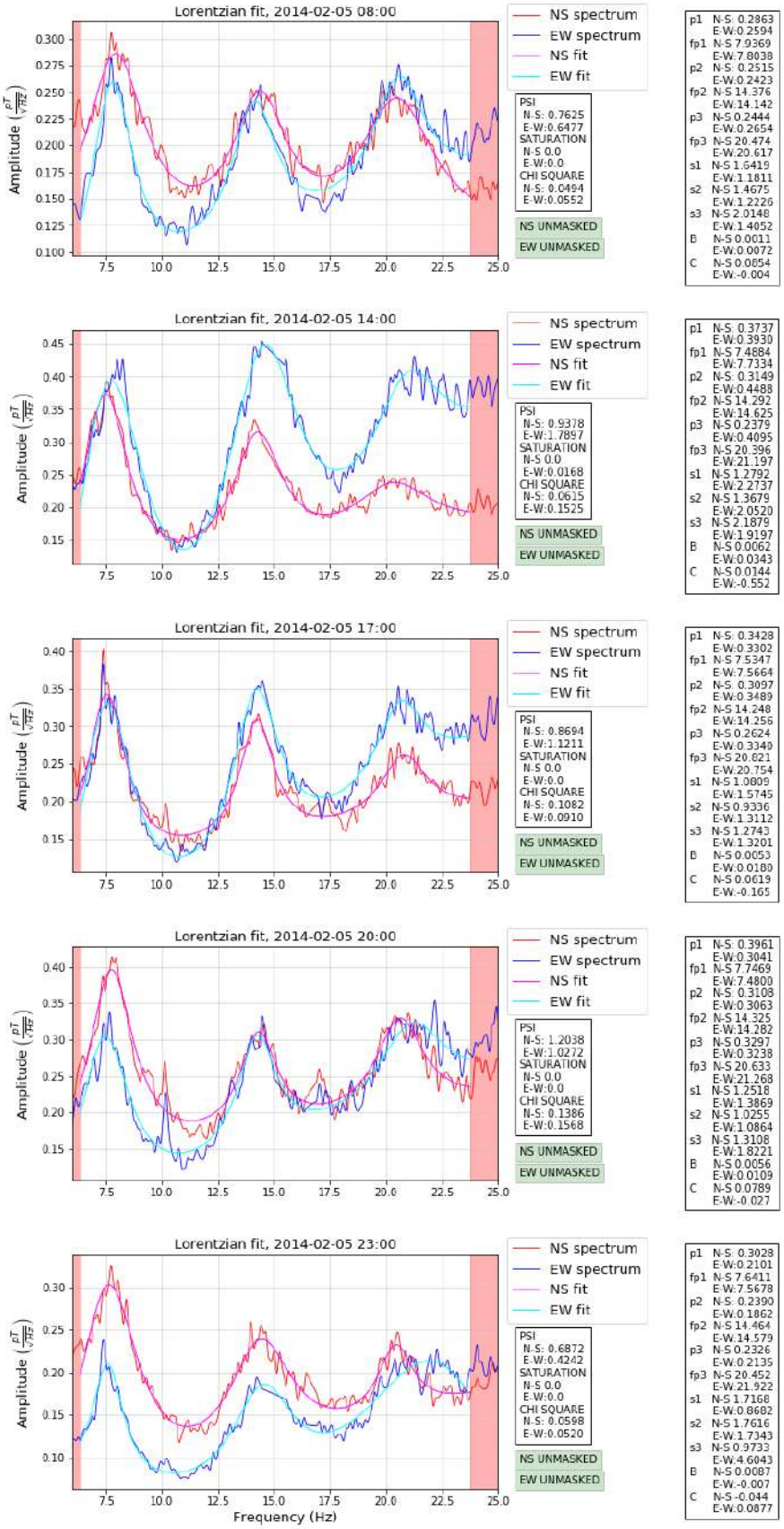

Figure 6.41. Amplitude spectra of three different 10 min time intervals recorded at Sierra Nevada ELF station on the 5th of February 2014.

the local maximum central frequencies and the half peak widths, together with the linear coefficients. The values of the power spectrum integral, the ratio of saturated 10 s windows and the χ^2 of the fit are also displayed. This function also indicates, in the lower right corner of the graph, if the NS and EW spectra correspond to a masked interval, and in that case, the parameter whose value is out of the acceptable range given in Tables 6.1 and 6.2 is shown on the right with the word "MASK" in red on the right.

6.3.14. Spectrogram

This function plots a spectrogram of the amplitude of the magnetic field recorded. Time is plotted in the x-axis and frequency is plotted in the y-axis. The function creates two plots, one for the NS recordings and another one for the EW recordings. It is possible to choose the color map of the chart using the input argument `'cmap'`. The spectrogram of the first year of SR recordings at Sierra Nevada is shown in Figure 6.42.

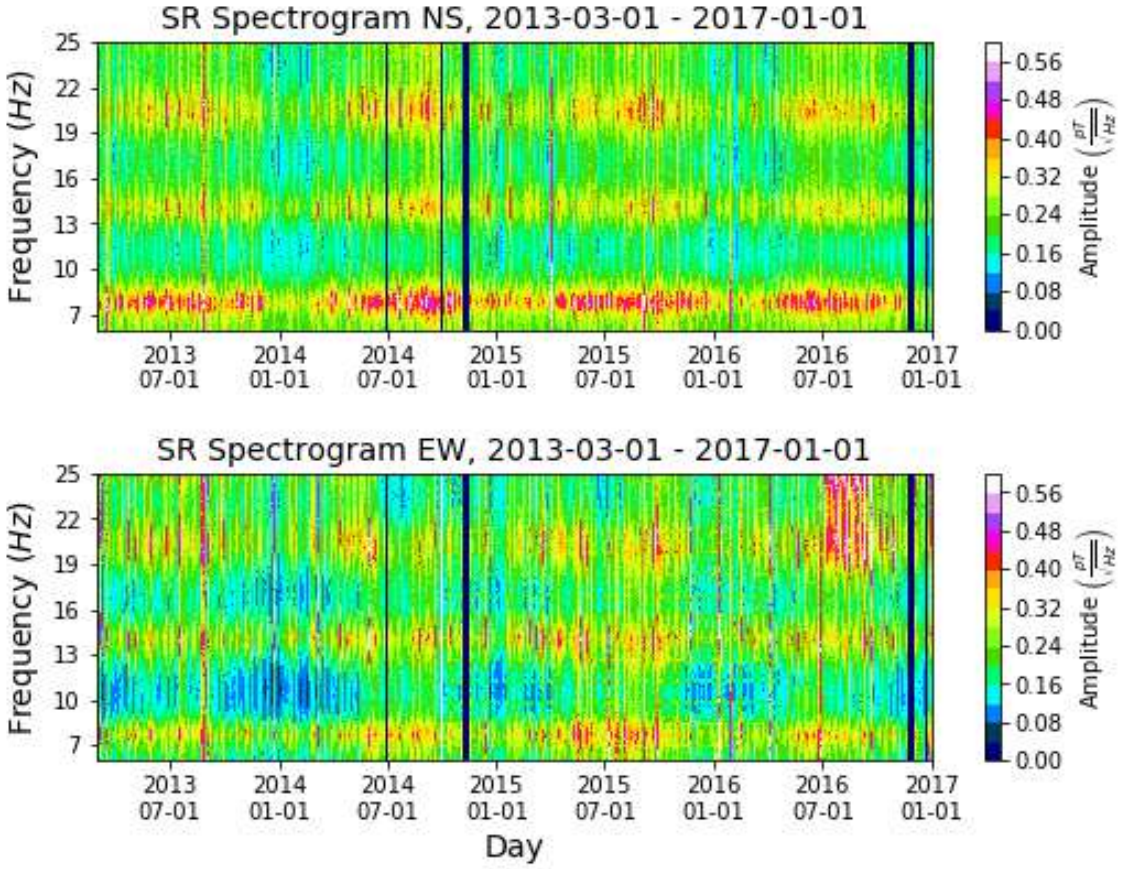

Figure 6.42. Spectrogram of the SRs recorded at Sierra Nevada from March, 2013 to December, 2016.

6.3.15. Statistical Distribution

The notebook `Statistical_Distribution.ipynb` has been designed to study and visualize the statistical distributions followed by the different parameters.

The main input arguments, apart from the temporal ones, are:

- `par`: a `str` parameter code. Examples: `'p1_0'`, `'fp2_1'`, `'psi_0'`.
- `gaussian`: a logical value. If `gaussian=True`, the Gaussian function with the same mean and std as our distribution is plotted.

This notebook has only one output argument, in which the data used to plot the histogram are stored:

- `hst`: it is made up by 2 arrays, where `hist[0]` is the relative frequency of each bin, and `hist[1]` is the central frequency of each bin.

Some examples of charts obtained with this notebook are Figures 6.2 and 6.3. Other examples are shown in Figures 6.43 and 6.44.

6.3.16. Dispersion

The notebook `Dispersion.ipynb` has been designed to study the correlation between the variations of two different parameters, using a dispersion plot. It is useful to analyze if high (or low) values of a parameter are related to high (or low) values of another parameter.

The most important input arguments of this notebook, apart from the temporal ones, are:

- `par1`: the `str` parameter code of the first parameter to be studied in the dispersion plot. Examples: `'p1_0'`, `'fp2_1`, `'psi_0'`.
- `par2`: the `str` parameter code of the second parameter to be studied in the dispersion plot. Examples: `'p1_1'`, `'fp3_1`, `'sat_0'`.
- `mask`: a logical value, if `mask=True` the vertical and horizontal lines delimiting the limits of the mask for the parameters will be shown on the graph. It is set to `True` by default.
- `fit`: a logical value, if `fit=True`, the linear fit of the points will be shown on the plot. It is set to `True` by default.

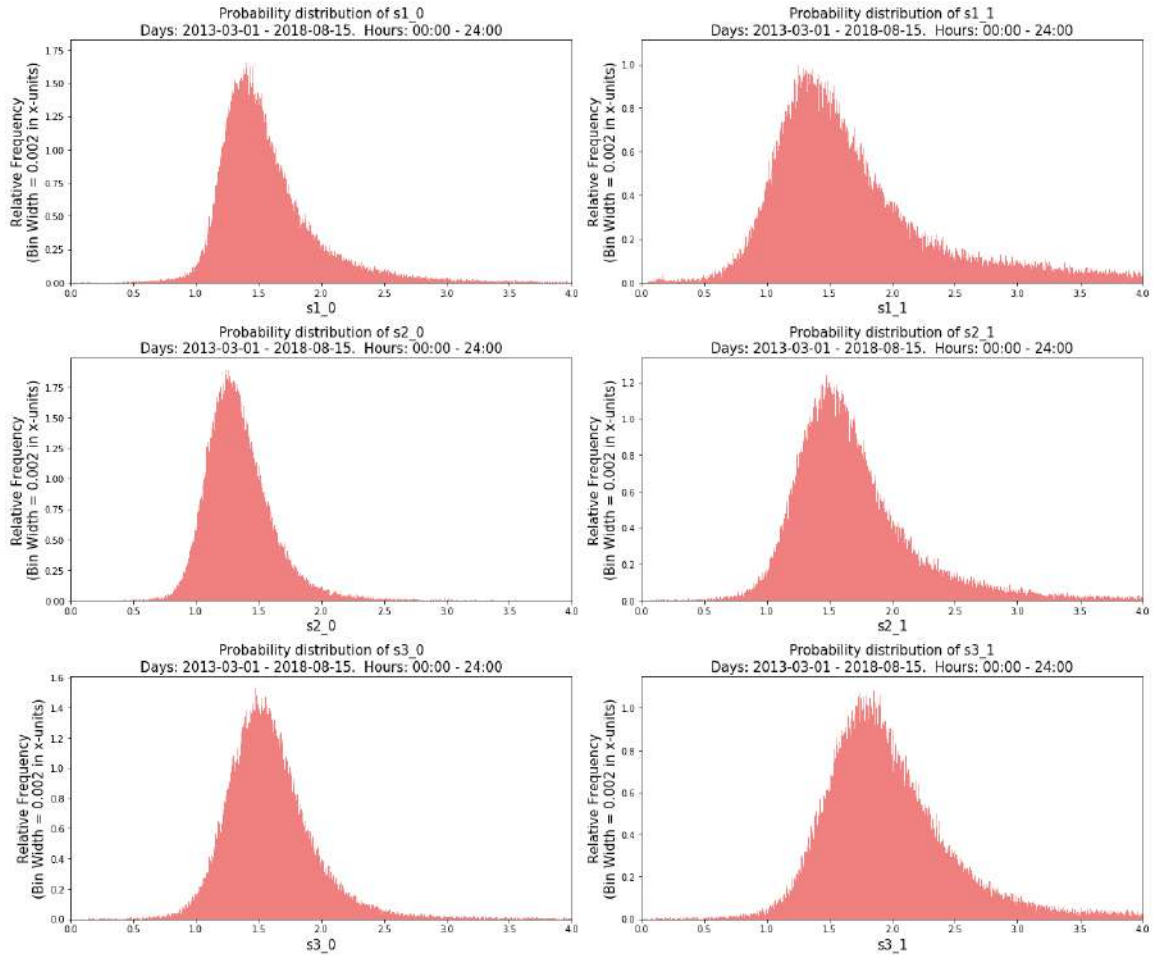

Figure 6.43. Statistical distributions of the widths at half peak of the 1st mode (first row), the 2nd mode (second row) and the 3rd mode (third row), for the NS magnetic field component (left) and the EW magnetic field component (right).

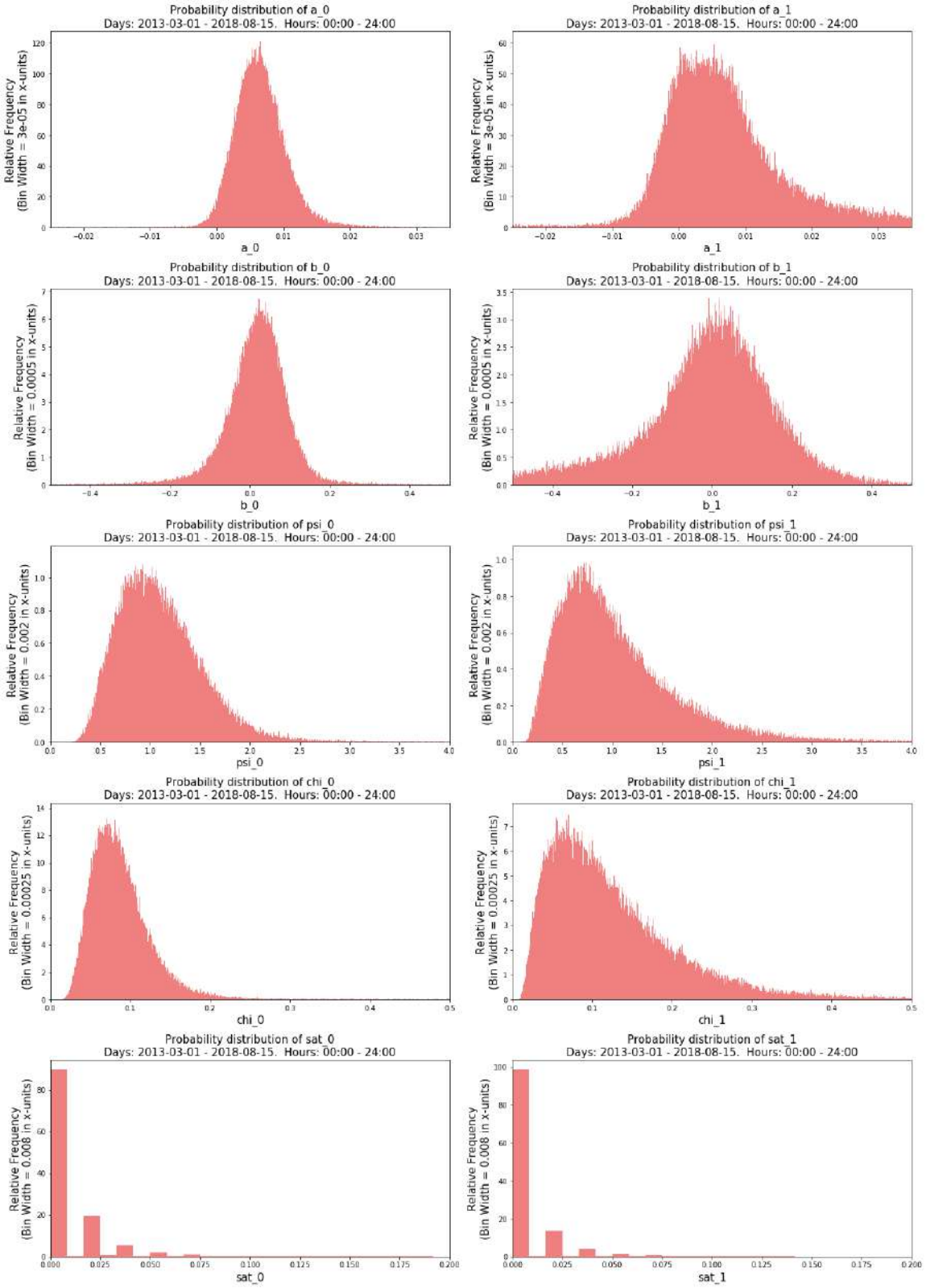

Figure 6.44. Statistical distributions of the linear terms (slope, `a`, and intercept, `b`), the power spectrum integral (`psi`), the chi-square of the lorentzian fit and the ratio of saturation, for the NS magnetic field component (left) and the EW magnetic field component (right).

– `text`: a logical value, if `text=True` a text box is shown containing some information.

The output arguments of this notebook are:

– `y1[`$\tilde{}$`(y1.mask+y2.mask)]`: the values of `par1` taken to do the scatter plot, for the time intervals for which neither the values of `par1` nor the values of `par2` are masked.

– `y2[`$\tilde{}$`(y1.mask+y2.mask)]`: the values of `par2` taken to do the scatter plot, for the time intervals for which neither the values of `par1` nor the values of `par2` are masked.

The chart generated by the notebook also displays the value of the slope and the intercept of the linear fit of the scatter dots, as well as the regression coefficient (r) and the determination coefficient (r^2), if the input argument `text` is set to `True`.

Some examples of dispersion plots using this notebook are shown in Figures 6.45, 6.46 and 6.47.

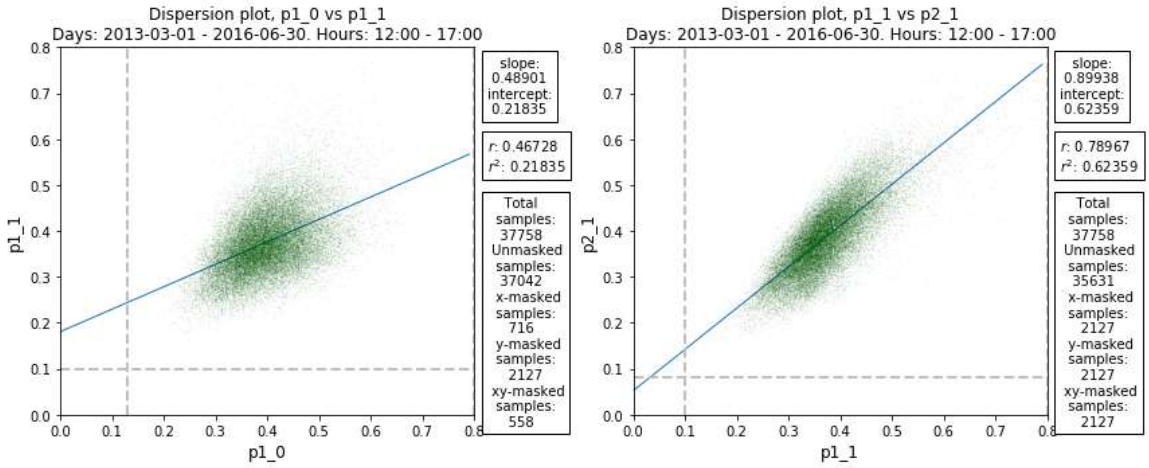

Figure 6.45. Dispersion plot showing the SR1 global peak amplitude for the NS component, `p1_0`, vs the SR1 global peak amplitude for the EW component, `p1_1` (left). Dispersion plot showing the SR1 global peak amplitude for the EW component, `p1_1`, vs the SR2 global peak amplitude for the EW component, `p2_1` (right). Both charts are calculated for the dates and hours indicated in their titles.

We can observe in these figures a certain correlation between `p1_1` and `p2_1`, but no significant correlation exists between `p1_0` and `p1_1`, `fp2_0` and `fp2_1` or `fp2_1` and `fp3_1`.

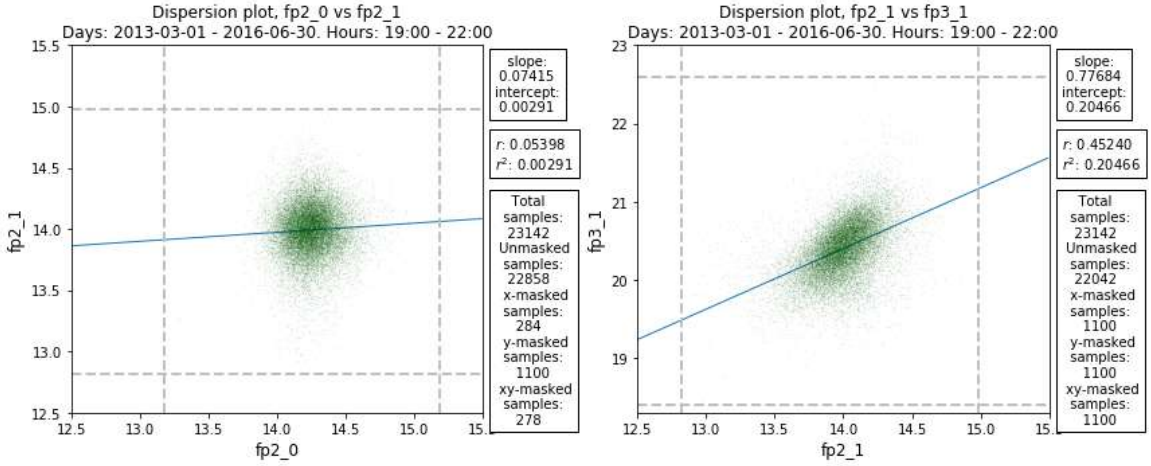

Figure 6.46. Dispersion plot showing the SR2 global peak central frequency for the NS component, `fp2_0`, vs for the EW component, `fp2_1` (left). Dispersion plot showing the SR2 global peak central frequency vs the SR3 global peak central frequency for the EW component, `fp2_1` vs `fp2_1`, (right). Both charts are calculated for the dates and hours indicated in their titles.

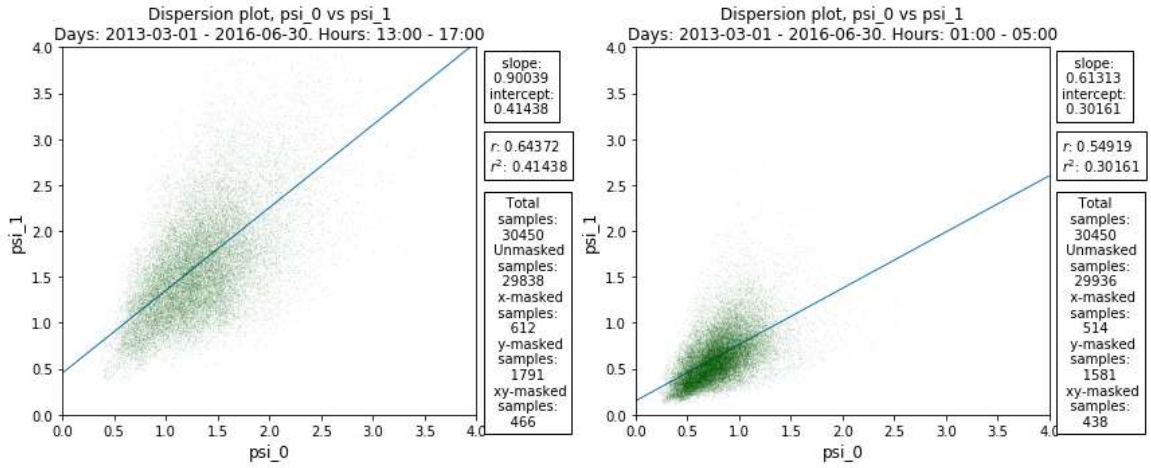

Figure 6.47. Dispersion plot showing the Power Spectrum Integral (PSI) for the NS component vs for the EW component, `psi_0` vs `psi_1`. The dispersion plot is shown taking the data from 13:00 to 17:00 (left) and from 01:00 to 05:00 (right).

6.3.17. Create Table

The notebook `Create_Table.ipynb` does not produce any chart. This notebook makes use of the pandas package, that offers data structures and methods to work with numerical tables and time series. One of these structures is the dataframe, which facilitates to work with data structured in tables. The notebook `Create_Table.ipynb` returns a pandas dataframe with the values of a specified parameter between two specified dates (rows) and two specified hours of the day (columns). We can directly create an Excel (.xlsx) file with these data if the input argument `write` is set to `True`.

It is useful to share data with other stations or with researchers from other fields that do not use a similar format to our `npz` files.

	12:00	12:10	12:20	12:30	12:40	12:50	13:00	13:10	13:20	13:30	13:40	13:50	14:00
2013-03-01	0.341072	0.340802	0.342844	0.359293	0.380690	0.392518	0.380810	0.378440	0.424017	0.406445	0.399662	0.417086	0.404709
2013-03-02	0.358832	0.397688	0.388773	0.417550	0.388762	0.378473	0.388809	0.426351	0.396298	0.404628	0.390804	0.404613	0.440283
2013-03-03	0.325782	0.340115	0.348239	0.344763	0.341806	0.351413	0.327512	0.325793	0.351640	0.344688	0.366558	0.349879	0.333964
2013-03-04	0.258068	0.252272	0.260185	0.273343	0.275916	0.272608	0.276352	0.279453	0.290974	0.286739	0.300703	0.292038	0.300229
2013-03-05	0.326316	0.361208	0.336481	0.322505	0.365191	0.351349	0.355235	0.349934	0.329942	0.369612	0.352615	0.345286	0.350658
2013-03-06	0.337051	0.313765	0.317820	0.316470	0.335189	0.311538	0.308022	0.327567	0.319789	0.327682	0.319891	0.316680	0.346355
2013-03-07	0.465018	0.421256	0.439155	0.439446	0.417513	0.433157	0.410303	0.438809	0.444783	0.445894	0.441257	0.422393	0.436412
2013-03-08	0.360785	0.367371	0.376508	0.399619	0.381951	0.383001	0.402381	0.387982	0.398875	0.382384	0.398836	0.388117	0.387557
2013-03-09	0.385293	0.372322	0.383474	0.390687	0.367453	0.386993	0.392491	0.392298	0.450157	0.404786	0.414447	0.439584	0.425779
2013-03-10	0.345180	0.331550	0.330375	0.354441	0.333909	0.356593	0.389067	0.378365	0.336978	0.354048	0.347771	0.334872	0.340158

Figure 6.48. Pandas dataframe with the values of the SR1 local maximum amplitude for the NS component, `p1_0`, from 1st March to 10th March, 2013, between 12:00 and 14:00.

6.3.18. Summary

The notebook `Summary.ipynb` does not produce any chart. It returns a pandas dataframe with statistical information about the values of a given parameter for each day in an interval between an initial and a final date. That statistical information collected in the table includes, for each day:

- the **mean** value.
- the **standard deviation**.
- the **maximum** value of the parameter in the day.
- the time of the day at which the maximum value is reached.
- the **minimum** value of the parameter in the day.
- the time of the day at which the minimum value is reached.
- the **percentile 25**.
- the **percentile 50**.
- the **percentile 75**.

This function is useful if we are interested in the evolution of any of the statistical parameters above. We can write this information in an Excel (.xlsx) file with these data if the input argument `write` is set to `True`. An example of a pandas dataframe obtained with this notebook is shown in Figure 6.49.

Par	+	Day	Mean	Std	Max Time	Max	Min Time	Min	Perc 25
p1	NS	13-03-01	0.3511091271547885	0.06738725235297859	15:10	0.545367938107174	05:30	0.25389984866255844	0.2878487609664415
		13-03-02	0.357402296806116	0.0398997244259233	15:10	0.4549041649166366	01:00	0.26719637394728457	0.32928036986868836
		13-03-03	0.31598826212193704	0.03084197878353341	11:20	0.3871107933509387	01:10	0.25362955746055516	0.29055741290196707
		13-03-04	0.2922579799013248	0.027454550243272396	05:10	0.4060200034374426	01:10	0.22538783089501263	0.27606944569252145
		13-03-05	0.3034589795735563	0.044557540144917265	14:20	0.3828871478640951	03:30	0.22622338260661928	0.25149768306787157
		13-03-06	0.31148650060994176	0.05050236438392142	21:50	0.4706048406687285	02:50	0.22772749523865632	0.25992351659229573
	EW	13-03-01	0.29639779576591535	0.10475928792119796	15:50	0.5365348590706329	06:00	0.16653593984901754	0.21098510143260385
		13-03-02	0.3087034281983138	0.0729278310070138	15:00	0.47740207038124927	22:00	0.17694463976496394	0.24943670221616712
		13-03-03	0.25167934221076277	0.06712741755262397	13:50	0.40724511491653537	02:10	0.1554549622185025	0.20595386404711574
		13-03-04	0.2342316102438365	0.05950877507605621	14:40	0.36647582345711543	01:10	0.1444392394317228	0.1855186953657345
		13-03-05	0.2887377144069164	0.06699825098420646	15:40	0.42243552660290196	03:30	0.18760117604746185	0.23618486157514867
		13-03-06	0.2242264860175116	0.0630203965055494	16:40	0.34934499515318984	02:10	0.13854614649671812	0.1697599088543325

Figure 6.49. Pandas dataframe that collects the statistical information on the SR1 local maximum amplitude for the NS and the EW components, `p1_0` and `p1_1`, from 1st March to 6th March, 2013, between 01:00 and 22:00. The percentiles 50 and 75 are not shown in the figure due to a lack of space.

Some input arguments of the notebooks above have not been mentioned so far for the sake or brevity. Many of them are common to more than one notebook, and most of them are used to customize the appearance of the charts. All of these input arguments are optional and, if they are not explicitly defined, they will be given a default value. Some the most important ones are mentioned below:

- `masked`: a logical value. If `masked=True`, the data corresponding to the masked intervals will not be taken into consideration for the analysis or for the charts, if `masked=False`, the masked intervals will be taken into consideration for the analysis and for the charts. It is set to `True` by default.
- `leg`: a logical value, if `leg=True` a legend is shown, if `leg=False` it is not shown. It is set to `False` by default.

- `grid`: a logical value, if `grid=True` a grid is shown, if `grid=False` it is not shown. It is set to `True` by default.

- `ax`: a matplotlib.Axes object where we want to plot the chart. If we do not define the axes, the function creates them.

- `ylim`: a list containing two `float` values that sets the lower (`ylim[0]`) and the upper (`ylim[1]`) limits for the y-axis. If `ylim=None`, the limits are set automatically by matplotlib. If `ylim[0]=None` or `ylim[1]=None`, the lower or upper limit, respectively, are automatically set by matplotlib. Examples: `[0,0.8]`, `[0,None]`, `[None,1]`.

- `title`, `xl`, `yl`, `fsize`, `ls`, `lw`, `marker`: these parameters can be used to control the title, the axis labels, and also the fontsize, linestyle, linewidth and markers, when the plot consists in one or several lines.

- `xticks` and `yticks` are used to define the ticks of the plots, also if they have format of time or date; `xtrot` and `ytrot` are used to rotate the axis labels if desired.

- `xticks_format` / `yticks_format`: a `str` value specifying the format to print the labels with a date format. When the axis units are days, it is set to `'%Y-%m-%d'` by default. When the axis units are hours, it is set to `'%H:%M'`. Examples: `'%m-%d'`, `'%m-%d'`, `'%H'`.

- When the plot consists of a color mesh, `cmap` is a `str` value containing a valid matplotlib colormap code to be used for the plot; `cblim` is a list containing the color scale limits (lower and upper); `cbar` is a logical value, if `cbar=True` the colorbars are shown on the right of the plots, and `cbarl` is used to set the color bar label.

- When more than one plot is generated, `same_ylim` and `same_scale` are logical values. If they are equal to `True`, the y-axis limits or the color map scales will be the same in all the plots.

- `save`: if `save=False` the figure created will not be saved, if `save` is a `str` value the figure created will be saved in the directory and with the name specified in `save`, and if `save=True`, it will be saved in the directory specified in the variable `pathgra` with a default name. It is set to `False` by default.

- `save_format`: a `str` specifying the format to save the figure. Depending on the notebook, it is set to `'pdf'` or to `'png'` by default.

Chapter 7. Four Year Study of the Schumann Resonance Regular Variations Using the Sierra Nevada Station Ground-Based Magnetometers

This chapter has been published in the paper:

Four Year Study of the Schumann Resonance Regular Variations Using the Sierra Nevada Station Ground-Based Magnetometers

Authors: **J. Rodríguez-Camacho**[1], A. Salinas[2], M.C. Carrión[1], J. Portí[1], J. Fornieles-Callejón[2], and S. Toledo-Redondo[3] (2022).

[1]Department of Applied Physics, University of Granada, Granada, Spain,
[2]Department of Electromagnetism and Matter Physics, University of Granada, Granada, Spain,
[3]Department of Electromagnetism and Electronics, University of Murcia, Murcia, Spain

Correspondence to: A. Salinas, asalinas@ugr.es

Journal of Geophysical Research: Atmospheres, 127, e2021JD036051.

https://doi.org/10.1029/2021JD036051

Impact factor (JCR 2021): 5.217.
Q1, 22/94 in Meteorology and Atmospheric Sciences.

Key Points:

- Long term analysis of the Schumann resonance (SR) records at Sierra Nevada, from March 2013 to February 2017
- The results obtained partially confirm the general aspects of the long-term evolution of the SRs, but new aspects appear
- Recent results on the influence of the El Niño phenomenon and the solar cycle on the SRs are confirmed

Abstract

We present a study of the Schumann resonance (SR) regular variations (March 2013–February 2017) using the ground-based magnetometers from the Sierra Nevada station, Spain (37^{o}02'N, 3^{o}19'W). The study is based on the fitting parameters obtained by the Lorentzian fit, calculated for each 10-min interval record, namely, peak amplitudes, peak frequencies, width of the resonances, and the power spectrum integral for the first three SR modes. We consider three time-scales in the study: seasonal, monthly, and daily variations. The processed data collected by the Sierra Nevada station are also made public with this work. The general characteristics of the long-term evolution of the SR are confirmed, but discrepancies appear that require further study comparing recent measurements from different stations. Signatures of the influences of the El Niño phenomenon and the solar cycle to SR have been found.

7.1. Introduction

The Schumann resonances (SRs) are related to the propagation of the electromagnetic (EM) field generated mainly by lightning events in the EM cavity delimited by the lower ionosphere and the Earth's surface. This EM field belongs to the extremely low frequency (ELF) band of the EM spectrum, which goes from a few hertz to around 50 Hz, and its spectrum shows resonances at certain frequencies. This phenomenon is called SRs. In addition to the lightning events produced in thunderstorms, there are some other phenomena that may contribute to the SRs, such as the transient luminous events (TLEs) (Price, 2016).

The SR were theoretically predicted by Schumann (1952) and measured for the first time by Balser and Wagner (1960). A historical review of the SRs and of Schumann can be found in Besser (2007), which shows a review of relevant works about the physical and mathematical concerns of the SRs. A wide review of the theoretical basis and the experimental works aimed at the study of SRs, with an emphasis on the ELF band measurement stations, can be found in Nickolaenko and Hayakawa (2002). More recent works about the SRs are Nickolaenko et al. (2016), Price (2016), and Simões et al. (2012). In Simões et al. (2012), the authors point out as "one of the most challenging issues identifying possible correlations between long term SR variability and climate trends." Also, the books by Nickolaenko and Hayakawa (2014) and Surkov and Hayakawa (2014) make up an extensive bibliographical source about the SRs and the ELF field propagation in the atmosphere. The chapter about the SRs written by Sátori, Mustak, and Williams in Betz et al. (2009) is also of great interest.

The research on the SRs had a resurgence at the end of the twentieth century due to its relation to different climate concerns. In Price (2000), the link between lightning, a primary SRs source, and upper tropospheric water vapor is found. The relation between the average temperature in the tropics and the monthly variations in the SR parameters is shown in Williams (1992). This study was strengthened by Füllekrug and Fraser-Smith (1997), which linked the global lightning activity on a seasonal time scale and the magnetic field variations in the lower ELF range. The SRs are a useful tool to study other climatic phenomena that are influenced by the global thunderstorm activity. In Sátori and Zieger (1999), the variation of the global thunderstorm position southwards in warm El Niño years and northwards in cool La Niña years is observed in the self-consistent behavior of the frequency level and semiannual intensity variations of the first three SR modes. In a latter work, the global lightning activity on the El Niño Southern Oscillation (ENSO) time scale is studied using the SRs together with data from optical transient detector (OTD) and lightning imaging sensor (LIS) satellites in space (Sátori et al., 2009). More recently, Williams et al. (2021) have studied the transition between two Super-Niño periods, occurring in 1997/1998 and in 2015/2016, using data from different stations. The main conclusion is that the variations in the intensity of the SRs may serve as a precursor for these extreme climate events (Williams et al., 2021).

The solar cycle has also an impact on the SRs. In Kulak et al. (2003), it is shown that the first resonant frequency increases when the solar activity increases and that there is a small decrease in the attenuation coefficient of the North-South (NS) component of the horizontal magnetic field measured in the East Carpathian Mountains for 6 years—with some gaps in the recordings. In Sátori et al. (2005), data from three different ELF stations are used to confirm a rise in the frequencies and in the quality factors when the solar activity increases, due to an increase in the X-ray radiation. In addition to the previous results, Ondrášková et al. (2011) uses electric field records to find a reduction of the differences between effective thunderstorm areas during the austral and the boreal summer and thus a prevalence of the semi-annual variations during the years of the deep solar minimum. Toledo-Redondo et al. (2012) showed a possible dependence of the effective reflection height of the Earth-ionosphere cavity and the solar cycle. In Nickolaenko et al. (2015), the 11-year solar cycle is analyzed using data from an ELF station in Antarctica and another ELF station located on the North Pole is added in Koloskov et al. (2020). The experimental observations of these works can be explained by the point source model.

The importance of lightning for climate studies is increasingly recognized (Aich et al., 2018; Williams, 2005). The use of the SRs for inferring the global lightning activity achieved a broad interest, see, for example, Nickolaenko and Rabinowicz (1995) and

included bibliography. The relation between the global thunderstorm activity and the diurnal first mode resonant frequency in the vertical electric field component is studied in this work. This connection between the global thunderstorm activity and the SRs also affects the SR amplitudes via annual and semi-annual variations (Nickolaenko et al., 1999; Nickolaenko et al., 1998). A similar analysis can be found in Füllekrug and Fraser-Smith (1997), where the profiling of the global thunderstorm activity is made on a seasonal timescale. Another verification of the relation between the SR intensity and the global surface temperature can be found in Sekiguchi et al. (2006), where the annual and semi-annual variations are also studied using principal component analysis (PCA). In Belyaev et al. (1999), the thunderstorms are determined making use of the Poynting vector, obtained with the horizontal components of the magnetic field and the vertical component of the electric field. Some advantages of the use of the Poynting vector are noted in this paper, especially when records from only one station are used. This work finds a night-time peak in African thunderstorm activity.

The thunderstorm activity on the Earth occurs mainly in three regions, located at different longitudes, with a predominance of land areas. These zones are located in Central Africa and Madagascar (African chimney), South and Central America, Caribbean Basin (American chimney), and South-East Asia and Indonesia (Asian chimney), as shown by Christian et al. (2003). These locations have their peak of activity during the local afternoon and they largely modulate the diurnal variations of the SR (Toledo-Redondo et al., 2010).

First studies of the long-term observations of SR can be found in Sátori (1996) and Sátori (1996) with data from the ELF station at the Nagycenk Observatory (47.6°N, 16,7°E), Hungary. These works analyze the SR peak frequencies and amplitudes for the first three modes for 2 years. In Nickolaenko et al. (1998), records for an extra year are added to the previous works and the daily frequency range variations are explored. The seasonal variations of the average daily frequency pattern are also analyzed. A study of the long-term (4 years) diurnal, seasonal and inter-annual variations in the SR parameters can be found in Price and Melkinov (2004). The data are obtained from the ELF station (35.45°E, 30.35°N) near the town of Mitzpe Ramon, in the Negev desert, Israel. The influence of the solar terminator passages on the SR parameters in these records is addressed in Melnikov et al. (2004). In Ondrášková et al. (2007), a summary of more than 4 years of continuous SR monitoring of the vertical electric component at Modra Observatory (48.37°N 17.27°E) in Slovakia is presented. The monthly averaged diurnal variations of the four firsts modes are analyzed. In addition, the diurnal-seasonal variations of the amplitudes, frequencies and quality factors for each year are also studied. The overall pattern of diurnal and seasonal variations in SR frequencies is confirmed from measurements as reported from

other observatory sites. Yatsevich et al. (2005) present results from the Lehta station (65°N, 34°E) in Russia from August 1999 to March 2005. In Ouyang et al. (2015) and Zhou et al. (2013), 2 year long records from some low latitude ELF stations in China are examined. The diurnal and seasonal variations in mode amplitudes and frequencies of the first four modes of SR magnetic components are presented.

In this work, the SR regular variations obtained from the ELF station at Sierra Nevada, Spain (Fornieles-Callejón et al., 2015), are analyzed from March 2013 to February 2017. This ELF station records both horizontal magnetic field components, NS and East-West (EW) oriented. The processing of the records is described in Rodríguez-Camacho et al. (2018). With this work, the scientific community is granted access to the processed data from the Sierra Nevada ELF station records. The format of these data is also described in Rodríguez-Camacho et al. (2018). We consider that providing the data is needed to pursue a common goal set by the SR research community and, in general, by the atmospheric electrodynamics research community, which is the creation of a shared database of the different worldwide ELF stations. The 4-year study presented in this paper is intended to carry out an analysis of most the common aspects concerning SR regular variations and comparing these signatures with the results reported by other authors. To the authors knowledge, there is no published study of regular variations of SR corresponding to the years considered in this work. This is especially important for a phenomenon like this, which is extremely difficult to measure and which, in addition, cannot be artificially reproduced in a laboratory. It is also worth noting that the results of the study are also intended to validate the SR measurements that we provide with this work, which is an important point when data are shared with the research community. Finally, it is our opinion that the study presented may help in the use of these data by other authors at the initial stages.

The data used in the analysis presented in this work is the output of the processing scheme applied on the raw data. A brief explanation of this scheme is found in Rodríguez-Camacho et al. (2018). Basically, each file corresponds to the amplitude spectrum of each 10 min interval and the corresponding Lorentzian fitting parameters for each month in the measurement period of the Sierra Nevada ELF station.

This paper is structured as follows: the features and structure of the Sierra Nevada ELF station records are described in Section 7.2; the diurnal variations of the different SR parameters are studied in Section 7.3: the seasonal variations are addressed in Section 7.3.1, and the annual variations extracted from monthly averages are considered in Section 7.3.2. The time evolution of the SR parameters averaging over a

certain number of days, weeks or months is shown in Section 7.4. Lastly, Section 7.5 corresponds to the conclusions of this work.

7.2. The Sierra Nevada ELF Station Records

The ELF station is located in the heart of the Sierra Nevada mountains, Granada, Spain, 2,500 m above sea level, in the area surrounding the mountain hut "Refugio del Poqueira" (37^{o}02'N, 3^{o}19'W) (Fornieles-Callejón et al., 2015). The ELF station at Sierra Nevada is equipped with two magnetometers, NS and EW oriented. The signal detected by these magnetometers is amplified, digitized, and registered directly in the time domain. The station is provided with a data acquisition system with a sampling frequency of 256 Hz. The frequency response of the magnetometers ranges from a few tenths of a hertz to 45 Hz. Frequencies from 6 to 25 Hz have been calibrated, thus including the first three SR modes, located around 8, 14, and 21 Hz, which are the target of the Sierra Nevada ELF station. The analog-to-digital converter uses 16 bits to digitize samples in the range ±10 V. The system minimum resolution is therefore 10/215 = 3.052E^{-4} V. Saturation limits are fixed at ±9.990 V.

The time domain data are processed using 10-min-long windows. For each window, the average of the amplitude spectra obtained using FFT in 10-s-long intervals is calculated using the Hann window and a 5-s overlap (Welch method). A Lorentzian curve, obtained as a combination of three Lorentzian functions and a straight line, is fitted to the amplitude spectrum between the frequencies 6.35 and 23.75 Hz, named in this paper as the fitting band. It is worth noting that the fitting is applied to the amplitude spectrum as in Price and Melkinov (2004). It is also common the use of the intensity spectrum, instead. This fact must be taken into account when comparing different results, especially with regards to the width of each resonance. For further details of this method, see Rodríguez-Camacho et al. (2018).

As final result of the process, a file containing the following data is generated for each month and sensor, which is generated by Numpy, a Python-based package (http://www.numpy.org):

1. Saturation level (ratio of saturated 10 s long segments for each 10 min interval).
2. Amplitude spectrum for each 10 min interval.
3. Amplitude spectrum of the fitted signal (the fitting curve).
4. Calibrated and fitting frequencies.

5. Fitting parameters.

6. UTC hour for the beginning of each 10 min interval.

The format is that generated by Numpy, a Python-based package (http://www.numpy.org).

Concerning the Lorentzian fitting function, as explained in Rodríguez-Camacho et al. (2018), there are 11 fitting parameters: three individual mode amplitudes, three resonant frequencies, three Full Widths at Half Maximum (FWHMs), and two parameters corresponding to a linear correcting part (the slope and the intercept). Once this fitting curve has been obtained, we get the maximum amplitudes, P_i, and the frequencies at which these maximum values appear, f_i, for the ith mode ($i = 1, 2, 3$). These quantities will be referred to as peak amplitudes and peak frequencies, respectively, and will be used for the long-term analysis as they best describe the global behavior of the SRs. The power spectrum integral (PSI), over the fitting bandwidth (6.35–23.75 Hz), of the magnetic field recorded in each sensor has also been included as a parameter for the study.

As commented above, the study of the regular variations of the SRs is based on the fitting parameters obtained by the Lorentzian fit, calculated for each 10-min interval records. For some intervals, the parameter values are unacceptable. This can be due to different reasons (strong lightning activity near the station, bad performance of the Lorentzian fitting algorithm, etc.). For this reason, a mask is used to discard the 10-min intervals for which the values of the peak amplitudes or the peak frequencies are unacceptable. The chosen acceptable values for the peak amplitudes and for the peak frequencies are shown in Table 7.1.

Table 7.1
Lowest and Highest Chosen Acceptable Values for the Peak Amplitudes (P_1, P_2, P_3) and the Peak Frequencies (f_1, f_2, f_3) for the Three First Modes and for Each Sensor

	P_1 (pT/sqrt (Hz))		f_1 (Hz)		P_2 (pT/sqrt (Hz))		f_2 (Hz)		P_3 (pT/sqrt (Hz))		f_3 (Hz)	
	NS	EW	NS	EW	NS	EW	NS	EW	NS	EW	NS	EW
Lower limit	0.13	0.10	6.80	6.70	0.10	0.08	13.18	12.82	0.08	0.08	19.15	18.40
Upper limit	0.80	0.80	8.35	8.22	0.80	0.80	15.19	14.98	0.80	0.80	21.98	22.60

In order to have a global picture of the data recorded by the Sierra Nevada ELF station, the PSI is shown in Figure 7.1 for both sensors. The days are represented in the horizontal axis and the 10 min intervals of the day are represented in the vertical axis. The PSI values are shown using the colormap on the right side of the chart. The dashed white line indicates the dusk and dawn times. Vertical white lines correspond to missing data.

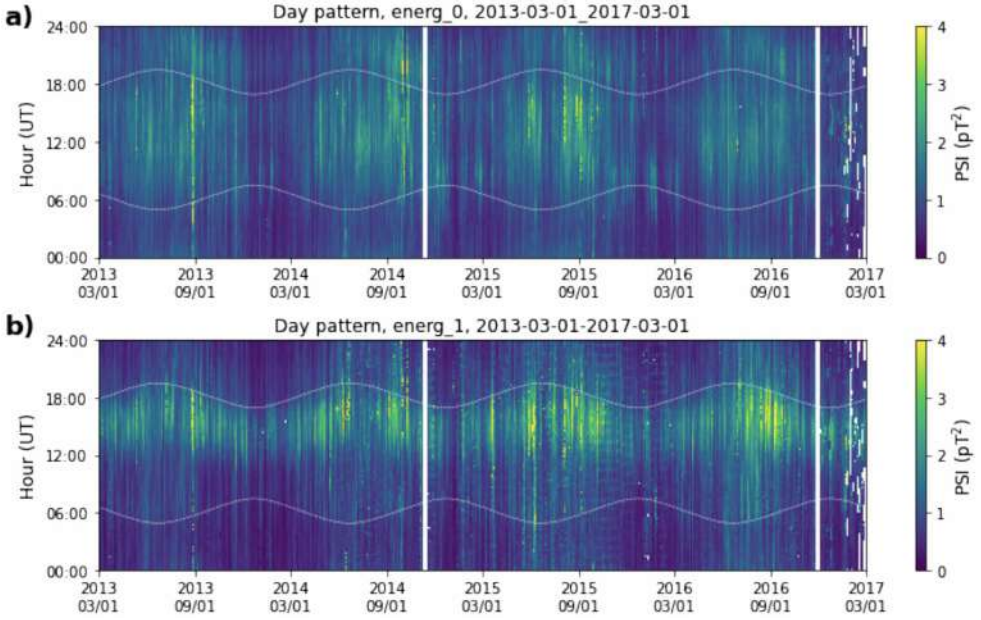

Figure 7.1. Power spectrum integral (PSI) for the recordings at Sierra Nevada extremely low frequency station, from March 2013 to February 2017. The upper chart corresponds to the North-South magnetometer and the lower one to the East-West magnetometer.

7.3. Diurnal Variations

7.3.1. Diurnal Variations for Seasonal Periods

The peak amplitudes of each horizontal magnetic field component are shown in Figure 7.2 for each mode through a day (diurnal variations), averaged within each one of the four astronomical seasons for the period of four years (from March 2013 to February 2017). A comparison of the amplitude of each magnetic field component in Figure 7.2 with those presented in Zhou et al. (2013) from ELF stations located in China shows that latter amplitudes are higher due the proximity of the Maritime Continent (MC) thunderstorms to the Chinese stations. The amplitudes obtained in Sierra Nevada station oscillate between 0.20 and 0.45 pT/sqrt (Hz) whereas in Zhou et al. (2013), they oscillate between 0.4 and 1.2 pT/sqrt (Hz). The different thunderstorm chimneys and their impact on each component of the horizontal magnetic field can be clearly noted. It can be seen that the African thunderstorms are dominant about 1500 UT in the EW component, whereas the thunderstorms in the MC and America are detected in the NS magnetometer with intensity peaks at 1030 and 2000 UT, respectively, although the exact maximum time varies with the season. This general form of the amplitudes for the first mode can be justified by the two-source model that considers a localized storm center which moves following a circle near or defined by the equator and surrounding the entire Earth during the day and another permanent center distributed throughout the line described by the first source. The moving

source defines the maximum and minimum hours in the amplitudes while the second source provides an average amplitude level that brings the signal generated by the first source closer to that experimentally observed (Yatsevich et al., 2008; Yatsevich et al., 2005).

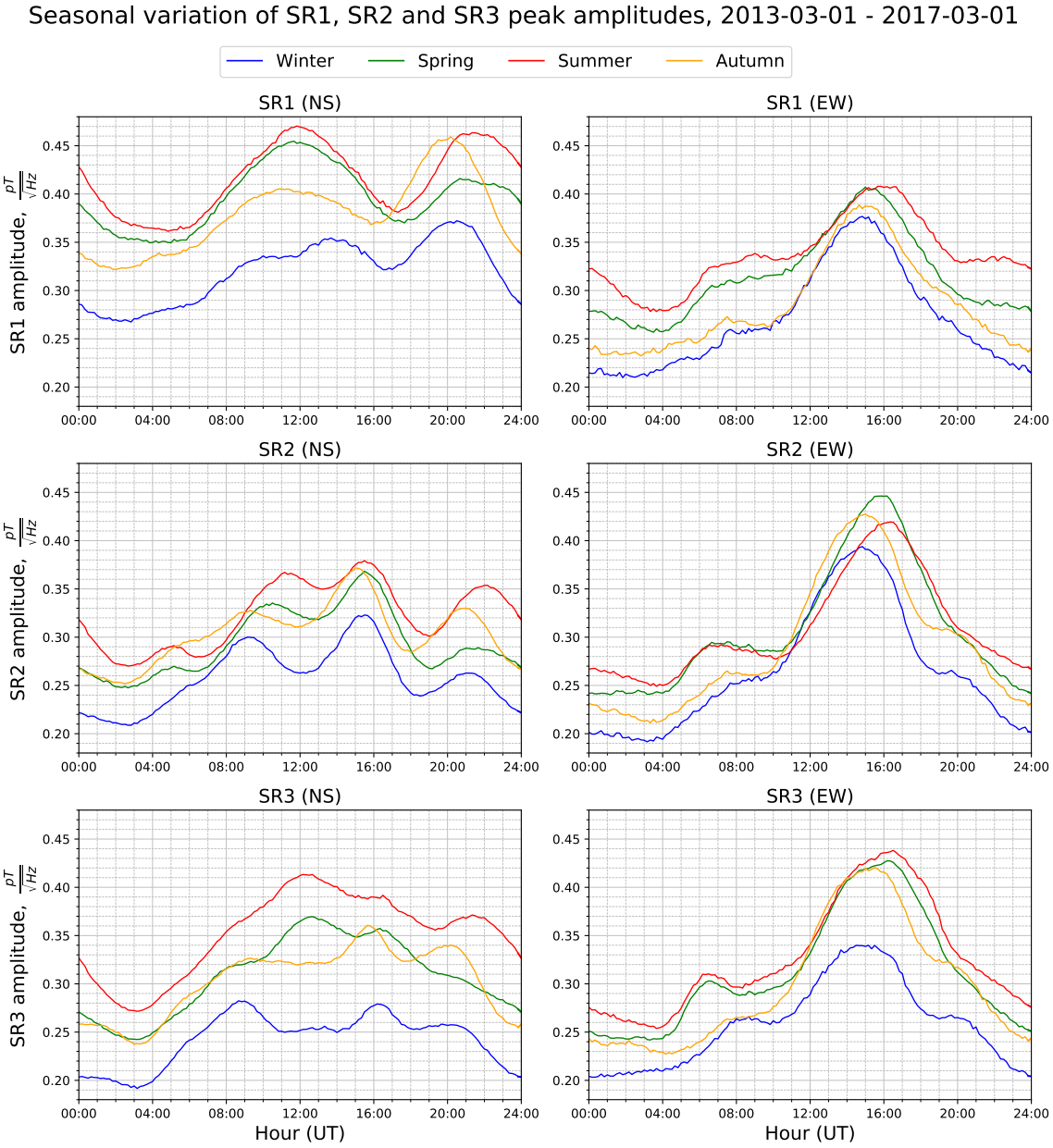

Figure 7.2. Diurnal variations of the peak amplitudes for the three first modes (SR1, SR2, and SR3), in the different seasons over the recording period (2013–2017). The left column corresponds to the North-South magnetometer and the right one to the East-West (EW) magnetometer. Each row corresponds to a different mode (SR1, SR2, and SR3).

In the NS component the MC activity starts rising at 0400 UT and hits a maximum about 1030 UT for the first mode. This maximum amplitude recorded at Sierra Nevada in this sensor may be due to the superposition of the MC thunderstorms and other thunderstorms that would be located at an intermediate distance, like India. In Yatsevich et al. (2008), the peak amplitude for this storm center is between 0800 UT

and 1000 UT. Other authors, like Price and Melkinov (2004) and Zhou et al. (2013), report that the maximum amplitude for the first mode about 0800 UT corresponds to the MC thunderstorms but this peak does not appear in the Sierra Nevada data. The reason for this may be due to the effect of the proximity of the Australian and the MC to the antipode point relative to the Sierra Nevada ELF station location or a shift in storm activity to regions closer to the Sierra Nevada station, such as India. For this chimney, the amplitude is dominant in summer, followed by spring, autumn and far below during winter. This situation also occurs for the American thunderstorms, but this chimney shows more activity in autumn than in spring. The time at which this American peak happens has a strong seasonal dependence. The smallest intensity for this chimney is observed in winter, though it is the most active thunderstorm center in winter and for the first mode during the whole day. In addition, throughout the day, a drop in the amplitude of the second and third modes is observed with regard to the first mode, and the second and third modes are very sensitive to the African thunderstorms (between 1500 and 1600 UT). The complicated patterns observed in SR2 (NS) and SR3 (NS) could be explained by the random variation between the source-observer distance (SOD).

For the EW component, which is more sensitive to the African thunderstorms, the amplitude and shape are similar in the three modes. An amplitude peak is observed in the three modes about 1500 UT and it has a stronger activity in summer for the first and the third modes, whereas the second mode is higher in spring. A change in the time of this maximum is observed when the seasons change. It goes from 1600 to 1500 UT from summer, spring, autumn, and winter, and its amplitude also decreases in this order (except in the second mode, for which summer and spring exchange maximum amplitudes as previously noted). This peak in summer, due to the African thunderstorms, cannot be justified by the lightning observations in Blakeslee et al. (2014), where the African thunderstorms have a minimum activity in summer. This discrepancy could be due to the different years used for observation in both studies or also considering the storms of Europe and West Asia (Yatsevich et al., 2008). The EW magnetometer also collects a minor peak about 0600 UT, observed mainly in summer and spring, which could be connected to the nighttime thunderstorms in Africa (Belyaev et al., 1999). This nighttime peak is also present in Price and Melkinov (2004) and (Yatsevich et al., 2008).

The diurnal variations of the peak frequencies (the local maximum frequencies) for the first three modes, seasonally averaged, are shown in Figure 7.3. These variations of the peak frequencies are linked to the source-observer geometry (e.g., Nickolaenko and Hayakawa 2002; or Toledo-Redondo et al. 2016; Toledo-Redondo et al. 2010). Considering a “Hot Spot” or localized source model, described in Nickolaenko and

Hayakawa (2014), the peak frequency of the magnetic field for the first mode should have a minimum when the source is closest to the observer and a maximum when the source is farthest from the observer. However, as we will see below, this is only roughly observed for the NS sensor. For both sensors, the minimum and maximum frequencies observed greatly depend on the mode, the hour of the day and the temporal definitions of the seasons themselves, as it will be shown below. In the Sierra Nevada records, unlike in other ELF stations (Price & Melkinov, 2004; Zhou et al., 2013), there is not a strong seasonal dependence of the diurnal frequency variation. A transition from "winter-type" to "summer-type" diurnal frequency variation is not observed. As noted in (Price & Melkinov, 2004; Yatsevich et al., 2008) an attempt to explain these frequency variations should be done in the future using a theoretical model for a better agreement between the model and the experiment.

The analysis of the peak frequency diurnal variations shows a different behavior for the NS and EW components. For the NS component, the number of maxima and minima observed increases by two for each mode, starting from two maxima and two minima for the first mode. The first mode frequency is highest about 0800 UT and 2000 UT, and lowest about 0300 UT and 1500–1600 UT. This location of maximum and minimum corresponds approximately to that expected according to the SOD with the sources located in Asia and America and it is similar to the one detected by the Letha station presented in Yatsevich et al. (2008). These maxima and minima are also observed in the second mode at the same times, together with two more maxima about 0100 UT and 1200 UT and two more minima about 1000 UT and 2300 UT. In the second mode, more evident distinctions appear among the different seasons, but the general pattern is still conserved. However, for the third mode, there is a clear distinction between the spring-summer seasons and the autumn-winter seasons. It is remarkable that the third mode frequency is highest about 1400 UT in spring-summer while it shows a relative minimum in winter at the same hour. This increase in the number of maxima and minima is also observed in Price and Melkinov (2004).

For the EW component the diurnal peak frequency variation for the three modes reflects a rather similar pattern, with a remarkable maximum value. The highest frequency appears at 1200 UT, 1300 UT, and 1400 UT, respectively, for each mode in all seasons. Also, a relative maximum is seen around 0000 UT that, for the first mode, is highest in summer and it is smaller, in a decreasing order, in spring, autumn and winter. For the second and third modes, the order is reversed. Minimum frequencies appear about 0600–0700 UT and 1800 UT for the second and the third modes, while for the first mode there is a clear minimum that occurs about 1700 UT in spring-summer and about 2000 and 2100 UT in autumn and winter, respectively. For this sensor, a minimum should be obtained when storms in Africa are most active.

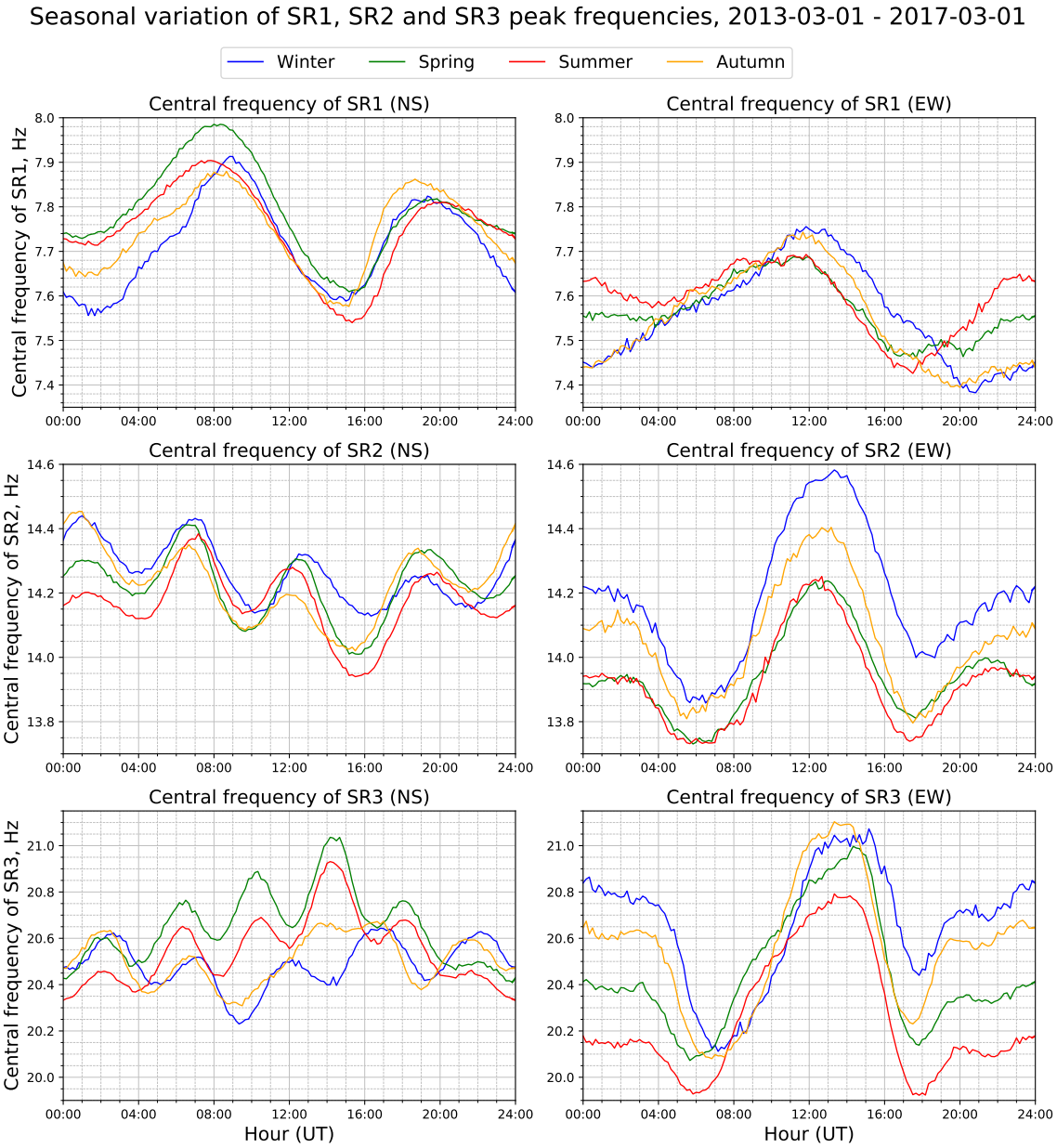

Figure 7.3. Diurnal variations of the peak frequencies for the three first modes, in the different seasons over the recording period (2013–2017). The left column corresponds to the North-South magnetometer and the right one to the East-West magnetometer. Each row corresponds to a different mode (SR1, SR2, and SR3).

However, we can see that this peak is displaced and also this displacement increases with the autumn and winter seasons.

Regarding the widths of the resonances, they show a more fluctuating behavior than the other parameters. In Figure 7.4, it can be observed that these fluctuations do not depend much on the season and they are similar for both the NS and EW components. The widths are higher for the EW sensor than for the NS sensor for all the modes. It is lowest in the second mode. For the third mode, during winter, several peaks

are observed in the width for the EW sensor: it shows values around or higher than 7 Hz, whereas it shows values between 3 and 3.5 Hz in the other seasons.

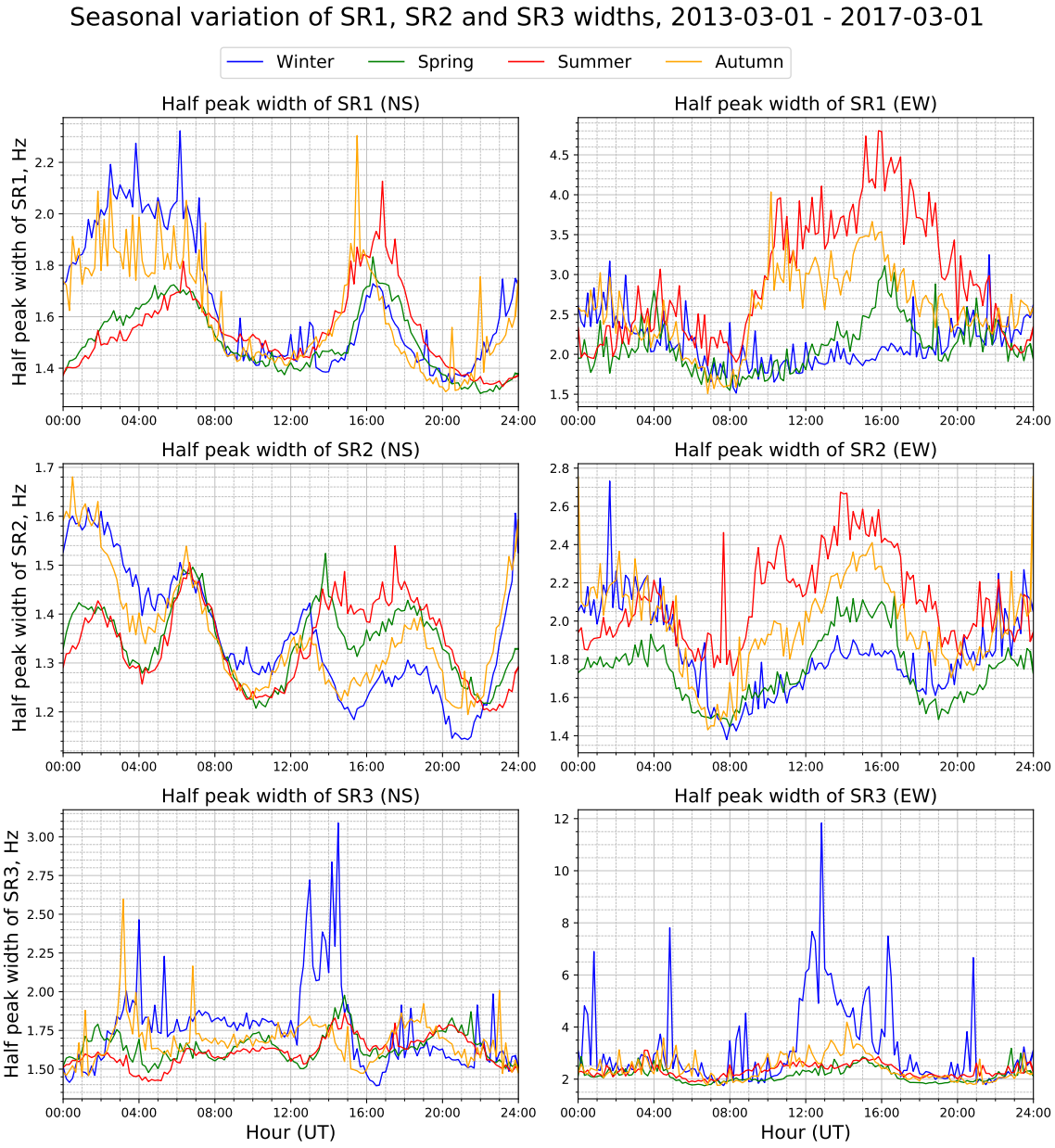

Figure 7.4. Diurnal variations of the Full Widths at Half Maximum of the resonances for the three first modes, in the different seasons over the recording period (2013–2017). The left column corresponds to the NS magnetometer and the right one to the East-West magnetometer. Each row corresponds to a different mode (SR1, SR2, and SR3).

An analysis of the PSI is shown in Figure 7.5 for the different seasons. This parameter is sensitive (in a nonlinear way) to the contributions of the three modes, thus it can be a good indicator to be compared to the direct lightning observations from satellites, like that presented in Blakeslee et al. (2014). As in previous results, we can observe in sensor NS the activation of the thunderstorms in North America in the summer and autumn and in South America in winter around 2100 UT; with respect to the Asian thunderstorms (mainly observed in the NS sensor), they are maximum in summer

and spring, and we can also see the activation of Australian thunderstorms in winter around 0800 UT. There are, though, some differences between the observations via satellite and those obtained from the SRs: the peak detected in the EW sensor around 0500 UT in the summer and spring (which possibly comes from African thunderstorms, as it has been commented previously) does not appear in Blakeslee et al. (2014); in the EW sensor, the African thunderstorms cause a maximum around 1600 UT in the (boreal) summer, whereas in Blakeslee et al. (2014), they show a minimum activity in the (boreal) summer. Figure 7.5 is similar to Figure 7.6a and 7.6b of Price and Melnikov et al. (2004). The latter represents the sum of the amplitudes of each of the first three modes and presents diurnal variations with averages for each year.

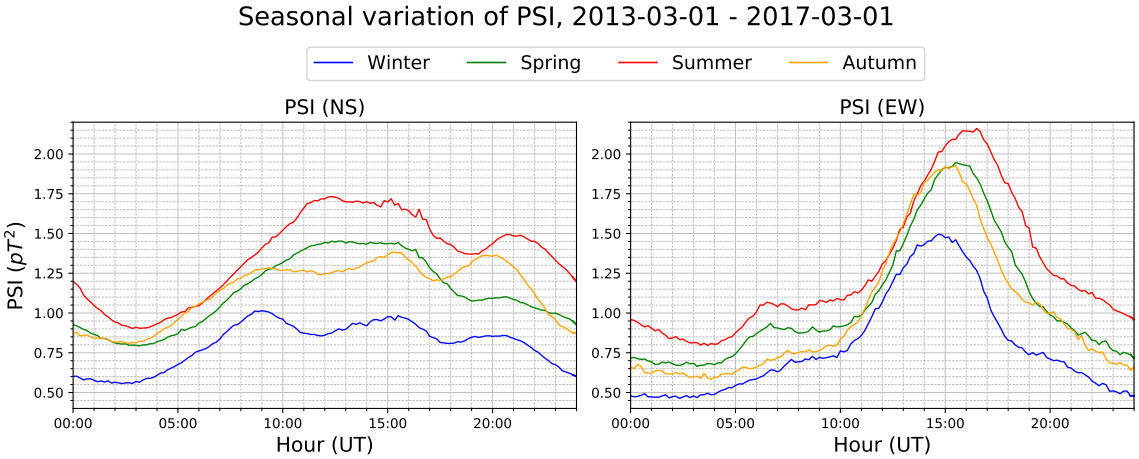

Figure 7.5. Diurnal variations of the power spectrum integral for the different seasons over the recording period (2013–2017), in the frequency range 6.35–23.75 Hz. The left chart corresponds to the North-South magnetometer and the right one to the East-West magnetometer.

The concept of EM seasons was introduced by Sátori (2003) and Sátori et al. (2003) and a definition based on SR measurements and a numerical model is made in Nickolaenko et al. (2015). The summer is set to last from June to September, the winter is set to last from February until March, and the rest of months belong to the spring or to the autumn. The diurnal variations seasonally averaged, taking into account the setting of the seasons made by Nickolaenko et al. (2015), are shown in Figure 7.6 for the PSI parameter. It is interesting to compare the diurnal variations of the different parameters for both sets of seasons, the astronomical seasons in Figure 7.5 to the electromagnetic seasons in Figure 7.6. It can be noted that the seasonally averaged diurnal variations are in phase for the different seasons, that is, the maxima and minima appear at the same UT hour for all seasons. A clear difference between EM summer and the other EM seasons is also clearly shown.

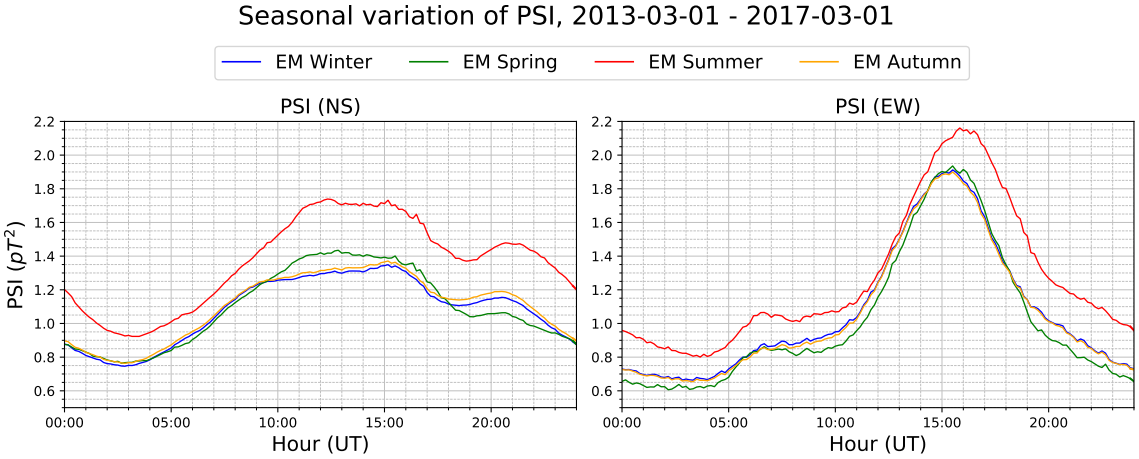

Figure 7.6. Diurnal variations of the power spectrum integral for the different electromagnetic seasons over the recording period (2013–2017). The left chart corresponds to the North-South magnetometer and the right one to the East-West magnetometer.

7.3.2. Annual Diurnal Variations

Another interesting indicator is the study of the diurnal variations of a parameter for a specific month for different years. The diurnal variations for the months of September, December, and February are shown in Figure 7.7 over several years for which the recordings at the Sierra Nevada station are available. The parameter plotted is the first mode peak amplitude for each one of the horizontal components. This figure is similar to (c)–(e) in Figure 3 in Williams et al. (2021). More precisely, Figure 7.7 is similar to the plot of the data from the Eskdalemuir station, located in a similar latitude to the Sierra Nevada station, with the only difference that the amplitude in the EW component was slightly higher in February 2016, than in 2014. These results confirm the conclusions on an intensification of the SRs during the transition months that precede the super El Niño episode that happened at the end of 2015 and the beginning of 2016. We can note an intensification of the, SRs in September 2014, with a maximum intensification from December 2014 to February 2015. We can also confirm a decrease in the thunderstorm activity in the declining phase of the phenomenon in February 2016, though in Sierra Nevada this decrease is lower in the EW sensor than that observed in the Eskadalemuir station (Williams et al., 2021).

Another interesting result is related to the PSI. The NS component is shown in Figure 7.8, where two different patterns can be noted. One of them corresponds to autumn-winter, where the three main thunderstorm centers are observed, with a predominance of the MC center in winter and American center in autumn. The other pattern corresponds to the summer behavior, where the African thunderstorms are dominant. However, in Figure 7.9 showing the PSI for the EW component—the most

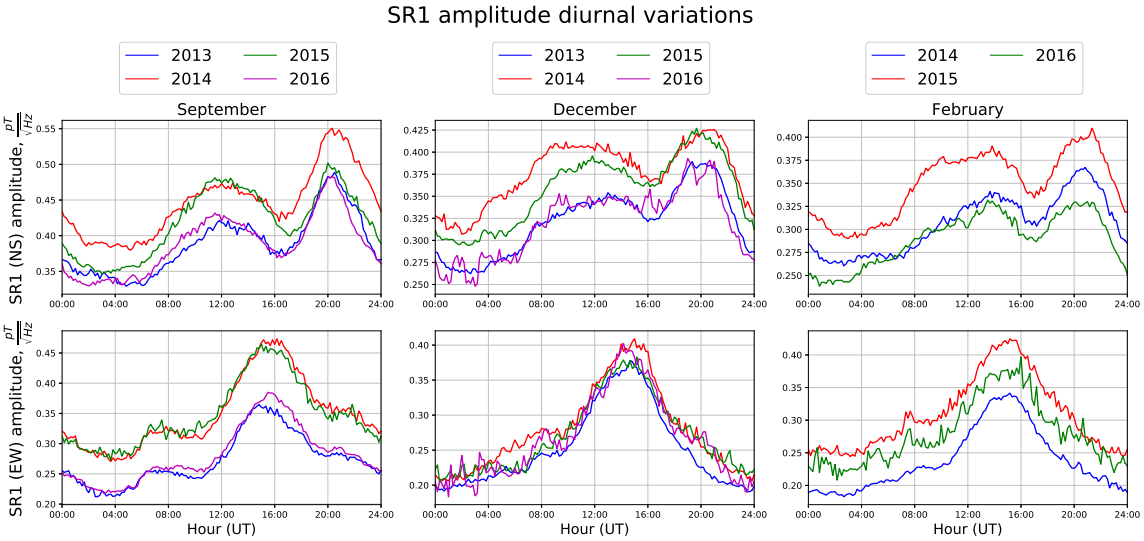

Figure 7.7. First mode peak amplitude annual diurnal variations for each one of the horizontal components for the months of September, December, and February, for several years.

sensitive to Africa—and over the different years of recording, the pattern repeats for all the months with only a slight reduction in the maximum during winter months, especially in December and January.

It can be noted in Figures 7.8 and 7.9 that the differences among the years persist throughout the whole day, that is, when a parameter is higher than usual for a certain year, it is higher for every time of the day. This feature is observed in all the parameters analyzed, even those not shown in these figures. This could indicate that there is some mechanism that affects SR on a global scale.

7.4. Daily Variations

After studying the diurnal variations, the daily evolution of the parameters over time will be addressed. In contrast to the diurnal variations, which provide average information on specific moment of the day, as regards the daily variations, we obtain a unique average value for each day and this value is again averaged over a larger time span, which will range from 1 to 6 months in our study. In practice, it is a mean value for the quantity during this larger period, disregarding hourly details. In all the cases presented below, the daily variation of this average is shown for the 4 years for which the records are available.

The PSI for both NS and EW sensors, averaged every 30 days, is shown in Figure 10. Three clear periods can be observed. The first one goes from 2013 to the beginning of 2015, where the NS component amplitude exceeds the EW one. The second

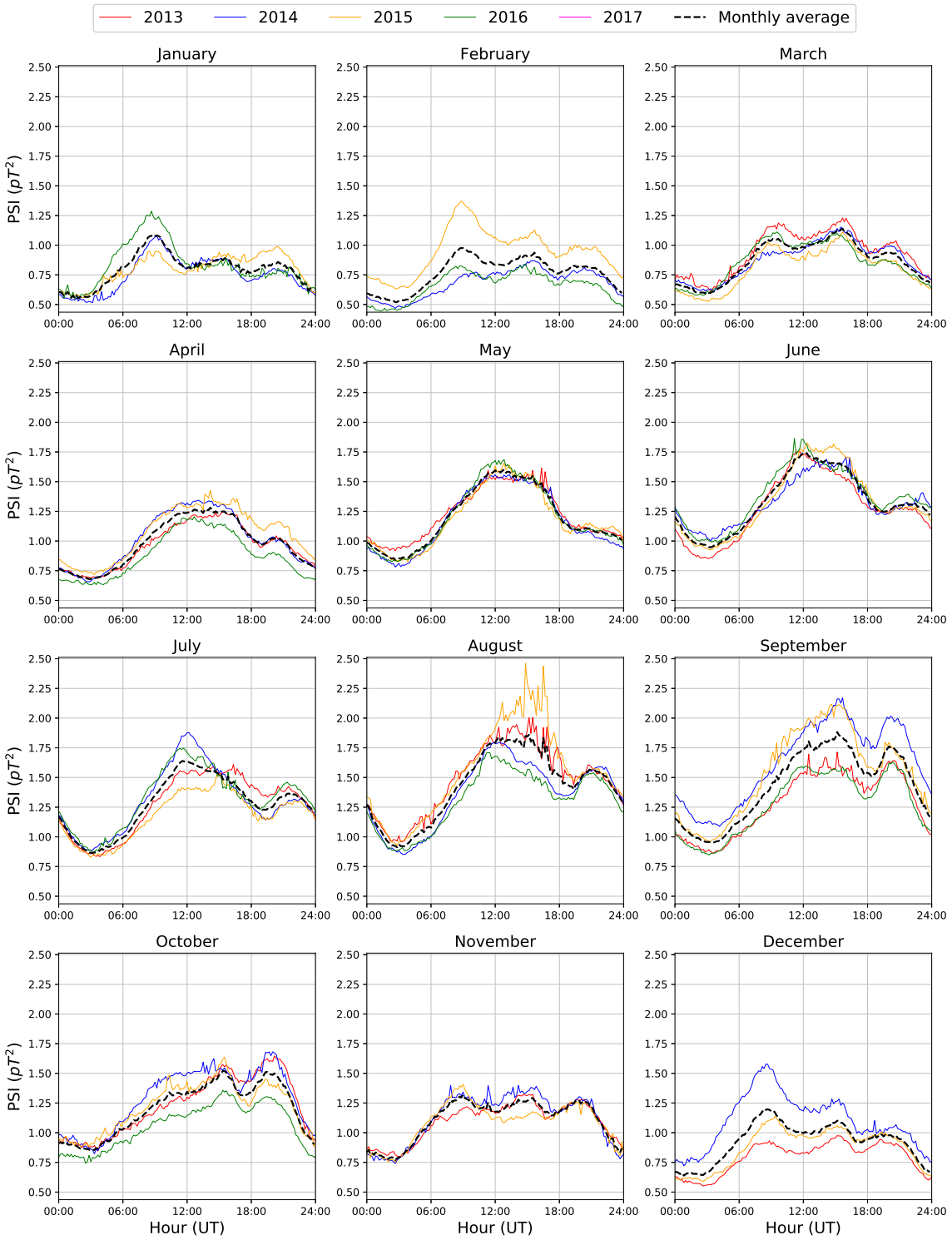

Figure 7.8. Monthly averaged diurnal variations of the power spectrum integral during the whole recording period of the station for the North-South sensors.

period extends over almost the whole 2015, where both components have the same amplitude. The third period begins in 2016 for which the EW amplitude exceeds the NS one. It is difficult to determine which thunderstorms centers are most active from

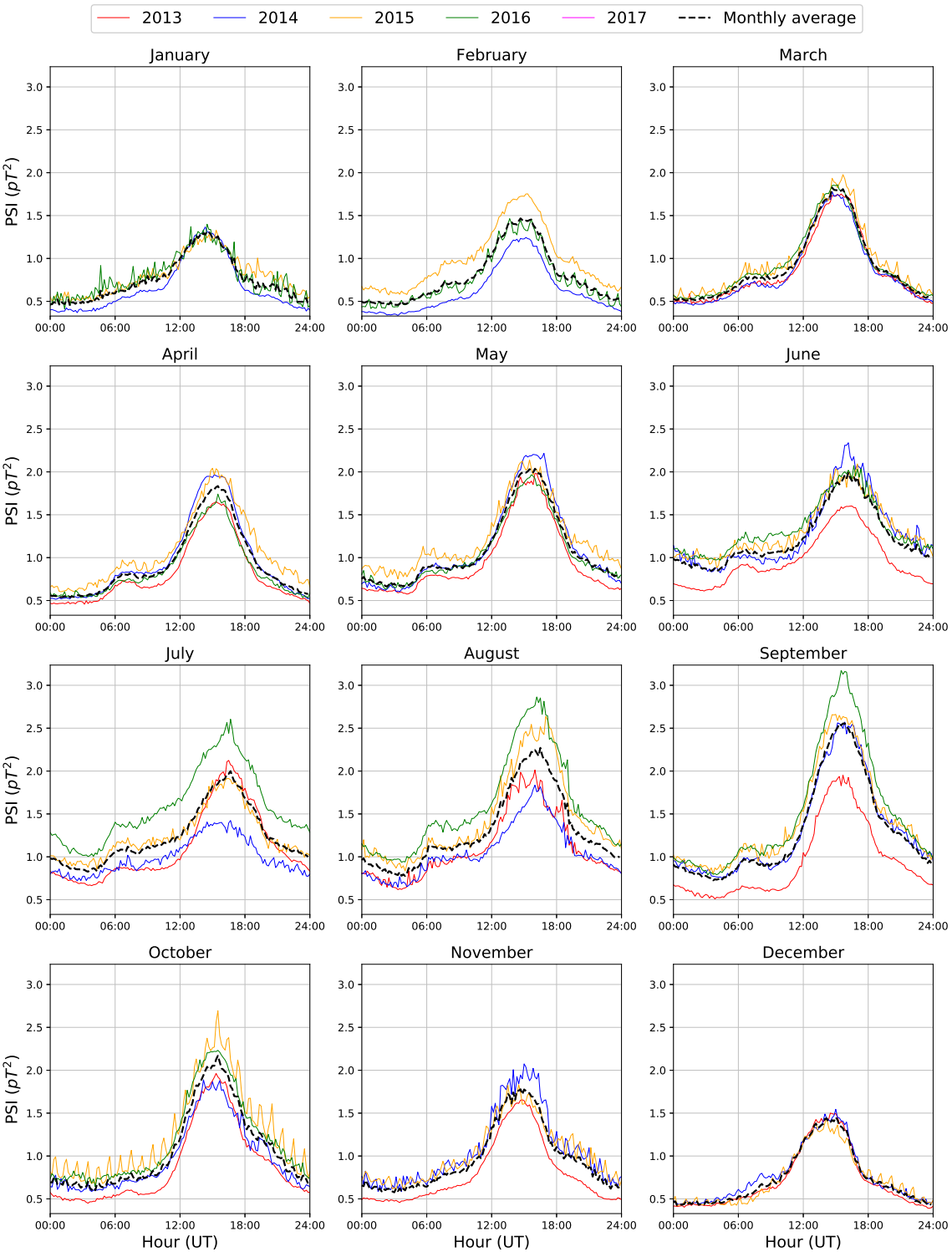

Figure 7.9. Monthly averaged diurnal variations of the power spectrum integral during the whole recording period of the station for the East-West sensors.

the PSI observations, since the contribution of the different modes varies with each center due to the source-observer distance. But it is clear that from the end of 2014 to the beginning of 2016 there was a transition period in which the source of the SRs

changed. This change may be related to a transition year from the Niña period to the Super El Niño phenomenon of 2015/2016 reported in Williams et al. (2021).

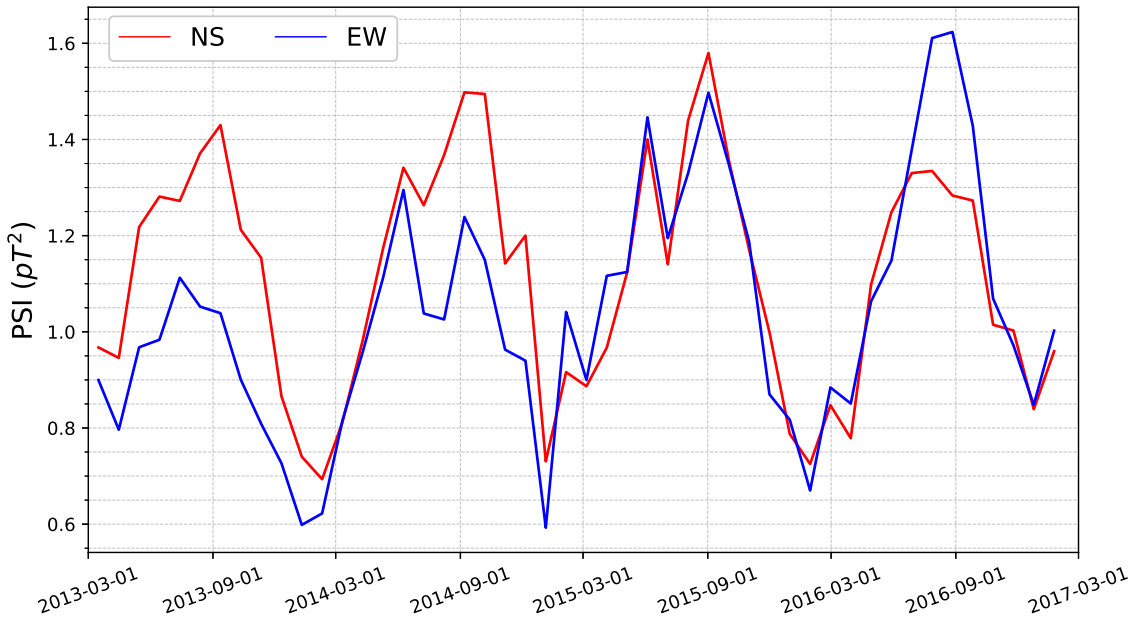

Figure 7.10. Power spectrum integral averaged every 30 days, for both North-South (red) and East-West (blue) components.

Another aspect to point out in Figure 7.10 is the increase in the maximum and minimum values of the PSI in both sensors that occurs during the 4 years of measurements. This fact could be related to global warming (Williams et al., 2019). However, as a preliminary step to this study, it would be necessary to confirm the trend of the PSI measured at Sierra Nevada with data from other stations. It is a pending work for the future, once a joint database of different ELF stations is available.

In Koloskov et al. (2020) the inter annual variations of the first mode resonant frequency is correlated to the 11-year cycle solar activity, during a period of large solar activity (2011–2017), which had a rise in 2014. The mode peak frequency variations are shown in Figure 7.11 for the three modes, semi-annually averaged. It can be seen that the variations and the evolution for the first mode, upper row of Figure 7.11, is very similar to that in Figure 1c in Koloskov et al. (2020).

Regarding the peak frequencies for the second and third modes it can be noted, in the semi-annually averaged data, that the frequencies also tend to decrease during the years except for the sensor EW in the third mode, when a notable rise occurs in 2016, but it is soon followed by a new decreasing trend. In these modes, in particular for the EW sensor, a steady semi-annual periodicity is observed in the maxima and the minima of the peak frequency.

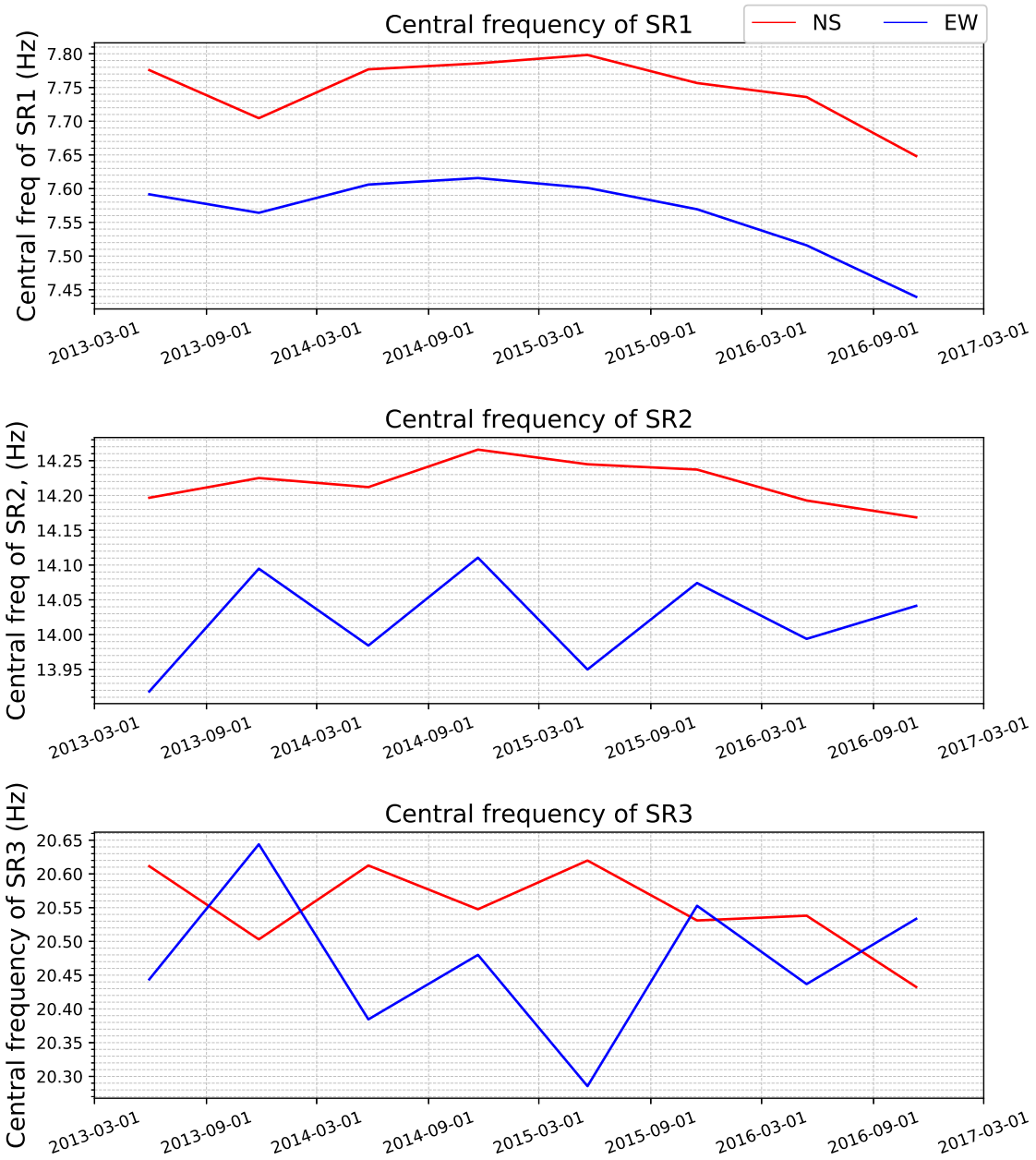

Figure 7.11. Peak frequency daily variations averaged for a 180-day time span for both North-South (red) and East-West (blue) sensors. Each row corresponds to a mode, from the first to the third, respectively.

Another relevant concern about the time evolution of the different parameters is the diurnal variation of the minimum to maximum range of peak amplitudes and peak frequencies, Figures 7.12 and 7.13, respectively. We can see that, for a 30 days average, the variations that show all the parameters in all the modes are higher for the EW sensor than for the NS sensor. In the EW sensor, we can clearly see an increase in the variations of the peak frequency of the second mode in the year 2015. It can also be noted that no annual variations are observed in any parameter.

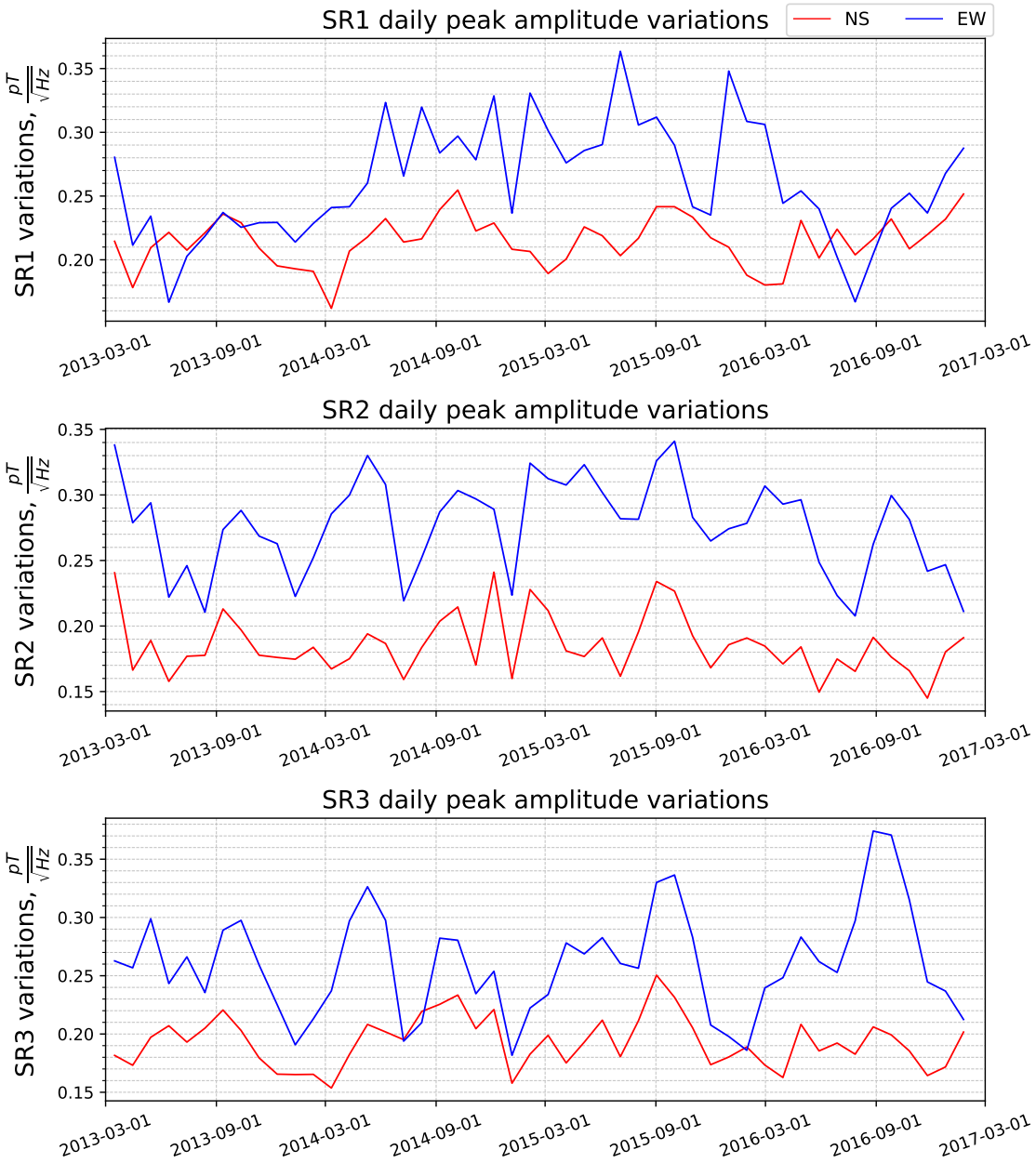

Figure 7.12. Daily variation of the minimum to maximum range of the peak amplitudes, averaged over 30 days, for the three first modes SR1, SR2, and SR3, in the first, the second and the third row, respectively. The North-South sensor is plotted in red, and the East-West sensor is plotted in blue.

7.5. Conclusions

In this work, we present a detailed analysis of the regular variations of the SRs during the period March 2013–February 2017, using the Sierra Nevada station (37^{o}02'N, 3^{o}19'W) ground-based magnetometers. Each component of the magnetic field measured has been processed by fitting Lorentzian functions to the amplitude spectrum, in a bandwidth of (6.35-23.75) Hz, for each 10 min interval of data. The regular variations of the SRs have been studied using the following parameters: peak amplitudes,

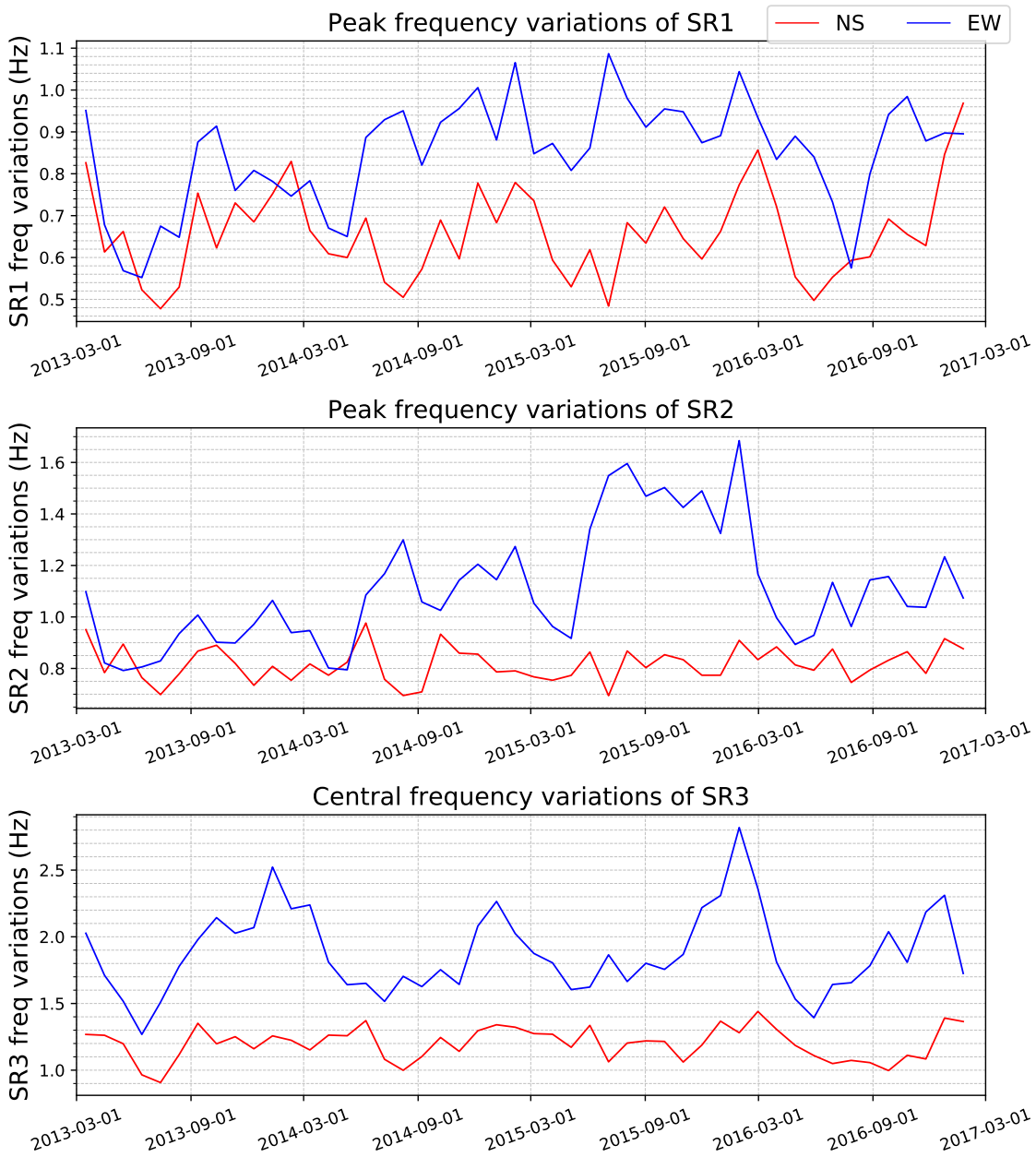

Figure 7.13. Daily variation of the minimum to maximum range of the peak frequencies, averaged over 30 days, for the three first modes SR1, SR2, and SR3, in the first, the second and the third row, respectively. The North-South sensor is plotted in red, and the East-West sensor is plotted in blue.

peak frequencies, the widths of the resonances, and the PSI for the three first modes. The processed data for the entire measurement period of the station are made public along with this work, and they are presented in a Numpy npz format, which allows easy reading and subsequent processing.

The main findings can be summarized as follows:

1. The general diurnal evolution of the three main storm centers on Earth, Africa, Asia, and America, has been confirmed. There is a predominance of stormy ac-

tivity in northern hemisphere summer and minimal in winter. The African center exhibits the larger intensity and the Asian center, the longest daily duration.

2. SR2 and SR3 diurnal peak amplitudes of the NS sensor are very sensitive to the African storm center. Diurnal peak amplitudes of SR1-3 in the EW sensor are similar in shape, while for the NS sensor the shape changes for each mode. Regarding the diurnal variation of the frequency, a very different pattern is observed between the EW and NS sensors, but no strong seasonal variations are observed. Sierra Nevada measurements do not exhibit a transition from winter-type to summer-type variations in the diurnal variations of the peak frequencies. Since that parameter is related to the source-observer distance (e.g., Toledo-Redondo et al., 2016), different stations are expected to exhibit different seasonal patterns. The widths of the resonances are highly fluctuating and it is very difficult to draw conclusions from the measurements. It is observed that the widths are greater for the EW sensor than for the NS one.

3. The peak amplitudes of diurnal averages measured by Sierra Nevada station are roughly half of the peak amplitudes reported by the stations in China. This difference can be attributed to the relative distance of each station to the storm centers. In addition, Sierra Nevada station does not detect a peak in activity around 08:00 UT, that activity is shifted to 10:30 UT. This may be explained by the different years considered in our study, but this requires further investigation.

4. The African storm center exhibits maxima of activity during boreal summer, according to our SR records. This is not well supported by global lightning data from satellites (e.g., Blakeslee et al. (2014)). A unified database involving several stations around the globe would be desirable to further test these results. The additional activation time, around 0600 UT, only detected by some stations, is observed by the ELF Sierra Nevada station.

5. Diurnal variations of PSI evolve with electromagnetic seasons rather than with astronomical seasons.

6. Predictions by Williams et al. (2021) about the effect of El Niño on SR seem to be detected in the annual diurnal variations of our measurements of the first mode peak amplitude. There are also variations between EW and NS sensors: the former shows a repeating pattern every month, while the latter has different patterns during summer and winter months.

7. We have obtained results that corroborate some conclusions on an intensification of the SRs during the transition months that precede the super El Niño episode which happened at the end of 2015 and the beginning of 2016, as indicated by

Williams et al. (2021). We also find results like those in Koloskov et al. (2020), connected to a tracking of the first mode resonant frequency and the 11-year cycle solar activity, during a period of large solar activity (2011–2017).

8. Daily variations of different parameters are stronger for EW sensor than for NS sensor.

Data Availability Statement

The data set of this paper will be available from http://hdl.handle.net/10481/71563.

Author Contributions:

Conceptualization: J. Rodríguez-Camacho, A. Salinas, M. C. Carrión, J. Portí, S. Toledo-Redondo
Formal analysis: J. Rodríguez-Camacho, A. Salinas, M. C. Carrión, J. Portí
Funding acquisition: M. C. Carrión, J. Fornieles-Callejón
Investigation: J. Rodríguez-Camacho, A. Salinas, M. C. Carrión, J. Portí, J. Fornieles-Callejón, S. Toledo-Redondo
Methodology: A. Salinas, J. Portí, J. Fornieles-Callejón, S. Toledo-Redondo
Project Administration: M. C. Carrión, J. Fornieles-Callejón
Software: J. Rodríguez-Camacho
Supervision: J. Portí, J. Fornieles-Callejón
Validation: J. Rodríguez-Camacho, A. Salinas, J. Portí, S. Toledo-Redondo
Visualization: J. Rodríguez-Camacho, A. Salinas, J. Portí
Writing – original draft: A. Salinas
Writing – review and editing: J. Rodríguez-Camacho, A. Salinas, J. Portí, S. Toledo-Redondo

Acknowledgements

This work has been supported by the investigation research projects FIS2017-90102-R, of the Ministry of Economy and Competitiveness (MINECO) of Spain, co-financed by the Fund European Regional Development (FEDER), and PID2020-112805GA-I00, of the Ministry of Science and Innovation of Spain, and the Ministry of Education, Science and Sport of Spain through the FPU grants for PhD studentship (reference: FPU15/04291). Funding for Open Access Charge: Universidad de Granada/CBUA. We are grateful to Parque Nacional Sierra Nevada for providing support to the project.

References

Aich, V., Holzworth, R., Goodman, S., Kuleshov, Y., Price, C., & Williams, E. (2018). Lightning: A new essential climate variable. *Eos*, *99*. https://doi.org/10.1029/2018eo104583

Balser, M., & Wagner, C. A. (1960). Observations of Earth-ionosphere cavity resonances. *Nature*, *188*, 638–641. https://doi.org/10.1038/188638a0

Belyaev, G. G., Schekotov, A. Y., Shvets, A. V., & Nickolaenko, A. P. (1999). Schumann resonances observed using Poynting vector spectra. *Journal of Atmospheric and Solar-Terrestrial Physics*, *61*(10), 751–763. https://doi.org/10.1016/S1364-6826(99)00027-9

Besser, B. P. (2007). Synopsis of the historical development of Schumann resonances. *Radio Science*, *42*(2), RS2S02. https://doi.org/10.1029/2006RS003495

Betz, H. D., Schumann, U., & Laroche, P. (2009). *Lightning: Principles, instruments and applications: Review of modern lightning research*. Springer Netherlands. https://doi.org/10.1007/978-1-4020-9079-0

Blakeslee, R. J., Mach, D. M., Bateman, M. G., & Bailey, J. C. (2014). Seasonal variations in the lightning diurnal cycle and implications for the global electric circuit. *Atmospheric Research*, *135-136*(Supplement C), 228–243. https://doi.org/10.1016/j.atmosres.2012.09.023

Christian, H. J., Blakeslee, R. J., Boccippio, D. J., Boeck, W. L., Buechler, D. E., Driscoll, K. T., Goodman, S. J., Hall, J. M., Koshak, W. J., Mach, D. M., et al. (2003). Global frequency and distribution of lightning as observed from space by the Optical Transient Detector. *Journal of Geophysical Research: Atmospheres*, *108*(D1), ACL–4–1–ACL 4–15. https://doi.org/10.1029/2002jd002347

Fornieles-Callejón, J., Salinas, A., Toledo-Redondo, S., Portí, J., Méndez, A., Navarro, E. A., Morente-Molinera, J. A., Soto-Aranaz, C., & Ortega-Cayuela, J. S. (2015). Extremely low frequency band station for natural electromagnetic noise measurement. *Radio Science*, *50*, 191–201. https://doi.org/10.1002/2014RS005567

Füllekrug, M., & Fraser-Smith, A. C. (1997). Global lightning and climate variability inferred from ELF magnetic field variations. *Geophysical Research Letters*, *24*(19), 2411–2414. https://doi.org/10.1029/97GL02358

Koloskov, A. V., Nickolaenko, A. P., Yampolsky, Y. M., Hall, C., & Budanov, O. V. (2020). Variations of global thunderstorm activity derived from the long-term Schumann resonance monitoring in the Antarctic and in the Arctic. *Journal of Atmospheric and Solar-Terrestrial Physics*, *201*, 105231. https://doi.org/10.1016/j.jastp.2020.105231

Kulak, A., Kubisz, J., Michalec, A., Zieba, S., & Nieckarz, Z. (2003). Solar variations in extremely low frequency propagation parameters: 2. Observations of Schumann resonances and computation of the ELF attenuation parameter. *Journal of Geophysical Research*, *108*(A7). https://doi.org/10.1029/2002JA009305

Melnikov, A., Price, C., Sátori, G., & Füllekrug, M. (2004). Influence of solar terminator passages on Schumann resonance parameters. *Journal of Atmospheric and Solar-Terrestrial Physics*, *66*(13), 1187–1194. https://doi.org/10.1016/j.jastp.2004.05.014

Nickolaenko, A. P., & Hayakawa, M. (2002). *Resonances in the Earth-Ionosphere Cavity*. Dordrecht, Netherlands: Kluwer Academy.

Nickolaenko, A. P., & Hayakawa, M. (2014). *Schumann Resonance for Tyros*. Springer, Japan.

Nickolaenko, A. P., Hayakawa, M., & Hobara, Y. (1999). Long-term periodical variations in global lightning activity deduced from the Schumann resonance monitoring. *Journal of Geophysical Research*, *104(D22)*, 27585–27591. https://doi.org/10.1029/1999jd900791

Nickolaenko, A. P., Koloskov, A. V., Hayakawa, M., Yampolski, Y. M., Budanov, O. V., & Korepanov, V. E. (2015). 11-year solar cycle in Schumann resonance data as observed in Antarctica. *Sun and Geosphere*, *10*(1), 39–49.

Nickolaenko, A. P., & Rabinowicz, L. M. (1995). Study of the annual changes of global lightning distribution and frequency variations of the first Schumann resonance mode. *Journal of Atmospheric and Terrestrial Physics*, *57*(11), 1345–1348. https://doi.org/10.1016/0021-9169(94)00114-4

Nickolaenko, A. P., Shvets, A., & Hayakawa, M. (2016). Extremely low frequency (ELF) radio wave propagation: A review. *International Journal of Electronics and Applied Research (IJEAR)*, *3*(2), 91.

Nickolaenko, A., Sátori, G., Zieger, B., Rabinowicz, L., & Kudintseva, I. (1998). Parameters of global thunderstorm activity deduced from the long-term Schumann resonance records. *Journal of Atmospheric and Solar-Terrestrial Physics*, *60*(3), 387–399. https://doi.org/10.1016/S1364-6826(97)00121-1

Ondrášková, A., Kostecký, P., Rosenberg, L., et al. (2007). Long-term observations of Schumann resonances at Modra observatory. *Radio Science*, *42*(02), 1–12.

Ondrášková, A., Ševćík, S., & Kostecký, P. (2011). Decrease of Schumann resonance frequencies and changes in the effective lightning areas toward the solar cycle minimum of 2008-2009. *Journal of Atmospheric and Solar-Terrestrial Physics*, *73*(4), 534–543. https://doi.org/10.1016/j.jastp.2010.11.013

Ouyang, X. Y., Xiao, Z., Hao, Y. Q., & Zhang, D. H. (2015). Variability of Schumann resonance parameters observed at low latitude stations in China. *Advances in Space Research*, *56*(7), 1389–1399. https://doi.org/10.1016/j.asr.2015.07.006

Price, C., & Melkinov, A. (2004). Diurnal, seasonal and inter-annual variations in the Schumann resonance parameters. *Journal of Atmospheric and Solar-Terrestrial Physics.*, *66(13-14)*, 1179–85. https://doi.org/10.1016/j.jastp.2004.05.004

Price, C. (2000). Evidence for a link between global lightning activity and upper tropospheric water vapour. *Nature*, *406*(6793), 290–293. https://doi.org/10.1038/35018543

Price, C. (2016). ELF electromagnetic waves from lightning: the Schumann resonances. *Atmosphere*, *7*(9), 116. https://doi.org/10.3390/atmos7090116

Rodríguez-Camacho, J., Fornieles, J., Carrión, M. C., Portí, J. A., Toledo-Redondo, S., & Salinas, A. (2018). On the need of a unified methodology for processing Schumann resonance measurements. *Journal of Geophysical Research: Atmospheres*, *123*(23). https://doi.org/10.1029/2018JD029462

Sátori, G. (1996). Monitoring Schumann resonances-II. Daily and seasonal frequency variations. *Journal of Atmospheric and Terrestrial Physics*, *58*(13), 1483–1488. https://doi.org/10.1016/0021-9169(95)00146-8

Sátori, G., Williams, E., & Lemperger, I. (2009). Variability of global lightning activity on the ENSO time scale. *13th International Conference on Atmospheric Electricity ICAE 2007*, *91*(2–4), 500–507. https://doi.org/10.1016/j.atmosres.2008.06.014

Sátori, G., Williams, E., & Mushtak, V. (2005). Response of the Earth–ionosphere cavity resonator to the 11-year solar cycle in X-radiation. *Journal of Atmospheric and Solar-Terrestrial Physics*, *67*(6), 553–562. https://doi.org/10.1016/j.jastp.2004.12.006

Sátori, G., Williams, E., & Boccippio, D. (2003). On the dynamics of the North-South seasonal migration of global lightning. *Paper presented at AGU Fall Meeting, San Francisco, December 8–12.*, *2003*, Abstract no.: AE32A–0167.

Sátori, G. (2003). On the dynamics of the North-South seasonal migration of global lightning. *Paper presented at 12th international conference on atmospheric electricity. Versailles, France. Global Lightning and Climate.*

Sátori, G., & Zieger, B. (1999). El Niño related meridional oscillation of global lightning activity. *Geophysical Research Letters*, *26*(10), 1365–1368.

Schumann, W. O. (1952). Über die stralungslosen Eigenschwingungen einer leitenden Kugel die von einer Luftschicht und einer Ionospärenhle umgeben ist. *Zeitschrift für Naturforschung*, *7a*, 149–154. https://doi.org/10.1515/zna-1952-0202

Sekiguchi, M., Hayakawa, M., Nickolaenko, A. P., & Hobara, Y. (2006). Evidence on a link between the intensity of Schumann resonance and global surface temperature. *Annales Geophysicae*, *24*(7), 1809–1817. https://doi.org/10.5194/angeo-24-1809-2006

Simões, F., Pfaff, R., Berthelier, J.-J., & Klenzing, J. (2012). A review of low frequency electromagnetic wave phenomena related to tropospheric-ionospheric coupling mechanisms. *Space Science Reviews*, *168*(1-4), 551–593. https://doi.org/10.1007/s11214-011-9854-0

Surkov, V., & Hayakawa, M. (2014). *Ultra and extremely low frequency electromagnetic fields.* Springer.

Toledo-Redondo, S., Parrot, M., & Salinas, A. (2012). Variation of the first cut-off frequency of the Earth-ionosphere waveguide observed by DEMETER. *Journal of Geophysical Research: Space Physics*, *117*, A04321. https://doi.org/10.1029/2011JA017400

Toledo-Redondo, S., Salinas, A., Fornieles, J., Portí, J., & Lichtenegger, H. I. M. (2016). Full 3-D TLM simulations of the Earth-ionosphere cavity: Effect of conductivity on the Schumann resonances. *Journal of Geophysical Research: Space Physics*, *121*, 5579–5593. https://doi.org/10.1002/2015JA022083

Toledo-Redondo, S., Salinas, A., Portí, J., Morente, J. A., Fornieles, J., Méndez, A., Galindo-Zaldívar, J., Pedrera, A., Ruiz-Constán, A., & Anahnah, F. (2010). Study of Schumann resonances based on magnetotelluric records from the western Mediterranean and Antarctica. *Journal of Geophysical Research: Atmospheres*, *115*(D22114). https://doi.org/10.1029/2010JD014316

Williams, E., Bozóki, T., Sátori, G., Price, C., Steinbach, P., Guha, A., Liu, Y., Beggan, C., Neska, M., Boldi, R., et al. (2021). Evolution of global lightning in the transition from cold to warm phase preceding two super El Niño events. *Journal of Geophysical Research: Atmospheres*, *126*(3), e2020JD033526.

Williams, E., Guha, A., Boldi, R., Christian, H., & Buechler, D. (2019). Global lightning activity and the hiatus in global warming. *Journal of Atmospheric and Solar-Terrestrial Physics*, *189*, 27–34. https://doi.org/10.1016/j.jastp.2019.03.011

Williams, E. R. (1992). The Schumann Resonance: A global tropical thermometer. *Science*, *256*(5060), 1184–1187. https://doi.org/10.1126/science.256.5060.1184

Williams, E. (2005). Lightning and climate: A review. *Atmospheric research*, *76*(1-4), 272–287. https://doi.org/10.1016/j.atmosres.2004.11.014

Yatsevich, E. I., Nickolaenko, A. P., & Pechonaya, O. B. (2008). Diurnal and seasonal variations in the intensities and peak frequencies of the first three Schumann-resonance modes. *Radiophysics and Quantum Electronics*, *51*(7), 528–538. https://doi.org/10.1007/s11141-008-9056-0

Yatsevich, E. I., Shvets, A. V., & Rabinowicz, L. M. (2005). Two component model of the Schumann resonance signal. *Telecommunications and Radio Engineering*, *64*(7-12). https://doi.org/10.1615/TelecomRadEng.v64.i10.100

Zhou, H., Yu, H., Cao, B., & Qiao, X. (2013). Diurnal and seasonal variations in the Schumann resonance parameters observed at Chinese observatories. *Journal of Atmospheric and Solar-Terrestrial Physics*, *98*, 86–96. https://doi.org/10.1016/j.jastp.2013.03.021

Chapter 8. Additional concerns to the study of the Schumann Resonance variations measured in Sierra Nevada

In addition to the study of the regular variations of the SR parameters by analyzing their evolution in different charts, as we have done in the previous chapters, some studies have made use of statistical techniques to extract the principal components of the temporal evolution of the SR parameters, obtaining the annual, the semiannual, and other components. In Nickolaenko and Hayakawa (2014) and in Sekiguchi et al. (2006), the Singular Spectrum Analysis (SSA) is applied. Nickolaenko also uses the Caterpillar algorithm. In this thesis, the SSA will be used to obtain the principal components of the temporal variation of the SR1, SR2 and SR3 local maximum amplitudes and local maximum central frequencies, extracted from the Sierra Nevada station measurements.

Also, little attention has been paid so far in the literature to the study of the anomalies that are occasionally observed in the amplitude spectra. Using the amplitude spectra of the measurements at the Sierra Nevada station, a systematic record of the anomalies observed in the spectra has been done by visual inspection, and a series of codes and functions have been designed for the analysis of this information.

This chapter is thus divided into two sections:

- The application of the SSA to obtain the principal components of the temporal variations of the SR1, SR2 and SR3 amplitudes and central frequencies measured at the Sierra Nevada station from March, 2013 to February, 2018 (5 years).
- The detection and study of the anomalies identified in the amplitude spectra of the SR measurements at the Sierra Nevada station from March to July, 2013.

8.1. Application of the Singular Spectrum Analysis to the temporal variations of the SR parameters

As an important part of the long term SR analysis, we are interested in obtaining the principal components of the time variations of the SR parameters. It can be

interesting to correlate them with some environmental phenomena. In this section, the SSA will be used to extract these principal components.

The results shown in this section were partially presented in Rodríguez-Camacho et al. (2021). In that work, only the amplitude and the central frequency of the SR1 were considered. In this thesis, we also study the principal components of the SR2 and the SR3 amplitudes and central frequencies.

The SSA technique was first presented in Broomhead and King (1986), and has been used and applied to many different problems since then (Hassani 2007). The aim of the SSA technique is the decomposition of an original series into the sum of a small number of independent and interpretable components.

According to the notation used in Hassani (2007), the time series of the values of a parameter will be noted $Y = (y1, \ldots, y_T)$, and a number of K series $X_1, \ldots, X_K$ will be obtained by lagging the vector Y, $X_i = (y_i, y_{i+1}, \ldots, y_{i+L-1})$, for $i = \{1, ..., K\}$, where the condition $K = T-L+1$ is verified. We must consider the matrix $X = [X_1, \ldots, X_K]$:

$$X = \begin{pmatrix} y_1 & y_2 & y_3 & \cdots & y_K \\ y_2 & y_3 & y_4 & \cdots & y_{K+1} \\ \vdots & \vdots & \vdots & \ddots & \vdots \\ y_L & y_{L+1} & y_{L+2} & \cdots & y_{K+L-1} \end{pmatrix}$$

In order to obtain the principal components of the temporal evolution of a parameter, we apply the Singular Value Decomposition (SVD) to the matrix X, which gives us the eigenvalues of the matrix XX^T. These eigenvalues are denoted by Λ_1, ..., Λ_L, and the corresponding system of orthonormal eigenvectors, $U_1, \ldots, U_L$, as well as the eigenvectors of X^TX, denoted by $V_1, \ldots, V_L$, which verify

$$V_i = X^T U_i / \sqrt{\Lambda_i}$$

The eigenvectors can be grouped taking into account that some of them may describe a variation of the same frequency and thus they may correspond to the same principal component. In our application of the SSA technique we will find that most of the eigenvectors can be grouped in pairs to form the principal components. In order to discover the most appropriate grouping, the correlation among the contributions to the global signal by the different principal components, shown in Figures 8.3 and 8.4, must be taken into account as explained in Hassani (2007). If two components have a very strong correlation, it means that they form together the same principal component.

If Λ_{i1}, U_{i1} and Λ_{i2}, U_{i2} are two eigenvalues and two eigenvectors that describe a variation of the same frequency, they form a principal component together. Then, the contribution of this principal component to the global time series is

$$X_{i_1,i_2} = \sqrt{\Lambda_{i_1}} U_{i_1} V_{i_1}^T + \sqrt{\Lambda_{i_2}} U_{i_2} V_{i_2}^T$$

The sum of the contributions of all the principal components equals the original signal. The normalized contribution of each principal component to the global time series of the parameters will be shown in this section.

In this work, the SSA technique has been applied to the temporal series of the SR parameters extracted from the measurements at Sierra Nevada from March, 2013 to February, 2018, i.e., to 5-year long time series. We have used two different values for the temporal resolution of the series:

- One sample per month, i.e., the monthly average value of the parameter value is calculated for each month. In this case, the total number of samples of the series is $T = 60$, and we have $L = 24$ and $K = 37$.
- One sample per day, i.e., the daily average value of the parameter value is calculated for each month. In this case, the total number of samples of the series is $T = 1826$, and we have $L = 730$ and $K = 1097$.

Both temporal resolutions lead to similar results. In this section, for the sake of brevity, only the principal components using 1 sample per day will be shown. No relevant differences are observed in the results when using 1 sample per month.

In order to apply the SSA to the temporal variations of the parameters, it is essential to fill the data gaps that appear as a consequence of technical failures of the station, even if the rate of gaps in the recordings is small. These gaps may last for 10 minutes (if there is only one missing value) or for many weeks (even up to 10 weeks) for serious failures, as shown in Figure 8.1(a). The percentage of time intervals for which there are no recordings is of the order of 5%.

The idea to fill these gaps consists of using the value of the parameter for time intervals with a similar date or with a similar hour to the missing data. The closer a recording is to a missing interval, the more it will be taken into account for the filling. The relative importance that will be given for the close recordings to estimate the value of a missing interval is shown in a mesh in Figure 8.2. The filled time series for the SR1 local maximum amplitude is shown in Figure 8.1(b).

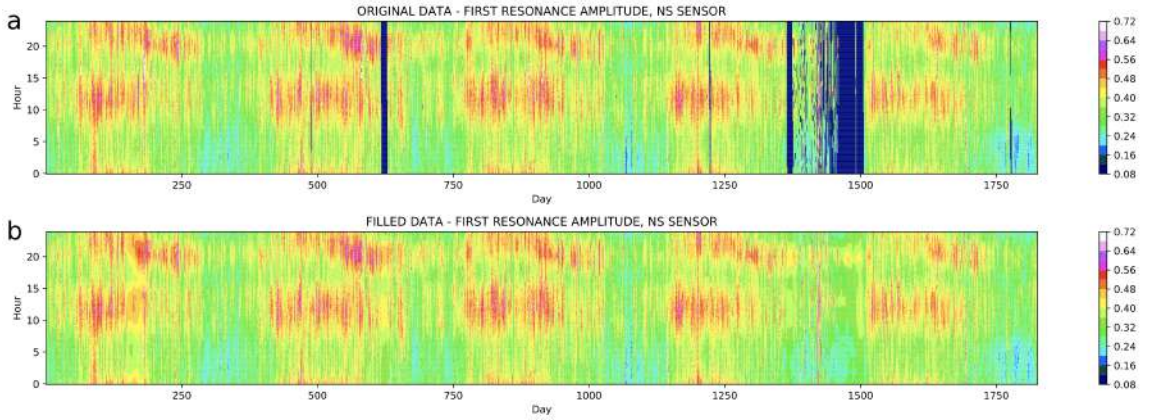

Figure 8.1. (a) Original values for the SR1 local maximum amplitude (NS component), parameter p1_0, where some gaps can be observed in the data. (b) Filled data of the SR1 local maximum amplitude (NS component), parameter p1_0, the gaps have been filled with the scheme described.

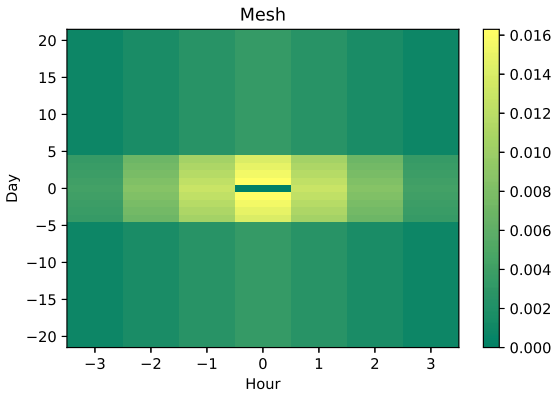

Figure 8.2. Relative importance given to the close recordings to estimate the value of a missing interval. The closer an interval is in date and time to the missing interval, the more importance it will be given. For short blanks only the closest intervals determine the value of the blank, but further intervals have to be considered for long periods of missing data.

The Matlab code to apply the SSA to our data is available for download, together with the time series of the SR parameters, in the link below. The results shown in this section can be obtained with this code.

https://hdl.handle.net/10481/78099

The folder that can be downloaded from the link above contains:

- Two files with the codes to apply the SSA: `SSA_Daily.m` (for 1 sample per day) and `SSA_Monthly.m` (for 1 sample per month). They can be directly run in Matlab to generate the graphs shown in this chapter.
- Another Matlab code to produce other results: the filled data and the reconstruction of the signal.

- The data files containing the filled data of the parameters (there is a total of 14 files).
- A folder called `Figures` with all the graphs shown in this chapter, and also with the graphs when 1 sample per month is considered.

The results of the application of the SSA to the SR parameters obtained in the Sierra Nevada ELF station are shown in the next pages. The correlation between the different eigenvalues is shown in Figure 8.3 for the parameters of the NS component, and in Figure 8.4 for the parameters of the EW component. The correlation plot indicates that some of the eigenvalues correspond to variations of the same frequency, so they must be grouped (or superposed) to obtain a principal component of the variation. The principal components of the temporal variations of the local maximum amplitudes are shown in Figure 8.5 for the NS component and in Figure 8.6 for the EW component. Also, the principal components of the temporal variations of the local maximum central frequencies are shown in Figure 8.7 for the NS component and in Figure 8.8 for the EW component. The Fast and Discrete Fourier Transform (FDFT) describing the frequency content is shown on the right side for each variation. Finally, Figure 8.9 shows the principal components for the Power Spectrum Integral for both components, together with their FDFT.

Looking at the results, we can confirm that the principal components for all the parameters have some similarities. The first principal component corresponds to the constant part of the variation, and its content in the frequency domain decreases with the frequency (increases with the period). The second principal component corresponds to the annual variation, and its content in frequency shows a maximum around 365 days. The third principal component, for many of the parameters, is the semiannual variation, and its content in frequency has a maximum around 180 days. The biggest part of the intensity of the signals is by far due to the first principal component, whereas the contribution to the intensity by the rest of the principal components quickly decreases.

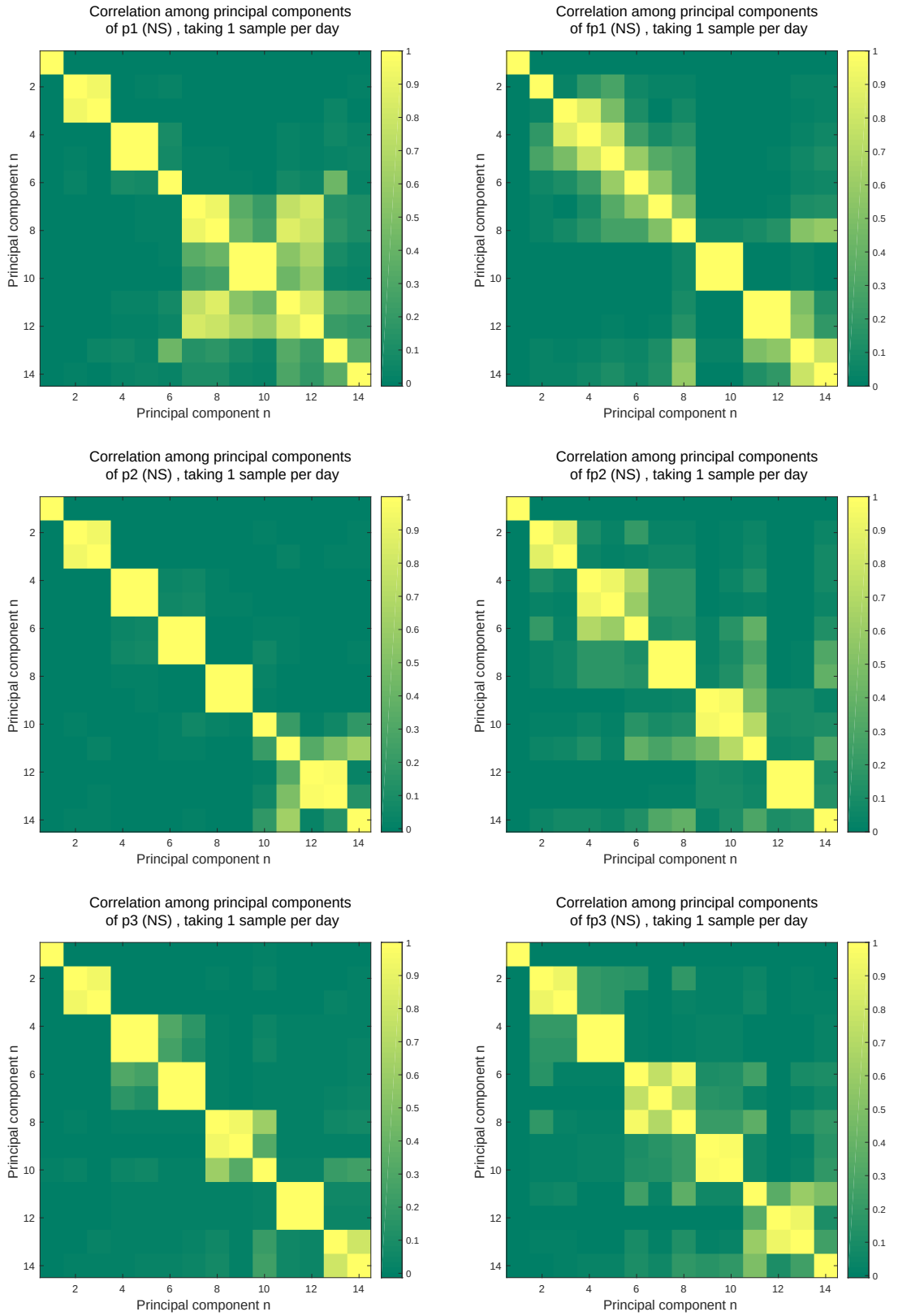

Figure 8.3. Correlation among the different principal components obtained for the temporal variations of different parameters for the NS component. The principal components must be grouped if they have a strong correlation, as this means that they correspond to a variation of the same frequency. For example, for p1 (NS), the components 2 and 3, and also the components 4 and 5, must be grouped.

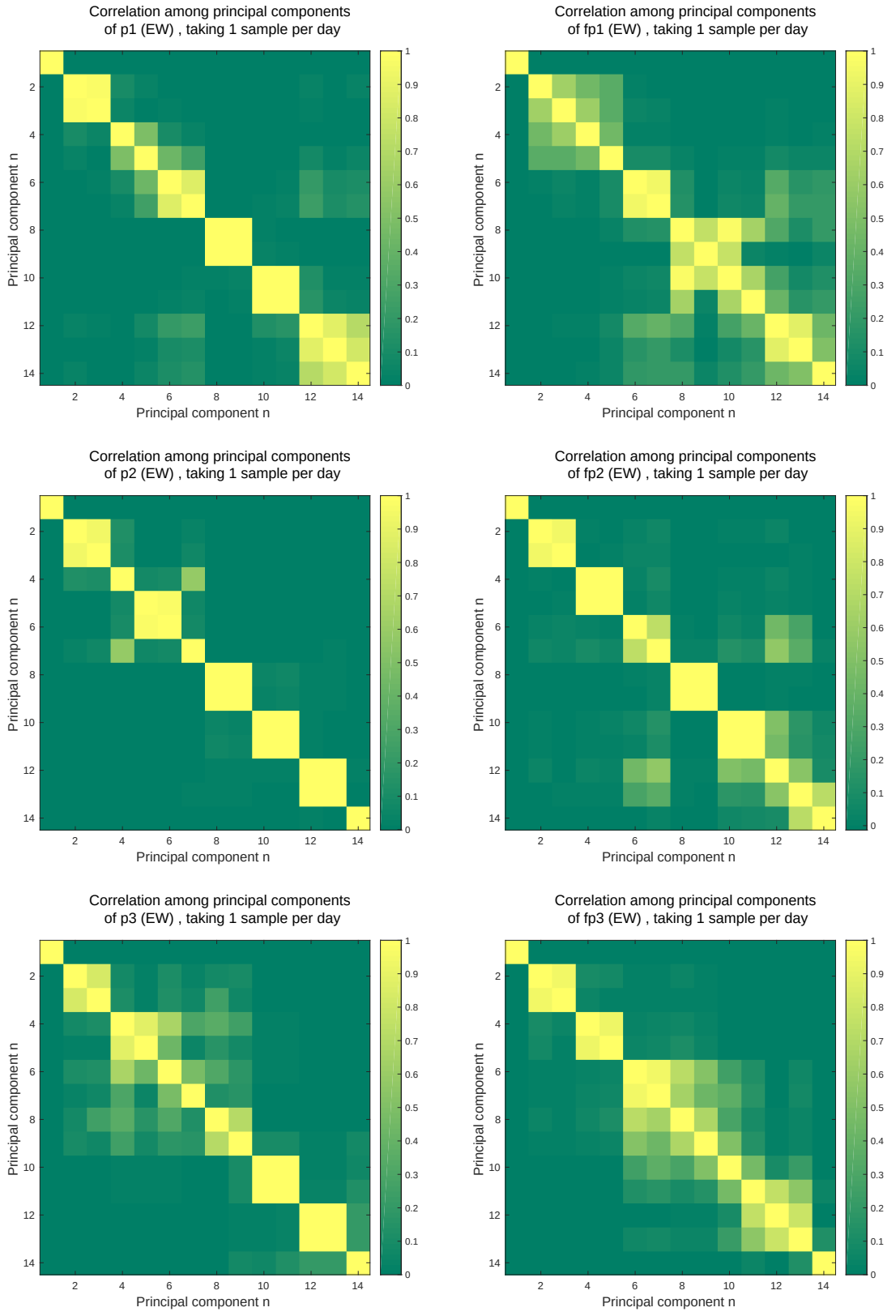

Figure 8.4. Correlation among the different principal components obtained for the temporal variations of different parameters for the EW component.

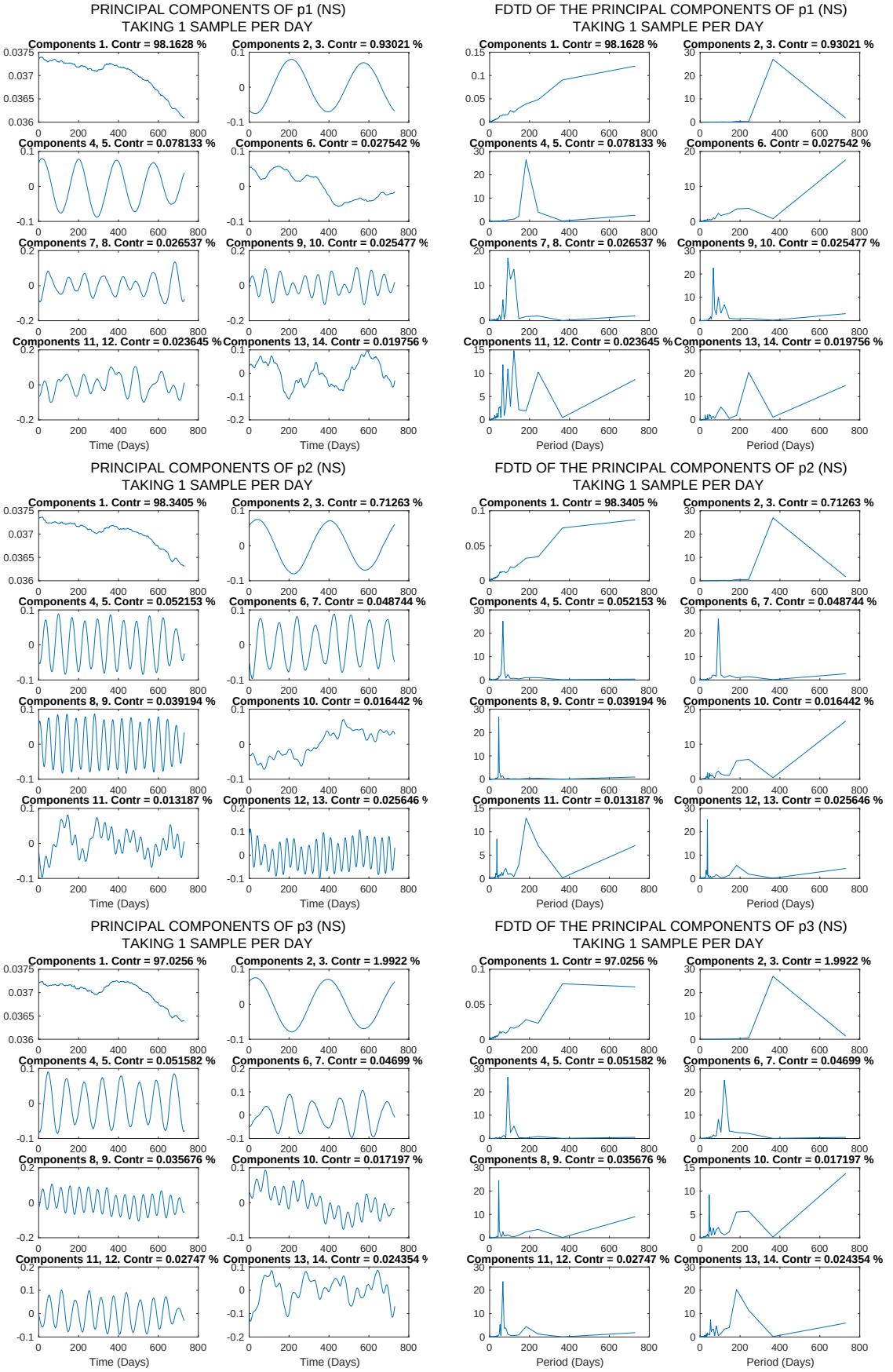

Figure 8.5. On the left, the principal components of the temporal evolution of the global local maximum amplitudes of SR1, SR2 and SR3 for the NS component (p1_0, p2_0, p3_0). On the right, their FD Fourier Transforms. One sample per day is used.

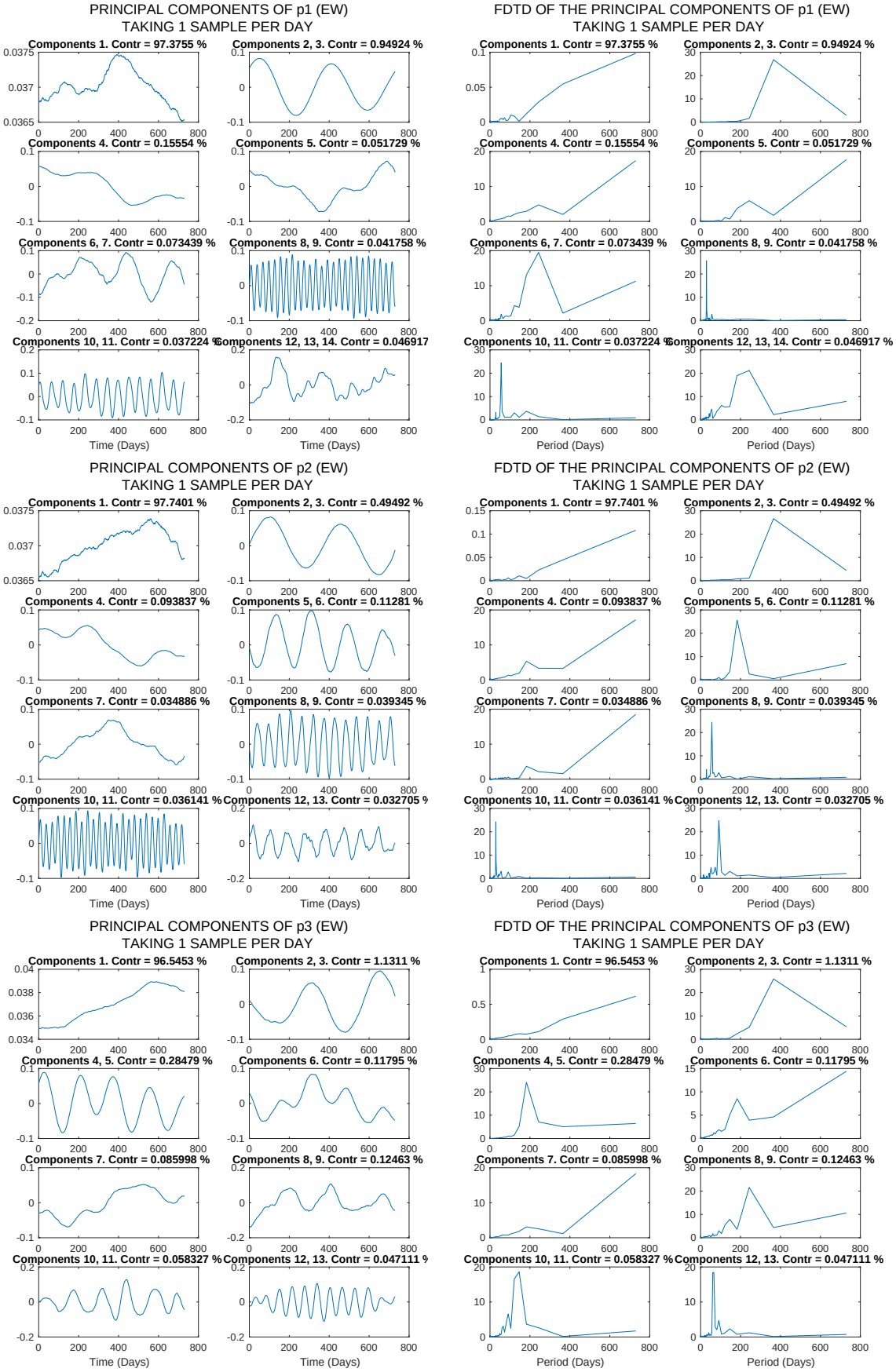

Figure 8.6. On the left, the principal components of the temporal evolution of the global local maximum amplitudes of SR1, SR2 and SR3 for the EW component (p1_1, p2_1, p3_1). On the right, their FD Fourier Transforms. One sample per day is used.

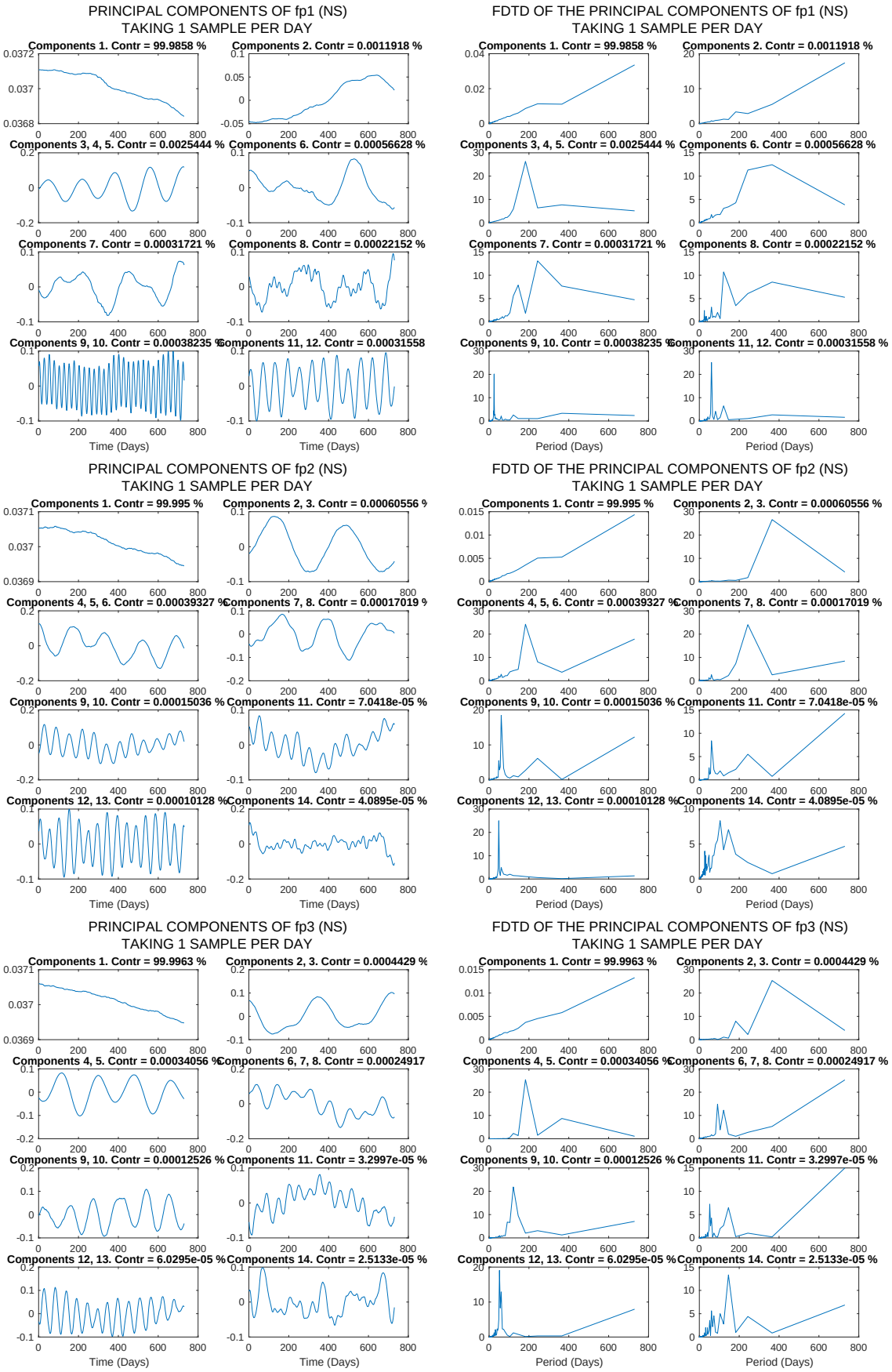

Figure 8.7. On the left, the principal components of the temporal evolution of the global local maximum central frequencies of SR1, SR2 and SR3 for the NS component (fp1_0, fp2_0, fp3_0). On the right, their FD Fourier Transforms. One sample per day is used.

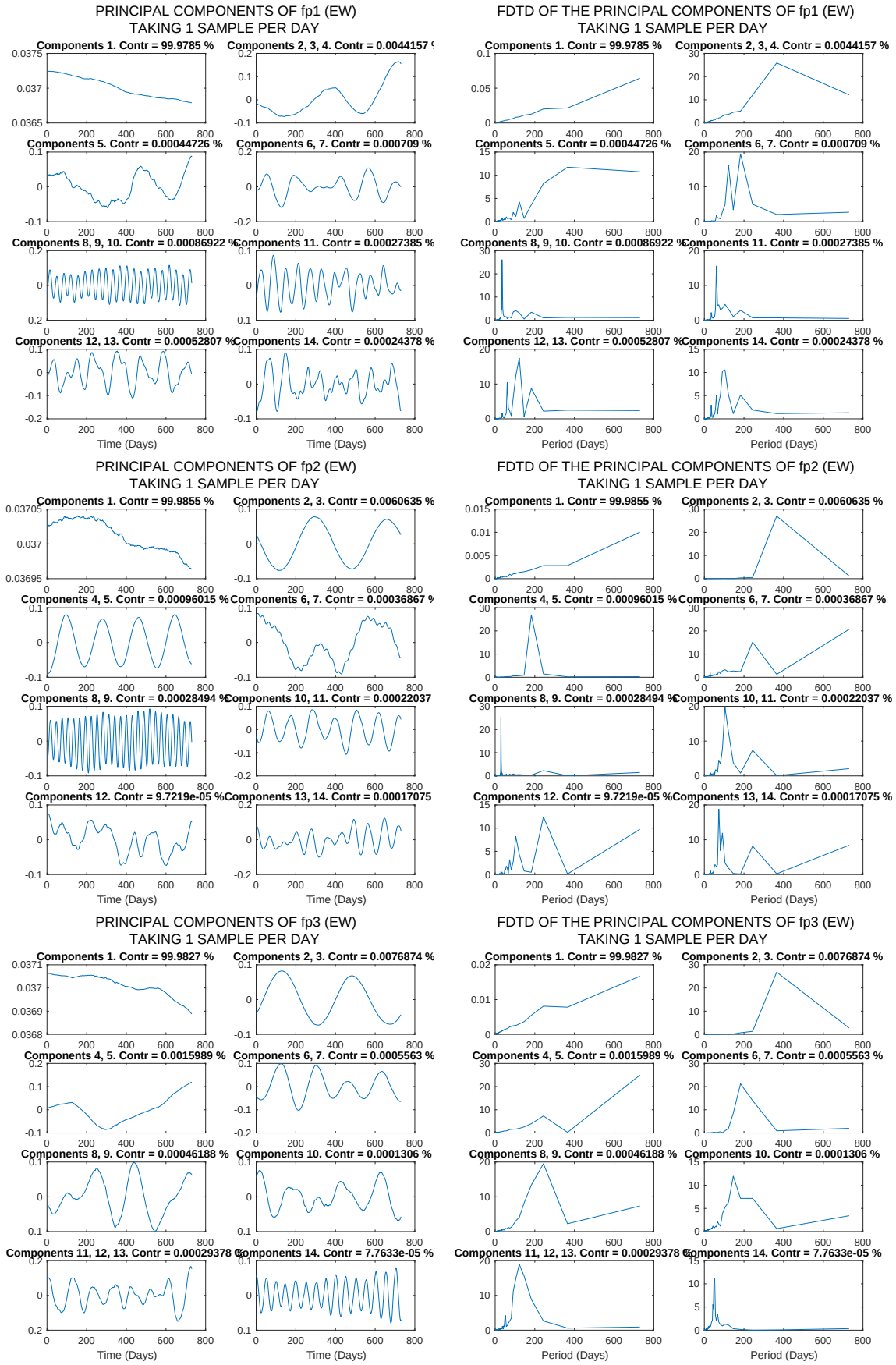

Figure 8.8. On the left, the principal components of the temporal evolution of the global local maximum central frequencies of SR1, SR2 and SR3 for the EW component (fp1_1, fp2_1, fp3_1). On the right, their FD Fourier Transforms. One sample per day is used.

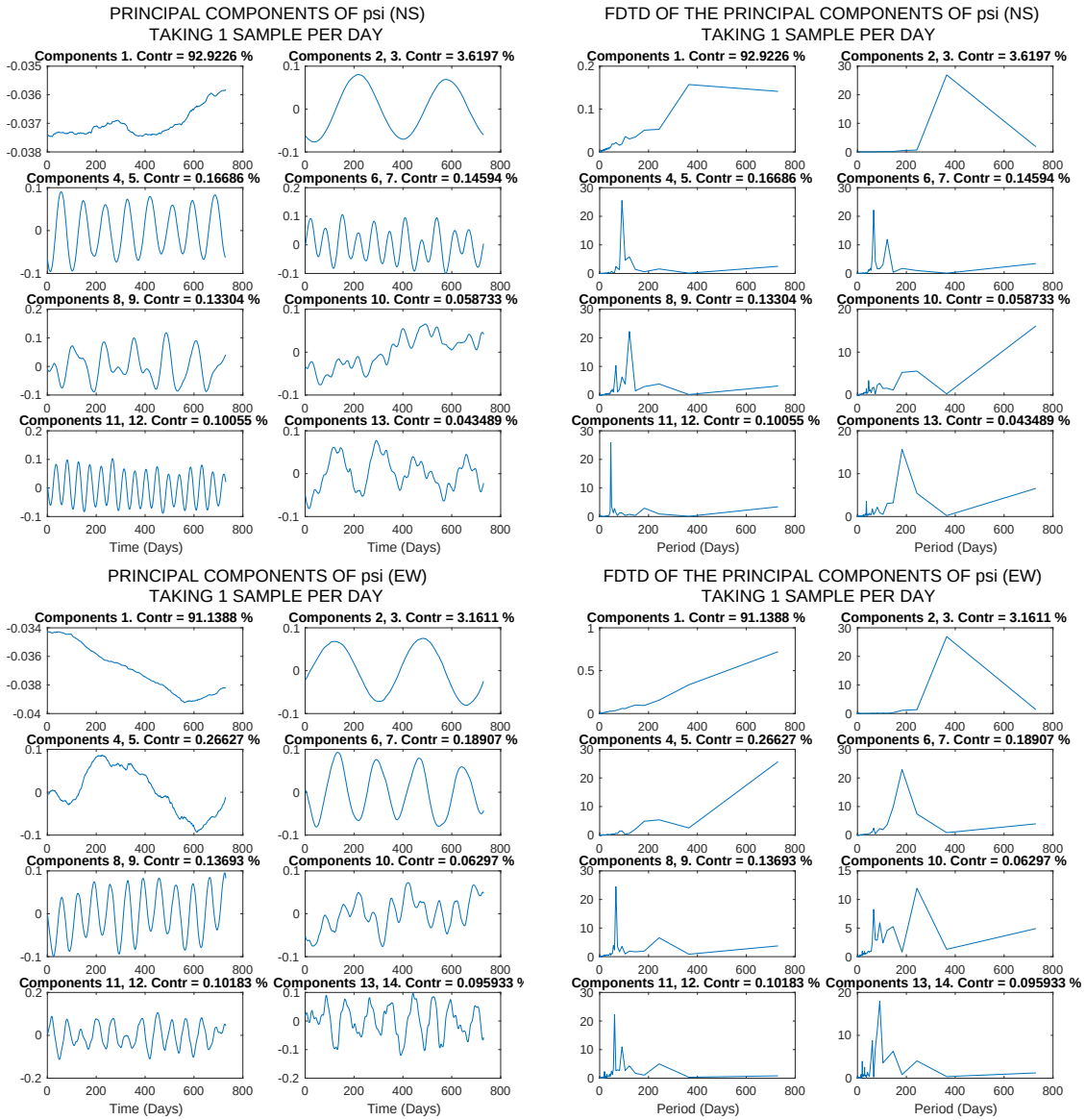

Figure 8.9. On the left, the principal components of the temporal evolution of the Power Spectrum Integral (PSI) for the NS and for the EW components (psi_0 and psi_1). On the right, their FD Fourier Transforms. One sample per day is used.

Finally, after obtaining the principal components of a signal, it can be reconstructed to observe how many principal components are needed to manage a satisfactory reconstruction. We show this in Figure 8.10. As more principal components are taken into consideration for the reconstruction of the signal, the similarity between the original signal and the reconstructed one increases.

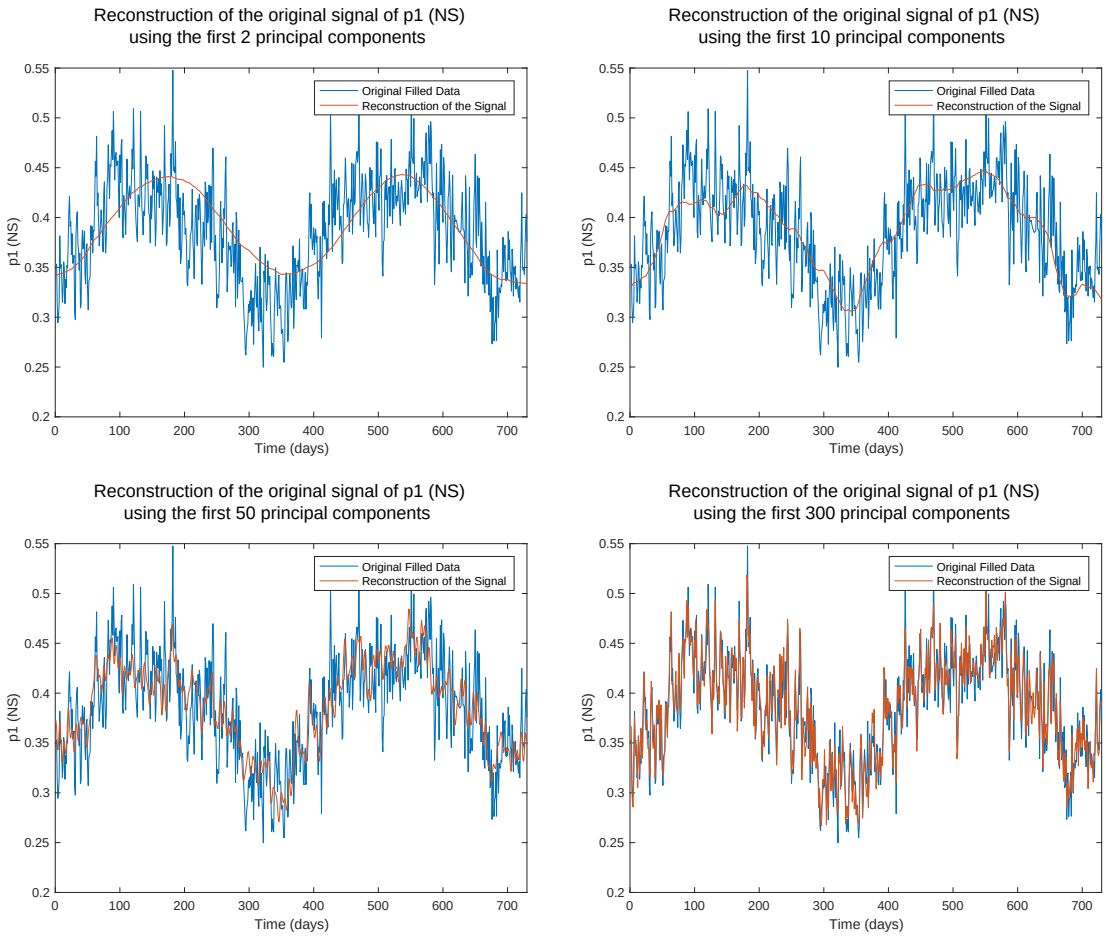

Figure 8.10. Result of reconstructing the filled signal using the first n principal components of the temporal variation, for the global local maximum amplitude of SR1 (NS), p1_0. Different values of n have been chosen: 2, 10, 50 and 100.

8.2. Detection and study of anomalies in the amplitude spectra

So far, the long term study of the SR regular variations has been addressed. In this section, we focus on the anomalous spectra, that are those spectra which show any particular feature that is not usually observed. This analysis is complementary to the analysis of the regular variations.

The detection of these anomalous spectra is made by visual inspection of the amplitude spectra corresponding to all the 10 min time intervals, using the `Interact` package within the Python module `ipywidgets` as explained in section 5.5. When a particularity is detected for a spectra, we write it in a `txt` file (there is a `txt` file for each month of recordings): (i) the hour and date of that time interval, (ii) the type of anomaly or anomalies observed, (iii) the component -NS, EW or both- in which the anomaly appears.

This scheme has been performed on the Sierra Nevada station measurements from March to July, 2013. It has been possible to classify the irregularities detected in the recordings into the following types:

- Anomalous peaks at certain frequencies of the spectra. They are labelled as '`P`' followed by the frequency at which the peak is observed. For example, '`P18`' is an anomalous peak at 18 Hz, and '`P105`' is an anomalous peak at 10.5 Hz.
- Amplitude spectra in which the SRs are not clearly visible. These spectra are labelled as '`S`'.
- Strong noise or stochastic component is observed in the amplitude spectra. They are labelled as '`R`'.
- Anomalous wavy or curly fluctuations in some part of the spectra. They are labelled as '`Z`'.
- An unusually high value for the amplitude spectra for frequencies lower that the SR1 peak frequency. This is labelled as '`B`'.
- An unusually high value for the amplitude spectra for frequencies higher that the SR3 peak frequency. This is labelled as '`A`'.
- Many narrow peaks are observed in the amplitude spectra. This anomaly is labelled as '`M`'.
- The first anthropogenic noise peak (at 14.85 Hz) has not been completely removed. This is labelled as '`E1`'.

- The second anthropogenic noise peak (at 15.25 Hz) has not been completely removed. This is labelled as '`E2`'.
- The first and the second anthropogenic noise peaks have not been completely removed. This is labelled as '`E12`'.
- The third anthropogenic noise peak (at 16.67 Hz) has not been completely removed. This is labelled as '`E3`'.
- Other anomalies that can not be classified as any of the types above. They are labelled as '`X`', and an example is given in Figure 8.11, lower right, where the NS amplitude spectrum does not decrease between SR1 and SR2.

The label is written in uppercase when the observed anomaly is clear and considerable, whereas it is written in lowercase and with the letter 'l' annexed when the anomaly is slight and not too clear.

Also, if the anomaly only appears in the NS component, we add '`_0`' to the label, and if the anomaly only appears in the EW component, we add '`_1`' to the label. When the anomaly appears in both components, no suffix is added to the label.

Some examples of anomalies are shown in Figures 8.11 and 8.12. The physical cause of these anomalies has not been determined.

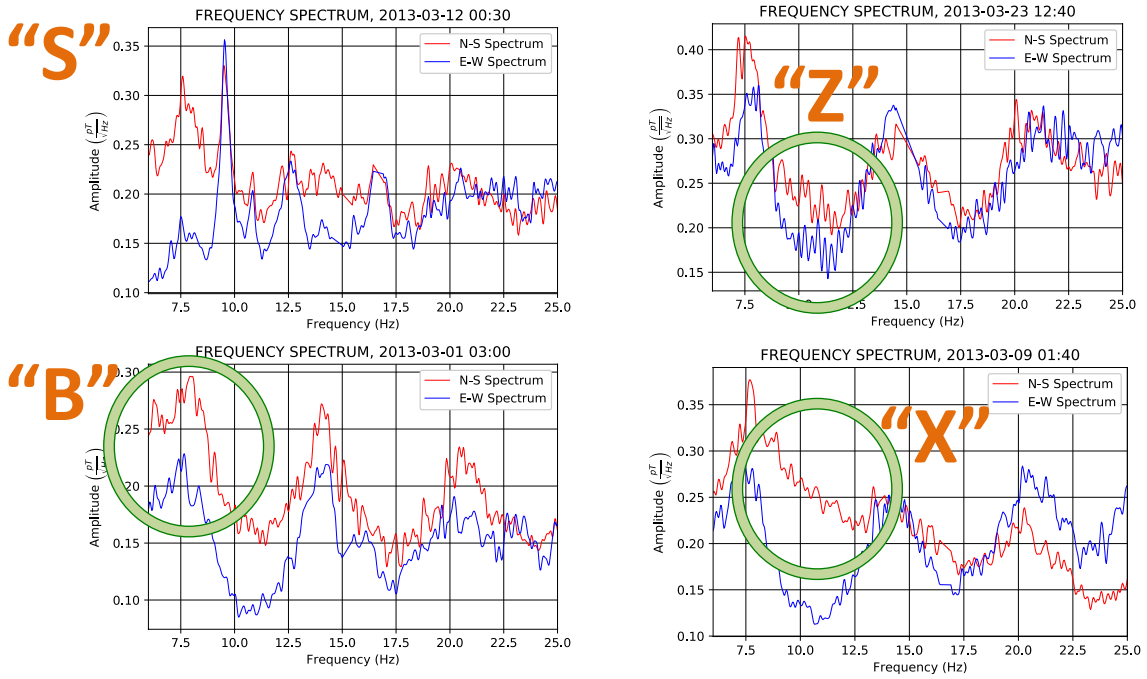

Figure 8.11. Some anomalies detected in the amplitude spectra.

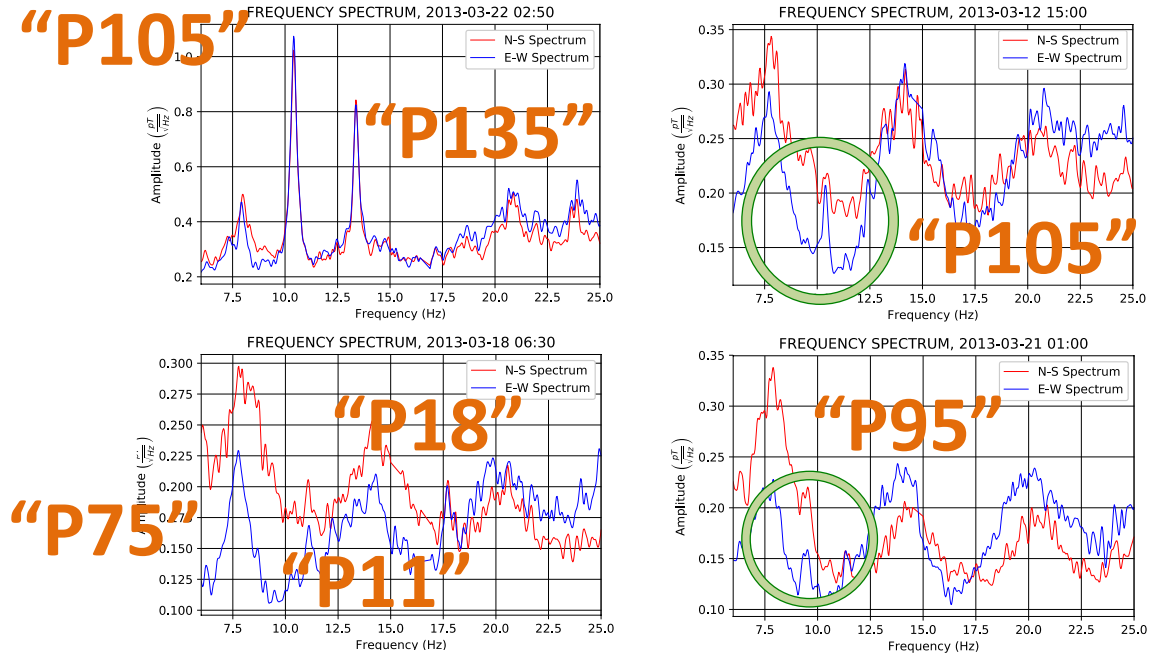

Figure 8.12. Some anomalous peaks detected in the amplitude spectra.

In order to facilitate the analysis of the anomalous spectra, two notebooks have been created:

- The notebook `Generation_Anomalies.ipynb` generates, from the visual recordings of the anomalies mention above (stored in the folder `Records`), a `npy` file for each type of anomaly that contains the time intervals for which that anomaly is observed.
- The notebook `Anomalies.ipynb` contains some functions to visualize and study the spectra for those intervals that show any anomaly. It contains many more examples of anomalies.

Both notebooks, together with the data, can be downloaded from the link:

https://hdl.handle.net/10481/78098

Some functions are proposed in `Anomalies.ipynb` to deal with the anomalous spectra.

The first function is `localize_anom`. It has been created to know for which time intervals a certain anomaly occurs. The chart generated is a color mesh that indicates the time intervals for which the anomaly occurs in both components (NS) and (EW) and the time intervals for which only one component shows the anomaly. We have an example of plot using this function in Figure 8.13.

For the anomalies of the types `'S'`, `'Z'`, `'A'` and `'X'` there is not an hour of the day in which they occur more frequently. For the anomaly `'B'`, we observe that it happens

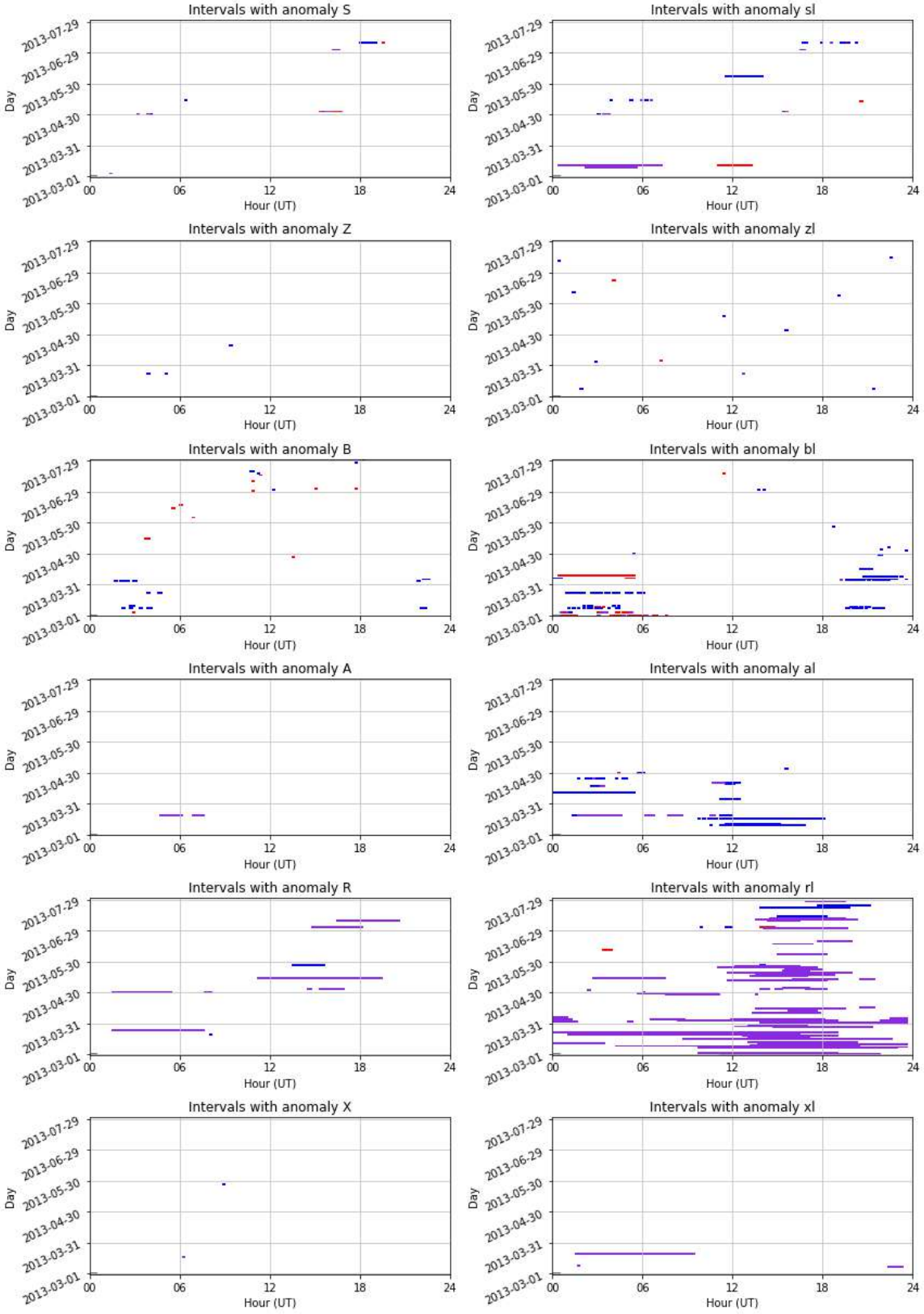

Figure 8.13. Time intervals for which each of the anomalies occurs. In purple, the time intervals for which the anomaly occurs both for the NS and for the EW components. In red (or blue), the time intervals for which the anomaly occurs only for the NS (or for the EW) component.

mostly during the evening and the night, and the anomaly `'R'` is mainly detected in the afternoon. March is the month with the greatest number of anomalous intervals in the analyzed series.

In the notebook `Anomalies.ipynb`, the dates and times at which the rest of the anomalies appear are shown.

The second function defined in that notebook is `identify_anom`. It finds the time intervals for which a certain anomaly is observed. The input of this function is the code of the anomaly, `cod`, and the outputs are:

- `len(intervs)`: the number of time intervals for which the anomaly `cod` is present.
- `times`: an array containing the dates and hours of the time intervals for which the anomaly `cod` is present.
- `intervs`: a 3 element array containing the number of the day, the number of the day time interval and the chronological number of order for all the time intervals that have the anomaly `cod`.

For example, if the function `identify_anom` is called with the parameter `'pl14'`, the number of intervals with that anomaly is `9`, those time intervals are:

```
'2013-03-18 08:50:00' '2013-03-18 09:20:00' '2013-03-19 00:50:00'
'2013-03-19 06:30:00' '2013-03-19 07:30:00' '2013-03-19 08:40:00'
'2013-06-21 04:00:00' '2013-07-01 08:40:00' '2013-07-14 15:50:00'
```

For some time intervals, more than one anomaly occur. The third function of the notebook is `all_anomalies`, and it returns all the anomalies that affect the amplitude spectra in a given day and hour. Examples of the use of this function are:

- `all_anomalies('2013-03-18','06:50')=['pl18'].`
- `all_anomalies('2013-06-11','14:30')=['el1_0','el2_0','pl21_0'].`
- `all_anomalies('2013-03-10','02:40')=['B_1','sl'].`

The fourth function of the notebook, `plot_anom`, defined in the cell below, allows to plot the spectra for a time interval showing a specific anomaly. The input arguments of this function are `cod` (the anomaly that we are looking for) and `kk` (the number of order of the time interval to visualize among all those that have the anomaly indicated by `cod`). An example of use of this function is shown in Figure 8.14.

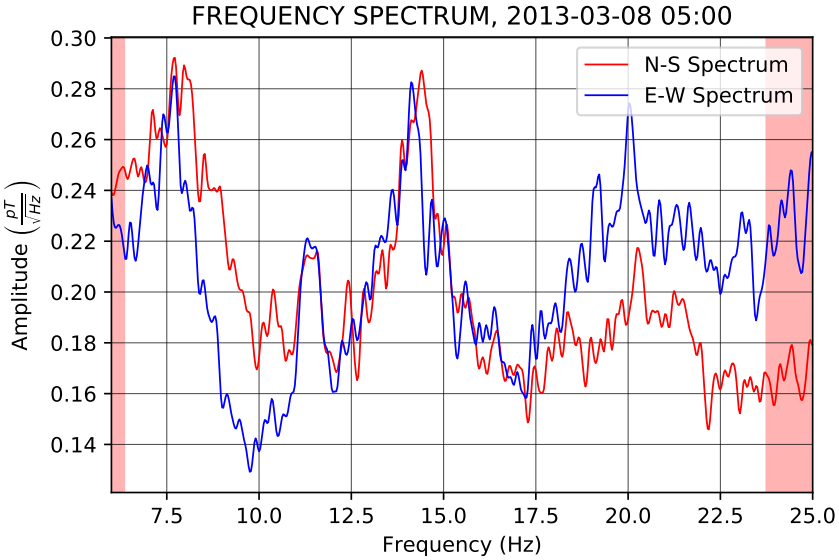

Figure 8.14. Spectra for a time interval that shows the anomaly `'P115'`, obtained calling `all_anomalies('P115',1)`.

The fifth function for the study of the anomalous intervals is `anomalies_table`. It creates a table that collects the number of time intervals that show each anomaly for each month within two given dates. If we run the function between the dates `'2013-03-01'` and `'2013-07-31'`, we obtain the information given in Table 8.3.

Anomaly	March	April	May	June	July	Total
rl	1017	362	343	50	134	1906
P105	381	0	0	0	0	381
pl8	48	2	165	1	0	216
pl105	183	0	1	0	0	184
al_1	112	71	1	0	0	184
R	37	27	62	0	45	171
pl8_0	0	6	127	4	3	140
bl_1	61	62	4	0	2	129
P13	96	0	0	0	0	96

Table 8.3. Number of time intervals affected by each anomaly, for each month between March, 2013 to July, 2013, obtained using the function `anomalies_table`.

As we can see in that table, the most frequent anomaly is, by far, `rl`, followed by `P105`, `pl8`, `pl105`, `al_1`, `R`, `pl8_0` and `bl_1`. March is the month with the greatest number of anomalies.

The seventh function is `plot_all_affected`. It can be used to plot all the spectra that show a given anomaly, sorted by chronological order. Some examples of its use can be seen in the notebook.

The eighth and last function that will be presented in this section is `anomalies_influence`. This function has been created to study how the presence of a certain anomaly affects the value of the SR parameters. The most important input arguments of the function are the following ones:

- `cods`: a list of `str` with the codes of the anomalies whose influence in the variation of the parameter `par` is studied.
- `par`: a `str` with the code of the SR parameter for which we want to determine if its variations are influenced by the anomalies listed in `cods`.
- `fei`: the initial date of the study, in `str` format.
- `fei`: the final date of the study, in `str` format.
- `masked`: a boolean value, if `masked=True`, only the unmasked time intervals are plotted in the graph, whereas if `masked=False`, both the masked and the unmasked time intervals are plotted in the graph.

As can be seen in the notebooks, the parameter variations are plot in green for the time intervals that do not show any anomaly, in blue for the time intervals that show any anomaly (different from the anomalies selected in `cods`), and in red for the time intervals that show the anomalies selected in `cods`. Some examples of figures obtained with this function are in Figure 8.15. In those graphs, the influence is analyzed only for the days between 1st and 7th of May 2013, in order to clarify the graphs. In the notebook `Anomalies.ipynb` the graphs can be customized.

We observe an influence of the `'S'`, `'S_0'`, `'s'` and `'s_0'` anomalies on the parameter `fp1` for the NS sensor within the days plotted. When these anomalies are present in the spectra, the parameter `fp1` for the NS component shows an unusually low value.

By changing the parameter `par` in the notebook, it can be seen that all the parameters (`p1_0`, `p2_0`, `p3_0`, `fp1_0`, `fp2_0`, ...) show anomalous values when the anomalies `'S'`, `'S_0'`, `'s'` and `'s_0'` are present.

We can also observe in Figure 8.15 that the value of the parameter `p1` for the NS component is particularly high for the intervals that show the anomalies `'R', 'R_0'`. The same conclusion is valid for the rest of the parameters, what can be checked by changing the input parameter `par` of the function in the notebook.

When the anomalies `'rl'`, `'r_0'` are present, the parameter `p1` for the NS component usually shows an ordinary value, only sometimes it shows an anomalous value. The same conclusion is valid for the rest of the parameters, what can be checked by changing the parameter for the plot in the notebook.

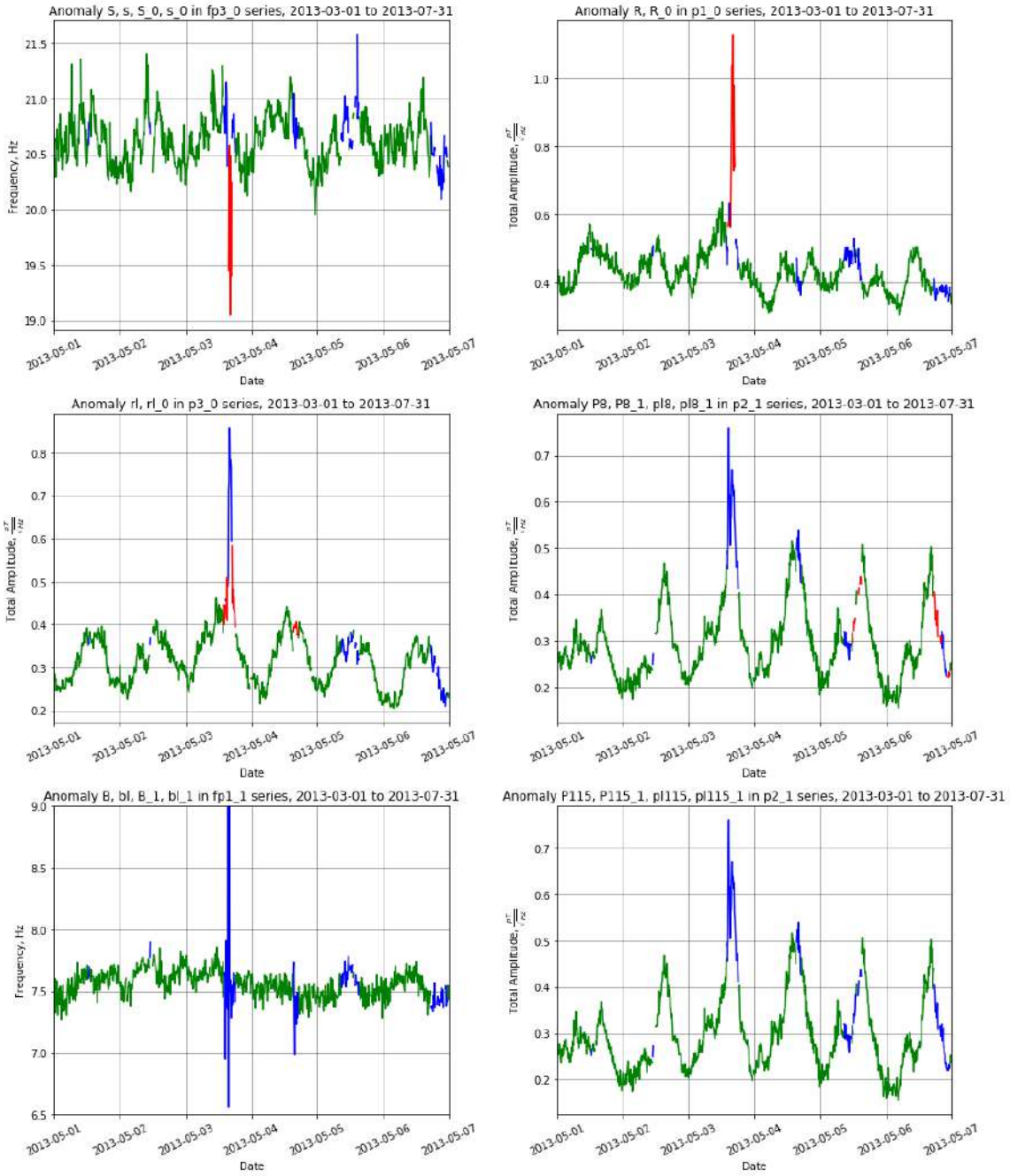

Figure 8.15. The parameter values for the time intervals in which no anomaly is present are plotted in green. When an anomaly different from the anomalies listed in `cods` is present, the parameter values are plotted in blue. When one of the anomalies listed in `cods` is present, the parameter values are plotted in red. The selected anomalies are listed, for each plot, in its title.

When the anomalies `'P8'`, `'P8_1'`, `'pl8'`, `'pl8_1'` are present, sometimes the value of `p2_1` is anomalous, but sometimes it is ordinary. This is also valid for the other parameters. When the anomalies `'B'`, `'b'`, `'B_1'`, `'bl_1'` are present, the value of `'fp1_1'` is usually anomalous. The anomalies `'P115'`, `'P115_1'`, `'pl115'`, `'pl115_1'`, however, do not affect the value of `p2_1`.

Chapter 9. Conclusions

1. A processing methodology to extract the SR parameters from the horizontal (NS and EW components) magnetic field recorded at the Sierra Nevada ELF station has been presented. It is divided into four stages.

   In the first stage, the amplitude spectra for each ten minute time interval of recordings has been obtained using the Welch method and employing a normalized Hann window. Three different time windows, of 10-, 20-, and 30-s duration, have been considered. As regards the second stage, the measurements at the Sierra Nevada ELF station are affected by anthropogenic noise, which appears as 3 narrow peaks in the amplitude spectra, located always at the same frequency bands, that follow a diurnal pattern of evolution. The linear interpolation has been applied to remove this noise because it is faster, more effective and more reproducible than the statistical techniques attempted. It works adequately with almost all the spectra. The third stage consists of the curve fitting process. Lorentzian and Gaussian functions have been considered. The optimization methods CG, QN and LM have been compared. A comparison of several fitting bands has been performed, using the band 6.35-23.75 Hz as a reference. Finally, different possibilities to define the SR amplitudes and central frequencies have been explored: (i) the individual mode amplitudes and the individual resonance frequencies; (ii) the global mode amplitudes and the individual resonance frequencies; and (iii) the local maximum amplitudes and the local maximum central frequencies.

2. The values obtained for the SR parameters considerably depend on the choice of the options and the parameters that appear in the methodology. The procedure to extract the SRs from ELF station measurements is far from being uniquely defined. The existence of a future global network of ELF stations to use the recorded data for the study of global atmospheric, climate and space phenomena has been proposed by the scientific community in different occasions, however, some decisions on the methodology used to obtain the SR parameters should be addressed before to standardize the processing method.

   The MRD of the results obtained using different Hann window sizes may reach the 6%. The 10-s windows are better to deal with the saturations. If the noise filtering process is applied to all the time intervals, even when no human noise is detected, the difference between the resulting SR parameters values is below 2% with respect to the application of the filter only when the noise is detected.

   Lower square error values appear when using Lorentzian functions. Gaussian functions frequently give results out of the expected range. The QN and LM

methods give more precise fits. The LM method is 1 order of magnitude faster than the QN. Differences up to 25% may appear for the individual mode amplitudes and the resonance widths for different minimization methods (LM vs QN). These differences reduce to less than 2% for the individual mode central frequencies and for the global mode amplitudes. The local maximum amplitudes and the local maximum central frequencies are more stable, interpretative and exact values. Differences below 1% have been found between global mode amplitudes and local maximum amplitudes, and between the corresponding frequencies.

3. A scheme to perform a systematic study of the regular variations of the SR parameters has been presented.

   The time intervals that present anomalous values for the SR parameters must be masked (discarded) from the study of the long term regular variations. A masking process has been proposed, and the acceptable ranges for the values of the parameters have been determined making use of a statistical study.

   A wide collection of notebooks has been designed to easily visualize and study the regular variations of the SRs at different time scales (diurnal, daily, monthly, seasonal, annual). Other information, like the saturation rate, the ratio of masked intervals or the χ^2 of the fits has also been taken into consideration in our study.

4. The diurnal, daily, seasonal, monthly and annual variations of the SR parameters (amplitudes, central frequencies, widths and power spectrum integrals) have been presented for the recordings at the Sierra Nevada station between March, 2013, and February, 2017.

5. The relation between the SR variations and some atmospheric and space phenomena has been studied.

   The diurnal pattern of evolution of the three main lightning centers on the globe (Africa, Asia, and America) has been confirmed. The lightning activity is maximal in the boreal summer, whereas it is minimal in the boreal winter. The African center shows the largest intensity, and the Asian center shows the longest daily duration.

   The interannual variation of the SR1 central frequency shows a minimum in 2014, when the solar activity had a rise.

   Some previous predictions about the effect of El Niño on the SRs seem to be detected in the annual variation obtained for the first mode peak amplitude, `p1`. An intensification of the SRs is observed during the transition months that precede the super El Niño episode (between the end of 2015 and the beginning of 2016).

6. The principal components of the temporal evolution of the SR parameters extracted from the Sierra Nevada recordings have been obtained using Singular Spectrum Analysis, together with their frequency content.

   For almost all the parameters studied, the three first principal components correspond to a constant component, an annual component and a semiannual component, respectively.

7. Some time intervals show anomalies in their amplitude spectra. A visual inspection of these anomalies has been performed. These anomalies can be classified into different types, and their influence on the value of the SR parameters can be analyzed.

   A collection of functions have been devised to visualize and study these anomalies.

   We have found that, when the SRs are not clearly distinguishable in the spectra (anomaly `'S'` and related), it affects the value of the parameters. When the spectra are noisy (anomaly `'R'` and related), it sometimes affects the value of the parameters, but sometimes there is no influence. The anomalies that corresponds to strange peaks in the spectra, only sometimes affects the value of the parameters.

8. The data and the codes, functions and notebooks used in this thesis have been put at disposal of the scientific community. The data and the codes have been shared at three different levels of processing: (i) the raw TD magnetic field (NS and EW components) recordings at the Sierra Nevada ELF station; (ii) intermediate results with the amplitude spectra and the SR parameters values, as well as other relevant information listed in chapter 5, in the form of npz files for each month and sensor of the recordings; and (iii) the final set codes, functions and notebooks, together with the final SR parameters data in the form of tables and some results (charts) of the study of their variations. Links to the raw, intermediate and final data are at the end of chapter 5. The collection of notebooks to study the SR parameters variations is available at section 6.3. The code to apply the Singular Spectrum Analysis to the temporal evolution of the parameters is in section 8.1, and the notebooks to study the anomalies are available in section 8.2.

References

Aich, V., Holzworth, R., Goodman, S., Kuleshov, Y., Price, C., & Williams, E. (2018). Lightning: A new essential climate variable. *Eos*, *99*. https://doi.org/10.1029/2018eo104583

Balser, M., & Wagner, C. A. (1960). Observations of Earth-ionosphere cavity resonances. *Nature*, *188*, 638–641. https://doi.org/10.1038/188638a0

Balser, M., & Wagner, C. A. (1962). On frequency variations of the Earth-ionosphere cavity modes. *Journal of Geophysical Res.*, *67*(10), 4081–4083. https://doi.org/10.1029/JZ067i010p04081

Bartlett, M. S. (1948). Smoothing periodograms from time series with continuous spectra. *Nature*, *161*, 686–687. https://doi.org/10.1038/161686a0

Belyaev, G. G., Schekotov, A. Y., Shvets, A. V., & Nickolaenko, A. P. (1999). Schumann resonances observed using Poynting vector spectra. *Journal of Atmospheric and Solar-Terrestrial Physics*, *61*(10), 751–763. https://doi.org/10.1016/S1364-6826(99)00027-9

Besser, B. P. (2007). Synopsis of the historical development of Schumann resonances. *Radio Science*, *42*(2), RS2S02. https://doi.org/10.1029/2006RS003495

Betz, H. D., Schumann, U., & Laroche, P. (2009). *Lightning: Principles, instruments and applications: Review of modern lightning research*. Springer Netherlands. https://doi.org/10.1007/978-1-4020-9079-0

Blakeslee, R. J., Mach, D. M., Bateman, M. G., & Bailey, J. C. (2014). Seasonal variations in the lightning diurnal cycle and implications for the global electric circuit. *Atmospheric Research*, *135-136*(Supplement C), 228–243. https://doi.org/10.1016/j.atmosres.2012.09.023

Bozóki, T., Sátori, G., Williams, E., Mironova, I., Steinbach, P., Bland, E. C., Koloskov, A., Yampolski, Y. M., Budanov, O. V., Neska, M., Sinha, A., Rawat, R., Sato, M., Beggan, C., Toledo-Redondo, S., Liu, Y., & Boldi, R. (2021). Solar cycle-modulated deformation of the earth–ionosphere cavity. *Frontiers in Earth Science*, *9*, 735. https://doi.org/10.3389/feart.2021.689127

Broomhead, D. S., & King, G. P. (1986). Extracting qualitative dynamics from experimental data. *Physica D: Nonlinear Phenomena*, *20*(2-3), 217–236. https://doi.org/10.1016/0167-2789(86)90031-X

Castro, F., Toledo-Redondo, S., Fornieles, J., Salinas, A., Portí, J., Navarro, E., & Sierra, P. (2017). Modelling Schumann resonances from ELF measurements using non-linear optimization methods. *EGU General Assembly Conference Abstracts*, 7206.

Chen, A. B., Kuo, C. L., Lee, Y. J., Su, H.-T., Hsu, R. R., Chern, J. L., Frey, H. U., Mende, S. B., Takahashi, Y., Fukunishi, H., et al. (2008). Global distributions and occurrence rates of transient luminous events. *Journal of Geophysical Research: Space Physics*, *113*(A8). https://doi.org/10.1029/2008JA013101

Christian, H. J., Blakeslee, R. J., Boccippio, D. J., Boeck, W. L., Buechler, D. E., Driscoll, K. T., Goodman, S. J., Hall, J. M., Koshak, W. J., Mach, D. M., et al. (2003). Global frequency and distribution of lightning as observed from space by the Optical Transient Detector. *Journal of Geophysical Research: Atmospheres*, *108*(D1), ACL–4–1–ACL 4–15. https://doi.org/10.1029/2002jd002347

Dyrda, M., Kulak, A., Mlynarczyk, J., Ostrowski, M., Kubisz, J., Michalec, A., & Nieckarz, Z. (2014). Application of the Schumann resonance spectral decomposition in characterizing the main African thunderstorm center. *Journal of Geophysical Research: Atmospheres*, *119*, 13, 338–13, 349. https://doi.org/10.1002/2014JD022613

Fornieles-Callejón, J., Salinas, A., Toledo-Redondo, S., Portí, J., Méndez, A., Navarro, E. A., Morente-Molinera, J. A., Soto-Aranaz, C., & Ortega-Cayuela, J. S. (2015). Extremely low frequency band station for natural electromagnetic noise measurement. *Radio Science*, *50*, 191–201. https://doi.org/10.1002/2014RS005567

Füllekrug, M., & Fraser-Smith, A. C. (1997). Global lightning and climate variability inferred from ELF magnetic field variations. *Geophysical Research Letters*, *24*(19), 2411–2414. https://doi.org/10.1029/97GL02358

Geem, C. H., Jadin, M. S., & Mohamed, A. I. (2006). Observation of Transient Luminous Events (TLEs) in Pekan. *ARPN Journal of Engineering and Applied Sciences*, *10*(22).

Granger, B., & Perez, F. (2021). Jupyter: Thinking and storytelling with code and data. *Computer Science and Engineering*, *23*(2), 7–14. https://doi.org/10.1109/MCSE.2021.3059263

Greenberg, E., & Price, C. (2004). A global lightning location algorithm based on the electromagnetic signature in the Schumann resonance band. *Journal of Geophysical Research: Atmospheres*, *109*, D21111. https://doi.org/10.1029/2004JD004845

Greenberg, E., & Price, C. (2007). Diurnal variations of ELF transients and background noise in the Schumann resonance band. *Radio Science*, *42*, RS2S08. https://doi.org/10.1029/2006RS003477

Hassani, H. (2007). Singular spectrum analysis: Methodology and comparison. *Journal of Data Science*, *5*(2), 239–257. https://doi.org/10.6339/JDS.2007.05(2).396

Invernón, F. J. P. (2018). *Modelling atmospheric electricity phenomena in the atmospheres of Venus, Earth, Jupiter and Saturn* (Doctoral dissertation). Universidad de Granada.

Koloskov, A. V., Nickolaenko, A. P., Yampolsky, Y. M., Hall, C., & Budanov, O. V. (2020). Variations of global thunderstorm activity derived from the long-term Schumann resonance monitoring in the Antarctic and in the Arctic. *Journal of Atmospheric and Solar-Terrestrial Physics*, *201*, 105231. https://doi.org/10.1016/j.jastp.2020.105231

Kulak, A., Kubisz, J., Michalec, A., Zieba, S., & Nieckarz, Z. (2003). Solar variations in extremely low frequency propagation parameters: 2. Observations of Schumann resonances and computation of the ELF attenuation parameter. *Journal of Geophysical Research*, *108*(A7). https://doi.org/10.1029/2002JA009305

Kulak, A., Kubisz, J., Klucjasz, S., Michalec, A., Mlynarczyk, J., Nieckarz, Z., Ostrowski, M., & Zieba, S. (2014). Extremely low frequency electromagnetic field measurements at the Hylaty station and methodology of signal analysis. *Radio Science*, *49*, 361–370. https://doi.org/10.1002/2014RS005400

Melnikov, A., Price, C., Sátori, G., & Füllekrug, M. (2004). Influence of solar terminator passages on Schumann resonance parameters. *Journal of Atmospheric and Solar-Terrestrial Physics*, *66*(13), 1187–1194. https://doi.org/10.1016/j.jastp.2004.05.014

Mushtak, V. C., & Williams, E. R. (2009). An improved Lorentzian technique for evaluating resonance characteristics of the Earth-ionosphere cavity. *Atmospheric Res.*, *91*(2), 188–193.

Newville, M., Stensitzki, T., Allen, D. B., & Ingargiola, A. (2014). LMFIT: Non-linear least-square minimization and curve-fitting for Python. https://doi.org/10.5281/zenodo.11813

Nickolaenko, A. P., & Hayakawa, M. (2002). *Resonances in the Earth-Ionosphere Cavity*. Dordrecht, Netherlands: Kluwer Academy.

Nickolaenko, A. P., & Hayakawa, M. (2014). *Schumann Resonance for Tyros*. Springer, Japan.

Nickolaenko, A. P., Hayakawa, M., & Hobara, Y. (1999). Long-term periodical variations in global lightning activity deduced from the Schumann resonance monitoring. *Journal of Geophysical Research*, *104(D22)*, 27585–27591. https://doi.org/10.1029/1999jd900791

Nickolaenko, A. P., Koloskov, A. V., Hayakawa, M., Yampolski, Y. M., Budanov, O. V., & Korepanov, V. E. (2015). 11-year solar cycle in Schumann resonance data as observed in Antarctica. *Sun and Geosphere*, *10*(1), 39–49.

Nickolaenko, A. P., & Rabinowicz, L. M. (1995). Study of the annual changes of global lightning distribution and frequency variations of the first Schumann resonance mode. *Journal of Atmospheric and Terrestrial Physics*, *57*(11), 1345–1348. https://doi.org/10.1016/0021-9169(94)00114-4

Nickolaenko, A. P., Shvets, A., & Hayakawa, M. (2016). Extremely low frequency (ELF) radio wave propagation: A review. *International Journal of Electronics and Applied Research (IJEAR)*, *3*(2), 91.

Nickolaenko, A. P., Yatsevich, E. I., Shvets, A. V., Hayakawa, M., & Hobara, Y. (2011). Universal and local time variations deduced from simultaneous Schumann resonance records at three widely separated observatories. *Radio Science*, *46*, RS5003. https://doi.org/10.1029/2011RS004663

Nickolaenko, A., Sátori, G., Zieger, B., Rabinowicz, L., & Kudintseva, I. (1998). Parameters of global thunderstorm activity deduced from the long-term Schumann resonance records. *Journal of Atmospheric and Solar-Terrestrial Physics*, *60*(3), 387–399. https://doi.org/10.1016/S1364-6826(97)00121-1

Ogawa, T., Tanaka, Y., Miura, T., & Yasuhara, M. (1966). Observations of natural ELF and VLF electromagnetic noises by using ball antennas. *Journal of Geomagnetism and Geoelectricity*, *18*(4), 443–454. https://doi.org/10.5636/jgg.18.443

Ondrášková, A., Kostecký, P., Rosenberg, L., et al. (2007). Long-term observations of Schumann resonances at Modra observatory. *Radio Science*, *42*(02), 1–12.

Ondrášková, A., Ševčík, S., & Kostecký, P. (2011). Decrease of Schumann resonance frequencies and changes in the effective lightning areas toward the solar cycle minimum of 2008-2009. *Journal of Atmospheric and Solar-Terrestrial Physics*, *73*(4), 534–543. https://doi.org/10.1016/j.jastp.2010.11.013

Ondrášková, A., & Ševčík, S. (2013). The determination of Schumann resonance mode frequencies using iterative procedure of complex demodulation. *Contributions to Geophysics and Geodesy*, *43*(4), 305–326. https://doi.org/10.2478/congeo-2013-0018

Ondrášková, A., & Ševčík, S. (2014). The iterative complex demodulation applied on short and long Schumann resonance measured sequences. *Contributions to Geophysics and Geodesy*, *44*(4), 313–328. https://doi.org/10.1515/congeo-2015-0008

Oppenheim, A., & Shafer, R. W. (2009). *Discrete-Time Signal Processing, Prentice Hall Signal Processing Series* (3rd ed.). NJ: Prentice Hall.

Ouyang, X. Y., Xiao, Z., Hao, Y. Q., & Zhang, D. H. (2015). Variability of Schumann resonance parameters observed at low latitude stations in China. *Advances in Space Research*, *56*(7), 1389–1399. https://doi.org/10.1016/j.asr.2015.07.006

Pasko, V. P. (2010). Recent advances in theory of transient luminous events. *Journal of Geophysical Research: Space Physics*, *115*(A6). https://doi.org/10.1029/2009JA014860

Passas, M. (2017). Design and development of a spectrograph and polarimeter for the analysis of air plasmas produced by transient luminous events in the mesosphere of the Earth.

Pechony, O., & Price, C. (2006). Schumann resonances: Interpretation of local diurnal intensity modulations. *Radio Science*, *41*(2), RS2S05. https://doi.org/10.1029/2006RS003455

Peterson, M., Mach, D., & Buechler, D. (2021). A global LIS/OTD climatology of lightning flash extent density. *Journal of Geophysical Research: Atmospheres*, *126*(8), e2020JD033885. https://doi.org/10.1029/2020JD033885

Prácser, E., Bozóki, T., Sátori, G., Williams, E., Guha, A., & Yu, H. (2019). Reconstruction of global lightning activity based on Schumann resonance measurements: Model description and synthetic tests. *Radio Science*, *54*(3), 254–267. https://doi.org/10.1029/2018RS006772

Press, W., Flannery, B., Teukolsky, S., & Vetterling, W. (1992). *The art of scientific computing*. New York: Cambridge University Press.

Price, C., & Melkinov, A. (2004). Diurnal, seasonal and inter-annual variations in the Schumann resonance parameters. *Journal of Atmospheric and Solar-Terrestrial Physics.*, *66(13-14)*, 1179–85. https://doi.org/10.1016/j.jastp.2004.05.004

Price, C., & Rind, D. (1992). A simple lightning parameterization for calculating global lightning distributions. *Journal of Geophysical Research: Atmospheres*, *97*(D9), 9919–9933. https://doi.org/10.1029/92JD00719

Price, C. (2000). Evidence for a link between global lightning activity and upper tropospheric water vapour. *Nature*, *406*(6793), 290–293. https://doi.org/10.1038/35018543

Price, C. (2016). ELF electromagnetic waves from lightning: the Schumann resonances. *Atmosphere*, *7*(9), 116. https://doi.org/10.3390/atmos7090116

Rodríguez-Camacho, J., Fornieles, J., Carrión, M. C., Portí, J. A., Toledo-Redondo, S., & Salinas, A. (2018a). On the need of a unified methodology for processing Schumann resonance measurements. *Journal of Geophysical Research: Atmospheres*, *123*(23). https://doi.org/10.1029/2018JD029462

Rodríguez-Camacho, J., Salinas, A., Carrión, M. C., Portí, J., Fornieles-Callejón, J., & Toledo-Redondo, S. (2022). Four year study of the Schumann resonance regular variations using the Sierra Nevada station ground-based magnetometers. *Journal of Geophysical Research: Atmospheres*, *127*(6), e2021JD036051. https://doi.org/10.1029/2021JD036051

Rodríguez-Camacho, J., Blanco, D., Gómez-Lopera, J. F., Fornieles-Callejón, J., & Carrión, M. C. (2017). A new method for anthropogenic noise removal in the ELF band based on ICA technique. *2017 Computing and Electromagnetics International Workshop (CEM)*, 23–24. https://doi.org/10.1109/CEM.2017.7991868

Rodríguez-Camacho, J., Blanco-Navarro, D., Gómez-Lopera, J. F., & Carrión, M. C. (2021). Application of the Singular Spectrum Analysis to the time variations of the amplitude of Schumann resonance measurements. *2020 28th European Signal Processing Conference (EUSIPCO)*, 2215–2219. https://doi.org/10.23919/Eusipco47968.2020.9287566

Rodríguez-Camacho, J., Blanco-Navarro, D., Gómez-Lopera, J. F., Fornieles-Callejón, J., & Carrión, M. C. (2018b). Separation of anthropogenic noise and Extremely Low Frequency natural magnetic field using statistical features. *2018 26th European Signal Processing Conference (EUSIPCO)*, 2405–2409. https://doi.org/10.23919/EUSIPCO.2018.8553019

Rodríguez-Camacho, J., Fornieles-Callejon, J., Gomez-Lopera, J. F., Salinas, A., Portí, J., Blanco, D., & Carrión, M. C. (2019a). An approach for long-term study of Schumann resonances. *Geophysical Research Abstracts*, *21*.

Rodríguez-Camacho, J., Lopera, J. F. G., Salinas, A., Fornieles-Callejón, J., Portí, J., Blanco-Navarro, D., Carrión, M. C., & Camba, E. N. (2019b). Graphical schemes designed to display and study the long-term variations of Schumann resonance. *2019 27th European Signal Processing Conference (EUSIPCO)*, 1–5. https://doi.org/10.23919/EUSIPCO.2019.8903030

Roldugin, V. C., Maltsev, Y. P., Vasiljev, A. N., Schokotov, A. Y., & Belyajev, G. G. (2004). Diurnal variations of Schumann resonance frequency in NS and EW magnetic components. *Journal of Geophysical Research: Space Physics*, *109*, A08304. https://doi.org/10.1029/2004JA010487

Roldugin, V. C., Vasiljev, A. N., & Ostapenko, A. A. (2006). Comparison of the Schumann resonance parameters in horizontal magnetic and electric fields according to observations on the Kola Peninsula. *Radio Science*, *41*(2), RS2S07. https://doi.org/10.1029/2006RS003475

Rycroft, M. J., Israelsson, S., & Price, C. (2000). The global atmospheric electric circuit, solar activity and climate change. *Journal of Atmospheric and Solar-Terrestrial Physics*, *62*(17), 1563–1576. https://doi.org/10.1016/S1364-6826(00)00112-7

Rycroft, M. J., Harrison, R. G., Nicoll, K. A., & Mareev, E. A. (2008). An overview of Earth's global electric circuit and atmospheric conductivity. *Space Science Reviews*, *137*, 83–105. https://doi.org/10.1007/978-0-387-87664-1_6

Salinas, A., Rodríguez-Camacho, J., Portí, J., Carrión, M. C., Fornieles-Callejón, J., & Toledo-Redondo, S. (2022a). Schumann resonance data processing programs and four-year measurements from Sierra Nevada ELF station. *Computers and Geosciences*, 105148.

Salinas, A., Toledo-Redondo, S., Navarro, E. A., Fornieles-Callejón, J., & Portí, J. A. (2016). Solar storm effects during Saint Patrick's Days in 2013 and 2015 on the Schumann resonances measured by the ELF station at Sierra Nevada (Spain). *Journal of Geophysical Research: Space Physics*, *121*, 12, 234–12, 246. https://doi.org/10.1002/2016JA023253

Salinas, A., Rodríguez-Camacho, J., Portí, J., Carrión, M. C., Fornieles-Callejón, J., & Toledo-Redondo, S. (2022b). Four-year measurements from Sierra Nevada ELF station. Zenodo. Year 2014 [Data set]. https://doi.org/10.5281/zenodo.6348691

Salinas, A., Rodríguez-Camacho, J., Portí, J., Carrión, M. C., Fornieles-Callejón, J., & Toledo-Redondo, S. (2022c). Four-year measurements from Sierra Nevada ELF station. Zenodo. Year 2015 [Data set]. https://doi.org/10.5281/zenodo.6348773

Salinas, A., Rodríguez-Camacho, J., Portí, J., Carrión, M. C., Fornieles-Callejón, J., & Toledo-Redondo, S. (2022d). Four-year measurements from Sierra Nevada ELF station. Zenodo. Year 2016 [Data set]. https://doi.org/10.5281/zenodo.6348930

Salinas, A., Rodríguez-Camacho, J., Portí, J., Carrión, M. C., Fornieles-Callejón, J., & Toledo-Redondo, S. (2022e). Four-year measurements from Sierra Nevada ELF station. Zenodo. Years 2013, p.2017 [Data set]. https://doi.org/10.5281/zenodo.6348930

Sátori, G. (1996). Monitoring Schumann resonances-II. Daily and seasonal frequency variations. *Journal of Atmospheric and Terrestrial Physics*, *58*(13), 1483–1488. https://doi.org/10.1016/0021-9169(95)00146-8

Sátori, G., Williams, E., & Lemperger, I. (2009). Variability of global lightning activity on the ENSO time scale. *13th International Conference on Atmospheric Electricity ICAE 2007*, *91*(2–4), 500–507. https://doi.org/10.1016/j.atmosres.2008.06.014

Sátori, G., Williams, E., & Mushtak, V. (2005). Response of the Earth–ionosphere cavity resonator to the 11-year solar cycle in X-radiation. *Journal of Atmospheric and Solar-Terrestrial Physics*, *67*(6), 553–562. https://doi.org/10.1016/j.jastp.2004.12.006

Sátori, G., Williams, E., & Boccippio, D. (2003). On the dynamics of the North-South seasonal migration of global lightning. *Paper presented at AGU Fall Meeting, San Francisco, December 8–12.*, *2003*, Abstract no.: AE32A–0167.

Sátori, G. (2003). On the dynamics of the North-South seasonal migration of global lightning. *Paper presented at 12th international conference on atmospheric electricity. Versailles, France. Global Lightning and Climate.*

Sátori, G., Rycroft, M., Bencze, P., Märcz, F., Bór, J., Barta, V., Nagy, T., & Kovács, K. (2013). An overview of thunderstorm-related research on the atmospheric electric field, Schumann resonances, sprites, and the ionosphere at Sopron, Hungary. *Surveys in Geophysics*, *34*(3), 255–292. https://doi.org/10.1007/s10712-013-9222-6

Sátori, G., & Zieger, B. (1999). El Niño related meridional oscillation of global lightning activity. *Geophysical Research Letters*, *26*(10), 1365–1368.

Schlegel, K., & Füllekrug, M. (2000). Diurnal harmonics in Schumann resonance parameters observed on both hemispheres. *Geophysical Research Letters*, *27*(17), 2805–2808. https://doi.org/10.1029/2000GL003774

Schumann, W. O. (1952). Über die stralungslosen Eigenschwingungen einer leitenden Kugel die von einer Luftschicht und einer Ionospärenhle umgeben ist. *Zeitschrift für Naturforschung*, *7a*, 149–154. https://doi.org/10.1515/zna-1952-0202

Sekiguchi, M., Hayakawa, M., Nickolaenko, A. P., & Hobara, Y. (2006). Evidence on a link between the intensity of Schumann resonance and global surface temperature. *Annales Geophysicae*, *24*(7), 1809–1817. https://doi.org/10.5194/angeo-24-1809-2006

Sentman, D. D. (1987). Magnetic elliptical polarization of Schumann resonances. *Radio Science*, *22*(4), 595–606. https://doi.org/10.1029/RS022i004p00595

Sentman, D. D., & Fraser, B. J. (1991). Simultaneous observations of Schumann resonances in California and Australia: evidence for intensity modulation by the local height of the D region. *Journal of Geophysical Research: Space Physics*, *96*(A9), 15973–15984. https://doi.org/https://doi.org/10.1029/91JA01085

Shvets, A. V., Hobara, Y., & Hayakawa, M. (2010). Variations of the global lightning distribution revealed from three-station Schumann resonance measurements. *Journal of Geophysical Research: Space Physics*, *115*(A12), A12316. https://doi.org/10.1029/2010JA015851

Shvets, A., & Hayakawa, M. (2011). Global lightning activity on the basis of inversions of natural ELF electromagnetic data observed at multiple stations around the world. *Surveys in Geophysics*, *32*(6), 705. https://doi.org/10.1007/s10712-011-9135-1

Sierra, F. P., Vázquez, H. S., Andrade, M. E., Mendoza, B., & Rodríguez-Osorio, D. (2014). Development of a Schumann-resonance station in Mexico: Preliminary measurements. *IEEE Antennas and Propagation Magazine*, *56*(3), 112–119. https://doi.org/10.1109/MAP.2014.6867687

Simões, F., Pfaff, R., Berthelier, J.-J., & Klenzing, J. (2012). A review of low frequency electromagnetic wave phenomena related to tropospheric-ionospheric coupling mechanisms. *Space Science Reviews*, *168*(1-4), 551–593. https://doi.org/10.1007/s11214-011-9854-0

Surkov, V., & Hayakawa, M. (2014). *Ultra and extremely low frequency electromagnetic fields*. Springer.

Toledo-Redondo, S., Parrot, M., & Salinas, A. (2012). Variation of the first cut-off frequency of the Earth-ionosphere waveguide observed by DEMETER. *Journal of Geophysical Research: Space Physics*, *117*, A04321. https://doi.org/10.1029/2011JA017400

Toledo-Redondo, S., Salinas, A., Fornieles, J., Portí, J., & Lichtenegger, H. I. M. (2016). Full 3-D TLM simulations of the Earth-ionosphere cavity: Effect of conductivity on the Schumann resonances. *Journal of Geophysical Research: Space Physics*, *121*, 5579–5593. https://doi.org/10.1002/2015JA022083

Toledo-Redondo, S., Salinas, A., Portí, J., Morente, J. A., Fornieles, J., Méndez, A., Galindo-Zaldívar, J., Pedrera, A., Ruiz-Constán, A., & Anahnah, F. (2010). Study of Schumann resonances based on magnetotelluric records from the western Mediterranean and Antarctica. *Journal of Geophysical Research: Atmospheres*, *115*(D22114). https://doi.org/10.1029/2010JD014316

Toledo-Redondo, S. e. a. (2012). *Numerical simulation and experimental study of the natural electromagnetic waves in the elf and vlf bands* (Doctoral dissertation). Granada: Universidad de Granada.

Welch, P. (1967). The use of fast Fourier transform for the estimation of power spectra: A method based on time averaging over short, modified periodograms. *IEEE Transactions on Audio and Electroacoustics*, *15*(2), 70–73. https://doi.org/10.1109/TAU.1967.1161901

Williams, E., Bozóki, T., Sátori, G., Price, C., Steinbach, P., Guha, A., Liu, Y., Beggan, C., Neska, M., Boldi, R., et al. (2021). Evolution of global lightning in the transition from cold to warm phase preceding two super El Niño events. *Journal of Geophysical Research: Atmospheres*, *126*(3), e2020JD033526.

Williams, E. R. (2009). The global electrical circuit: A review. *Atmospheric Research*, *91*, 140–152. https://doi.org/10.1016/j.atmosres.2008.05.018

Williams, E., Guha, A., Boldi, R., Christian, H., & Buechler, D. (2019). Global lightning activity and the hiatus in global warming. *Journal of Atmospheric and Solar-Terrestrial Physics*, *189*, 27–34. https://doi.org/10.1016/j.jastp.2019.03.011

Williams, E. R. (1992). The Schumann Resonance: A global tropical thermometer. *Science*, *256*(5060), 1184–1187. https://doi.org/10.1126/science.256.5060.1184

Williams, E. R. (1994). Global circuit response to seasonal variations in global surface air temperature. *Monthly Weather Review*, *122*(8), 1917–1929. https://doi.org/10.1175/1520-0493(1994)122<1917:GCRTSV>2.0.CO;2

Williams, E. R., Mushtak, V. C., Guha, A., Boldi, R. A., Bor, J., Nagy, T., Satori, G., Sinha, A. K., Rawat, R., Hobara, Y., et al. (2014). Inversion of multi-station Schumann resonance background records for global lightning activity in absolute units. *AGU Fall Meeting Abstracts*, *2014*, 1, AE24A–08.

Williams, E. (2005). Lightning and climate: A review. *Atmospheric research*, *76*(1-4), 272–287. https://doi.org/10.1016/j.atmosres.2004.11.014

Yamashita, K., Takahashi, Y., Sato, M., & Kase, H. (2011). Improvement in lightning geolocation by time-of-arrival method using global elf network data. *Journal of Geophysical Research: Space Physics*, *116*(A2). https://doi.org/10.1029/2009JA014792

Yatsevich, E. I., Nickolaenko, A. P., & Pechonaya, O. B. (2008). Diurnal and seasonal variations in the intensities and peak frequencies of the first three Schumann-resonance modes. *Radiophysics and Quantum Electronics*, *51*(7), 528–538. https://doi.org/10.1007/s11141-008-9056-0

Yatsevich, E. I., Shvets, A. V., & Rabinowicz, L. M. (2005). Two component model of the Schumann resonance signal. *Telecommunications and Radio Engineering*, *64*(7-12). https://doi.org/10.1615/TelecomRadEng.v64.i10.100

Zhou, H., Yu, H., Cao, B., & Qiao, X. (2013a). Diurnal and seasonal variations in the Schumann resonance parameters observed at Chinese observatories. *Journal of Atmospheric and Solar-Terrestrial Physics*, *98*, 86–96. https://doi.org/10.1016/j.jastp.2013.03.021

Zhou, H., Zhou, Z., Qiao, X., & Yu, H. (2013b). Anomalous phenomena in Schumann resonance band observed in China before the 2011 magnitude 9.0 Tohoku-Oki earthquake in Japan. *Journal of Geophysical Research: Atmospheres*, *118*(23), 13–338. https://doi.org/10.1002/2013JD020269

List of Figures